Thèse n° 7831

Experimental evaluation and modeling of fatigue of a 316L austenitic stainless steel in high-temperature water and air environments

Présentée le 2 octobre 2020

à la Faculté des sciences de base
Laboratoire de physique des réacteurs et de comportement des systèmes
Programme doctoral en science et génie des matériaux

pour l'obtention du grade de Docteur ès Sciences

par

Wen CHEN

Acceptée sur proposition du jury

Prof. D. Damjanovic, président du jury
Prof. Ph. Spätig, directeur de thèse
Prof. T. Kruml, rapporteur
Dr M. Bruchhausen, rapporteur
Prof. A. Nussbaumer, rapporteur

École
polytechnique
fédérale
de Lausanne

2020

I will work hard
I will stay strong
I will be kind
I will be happy
I will keep dreaming

To my wife, son and the big family...

Acknowledgements

As the PhD thesis is structured, the acknowledgments are placed before PhD work. Without those lovely people, who directed, supervised, trained, helped, encouraged, even criticized me during the last four years, this work would not have been possible.

First and foremost, I would like to express my sincere gratitude to my thesis director Prof. Dr. Philippe Spätig. Any complimentary words are not excessive to this open-mind, truth-seeking and humorous person. As a thesis director, he is perfect. He always kept his door open for my questions and is open-minded for any new information. When my idea went too high or wild, he treated it gently and guided me to land on the right track. When I am down, such as doing mistakes in experiment, he comforted me and cheered me up. He taught me how to look at mistakes correctly. He guided me in scientific research by working on the problems in experiments, results interpretation together with me, even though it would take him a lot of time. He tirelessly handled my "Chinese English" and helped me to improve my scientific writing. Besides the guidance in the PhD work, he also cared about my future like introducing me possible job opportunities and even helping me to prepare the job interviews.

Then I want to express my special gratitude to my supervisor Hans-Peter Seifert, who made this position possible. Teamed with Philippe, he gave me professional direction in corrosion and environmental assisted fatigue and fracture side. He was always supportive for my training, personal development and attending conferences. He treated my every question/discussion seriously with gorgeous pages of hand writing and prints. I admire his expertise, professional altitude, efficiency, kind heart and hard working. He always gave me pertinent suggestions. I really appreciate his understanding, care and support in my personal life, such as during getting married and having my first baby.

Besides my supervisors, Dr. Elisabeth Müller has spent a large amount of time in training, improving and handling the spontaneous technical issues in TEM. She is a nice lady and always smiling and gentle to the "high-risk" users like me. Working with the complicated and delicate scientific instruments is not easy, but she made my journey much comfortable. I also want to thank Dr. Juxing Bai, Dr. Zaiqing Que and Stefan Ritter. They trained me to use the SEM, EBSD, EDX and ECCI. Without their help, there would have been much trouble in this PhD work.

Furthermore, I want to thank the technician "master" Roger Schwenold and the other members of the technician team: Hans Kottmann, Beat Baumgartner and Lucas Oberer. Roger Schwenold's high-quality work ensured that my experiments ran without big interruption. I was always surprised by his magic technical solution. His effort kept me away from different kinds of technical issues like: water leakage, heater down, pump stop and thus I can focus on research work.

I also want to express my appreciation to Dr. Freytag Koen (on the FEM and constitutive modeling), Dr. Vicente Solaz Herrera (on fatigue and fracture basics), Dr. Diego Mendez Mora (on fracture mechanics), Dr. Oriol Carrido Costa (on crack growth rate law), Lijuan Cui (on TEM and FIB), Dr. Milan Heczko and Dr. Ignasi Villacampa (on crystollography and TEM analysis), Prof. Alain Nussbaumer (on short crack correction and acting as the expert jury for my PhD candidacy & annual exams), Prof. Gilbert Hénaff (for sharing common research interests), Dr. Xionglong Guo (on corrosion oxides remove), Dr. Jonathan Mann (on cyclic J integral) and the others, I cannot list them all. My PhD work benefits from their inputs. Furthermore, I would like to appreciate Prof. Alain Nussbaume, Prof. Tomas Kruml and Dr. Matthias Bruchhausen to have accepted to review my PhD thesis.

The work done by the summer students Yu-Hsuan Li & Shaoni Li and the visiting PhD student Dr. Veronika Mazanova has contributed to my PhD work. I appreciate their cooperation.

I want to thank Dr. Zaiqing Que and Dr. Juxing Bai again. They help me a lot in starting the work and living in Switzerland. Besides the colleagues I already mentioned, Dr. Nicolo Grilli, Dr. Rao Sudhakar, Dr. Suman Siddarth, Dr. Sriharitha Rowthu, Dr. Roman Mouginot, Aleksandra Treichel and Cansu Kursun, to whom I want to thank for sharing inspiring discussion during the lunch and coffee break.

Then I want to thank my parents and friends who help me to overcome difficulties. Last but not least, I want to express my love and appreciation to my dear wife Mengzhu Yu, who trusts, supports and gives me love and patience me without any reserve. She gave up her career in Beijing and moved to Switzerland and support me to make the dream come true.

Four years is short but enough to change my life. Thank you all for giving me the positive inputs.

PSI Villigen, March 26, 2020 Wen Chen

Abstract

Austenitic stainless steels is used in many components of nuclear power plants, particularly in the pipes of cooling systems. Owing to power transients and to start-ups and shutdowns, these components are subjected to thermo-mechanical loadings (low-cycle fatigue LCF & high cycle fatigue HCF) and flow-induced vibration (HCF). The corresponding fatigue design curves were established with solid smooth specimens tested in air at room temperature under strain-control. However, these curves do not consider the influence of LWR water environments that were shown to reduce fatigue life. US NRC Regulatory Guide 1.207 or other national equivalents (JSME Code in Japan) then were established taking strain rate, dissolved oxygen and temperature into consideration. Besides, a significant number of issues have been recently identified, which may have an impact on fatigue life but have not been sufficiently investigated, e.g., the potential negative effects of mean stress, mean strain, surface finish, long-term static hold, specimen geometry, multiaxial stress state were sensitivities not explicitly addressed. This study was launched to assess the effect of mean stress on fatigue behavior of a 316L austenitic steel in boiling water reactor environment with hydrogen water chemistry (BWR/HWC) at 288°C.

Load-controlled fatigue tests were selected as the easiest experimental technique to impose a pre-defined mean stress. The tests were carried out on hollow specimens at different stress amplitudes and mean stresses in BWR/HWC environment and in air at 288°C, the latter serving as reference environment to evaluate the life reduction induced by the BWR/HWC medium. Few tests in strain-controlled were performed to derive a consistent way to represent the data obtained with the two control modes together.

The test results reported in the form of stress-life curves showed that, in LCF regime ($< 10^5$ cycles), positive and negative mean stresses increase and BWR/HWC environment decreases fatigue life. In the HCF regime, negative mean stress is always beneficial for fatigue life but positive mean stress decreases fatigue life in BWR/HWC. The beneficial effect of mean stress is attributed to its enhanced cyclic hardening on material, which leads to smaller strain amplitude at given stress amplitude. The load-controlled data were converted into strain-life presentation by considering the average strain amplitude over the whole loading cycles. Additionally, a modified Smith-Watson-Topper mean stress correction method was successfully used to correlate the results with and without mean stress. Finally we showed that strain energy density criteria are good alternatives to correlate all data.

Abstract

Crack growth rates were determined from the striation spacing on the fracture surfaces with high resolution scanning electron microscopy (HRSEM); crack initiation sites were also studied with HRSEM, and the microstructures were observed with transmission electron microscopy and electron channeling contrast imaging. From the striation spacing measurement, we concluded that BWR/HWC environment essentially reduces the number cycles needed to initiate a physical crack (crack depth = 50 μm) but modifies slightly the crack growth rate, which correlates well with a strain intensity factor and J-integral method.

Life predictions were also done by a well-trained artificial neuron network that considers mechanical, environmental and material properties factors.

Keywords: austenitic stainless steels, environmentally-assisted fatigue, mean stress, light water reactor environments, mean stress, fatigue in load control, fatigue in strain control.

Résumé

Les aciers austénitiques inoxydables sont utilisés dans de nombreux composants des réacteurs nucléaires, en particulier dans la tuyauterie des systèmes de refroidissement. En raison des variations de puissance, des démarrages et arrêts du réacteur, les composants sont soumis à des charges thermo-mécaniques, (responsable de fatigue oligo-cyclique voire de fatigue endurance), et subissent des vibrations induites par l'écoulement de l'eau de refroidissement. Les courbes de dimensionnement en fatigue ont été établies avec des éprouvettes de laboratoires lisses et cylindriques testées à température ambiante. Cependant, ces courbes ne prennent pas en compte l'influence des milieux qui sont connus pour réduire la durée de vie en fatigue. Le guide de réglementations US-NRC 1.207 aux USA ou celui JSME au Japon ont été établis pour prendre en compte certains effets du milieu, tels que la vitesse de déformation, la quantité d'oxygène dissous et la température. En outre, un certain nombre de problèmes potentiels ont été identifiés, qui peuvent avoir un impact négatif sur la durée de vie en fatigue et qui n'ont pas été suffisamment évalués. Par exemple, les effets potentiellement négatifs résultant de contrainte ou de déformation moyenne non-nulle, de l'état de surface, des périodes de chargement statique, des effets de taille/géométrie de éprouvettes et de chargement multi-axial n'ont pas été explicitement étudiés. Ce travail a été initié dans le but d'évaluer les effets de contrainte moyenne et leur interaction avec le milieu réacteur à eau bouillante (REB) d'un acier austénitique inoxydable 316L.

Des essais de déformation en force contrôlée ont été entrepris afin de bien contrôler les niveaux de contrainte moyenne. Les essais ont été réalisés avec des échantillons tubulaires pour différentes amplitudes de contrainte et de contrainte moyenne en milieu REB et air à 288°C. le milieu air représente le milieu de référence pour estimer la réduction de durée de vie. Quelques essais en déformation contrôlée ont été réalisés dans le but d'établir une description cohérente avec les données obtenues en mode force contrôlée.

Les résultats, reportés sous la forme contrainte - durée de vie, ont montré que dans le régime oligo-cyclique ($< 10^5$ cycles), les contraintes moyennes positives et négatives sont bénéfiques pour la durée de vie et que le milieu REB raccourcit les durées de vie. Dans le régime fatigue endurance, les contraintes moyennes négatives sont toujours bénéfiques alors que les contraintes réduisent la durée de vie en milieu REB. L'effet positif des contraintes moyennes est attribué au durcissement cyclique renforcé en présence de contraintes moyennes pour une amplitude de contrainte donnée. Les résultats obtenus en mode force contrôlée ont été

convertis en représentation déformation - durée de vie en considérant l'amplitude moyenne de déformation pendant l'essai. La méthode de Smith-Watson-Topper pour corriger les effets de contraintes moyennes a été légèrement modifiée et appliquée avec succès pour corréler les données avec et sans contrainte moyenne. Finalement, nous avons montré que des critères basés sur la densité d'énergie moyenne sont des alternatives crédibles pour corréler l'ensemble des résultats.

Les vitesses de croissance des fissures ont été déterminées grâce aux mesures d'espacements des stries sur les surfaces de fracture ; les sites d'initiation des fissures ont été observés par microscopie électronique à balayage haute résolution et les microstructures de déformation observées par microscopie électronique à transmission. De l'espacement des stries, nous avons conclu que l'environnement REB réduit la durée de vie essentiellement dans la phase d'amorçage des fissures, c'est-à-dire pour initier des fissures de 50 μm de long, alors que les vitesses de croissance des fissures plus longue n'est que peu modifiée. Les vitesses de croissances affichent une bonne corrélation avec le coefficient d'intensité des déformations et la méthode de l'intégrale J.

Des prédictions des durées de vie ont été réalisées avec un réseau neuronal artificiel entraîné pour prendre en compte les paramètres mécaniques, environnementaux et les propriétés mécaniques.

Mots-clés : aciers austénitiques inoxydables, fatigue assistée par environnement, milieu réacteurs à eau légère, contrainte moyenne, fatigue en force contrôlée, fatigue em déformation contrôlée

Contents

List of Figures

List of Tables

List of Symbols

σ_{ar}	full-reversed stress amplitude
σ_a	stress amplitude
σ_m	mean stress
σ_{max}	maximum stress
σ_{min}	minimum stress
$\sigma_f^{'}$	fatigue strength coefficient
σ_{fs}	fatigue strength/limit
σ_y	yield stress
σ_u	material ultimate tensile strength
N_f	fatigue life
$N_{f,air}$	fatigue life in air
$N_{f,water}$	fatigue life in water
ϵ_a	strain amplitude
ϵ_{ar}	full-reversed strain amplitude
$\epsilon_{a,p}$	plastic strain amplitude
$\epsilon_{a,e}$	elastic strain amplitude
$\epsilon_f^{'}$	fatigue ductility coefficient
$\dot{\epsilon}$	strain rate
E	elastic Young's modulus
$\triangle$K	stress intensity factor range
$\triangle$K$_{eff}$	effective stress intensity factor
$\triangle$K$_{max}$	maximum stress intensity factor
F_{en}	environmental factor
F_{σ_m}	mean stress factor
$\triangle W_t$	total strain energy density
$\triangle W_p$	plastic strain energy density
$\triangle W_e$	elastic strain energy density
$\triangle W_{ane}$	anelastic strain energy density
n	material cyclic hardening exponent
T^*	transformed parameter of temperature
$\dot{\epsilon}^*$	transformed parameter of strain rate
O^*	transformed parameter of dissolved oxygen

List of Abbrevations

ACI	American Concrete Institute
AIDE	Adsorption-Induced Dislocation Emission
AISI	American Iron and Steel Institute
ASME	American Society of Mechanical Engineers
ANL	Argonne National Laboratory
ANN	Artificial Neural Network
BCC	Body Centered Cubic
CASS	Cast Stainless Steel
CSS	Cyclic Stress-Strain
DO	Dissolved Oxygen
EBSD	Electron Back Scatter Diffraction
ECCI	Electron Channeling Contrast Imaging
ECP	Electrochemical Corrosion Potential
FCC	Face Centered Cubic
FIV	Flow-induced Vibrations
GB	Grain Boundary
HCF	High Cycle Fatigue
HEAC	Hydrogen Environment Assisted Cracking
HELP	Hydrogen-Enhanced Localized Plastic
HEDE	Hydrogen-Enhanced Decohesion
HTA	High Temperature Air
HTW	High Temperature Water
HWC	Hydrogen Water Chemistry
IPF	Inverse Pole Figure
IQ	Image Quality
LCF	Low Cycle Fatigue
LEFM	Linear Elastic Fracture Mechanics
LWR	Light Water Reactor
MSC	Micro-Structurally Small Cracks
NDT	Non-Destructive Testing
NPP	Nuclear Power Plant
NRC	Nulear Regulatory Commission
NWC	Normal Water Chemistry
OM	Optical Microscopy

OLNC	On-line Noblechem
PPBC	Primary Pressure Boundary Components
PSB	Persistent Slip Band
RTW	Room Temperature Water
SCC	Stress Corrosion Cracking
SEM	Scanning Electron Microscopy
SFE	Stacking Fault Energy
SHE	Standard Hydrogen Electrode
SIF	Stress Intensity Factor
SVM	Support Vector Machine
SWT	Smith-Watson-Topper
EIF	Strain Intensity Factor
RPV	Reactor Pressure Vessel
SHE	Standard Hydrogen Electrode
SRO	Short Order Range
SS	Stainless Steel
SWT	Smith-Watson-Topper
TEM	Transmission Electron Microscopy
UHCF	Ultra High Cycle Fatigue
VHCF	Very High Cycle Fatigue

Introduction

Austenitic stainless steels (SSs) are extensively applied for construction of light water reactors (LWR), such as pressure-boundary components (pipes, surge lines, valves, etc.) in the primary or secondary reactor coolants circuit, where the components are exposed to aggressive environments of high-temperature water and subjected to complex thermo-mechanical loadings [1]. Fatigue is a failure mode threatening the integrity of the structural components. There is an increasing number of nuclear power plants that will extend their operation life beyond 50 years, even up to 80 years. The plants will have to face more frequent power adjustments and corresponding temperature changes as more time-dependent solar and wind power will be injected into the grid. Under these circumstances, correct evaluation of fatigue in nuclear power plant components is necessary.

Section III, Division 1 of the ASME Boiler and Pressure Vessel Code (hereafter called ASME Code) is the common reference for design against fatigue of primary/secondary pressure-boundary components. The ASME Code was derived mainly from strain-controlled low cycle fatigue (LCF) tests with small, solid, smooth specimens in air at room temperature. Initially, these tests did not consider potential influence of LWR environmental factors. The design curves were derived by reducing by factor of 2 on the strain or 20 on the fatigue life cycles to form a conservative design margin. The design margin was intended to cover the effects of material variability, surface finish, load sequence, size effects and atmosphere, which were not explicitly investigated in the tests.

Significant degradation effects of LWR coolant environment on fatigue lives were observed in recent years [2][3][4][5]. Under critical simulated LWR environmental conditions, i.e. when temperature, strain rate, dissolved oxygen (DO) level, and strain amplitude met certain threshold values, the fatigue lives of material could be much shorter than predicted by the design curves [3]. Therefore, the design curves in ASME Code may be less conservative than intended.

Different environmental evaluation approaches [2][3][6], such as US NRC Regulatory Guide 1.207, NUREG/CR-6909 and other national equivalents (JSME Code), were introduced to incorporating environmental effects into the ASME Code. The idea is to consider a reduction of the fatigue life by a factor, the so-called F_{en}, which is equal to the ratio of the fatigue life in air at room temperature by the fatigue life in LWR environment. In the F_{en} approaches, only temperature, strain rate and dissolved oxygen were considered. This situation led the

scientific community to identify a number of scientific knowledge gaps in environmental assisted fatigue (EAF), which were summarized in two comprehensive reports [7][8]. Actually, the thermo-mechanical loading and associated time history of real components is much more complex than the usual well defined experimental testing conditions selected for laboratory tests. Mean stress, non-proportional multiaxial loading, deformation/temperature history, water chemistry transients, surface roughness, strain amplitude (low cycle fatigue (LCF) versus high cycle fatigue (HCF)), hold time are just examples of parameters with potential effects on EAF that are not sufficiently understood and that have to be investigated more in detail. To reach a high level of acceptance in nuclear industry, determining environmental correction factors for the above mentioned potential effects need massive and systematic testing, which is very costly and time consuming. Basically, such research goes well beyond single institution research capacity and international cooperation is necessary. New international efforts were initiated; for example, the INCEFA+ project, started in mid-2015 within the European Commission Horizon-2020 program, was designed to deliver new experimental fatigue data to ultimately develop improved guideline in EAF [9][10]. Within INCEFA+ project, three parameters were chosen, namely mean strain/stress, hold time, and surface finish, to assess fatigue life sensitivity in light water reactor environment to these parameters.

This PhD works was undertaken in this context to contribute to a better understanding of the synergistic effects of mean stress effects on fatigue life of austenitic steels. In pressurized piping, mean stress may arise from, e.g., internal pressure, weld residual stress, dead weight loading or static temperature gradients. Mean stress effects on EAF were not investigated thoroughly so far. If at all, mean stress is taken into account in the ASME Code through a modified Goodman correction, which shows that positive tensile mean stress has a detrimental effect on fatigue life. However, for austenitic stainless steels it has been observed that, for a certain moderate positive mean stress in load-controlled tests, fatigue life increases [11][12][13]. Such an atypical behavior call for better understanding to avoid incorporating undue conservatism in the design curves.

The present thesis is organized in five chapters: literature review, materials and experimental methods, results, discussion, and conclusions and perspectives. The literature review chapter covers some general aspects of fatigue in metals, in light water reactor environments, mean stress influence on fatigue life, and models. The material and experimental methods chapter describes the investigated material and its general properties, the mechanical test facilities, the analysis of the data and the microstructural investigation techniques used. The results chapter presents successively the mechanical tests obtained, the fractographic observations, the crack growth rates, the microstructural investigations and correlation methods. The results are then discussed in more details in the chapter discussion. Finally, the manuscript closes with the conclusions and perspectives.

Objectives

The objective of this PhD study was to gain insight into a number of parameters that are known to affect fatigue life of austenitic stainless steels in light water reactor (LWR) environments but that have not yet been systematically studied. The PhD research program has been tailored to address two specific issues on a 316L steel:

i) mean stress effects on fatigue life and

ii) LWR environmental effect and its synergistic effect with mean stress on fatigue life.

In the first phase, fatigue tests with various combinations of environment, stress amplitude, temperature, mean stress, specimen wall thickness, strain rate and internal water pressure in hollow specimens were conducted. From the set of fatigue test data, the influence of mean stress and LWR environment on fatigue life was evaluated on a phenomenological basis. We emphasize here that to clearly observe LWR environment influence on fatigue, a relatively high strain rate was chosen, for which environmental effects are moderate but still visible. In addition, the experimental fatigue testing matrix was restricted to only BWR reactor water environment, namely boiling water reactor with hydrogen water chemistry (BWR/HWC).

In the second phase, the emphasis was placed on developing a comprehensive understanding of the underlying mechanisms of mean stress effects and environmental effects. To achieve this goal, we used optical and scanning electron microscopy (SEM) to observe fractography, transmission electron microscopy (TEM) and electron channeling contrast imaging (ECCI) to look at microstructures, electron backscatter diffraction (EBSD) to characterize local strain.

In the third phase, phenomenologically and numerically based fatigue life correlation and prediction models were considered and used to analyze the fatigue database obtained during the first two phases.

Ultimately, the mechanical fatigue data and microstructural investigations were put together and analyzed to develop knowledge where the effects of mean stress, LWR environment, strain amplitude, stress amplitude are integrated in a comprehensive way.

Main chapters of the thesis Part I

1 Literature Review

1.1 Fatigue of metals

Fatigue of metals is an old topic but there are still many open issues to be addressed. Fatigue is a kind of damage to materials caused by cyclic loading. It was first observed by Wilhelm August Julius Albert in 1837 and was later systematically studied by Wöhler in 1870 [14]. He observed, studied and reported the failure of mine hoist cables resulting from repeated small loads. Since then, fatigue has been treated in science and engineering because it occurs in many situations threatening materials integrity. At least half of all mechanical failures are estimated resulting from fatigue. For example, the cost of these failures constitutes around 4% of the USA GDP [15].

1.1.1 Low cycle fatigue, high cycle fatigue and very high cycle fatigue

A clear distinction between low cycle fatigue (LCF), high cycle fatigue (HCF) and very high cycle fatigue (VHCF) is not well established. Nonetheless, in LCF, the load amplitudes are relatively high so that the plastic component ($\epsilon_{a,p}$) of the strain amplitude is larger than the elastic component ($\epsilon_{a,e}$), $\epsilon_{a,p} > \epsilon_{a,e}$. Thus, the fatigue ductility governs the fatigue life in LCF ($N_f \approx 10^4 - 10^5$ cycles). In HCF, the load amplitudes are small enough to have $\epsilon_{a,p} < \epsilon_{a,e}$. Thus, the fatigue strength controls the fatigue life ($N_f \approx 10^5 - 10^7$ cycles). VHCF, also called ultra-high cycle fatigue UHCF, refers to unexpected fatigue failures at cycles exceeding $\approx 10^8$, and occurs at normally safe low load amplitudes, lying below the HCF fatigue limit [16]. Fig. 1.1 is a schematic illustration of LCF, HCF and VHCF ranges. Crack propagation dominates the whole fatigue life in LCF. On the contrary, crack initiation accounts for most of the life time in HCF and even more in VHCF. Irreversible cyclic slip develops persistent slip bands (PSB), which emerge on free surface forming extrusions & intrusions. These extrusions and intrusions are initiation sites for cracks at the micro-scale level. In the LCF regime, the large imposed plastic strain leads to earlier PSB formation than in the HCF regime. The crack initiation period is accordingly shorter. However, in real components, surface defects may act as strong stress risers or pre-existing cracks may be even present so that crack initiation life can be absent in

LCF (range I in Fig 1.1) . Range II in Fig 1.1 is associated to the HCF regime and corresponds to the stress or strain amplitude threshold for PSB formation, i.e. PSB and rough surface profile are formed in range I and II while in range III and IV no PSB formation are observed. However, there are cases where PSB formation occurs below the expected threshold as observed by Stanzl-Tschegg et al. on ultrasonically fatigued copper polycrystal. These authors revealed PSB-like cyclic slip and rough surface profile below the PSB threshold [17] and [18]. Generally, the crack initiation mode changes from surface to subsurface in the transition from HCF to VHCF. Most common subsurface cracks originate from internal defects like inclusions and are called 'fish-eye' cracking, for example in [19]. In our study, only the fatigue behavior in LCF & HCF regimes was investigated.

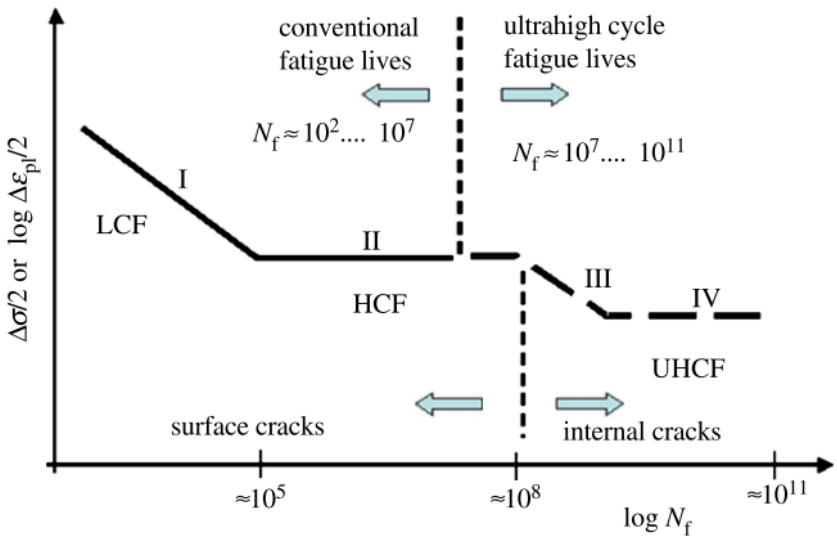

Figure 1.1 – Schematic illustration of LCF, HCF and VHCF fatigue ranges and transition from surface to internal crack formation [20].

1.1.2 Fatigue crack initiation and propagation

In this section, we focus on the crack initiation and propagation mechanisms of face centered cubic (FCC) metals in the LCF regime.

Crack initiation of FCC metals

In the case of FCC metals, four phases can be discerned during the overall fatigue process as schematically illustrated in Fig. 1.2 [16]. The borderlines are not well defined: in fact many definitions of crack initiation can be found in literatures and the measurement of initiation remains challenging. The phase I of strain localization and the phase II are commonly treated together as the crack initiation phase.

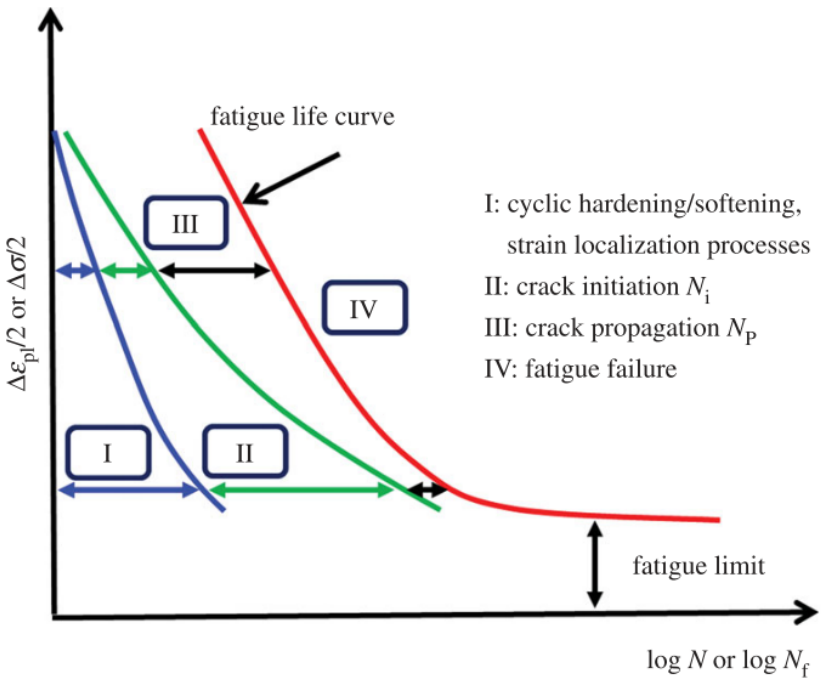

Figure 1.2 – Schematic illustration of four phases of fatigue process for ductile metals [16].

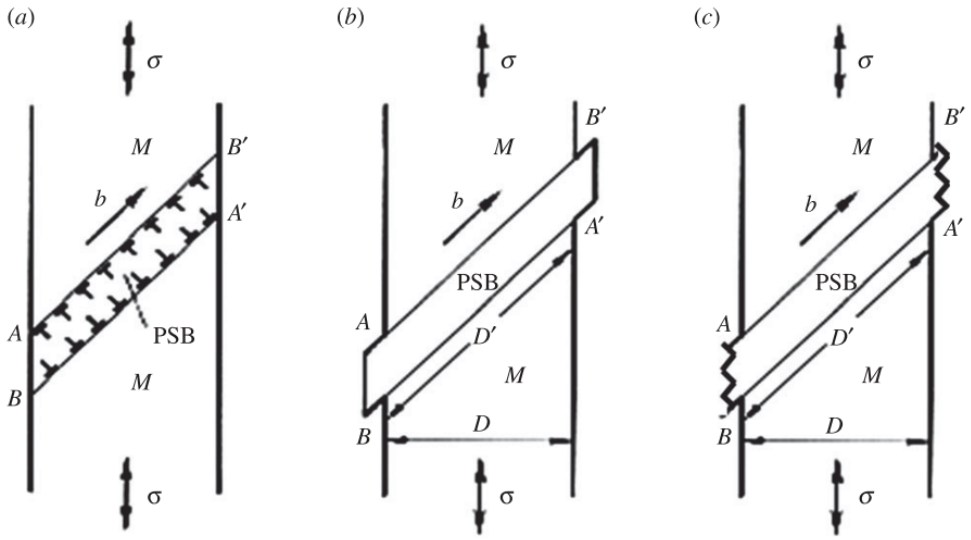

Figure 1.3 – A simplified Schematic illustration of PSB formation that leads to the formation of extrusions according to EGM model [21][22][16]. M stands for matrix, b is Burgers vector, D is the specimen diameter in single crystal or grain size in polycrystal. (a) shows pairs of PSB-matrix interface dislocation layers with opposite sign, (b) the interface dislocations glide out along the Burgers vector on both sides during cyclic deformation forming slip steps, (c) gradual extrusion of PSB structures by subsequent cyclic deformation result surface roughening.

Only plastic strain causes damage. Typically, in copper single crystal, cyclic strain localization forms PSBs, which run out of the bulk material forming surface profiles referred as to extrusions and intrusions as illustrated in Fig. 1.3. The EGM model proposed by Essmann et al. [21] describes the elongation of the PSB (static extrusions formation) in the direction of Burgers vector caused by vacancies produced by annihilation of edge dislocations. The EGM model predicts rapid extrusion formation. The extruded volume matches precisely the volume of vacancy-type defects that accumulate in cyclic saturation. The cracks initiate at the surface steps, which are located at the PSB-matrix interfaces. By revisiting the explanation of the production of extrusions at room and elevated temperatures, the interstitials and vacancies are highly mobile at the latter temperature and can easily be absorbed by edge dislocations in PSB walls.

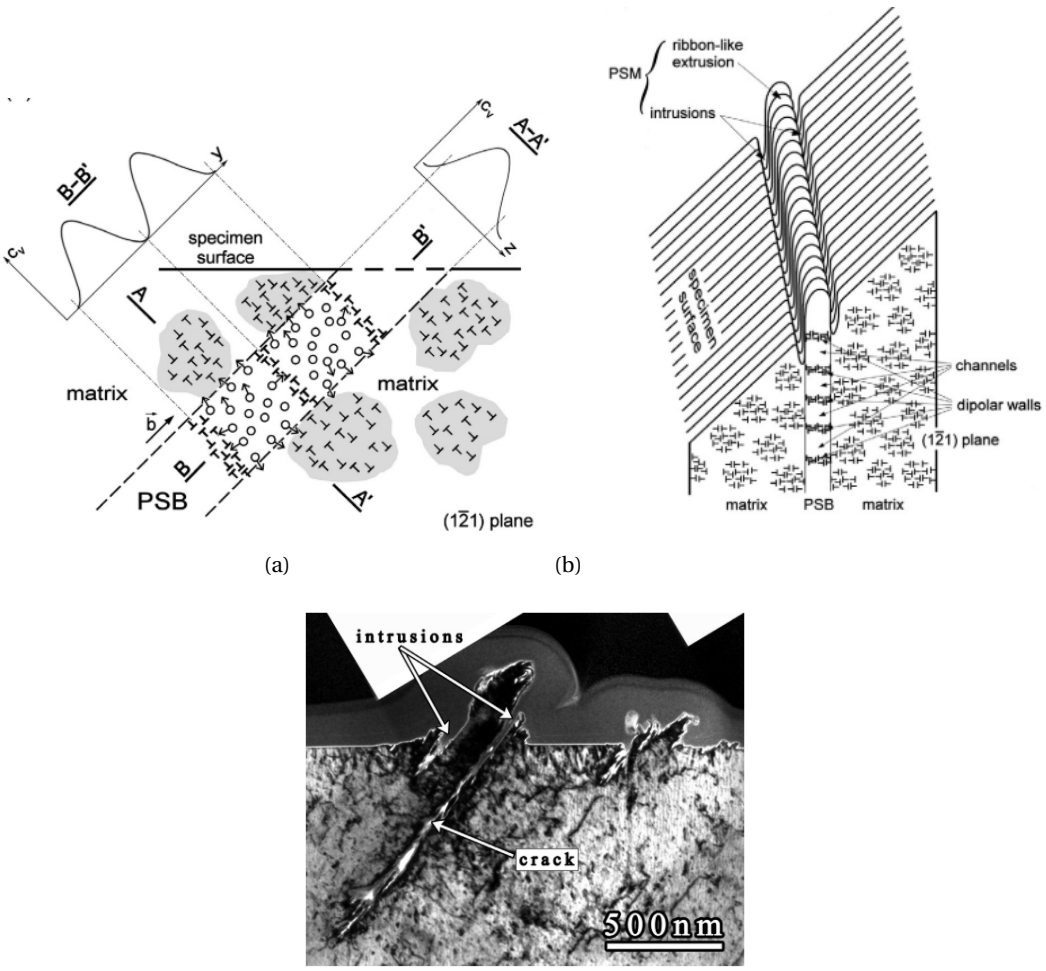

Figure 1.4 – PSB formation according to Polák model, (a) schematic illustration of point defect production in PSB and their migration to matrix, (b) resulting surface profile of extrusion and two intrusions, (c) experimental observation of surface profile in TEM of fatigued Sanicro 25 steel [23].

Polák modified the original EGM model by considering not only the formation of point defects in PSB but also their continuous migration within the PSBs and the matrix. Polák's model generally agrees with EGM's model point defect theory, except that it predicts the growth of intrusions at the PSB-matrix interfaces and the growth of extrusion in the center of PSBs [24][25]. The extrusions grow very early but intrusions growth is substantially delayed. Fig. 1.4 is a schematic illustration of Polák's model. The intrusions look like sharp surface crack-like defects that play a key role in the fatigue crack initiation mechanisms [23][26].

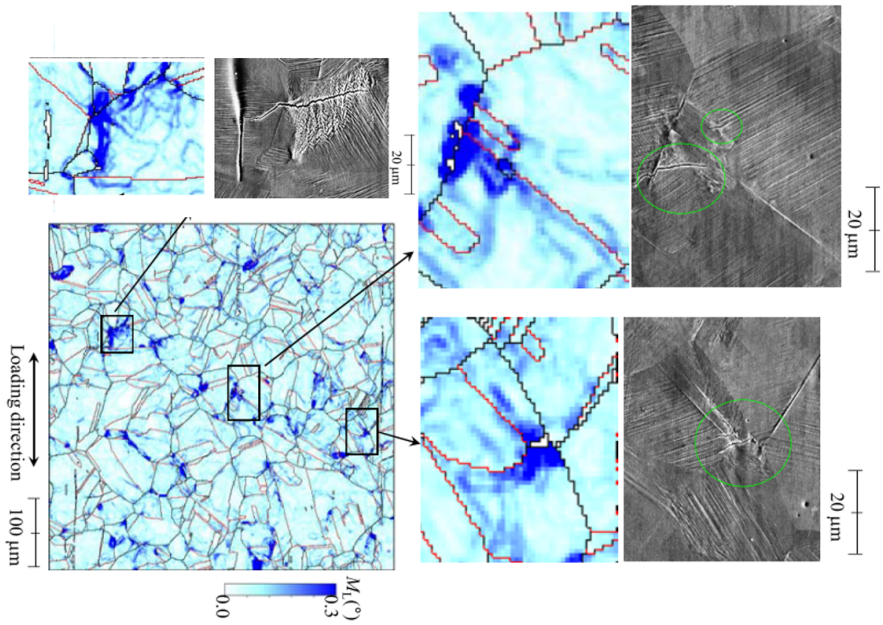

Figure 1.5 – Crack initiation at the grain boundaries and triple junctions in Kamaya's observation [27]. The color map indicates local misorientation magnitude. Red lines indicate twin boundaries.

Most crack initiation studies were performed on single crystals of copper/nickel or polycrystalline FCC materials. As discussed above, fatigue crack initiation at PSBs is probably the most studied case of fatigue damage. However, this is not the most common crack initiation mechanisms in commercial materials, in which persistent slip is largely suppressed by suitable alloying [28]. For instance, Kamaya observed that cracks initiated at grain boundaries (GB) (including twin boundaries and triple junctions) and slip steps in strain-controlled fatigue tests of 316L SS at room temperature air in Fig. 1.5 . The polished surface was observed with SEM and EBSD after each cyclic interval. Strain was localized at GBs.

The cases discussed above correspond to specimens with smooth surface tested in air without mean stress. The end of the crack initiation phase can be defined in different manners. Murakami et al. [29] defined the crack initiation phase as that of growing cracks so small that their propagation cannot be described by fracture mechanics. Lukas similarly discussed the transition from nucleation to propagation as the transition from a system of microcracks

governed by cyclic plastic strain to crack propagation governed by fracture mechanics [30]. The physical crack initiation is normally defined as the crack size can be detected by optical microscopy.

Rough surfaces and corrosive environments may reduce or accelerate the crack initiation phase. This will be discussed in the Section 1.3 below.

Crack propagation

Crack propagation is divided into three phases. A representative drawing by Zerbst et al. is shown in Fig. 1.6 [31], where cracks are classified as microstructurally short crack (stage I), mechanically short crack (stage I) and long crack (stage II). Some authors consider a high stress intensity ($\triangle$K) factor stage, beyond the Paris stage, referred as to stage III, where $\triangle$K is larger than the fracture toughness K_{IC} and sudden/rapid failure occurs [32].

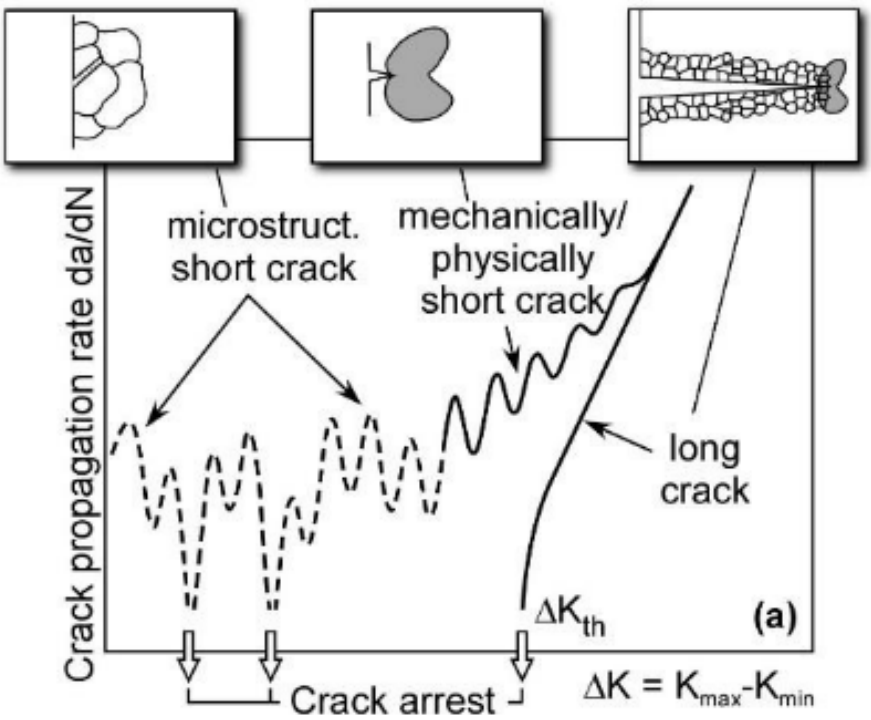

Figure 1.6 – Stages of fatigue crack propagation [31].

The microstructurally short crack in stage I grows along a slip plane inclined at an angle of $\approx 45°$ to the loading axis, as a shear crack (mode II). The microstructurally short crack may extend across one to several grains before the stress/strain intensity is high enough to activate plastic deformation on slip systems different from the primary slip system. In mechanically short crack in stage I propagates in fracture mode I, i.e. normal to the stress axis. In stage I, linear elastic fracture mechanics (LEFM) concept is not applicable as the crack size is in

the same order of plastic zone size. Thus, parameters like the effective stress intensity factor (ΔK_{eff}) [31][33], or the cyclic J-integral [34][35][36][37] can be used to correlate crack growth rate in this stage. Cracks may be arrested due to plastic strain accumulation, fracture surface roughness and oxide-induced crack closure. Usually a large number of microstructurally short cracks are initiated but most of them are arrested. Thus, the fatigue limit is defined at the stress level below which all these cracks are arrested [31]. In stage II, the plastic zone at crack tip is relatively small compared with crack size, where the LEFM concept and Paris law are applicable. In stage I, especially for microstructurally short crack, microstructures affect strongly the crack propagation, but their influence fades out in later stages, where fracture mechanics controls it.

Formation of an engineering crack in austenitic steels

However, Chopra separates the formation of an engineering crack size on smooth specimen into two stages, where the stage I corresponds to the growth of a microstructurally short crack as defined above, and the stage II corresponds to a mechanically short crack growth up to an engineering crack size (≈ 3 mm depth) [38]. Mechanically short cracks are considered as cracks greater than a critical size show little or no influence of microstructure. Chopra estimated the size of microstructurally short crack is in the order of approximate eight times of grain size [3]. Only two stages are categorized as illustrated in Fig. 1.7(a). In Fig. 1.7(b), crack growth decelerates with crack propagation for microstructurally short crack.

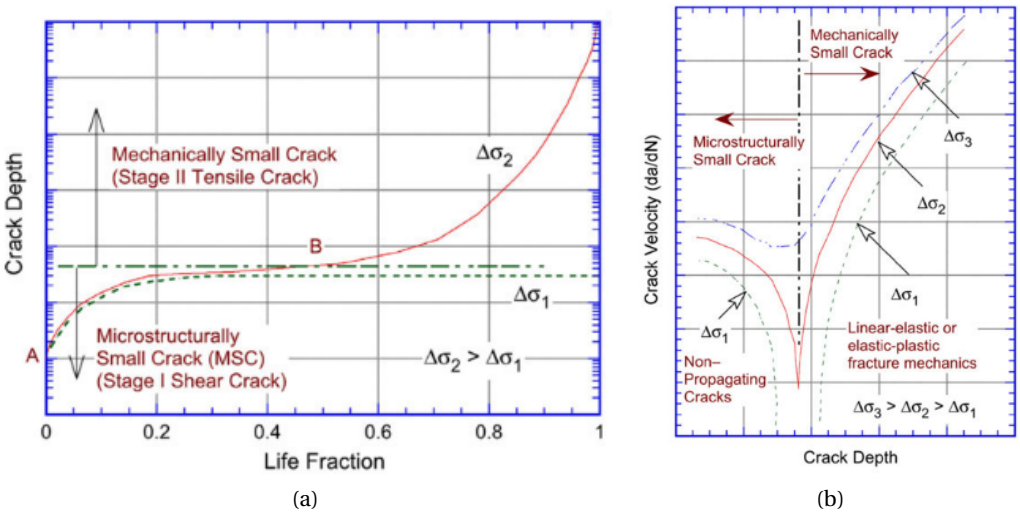

Figure 1.7 – Schematic illustration of (a) crack length versus fatigue life fraction and (b) crack growth rate versus crack length [3].

1.2 Fatigue in nuclear power plants

Most nuclear power plants (NPP) face long-term operation. Most of U.S. light water reactors (LWRs) got licence renewals from 40 years to 60 years and the first reactor recently got a second licence renewal to 80 years lifetime at the end of 2019 [39]. Fatigue is responsible for ≈ 20% of cracking incidents in LWR components, but there were only few incidents in fatigue-designed pressure boundary components. About 90% of the incidents were related to HCF through flow-induced vibrations (FIV) after power up-ratings (e.g., BWR steam dryers, socket welded small diameter instrument lines). The other 10% were caused by thermal or thermal-mechanical fatigue (LCF & HCF) that were caused by complex thermal-hydraulic phenomena such as thermal stratification, thermal striping or mixing which were not or only partially considered in the original component design (like the ASME Code). Thermal stratification is typically caused by slow injection of relatively cold feed water during plant startup or hot stand-by. In contrast, thermal striping is caused by rapid and localized fluctuation of hot and cold feedwater [3]. An aggravation of this fatigue damage (in particular LCF) by environmental effects cannot be excluded. This materials degradation phenomenon is regularly monitored and evaluated. Its proper evaluation is a critical element in plant aging management to ensure their safe and economic long-term operation [40].

1.2.1 Components manufactured with austenitic stainless steels and their fatigue degradation

Fig. 1.8 outlines the commonly used materials in pressurized water reactor components. In LWRs, corrosion-resistant, low-carbon (AISI 304L, 316L, 316NG) or Ti- or Nb-stabilized austenitic stainless steel (SS) grades (AISI 321 and 347) and their corresponding weld filler metals (e.g., AISI 308L and 309L) are widely used as a construction material for piping, vessels, claddings and reactor internals, which enclose or come into contact with the primary reactor coolant. Cast duplex SS (CASS, e.g., ACI CF-3, CF-8 and CF-8M) are used for primary circuit components with complex shape (e.g., pump housings). The direct contact with the reactor coolant may reduce the fatigue initiation life and accelerate fatigue crack growth under certain circumstances.

According to a review of fatigue failures of NPP components in Japan [41], fatigue cracking incidents in the reactor pressure vessels were extremely rare. However, fatigue incidents occurred occasionally in piping systems, valves and pumps; Particularly, in cases with inadequate fatigue design or service fatigue assessment. Primary pressure boundary components (PPBC) are designed against fatigue. Nowadays, critical component locations are additionally equipped with fatigue monitoring systems. As a consequence, fatigue cracking incidents have rarely occurred in PPBC in recent years.

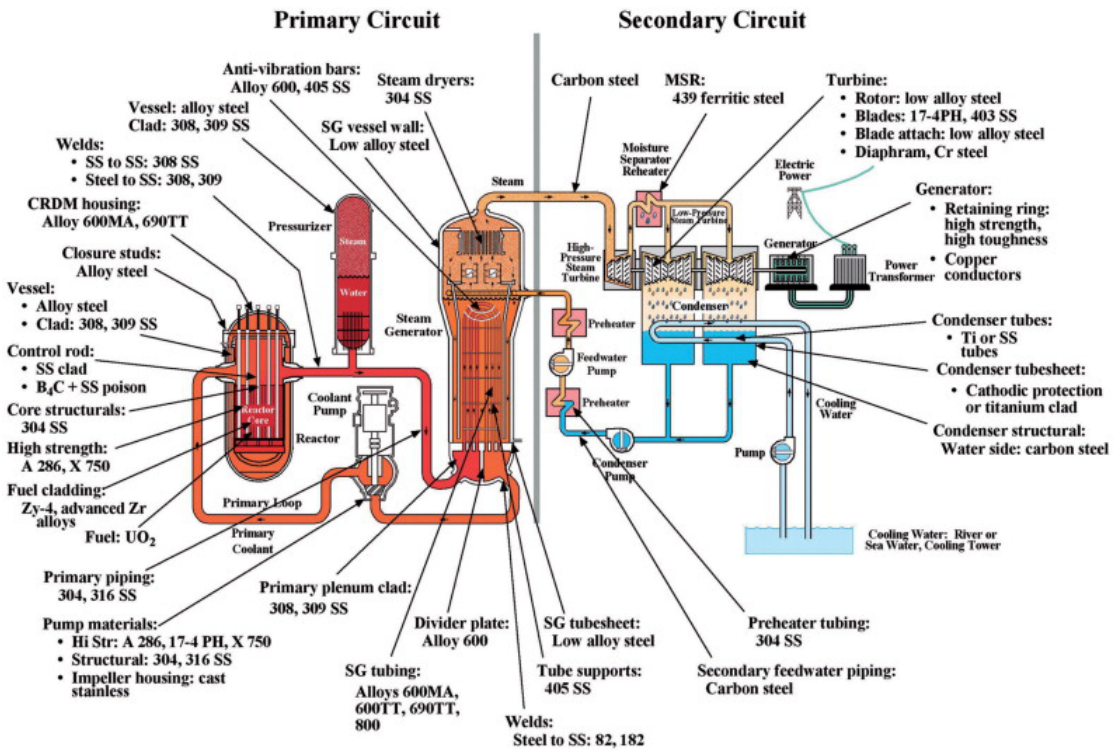

Figure 1.8 – Outline of PWR components with used materials . Courtesy of R. Staehle.

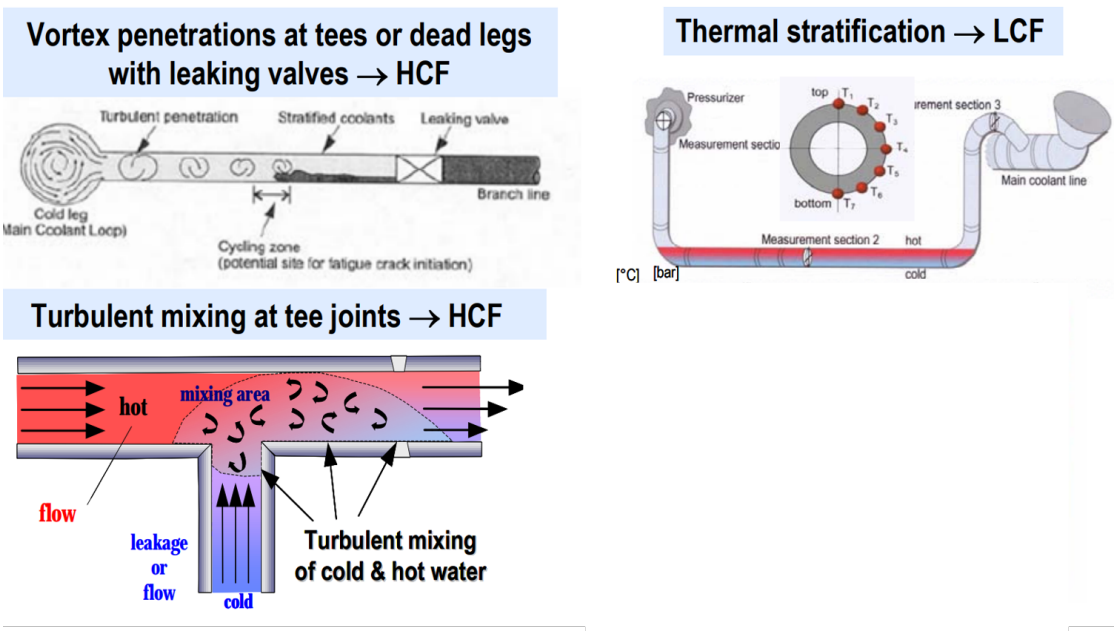

Figure 1.9 – Examples of thermal fatigue in LWR components [42].

1.2.2 LWR water chemistries and corrosion of austenitic stainless steels

LWR water chemistries

Corrosion and the water chemistry may affect the fatigue behavior of SS. There are two basic types of LWRs, boiling water reactors (BWR) and pressurized water reactors (PWR). They cover about 25 and 75 % of the LWR fleet worldwide and have different water chemistries.

Western PWRs operate with slightly alkaline, borated, lithiated and hydrogenated water in the primary coolant circuit. The inlet and outlet core temperatures are about 290 and 320°C, respectively, and the temperature in the pressurizer is about 343°C. H_3BO_3 is added to control the reactivity and its concentration reduces with increasing fuel burn-up. In order to minimize the release of corrosion product, activation and CRUD formation on the fuel elements, LiOH is added accordingly to keep the $pH_{290°C} \approx 7$, where solubility of the protecting oxide films is minimal. Some amount of hydrogen is added to suppress the radiolysis (to shift the equilibrium towards the H_2O side) in the reactor core and to achieve low free, open circuit electrochemical corrosion potential (ECP) of the structural materials from -800 to -700 mV_{SHE} (voltage refer to Standard Hydrogen Electrode). The resulting dissolved hydrogen (DH) content in the reactor water is typically 2 to 3 ppm.

BWRs are operated with neutral ($pH_{290°C}$ of 5.7), high-purity water. The inlet and outlet core temperatures are about 274 and 288°C, respectively. In BWRs, due to boiling, high-purity water is needed to avoid excessive CRUD formation on the fuel elements and to reduce the enrichment of aggressive anions in cracks/crevices at high ECP to mitigate stress corrosion cracking (SCC). The environment and temperature strongly vary with the location in the primary coolant system (feedwater, reactor water, steam, condensate, etc.) and applied water chemistry. In normal water chemistry (NWC), no hydrogen is added to the system. The radiolysis of the cooling water in the reactor core produces stoichiometric amounts of reducing (H_2) and oxidizing (O_2, H_2O_2) species. Due to the non-volatility of H_2O_2 and strong partitioning of H_2 into the steam phase, there is an excess of oxidizing species in the reactor water. This results in high ECPs of the reactor internals or the RPV in the range of 100 to 250 mV_{SHE}. The reactor water typically contains 200 to 400 ppb dissolved oxygen (DO) and hydrogen peroxide as well as 15 to 35 ppb H_2. In hydrogen water chemistry (HWC), H_2 is injected into the feed water that recombines with O_2 and H_2O_2 to H_2O in the radiation field within the RPV and reduces the ECP. Due to the strong H_2 partitioning to the steam phase, this technique is less efficient than in the PWRs and the ECP are (together with the lower pH) higher than in PWRs and in the range from -500 to -200 mV_{SHE}. Above the upper core level and in the upper plenum or in the region of the feedwater nozzle corners, the environment remains highly oxidizing. To increase the efficiency and to reduce some negative side effects of HWC (increased 16N dose rates), the On-line Noblechem (OLNC) technique was developed, where platinum complex solutions are injected to the feed water during reactor operation and they finally deposit as nano-sized platinum particles on the water-wetted surfaces. Platinum particles electrocatalysis the recombination of H_2 with O_2 and H_2O_2 to produce H_2O. The

reactor water typically contains 20 to 40 ppb (if with OLNC) or 100 to 300 ppb (in moderate HWC) DH here. The majority of BWRs are now operating with HWC or HWC/OLNC. The main differences between BWR/NWC, BWR/HWC/OLNC and PWR with regard to corrosion are the different ECP, pH, H_2 contents and temperatures. It is also stressed that water chemistry during plant transients (e.g., start-up/shut-down) in thermal fatigue may deviate from the above specified conditions and change during the transients and fatigue cycles. On the other hand, the crack-tips are always deoxygenated and at low ECP in all three environments, and the environmental conditions under which cracks grow are quite similar.

Regarding to EAF, the situations are dependent on the material (low-alloy versus stainless steels) and material conditions (e.g., sensitisation versus solution-annealed SS). EAF lives of solution-annealed SS is in PWR and BWR/HWC environments are very similar and shorter than in oxidizing pure NWC environment. In sensitized SS or in presence of aggressive impurities like sulphate and chloride, the situation is opposite. An aggressive occluded crevice chemistry can be formed in NWC environment with strong enrichment of harmful anions like sulphate and chloride or sulphides from the dissolution of MnS inclusions in case of low-alloy RPV steels, and this is the other reason to keep the impurity level in water as low as possible for BWRs with NWC.

Corrosion and oxides formation of austenitic SSs

The typical two layer structure is shown in Fig. 1.10a: The outer layer consists of large particles (which are made of γ-Fe_2O_3 in NWC and Fe_3O_4/$NiFe_2O_4$ in HWC) and intermediate particles (α-Fe_2O_3). The inner layer consists of fine spinel grains ($Fe_xCr_{3-x}O_4$). A thin nickel-rich (and chromium depleted) metal surface was also observed below the inner layer as illustrated in Fig. 1.10b [43]. The outer layer composition depends on water chemistry, while the inner layer is less affected. In high DO water (e.g., NWC), the inner layer has a lower chromium content due to its oxidation to soluble chromate and smaller thickness. The chromium content of SSs affects the oxides formation. Higher chromium content results in a thinner oxide film and produces a shift from iron oxides (e.g., Fe_3O_4) to spinels (e.g., $FeCr_2O_4$), thus enhancing corrosion resistance. In HWC, hydrogen is added to decrease ECP and SCC susceptiblity. However, higher DH in hydrogenated high-temperature water (HTW) accelerates corrosion rate of 316 SS, reflected as a thicker oxide film. Analogously, an increased SCC initiation susceptibility was observed with increasing DH [44]. The reason invoked by Berge et al. [45], Dong et al. [46] and Kim [47] is the increase of iron solubility, which decreases the oxide stability with increasing the DH content.

$$(Ni,Cr)Fe_2O_4 + 6H^+ + H_2 \rightarrow (Ni^{2+}, Cr^{2+}) + 2Fe^{2+} + (4H_2O) \tag{1.1}$$

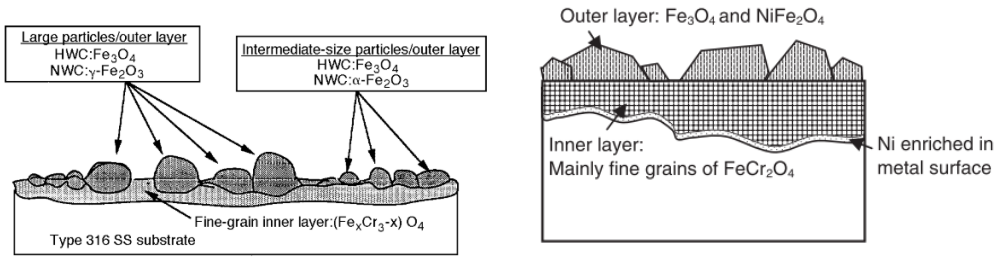

(a) (b)

Figure 1.10 – Schematic drawing (a) oxides formed on 316 SS in HWC or NWC [47][48] and (b) oxides formed on chromium rich SS in simulated PWR primary water [43].

The nature and characteristics of the oxide film and slight differences in various environments may affect the corrosion rates and the early stages of the EAF initiation behavior. The chromium content of the steel has a strong impact on repassivation rates and thus film repair after local mechanical damage and on EAF growth rates. The exact crack initiation and growth mechanism in EAF of SS in HTW is still under discussion. The slip-dissolution/oxidation mechanism is a valuable hypothesis in high DO environments, in particular for sensitized SS and SS with higher carbon contents or in case of harmful impurities like chloride and sulfate that strongly affect repassivation and may produce acidic pH shifts under these conditions. The strong reduction of fatigue life of SS in hydrogenated, low DO water cannot be explained by this mechanism and the higher corrosion rates (compared to high DO water) and hydrogen uptake and hydrogen-deformation mechanisms such as hydrogen-enhanced local plasticity (HELP), hydrogen-enhanced strain-induced vacancy (HESIV), hydrogen adsorption-induced dislocation emission (AIDE) probably play an important role here and is probably a surface or near-surface effect. The hydrogen content in the bulk material is controlled by the hydrogen fugacity of the (local) environment through the Sieverts law and thus too low for significant bulk hydrogen embrittlement effects in high-temperature water.

Occluded crevice chemistry at crack

It is well established through experiment and modeling that the crack tip environment is occluded and is not representative of the bulk environmental conditions. The crack tip conditions are determined by the balance between the surrounding high metal ion concentrations and the electrochemical polarization at the bulk surface (see Fig. 1.11). At the crack tip, anodic reaction kinetics dominates, whereas cathodic reaction kinetics dominates at bald surface near the crack mouth, due to the slow diffusion of O_2 into the crack and resulting in O_2 depletion at the crack tip. The established acidic crack tip results in EAC susceptible conditions and fast crack growth. Besides the development of acidic conditions, production of H near the crack tip via cathodic polarization was also recognized by Turnbull et al. [49]. The produced H is partially absorbed into the metal.

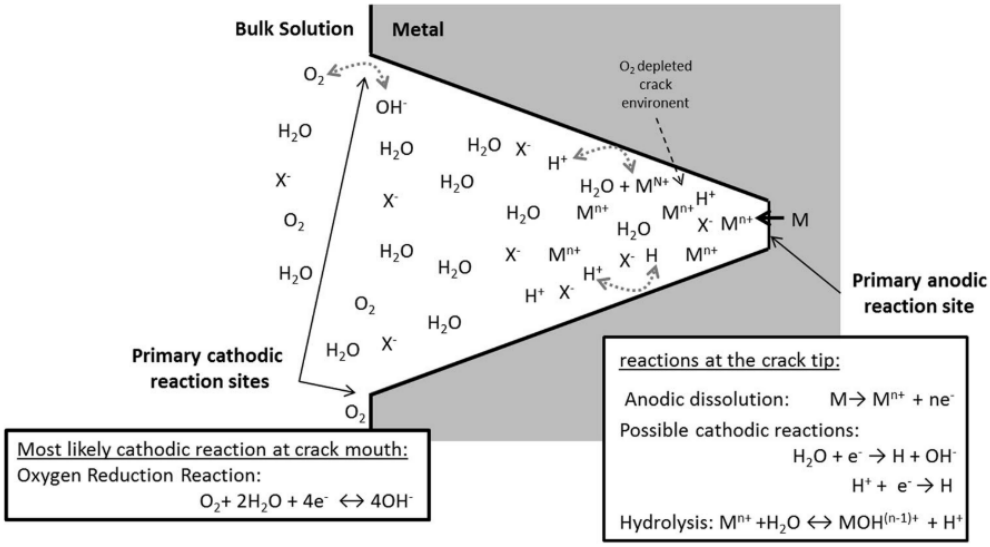

Figure 1.11 – Schematic of chemical and electrochemical reactions at EAC crack [50].

In oxygenated water (e.g., NWC), an aggressive occluded crevice chemistry can be formed at the crack-tip [51]. Oxygen mass transport by diffusion into the cracks is slower than its reduction and consumption by corrosion and reaction with hydrogen. Crack crevices with restricted mass transport (high depth to width ratio) readily consume all the oxygen over a short distance from the crack-mouth. Convection usually does not play a role in such tight cracks. This effect produces a potential drop between the de-aerated crack-tip (≈-500 mV_{SHE} and ≈-750 mV_{SHE} in BWR and PWR environment) and the aerated crack mouth (≈+100 mV_{SHE}), which causes migration of anions and cations towards the crack-tip and crack-mouth, respectively. The potential gradient increase with increasing DO and ECP. Thus, the crack-tip enriches with critical anionic impurities that affect the repassivation and can produce acidic pH shift in case of bulk environment impurities like Cl^- or SO_4^{2-}.

In oxygen-free, hydrogenated water, the H_2/H_2O reaction controls the ECP in both the crack-tip and crack-mouth [51]. For this reason, there is no potential gradient between the crack-tip and crack-mouth and the mass transport occurs only by diffusion. There is thus no enrichment of anionic impurities in the crack crevice environment. The dissolved hydrogen concentration in the environment at the crack-tip is similar or higher to the bulk environment, since there is essentially no consumption and limited creation of hydrogen.

1.2.3 Fatigue of stainless steel in air and fatigue design codes

Under cyclic loading, solution annealed SS usually exhibit rapid hardening during the first 50 to 100 cycles. The extent of hardening increases with increasing strain amplitude and decreasing temperature and strain rate. The initial hardening is followed by a softening and saturation stage at high temperatures, and by continuous softening at room temperature.

Secondary hardening may be observed at temperatures < 100°C by strain-induced martensite formation in grades with low austenite stability or with high defect density from previous metal working process [42][52] or above 200°C by DSA [42][53][54], in particular in steels with high free nitrogen content. Another explanation for secondary hardening at higher temperatures is the gradual increase of planar slip and growth of special Corduroy dislocation structure [12][55]. DSA and small strain amplitudes were found to promote this structure. A more distinct secondary hardening is often observed at small strain amplitudes and causes a decrease of plastic strain and increase of fatigue endurance limit. Cold-worked SS usually show an initial softening, which is followed by a saturation stage and a secondary hardening at temperatures < 100°C due to martensite formation in some cases [42][52].

Although the cyclic strain hardening behavior is likely to influence the fatigue limit of the material and the hardening behavior (and deformation mechanism) can strongly vary with temperature, strain rate, chemical composition and thermo-mechanical heat treatment condition, the fatigue lives of different are usually quite similar (within a factor of 2 to 3) over a wide range of different conditions. The fatigue behavior of SS can thus be reasonably described by a single curve (see Fig. 1.12).

Fig. 1.12 compares the corresponding ASME Code mean curve (prior to 2009 edition) with the best fit curves of the ANL model for strain-life data of austenitic SS in air at different temperatures gathered by NRC and JNES (Japanese Nuclear Energy Safety Organization). The best fits were obtained by fitting the data with Langer equation:

$$\epsilon_a = AN_f^{-b} + B \tag{1.2}$$

or in logarithmic expression:

$$lnN_f = \frac{lnA}{b} - \frac{1}{b} ln(\epsilon_a - B) \tag{1.3}$$

The best fit in air of ANL model (also called NUREG equation) in Fig. 1.12 is valid for 304, 304L, 316 and 316 NG SSs from 20°C to 400°C in the expression of:

$$lnN_f = 6.891 - 1.920 ln(\epsilon_a - 0.112) \tag{1.4}$$

In Fig. 1.12, ASME Code Section III (before 2009 Addenda) predicts longer fatigue life than recent experimental data when ϵ_a < 0.3%. A possible explanation for this discrepancy is that the carbon content was reduced in modern SS to mitigate and reduce SCC susceptibility with respect to the original SS, which formed the basis of the ASME III mean curve. The related reduction of yield strength has an effect of the shape of Langer curve, it improves and reduces fatigue life at high strain and small strain amplitudes, respectively. The air fatigue design curve

in ASME Code Section III of 2009 Addenda or later editions is based on the ANL model and consistent with the more recent experimental results.

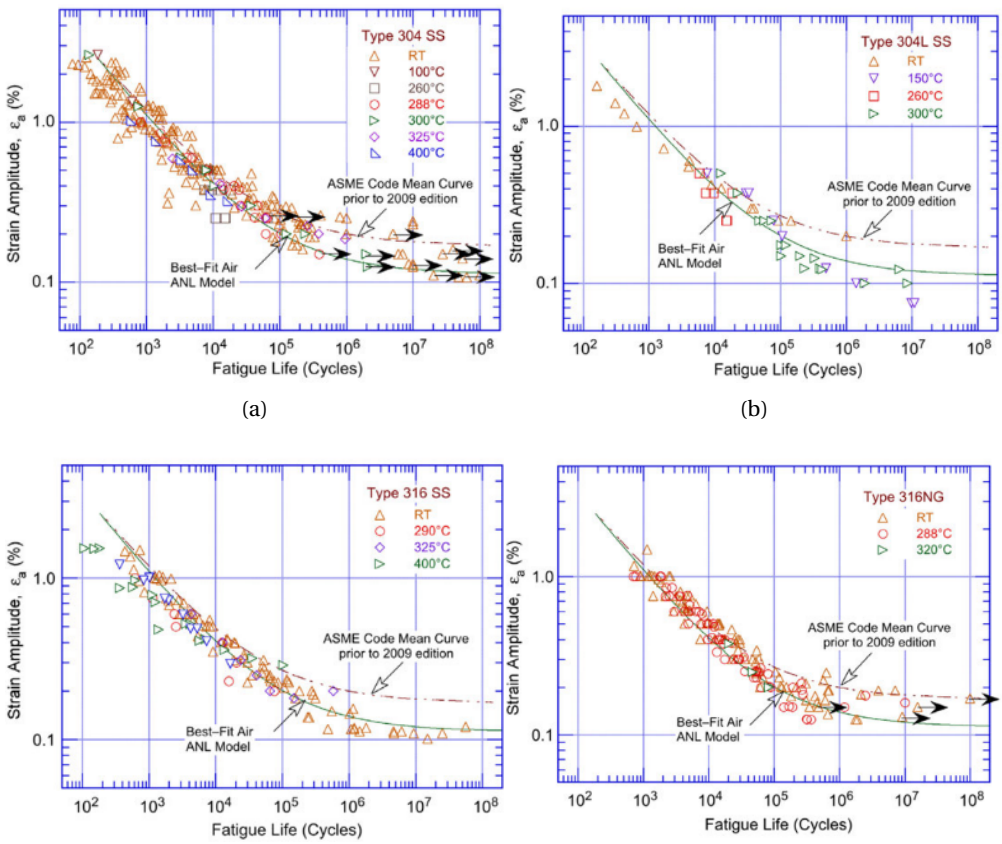

Figure 1.12 – Strain-life data of (a) 304, (b) 304L, (c) 316 and (d) 316NG SSs in air at various temperature. The data are gathered in NUREG/CR-6909 report from NRC and JNES results [3].

Design against fatigue of SS primary pressure-boundary components is often based on Section III, Subsection NB of the ASME Boiler and Pressure Vessel Code [56]. It relies on fatigue curves and endurance limits derived mainly from strain-controlled LCF tests with small, smooth specimens in air at room temperature, which do not directly consider possible effects of LWR environments.

A factor of 20 on cycles and 2 on strain was introduced to account for material variability, data scatter, size, surface finish and environments to form a conservative margin. Later, the environmental factor F_{en} (defined as the ratio of life in air at room temperature to that in water at the service temperature) to adjust component fatigue usage values for environmental effects of LWRs was first proposed by Mehta at General Electric [57][58] and by Higuchi and Iida in Japan [59]. Chopra and Shack from Argonne National Laboratory (ANL) assembled and analyzed environmental fatigue test data and derived F_{en} factors. The analysis is described in

the comprehensive report NUREG/CR-6909, which the Nuclear Regulatory Commission (NRC) issued the Regulatory Guide 1.207 in 2006 based on [6] and that is regarded as an acceptable method to evaluate LWR environmental effects on fatigue life. NUREG/CR-6909 and NRC Regulatory Guide 1.207 were both revised in 2018 [3]. Similarly, the ASME Code Case N-792 and alternatively the ASME Code Case N-761 were developed by the ASME with slight differences from NUREG/CR-6909, namely without a strain threshold for environmental effects to occur and providing strain rate dependent S-N curves. Actually several years before the U.S., the Japanese Ministry of International Trade and Industry (MITI) had issued the "Guidelines for Evaluating Fatigue Initiation Life Reduction in the LWR Environment" [60] in 2000 and the Thermal and Nuclear Power Engineering Society (TENPES) has accordingly issued "Guidelines on Environmental Fatigue Evaluation for LWR Components" [61] in 2002. Based on these two guidelines, the Japan Society of Mechanical Engineers (JSME) integrated the Environmental Fatigue Evaluation Method (EFEM) into its Codes for Nuclear Power Generation Facilities in 2006 and formed JSME S NF1-2006 [62], which was revised in 2009 with the most up-to-date knowledge [2]. Fig. 1.13 presents the dependence of F_{en} on strain rate and temperature of NRC/Chopra and MITI/Higuchi methods in BWR or PWR environments.

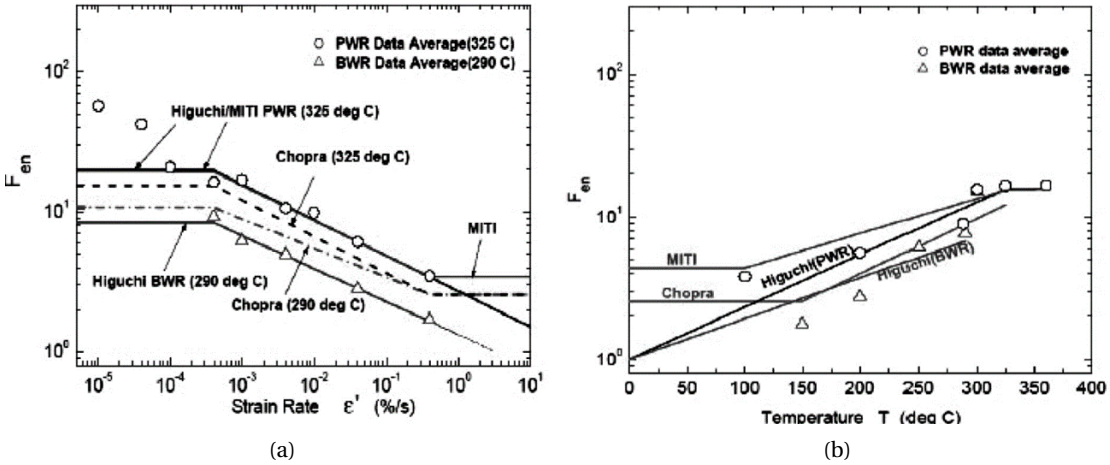

(a) (b)

Figure 1.13 – F_{en} dependence on (a) strain rate (b) temperature of NRC/Chopra and MITI/Higuchi methods [2].

1.3 Environmentally-assisted fatigue of austenitic stainless steels

The decrease of fatigue life depends on strain rate, DO level in water, and temperature and is usually more pronounced under PWR and BWR/HWC conditions at low corrosion potentials than under oxidizing BWR/NWC conditions for solution-annealed SS. The fatigue life is decreased significantly when three threshold conditions are satisfied simultaneously, i.e., when the applied strain range and service temperature are above a minimum threshold level (> 0.3 % and > 150°C), and the loading strain rate is below 0.4 %/s. Environmental effects are moderate, e.g., less than a factor of 2 decrease in life, when any one of the threshold

conditions is not satisfied. Under extreme conditions (e.g., high temperatures around 250 to 320°C and very slow strain rates), the fatigue life reductions can be more than a factor of 20 and fatigue lives thus be below the fatigue design curves (see Fig. 1.14). These observations thus have raised concerns about the adequacy of the margins in the current fatigue evaluation procedures.

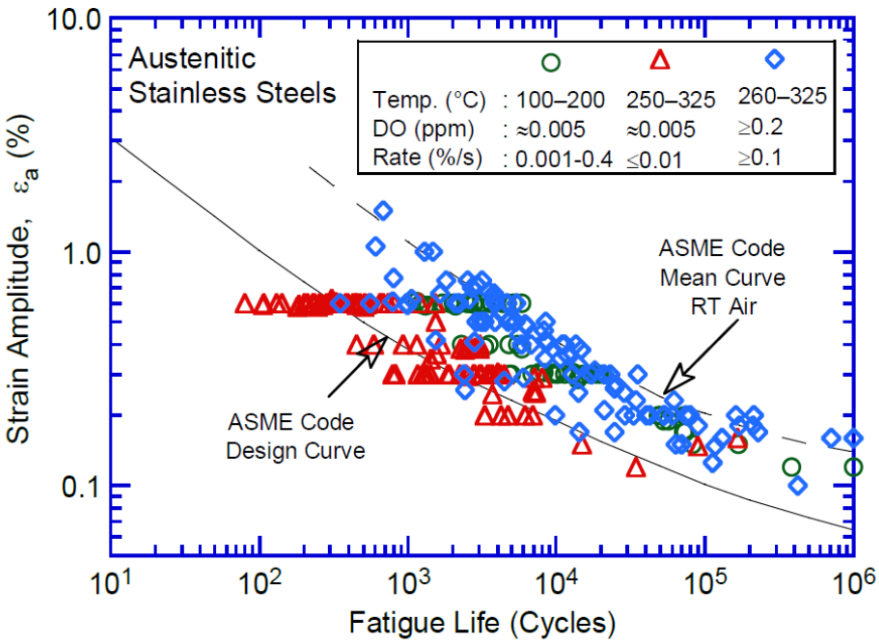

Figure 1.14 – Strain-life data of austenitic SSs tested in HTW with various temperature (100-315(°C), DO and strain rate [63].

The apparent discrepancy between (mostly isothermal) laboratory LCF test results (strong environmental effects) and field experience (only a few fatigue or EAF incidents under very specific circumstances, predominantly related to thermal transients) is mainly related to the large degree of conservatism in the fatigue evaluation procedures (in fatigue design or evaluation). The environmental effects are usually less severe than it appears, e.g., in Fig. 1.14. For many plant transients one or several of the threshold conditions are not satisfied and environmental effects are moderate. Slow thermal transients with slow strain rates produce the strongest environmental effects, but the resulting stresses/strains are small and their cycle number low. They are thus not as damaging with regard to (corrosion) fatigue usage accumulation as may appear at first glance. Fast transients like thermal shock produce high thermal stresses, but the strain rates are usually too high for significant environmental effects. The original fatigue design of these components was done by simplified elastic stress analysis as well as by choosing conservative design transients that are much more severe than the real ones. Environmental effects were not specifically considered, but are probably covered (at least partially) by the design margins that were chosen. Furthermore, the number of transients is limited and operational procedures/designs have now been optimized to reduce fatigue and

avoid thermal stratification. There are significant differences between real fatigue damage accumulation in components with complex boundary conditions (changing temperature, strain rates and water chemistry, strain gradients, multiaxial, complex load histories, technical surfaces, turbulent flow, ...), fatigue design (with simplified very severe transients and elastic stress calculations, ...) and simplified lab testing (isothermal, constant strain amplitude and strain rates, uniaxial, fully plastic ligaments, polished surface, low-flow or quasi-stagnant, ...) and these differences should always be kept in mind, when comparing lab results with service behavior.

Anyway, HTW in LWR environment was commonly recognized being detrimental to fatigue life. Parameters:

- Environmental T, DO, DH, imperities
- Mechanical stress/strain amplitude, strain rate, mean stress
- Material Type of SS, heat treatment, surface conditions

affect EAF life.

In the following paragraphs some selected important parameters (temperature, DO), mechanical (strain rate) and material (surface conditions) are briefly summarized. These observations are mainly based on isothermal, uni-axial strain-controlled LCF tests.

1.3.1 Temperature effects on EAF

The temperature varies with location in the reactor coolant circuits in LWRs and strongly change during plant transients (start-up/shutdown, ...) that may cause thermal fatigue. Elastic modulus, cyclic plastic deformation behavior, thermal expansion and, in particular, corrosive effects (solubility, reaction kinetics, diffusion, ...) all depend on temperature. Temperature thus can have a significant effect on EAF. Most fatigue tests for evaluating LWR environmental effects were performed under strain control. So, the following statements regarding temperature effects are made on the basis of strain-controlled tests. In Chopra's study with JNUFAD database [63], fatigue life is found to be independent of temperature from room temperature to 400°C in air. However, recent load-controlled data indicate that at temperature higher at 300°C, a fatigue limit higher than at 150°C can exist, because dynamic strain aging induces significant secondary hardening at high temperature. In contrast to air, temperature has a strong effect on EAF life in LWR environments. Fig. 1.15 suggests a threshold temperature of 150°C, above which $log(N_f)$ decreases linearly with temperature in water and strain rate, if the strain rate is below 0.4%/s. Environmental reduction of fatigue lives (< 2 x) and temperature effects are small below 150°C.

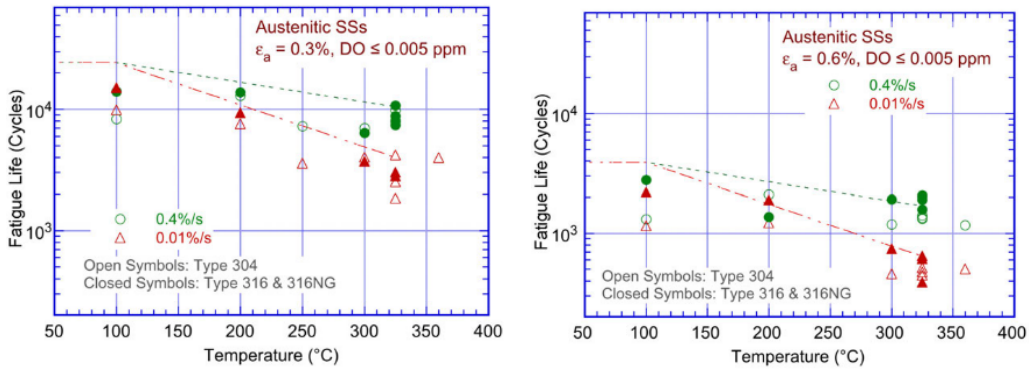

(a) (b)

Figure 1.15 – Fatigue lives of austenitic SSs versus temperature in low-DO water [3].

The F_{en} factor is defined as the ratio of the fatigue life in RT air over the fatigue life in water at tested temperature. Fig. 1.16 describes the relationship between F_{en} and temperature in BWR and PWR environments, at the strain rate $\dot{\varepsilon}$ of $0.001\%/s$. Fig. 1.16 suggests an increase of F_{en} and environmental reduction in fatigue lives with temperature.

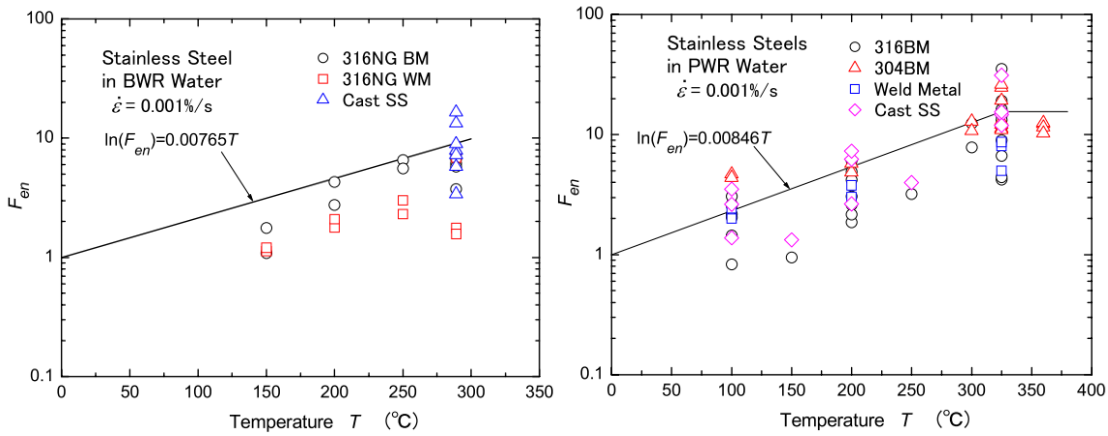

(a) (b)

Figure 1.16 – F_{en} of SSs versus temperature in (a) BWR (b) PWR environments [2].

1.3.2 Strain rate effects on EAF

The strain rate can strongly vary between different plant transients (very slow in thermal stratification, rather fast in case of thermal shocks) and (as with temperature) also change during the transients. Strain rate effects were mostly investigated in strain-controlled test with constant (or approximately constant) rates during the raising load phase of a fatigue cycle and during the tests. The fatigue life in air is independent (or only weakly dependent) on strain

rate in the range from 0.001 %/s to 1%/s. As shown in Fig. 1.17, in low-DO environments, $log(N_f)$ of austenitic SSs decreases linearly with decreasing strain rate, for strain rate lower than ≈ 0.4%/s, and saturates at ≈ 0.0004%/s.

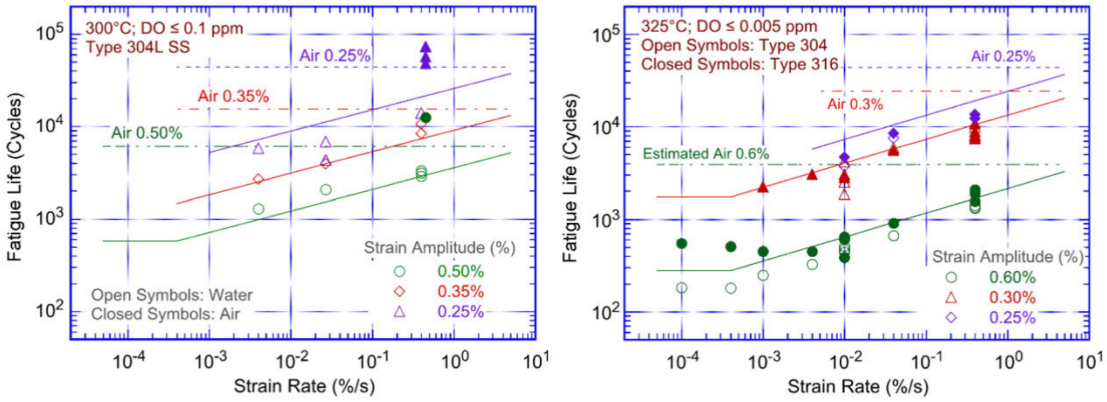

(a) (b)

Figure 1.17 – Change of fatigue lives of austenitic SSs with strain rate in low-DO water [3].

Fig. 1.18 describes the dependence of F_{en} on strain rate of SSs in BWR and PWR environments. F_{en} increases with decreasing strain rate. The least squares fitted trend lines, which are adopted in JSME codes, show that the effect of strain rate tends to saturate at 0.0004%/s for non-cast SSs and at 0.00004%/s for cast SSs [2][62][64]. Above a threshold strain rate of about 1%/s, the environmental effects disappear and fatigue lives are similar to those in air.

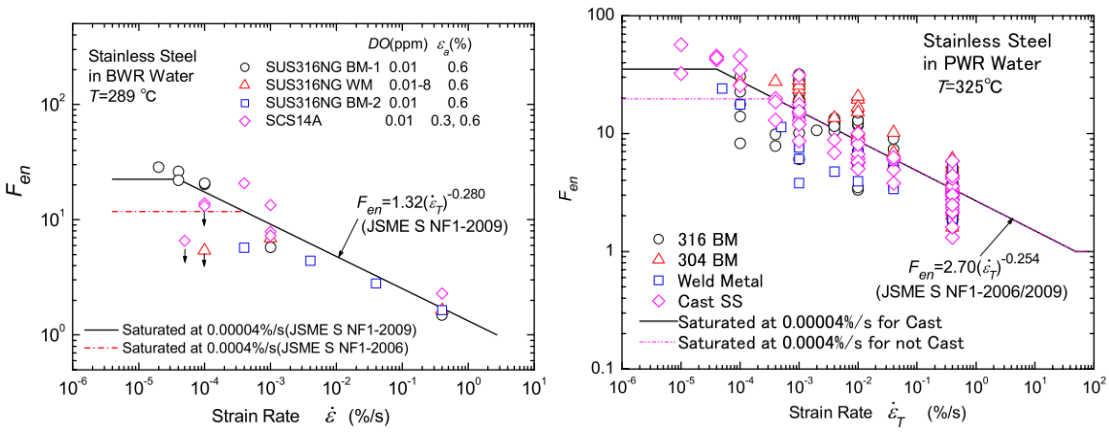

(a) (b)

Figure 1.18 – Dependence of F_{en} on strain rate for SSs in (a) BWR and (b) PWR environments [2][64]

In addition to the synergic effect of strain rate and corrosion on fatigue life, strain rate effects

on the stress-strain response and cyclic plastic deformation behavior were also observed. As can be seen in Fig.1.19, Delobelle reported that an increase of strain rate induces a larger stabilized stress range in strain-controlled LCF tests at temperatures between RT and 250°C. This is called a "positive sensitivity to strain rate". With increasing temperature, the stress response turns to a negative sensitivity up to 550°C, and becomes positive again above 600°C [65][66].

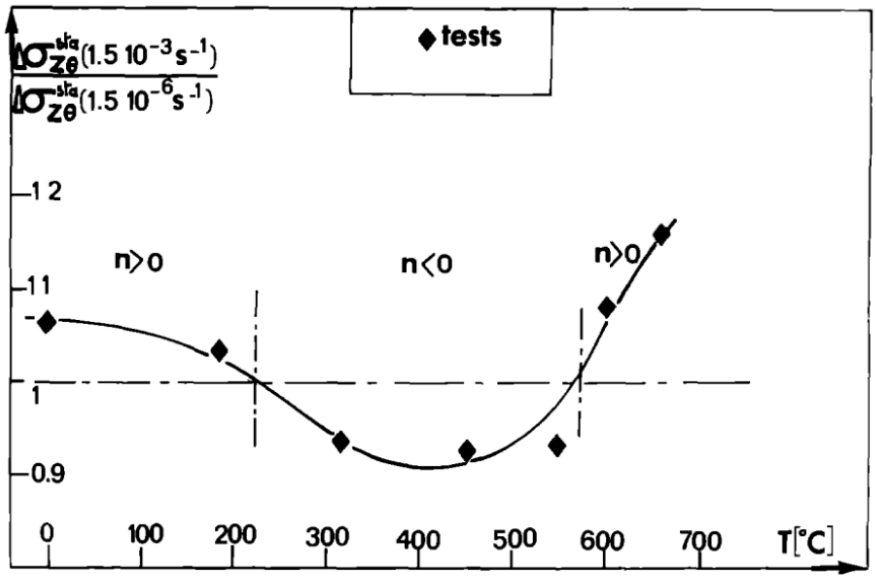

Figure 1.19 – Temperature dependence of the stabilized stress range ratio at a strain rate of 0.15 and 0.00015 %/*s* in strain-controlled LCF tests of a 316L SS [65].

Similarly, Kang et al. also reported, as Fig. 1.20 shows, positive sensitivity at RT and negative sensitivity of strain rate at 350°C [67].

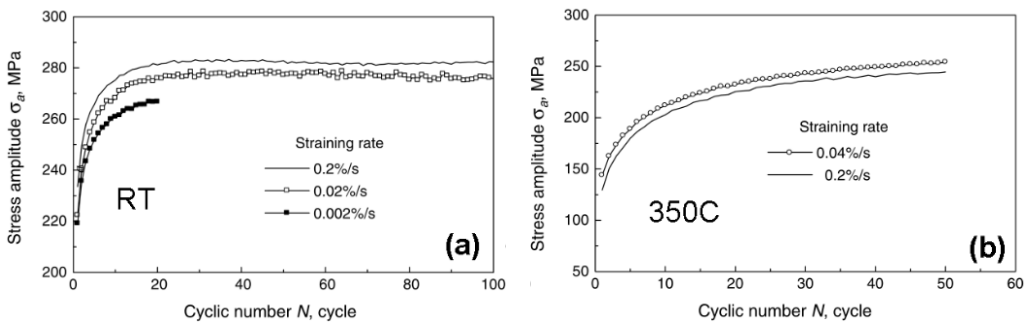

(a) (b)

Figure 1.20 – Stress amplitude variation with loading cycles of LCF tests on 304L (a) at 25°C and (b) at 350°C with different strain rates [67].

In the case of asymmetric strain or stress-controlled cycling tests (Fig. 1.21), the strain rate has a noticeable influence on the ratcheting (namely mean strain), in which the first cycle contributes most [67][68].

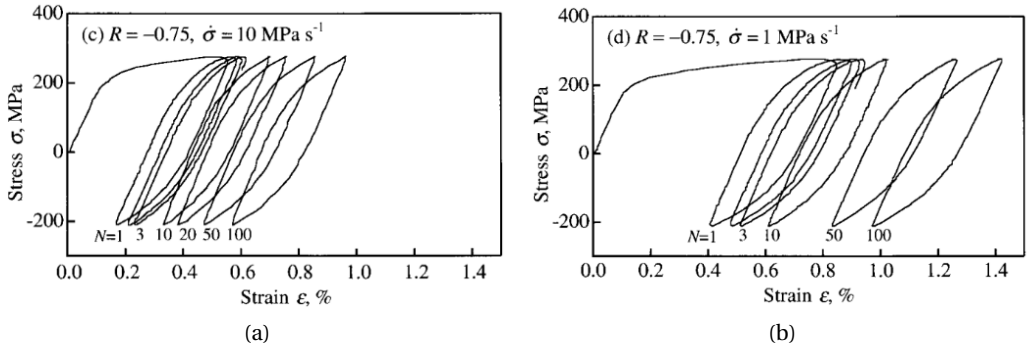

Figure 1.21 – Uniaxial fatigue tests of 316FR with ratcheting at RT with different stress rate (a) 10 MPa/s and (b) 1 MPa/s[68].

1.3.3 Surface roughness effects on EAF

The pressure boundary components in LWRs have a technical surface finish from fabrication. Surface conditions (roughness, cold-work, residual stress, corrosion deposit or pits and etc.) may affect the fatigue life and limit or threshold and are often poorly known and can significantly deviate from fabrication or component specifications. The surface defects are stress concentrators for crack initiation or can even represent the initial cracks [31]. Furthermore, in high DO water, an occluded aggressive crack crevice chemistry can be formed in such surface defects in presence of harmful anionic impurities like sulphate and chloride. In Coop [69] and NUREG/CR-6909-2007 reports [63] it is shown that surface finish leads to a transferability or safety factor of about 2 to 3.5 from fatigue lives measured with smooth specimens [70]. The fatigue design code was established on the basis of strain-controlled tests in air at room temperature with small smooth specimens, where the concomitant effects of surface finish and environments were not investigated. Thus a sub-factor was included to account for surface finish. Among the transferability factors, F_{en} was introduced to account for environmental effects. However, the coupling effects of surface finish and environments were not adequately addressed in the transferability factors.

As Fig. 1.22 illustrates, for austenitic SSs (316NG and 304 SS), specimens with rough surfaces have shorter fatigue life than that of smooth specimens in air. Whereas, the difference between smooth and rough specimens is smaller in water [63]. Poulain et al. [71][72] also observed a similar phenomenon and indicated that surface finish made no effect on cyclic stress response. This phenomenon may be attributed to materials whose fatigue life is dominated by crack propagation and thus is less sensitive to surface topography. Dahlberg et al. also indicate that the maximum irregularities are better indicators than the average value for characterizing

surface roughness [70].

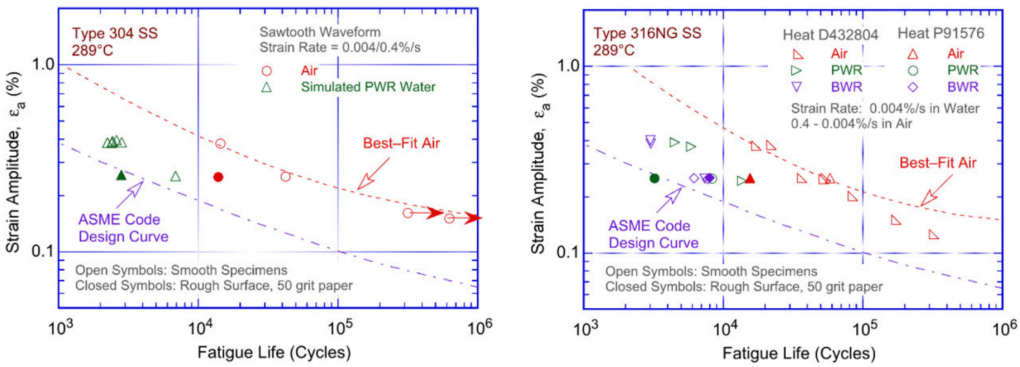

(a) (b)

Figure 1.22 – Investigation of surface roughness effect on fatigue life of (a) 304 and (b) 316NG SSs in 288°C air and LWR environments [63].

1.3.4 Dissolved oxygen effects on EAF

Solution annealed austenitic SSs have shorter fatigue lives in low-DO (i.e., < 0.05 ppm DO) water than in high-DO water, in contrast to the fatigue life behavior of carbon or low-alloy steels. In low-DO water, slower strain rate results in shorter life while the influence of composition and heat treatment is insignificant. In high-DO water, the occurrence of strain rate effects depends on composition and heat treatment. Strain rate effects are small for solution annealed materials whereas for sensitized they are as strong as (or even stronger than in low-DO water [63].

In the evaluation of LWR environmental effects on fatigue life, temperature, strain rate and DO are considered in F_{en} calculation. Besides these environmental effects, effects of hold time, dissolved hydrogen (DH), water conductivity, flow rate and material heat treatment were studied to a smaller and less systematic extent, but are not explicitly considered in F_{en} definition for the time being.

Flow rate and hold time at peak tensile strain have no effect on fatigue life in austenitic SSs [63][73]. Conductivity (or more specifically, harmful anionic impurities like sulphate) and ECP are reported as important parameters in ANL studies [74][75][76]. In high-DO water, fatigue lives of austenitic SSs decrease by factor of ≈ 2 with conductivity increasing from ≈ 0.07 to 0.4 $\mu S/cm$. Limited data indicate material fatigue life decreases with increasing level of sensitization in high-DO water, whereas its effect in low-DO water vanishes [76].

1.4 Mean stress effect on fatigue of austenitic stainless steels

In NPPs components, dead weight, water pressure, thermal stratification/transient and residual stresses may create mean stress in the internal components of pressure vessels and reactor coolant piping system [40][77][78][79]. The influence of mean stress is considered in ASME Section III-NB design code through the modified Goodman diagram, but is not explicitly justified and is not applied to SSs [7][80]. Hence, a significant knowledge gap exists in treating the possible influence of mean stress on fatigue, in particular, in EAF where the underlying mechanisms may be sensitive to mean stress.

It is typically recognized that positive (tensile) mean stress is detrimental and negative (compressive) mean tress is beneficial to fatigue life [81][82][83][84], but this is not totally correct. Mean stress shows a bigger impact on brittle materials than on ductile materials. Based on this knowledge, several mean stress correction models were developed, such as Soderberg, Gerber, Goodman and Morrow models, which predict shorter life for positive mean stress, as described in Fig. 1.27. Their detailed quantitative explanation will be discussed in Section 1.6.1. These models/relationships are applicable for mean stress correction in HCF of carbon and low alloy steels (LASs) whose endurance limit is lower than yield stress, but not applicable for the SSs since their endurance limits are usually larger than the yield stress [7].

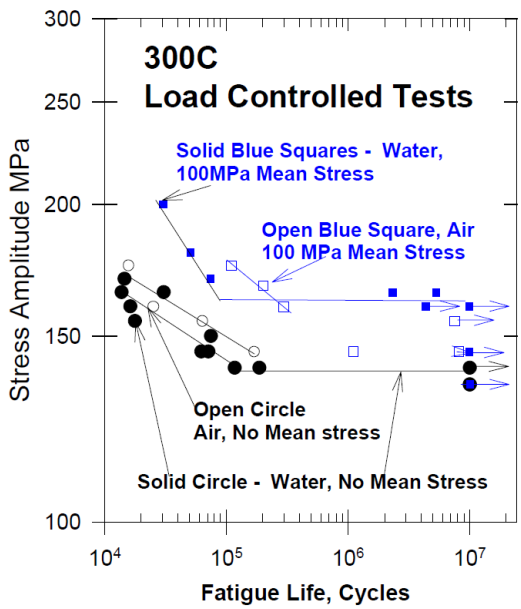

Figure 1.23 – Stress amplitude versus fatigue life (S-N) relationship of 304L SS tested under load-controlled condition with 100 MPa and without mean stress in 300°C air or water [13]

.

Solomon [13](as described in Fig. 1.23), Spätig [11], Wire [85], Zhu [84], Yuan [86], Miura [87] and Colin [88] et al. have shown that positive mean stress increases the fatigue life of austenitic SSs (either 304 SS or 316 SS) under load-controlled condition. Whereas, Vincent et al. [78]

reported positive mean stress being detrimental to fatigue life of austenitic SS, when it is tested under strain-controlled condition where constant mean stress conditions are maintained by adjusting mean strain. Therefore, it is in principle not necessary to correct the fatigue life for mean stress effect for load-controlled cyclic loading and if the ratcheting strain remains limited [80]. However, Kamaya [80] stated that mean stress slightly shortened fatigue life when applying the mean stress for the same strain range (this was also reported by Yuan et al. [86]).

Austenitic SSs undergo pronounced cyclic plastic deformation during cyclic loading so that cyclic hardening usually occurs during the first ≈ 100 cycles followed by softening, and secondary hardening may happen if the stress/strain amplitude is low enough and at high temperature. In case of non-zero mean stress, ratcheting is observed under load-control, so that more strain is accumulated in one direction. However, mean stress tends to quickly relax under strain-control. Thus, most tests designed to investigate mean stress effect are under load-control. The beneficial effect of mean stress is associated with materials cyclic hardening, which results in smaller strain amplitude than with zero mean stress for the same stress amplitude. A well accepted way of incorporating mean stress effects for austenitic SSs in design curve is not available and still subject to debate. In LWR environments, mean stress interacts synergistically with other factors such as stress/strain amplitudes, temperature, corrosion, etc. and impacts the fatigue behavior of components. The underlying physical mechanisms occurring in the level of the microstructures and controlling the plastic deformation and related damage processes have to be clearly understood to derive reliable fatigue life predictions when mean stresses are involved.

1.5 Correlation between microstructures and fatigue behavior of FCC materials

1.5.1 Single FCC crystal

Study of cyclic-induced dislocation structures and correlation with fatigue mechanical behavior starts from single crystal, mainly from copper crystal. Fig. 1.24 schematically describes the final saturation dislocation configuration of single copper crystals after uniaxial cyclic loading. Crystals with orientation close to [001] tend to develop "Labyrinth structures": those close to $[\bar{1}11]$ tend to develop "Cell structures" or "wall structures"at high strain amplitude and develop "vein structures" at low strain amplitude; and those close to [011] tend to develop "deformation bands" and dropping in the gray region in the stereographic triangle illustrated in Fig. 1.24 tends to develop "PSB ladders". They are gradually converted into labyrinth or cell structures, if the orientation changes toward [001] or $[\bar{1}11]$ direction [89][90][91][92].

In addition to the dependence on crystal orientation, cyclic-induced dislocation patterns also depend on cyclic stress-strain and slip mode (planar slip or wavy slip), which is largely governed by the stacking fault energy (SFE) and to a lower extent by the short range order (SRO) and the yield strength [30][93], as Fig. 1.25 describes. Lower SFE promotes planar slip

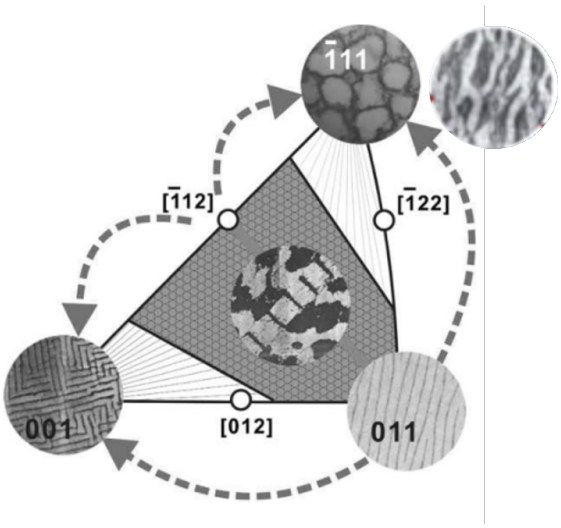

Figure 1.24 – General dependence of dislocation patterns on orientation of FCC single crystal [90][91][89]. Courtesy of Elsevier.

and higher SFE promotes wavy slip due to cross slip. For the same stress/strain amplitude, materials with higher SFE develop more 3D structures (like cells and slip bands) and materials with lower SFE develops more planar dislocation structures. For materials with the same SFE > 0.02 Jm^{-2}, cell structures are developed when subjected to high stress/strain amplitude (which results in short fatigue life), while persistent slip bands are formed at low stress/strain amplitude (long fatigue life) [30]. For materials with low SFE, the cross slip can be activated at certain high temperature, strain amplitude and accumulated plastic strain. This results in observation of more wavy slip characters with increasing number of loading cycles [94][95][96][97].

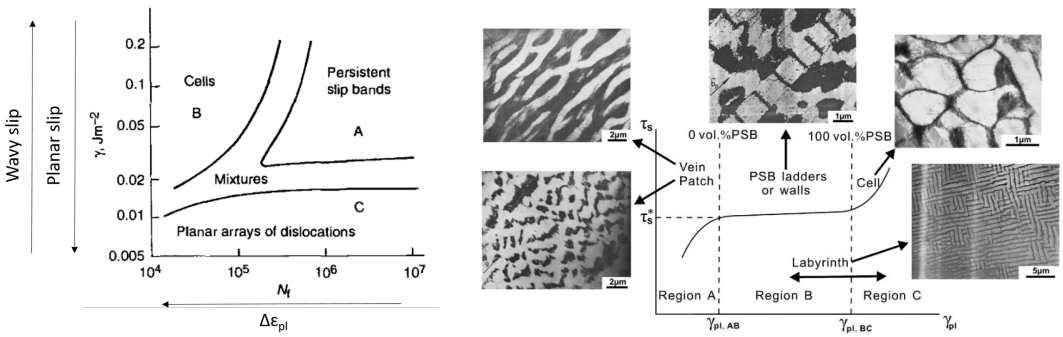

(a) (b)

Figure 1.25 – General dependence of fatigue-induced dislocation patterns on (a) slip mode/stacking fault energy (SFE)[30][93] and (b) cyclic stress-strain of copper single crystal[89][98]. Courtesy of Elsevier.

Mughrabi [98] established the cyclic stress-strain (CSS) curve (in Fig. 1.25b) by plotting the obtained saturation stress (τ_s) against the corresponding plastic shear strain amplitude (γ_{pl}) [98]. Experimental observation of dislocation structures of copper single crystal are presented in the three regions, which are categorized with different γ_{pl} value [89]. γ_{pl} can be expressed as [99]:

$$\gamma_{pl} = \gamma_{PSB} f_{PSB} + \gamma_M f_M \tag{1.5}$$

where f_M and f_{PSB} are the volume fractions of matrix and PSBs respectively. γ_M and γ_{PSB} are the plastic strain amplitudes carried by matrix and PSBs.

In region A ($\gamma_{PL} \leq 6 \times 10^{-5}$), dislocation veins are formed and the saturation stress increases with increasing strain. Region B ($6 \times 10^{-5} \leq \gamma_{PL} \leq 7.5 \times 10^{-3}$) is characterized by appearance of PSBs and also veins/walls or low dislocation density channel exist. With increasing strain, the saturation stress keeps unchanged (showing CSS curve plateau) and PSBs volume fraction increases correspondingly. When $\gamma_{PL} \leq 7.5 \times 10^{-3}$, the resolved stress increases again with increasing strain and dislocation cell and labyrinth structures are formed from transformation of PSBs [100][92][89][98][97].

1.5.2 Polycrystalline FCC metals

Poly-crystalline materials additionally involve grain boundaries and grains are either randomly oriented or have a certain texture. Depending on orientation, the resolved stresses on primary slip planes are different. Thus different dislocation structures may develop in grains with different orientation. Grain boundaries act as obstacles impeding dislocation movement and also as a source for dislocation generation. Higher stress/strain will localize around grain boundaries and leading to higher dislocation density or earlier formation of spatial dislocation structures [101][102][25][97].

1.5.3 Relationship between dislocation evolution and cyclic stress-strain response

In the first 50-100 cycles, materials firstly undergo cyclic hardening with an increase of dislocation density and interaction between dislocations (Lomer-Cottrell sessile junctions, dislocation tangles) and obstacles (solute atoms) [103].

With further cyclic loading, dislocations rearrange to form veins/walls or even PSBs. Veins and walls are regions with high dislocation density that act as strong obstacle for dislocation movement contributing to cyclic hardening. On the other hand, the channels with low dislocation density provide an easier path for dislocation movement; Formation of PSBs accommodates high local plastic strain. These two dislocation structures contribute to cyclic softening. Normally, softening effect outweighs hardening effect, thus resulting in a softening stage.

With continuing cyclic loading, established cellular structures acting as more effective obstacles for dislocation movement than wall and channel structures or PSBs. This compensates the softening effect resulting in a stabilized/saturation stage [104][105][106][107][108][97].

1.5.4 Mechanism for secondary hardening during cyclic loading

Secondary hardening stage appears in cyclic loading of austenitic SSs, which were tested either at room temperature with high amplitude (LCF) or tested at medium temperature (300°C to 500°C corresponding 0.3-0.5 T_m) with low amplitude (HCF) [1][109][96]. Secondary hardening occurring in LCF was supposedly associated with martensitic transformation [88][110], while Secondary hardening occurring in HCF is associated with formation of corduroy structures, which act as strong obstacles impeding dislocation movement (Fig. 1.26b). Martensitic transformation strongly depends on materials composition, local stress state, strain amplitude and local accumulated plasticity [111]. Higher fraction of homogeneously distributed martensite results in higher fatigue limit [112]. For HCF tests at high temperature (≈ 300°C), planar slip dominates and the accumulated cyclic plastic strain is very high [71][113][109]. This provides condition for formation of sufficient quantity of point defects and their aggregation before end of life. Two types of corduroy structures were observed in Pham's study [104][107][106]: (1) fine corduroy structure (≈18 nm spacing between lines) (Fig. 1.26b-I,II) consists of faulted dislocation loops (≈ 5 nm width) aligning in {111}<112>, which are formed as a result of point defects coalescence; (2) coarse corduroy structure (30-70 nm spacing) (Fig. 1.26b-IV,V) consists of unfaulted dislocation loops (10-20 nm width), which are originated from superjogs and multiple slip activity [114].

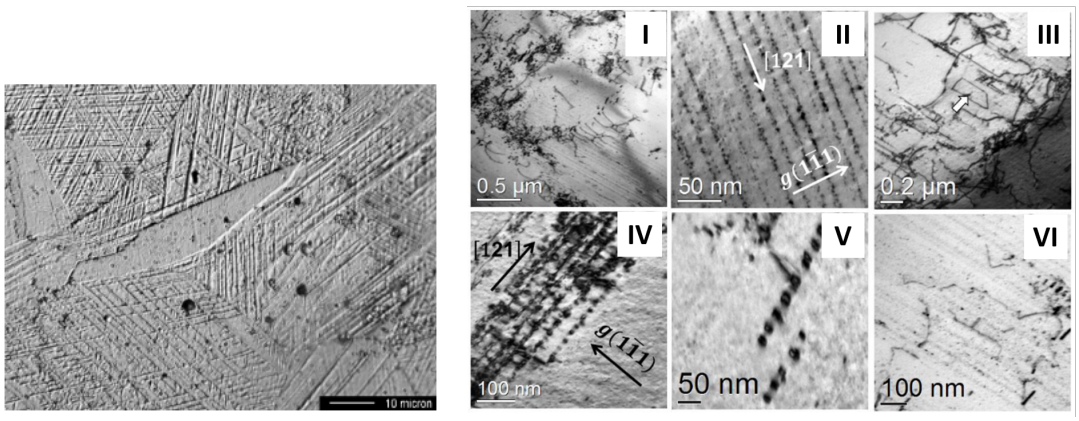

(a) (b)

Figure 1.26 – (a) Strain-induced martensite with 40% fraction in 301 metastable austenitic SS after cyclic loading with ϵ_a = 0.6% at -40°C [111] and (b) Observation of corduroy structures, which are formed either from faulted dislocation loops from point defects coalescence (I, II) or unfaulted dislocation loops from superjog movement or multiple slip activation (IV, V) [104]. Courtesy of Elsevier.

1.6 Fatigue life prediction models

1.6.1 Phenomenological models

For cases without mean stress

Metal fatigue was mainly studied in Wöhler plots (namely S-N plots.) until 1950s. Surprisingly, plastic strain was not considered as a relevant parameter to characterize fatigue life before that time [16]. In general, the stress-life formulation (Equ. 1.6) applies for HCF.

$$\sigma_a = \sigma_f^{'}(2N_f)^b \tag{1.6}$$

where $\sigma_f^{'}$ is the fatigue strength coefficient and b the fatigue strength exponent.

This situation changed after that Coffin [115] and Manson [116] introduced plastic strain into the fatigue life formula, which is known in its modified form by Morrow as Equ. 1.7 [117].

$$\epsilon_{a,p} = \frac{\triangle\epsilon_p}{2} = \epsilon_f^{'}(2N_f)^c \tag{1.7}$$

where $\epsilon_f^{'}$ is the fatigue ductility coefficient and c is the fatigue ductility exponent. This type of fatigue is typical for cases where the cyclic stresses are of thermal origin as in nuclear components for example. In such cases, the stress results from constrained thermal expansion and the fatigue life is associated with cyclic strain.

Then it was recognized that both plastic strain amplitude and stress amplitude are important to assess fatigue life [118]. The strain amplitude is then $\epsilon_a = \epsilon_{a,e} + \epsilon_{a,p}$. Dividing Equ. 1.6 by the Young's modulus E and combing with Equ. 1.7. Morrow obtain the total strain-life relationship given by:

$$\epsilon_a = \epsilon_{a,e} + \epsilon_{a,p} = \frac{\sigma_f^{'}}{E}(2N_f)^b + \epsilon_f^{'}(2N_f)^c \tag{1.8}$$

In Equation 1.8, the case when exponent b = 0 is exactly same expression of strain-life relation as Langer equation (Equation 1.2).

Mean stress corrections

In order to correct mean stress effect on fatigue life, various empirical mean stress correction methods are proposed to get a equivalent full-reversed stress amplitude σ_{ar}:

Goodman's equation [119]:

$$\frac{\sigma_a}{\sigma_{ar}} + \left(\frac{\sigma_m}{\sigma_u}\right) = 1 \tag{1.9}$$

Gerber's equation [120]:

$$\frac{\sigma_a}{\sigma_{ar}} + \left(\frac{\sigma_m}{\sigma_u}\right)^2 = 1 \tag{1.10}$$

Dietman's equation [121]:

$$(\frac{\sigma_a}{\sigma_{ar}})^2 + \left(\frac{\sigma_m}{\sigma_u}\right) = 1 \tag{1.11}$$

Soderberg's equation [122]:

$$\frac{\sigma_a}{\sigma_{ar}} + \left(\frac{\sigma_m}{\sigma_y}\right) = 1 \tag{1.12}$$

Morrow's eEquation [117]:

$$\frac{\sigma_a}{\sigma_{ar}} + \left(\frac{\sigma_m}{\sigma_f^{'}}\right) = 1 \tag{1.13}$$

Smith-Watson-Topper (SWT) equation [123][124]:

$$\sigma_{ar} = \sqrt{\sigma_{max}\sigma_a} \tag{1.14}$$

Walter's equation [125]:

$$\sigma_{ar} = \sigma_{max}^{1-\gamma}\sigma_a^{\gamma} \tag{1.15}$$

SWT equation corresponds to Walter's equation when $\gamma = 0.5$. The relationships of Goodman, Gerber, Sonderberg and Morrow Equations are schematically illustrated in Fig. 1.27. By combining Equ. 1.13 with Equ. 1.6 and Equ. 1.8 respectively, one obtains the Morrow relationship in stress-life:

$$\sigma_a = (\sigma_f^{'} - \sigma_m)(2N_f)^b \tag{1.16}$$

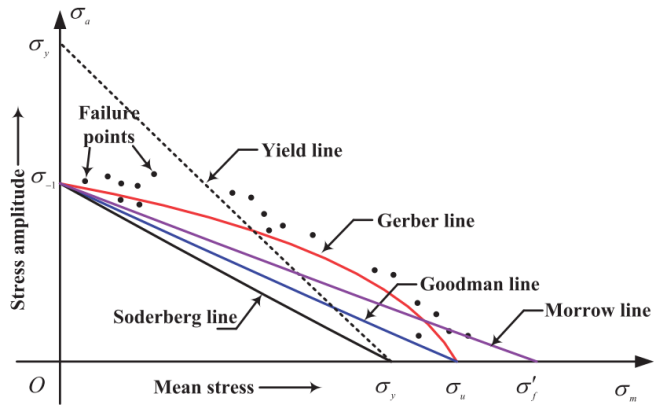

Figure 1.27 – Schematic illustration of Soderberg, Gerber, Goodman and Morrow diagrams for mean stress effect correction [84].

in strain-life:

$$\epsilon_{ar} = \frac{\sigma'_f - \sigma_m}{E}(2N_f)^b + \epsilon'_f(2N_f)^c \tag{1.17}$$

Equ. 1.17 implies that mean stress only affects the elastic part. However, later Manson and Halford [126] proposed to take mean stress effect in the plastic part into consideration:

$$\epsilon_{ar} = \frac{\sigma'_f - \sigma_m}{E}(2N_f)^b + \epsilon'_f(\frac{\sigma'_f - \sigma_m}{\sigma'_f})(2N_f)^c \tag{1.18}$$

Later, stress and strain or energy based models were proposed. Smith-Watson-Topper (SWT) [124] have proposed a model, which includes both stress and strain factors (in Equ. 1.20):

$$\sigma_{max} = E \cdot \epsilon_{a,e} = E \cdot \frac{\sigma'_f}{E}(2N_f)^b = \sigma'_f(2N_f)^b \tag{1.19}$$

Combine Equ. 1.8 with Equ. 1.19, thus get

$$\sigma_{max}\epsilon_{ar} = \sigma'_f\epsilon'_f(2N_f)^{b+c} + \frac{\sigma'^2_f}{E}(2N_f)^{2b} \tag{1.20}$$

Later, SWT parameter was modified by other researchers, such as Lorenzo and Laird [127] proposed to ignore the elastic part, thus:

$$\sigma_{max}\epsilon_{a,p} = \sigma'_f\epsilon'_f(2N_f)^{b+c} \tag{1.21}$$

however, this equation does not apply to HCF.

Dowling [81] has modified the SWT model by transferring to strain-life relationship with

introducing R value:

$$\epsilon_a = \frac{\sigma_f^{'}}{E}\left[2N_f\left(\frac{1-R}{2}\right)^{1/2b}\right]^b + \epsilon_f^{'}\left[2N_f\left(\frac{1-R}{2}\right)^{1/2b}\right]^c \tag{1.22}$$

Ince and Glinka [128] have modified the Morrow model in Equ. 1.8 by using the equivalent strain amplitude (ϵ_a^{eq}) to replace the measured amplitude (ϵ_a):

$$\epsilon_a^{eq} = \epsilon_{a,e}^{eq} + \epsilon_{a,p} = \frac{\sigma_{max}}{\sigma_f^{'}}\epsilon_{a,e} + \epsilon_{a,p} = \frac{\sigma_f^{'}}{E}(2N_f)^{2b} + \epsilon_f^{'}(2N_f)^c \tag{1.23}$$

This equation is derived from SWT equation:

$$\sigma_{max}\epsilon_{a,e} = \sigma_f^{'}(2N_f)^b \times \frac{\sigma_f^{'}}{E}(2N_f)^b = \frac{\sigma_f^{'2}}{E}(2N_f)^{2b} \tag{1.24}$$

thus

$$\frac{\sigma_{max}}{\sigma_f^{'}}\epsilon_{a,e} = \frac{\sigma_f^{'}}{E}(2N_f)^{2b} \tag{1.25}$$

which is similar to Morrow's Equation (Equ. 1.7), thus Ince and Glinka assumed $\frac{\sigma_{max}}{\sigma_f^{'}}\epsilon_{a,e} = \epsilon_{a,e}^{eq}$

Finally, Golos & Ellyin [129], Kujawski [130][131], Chiou & Yip [132], Zhu et al. [84][133][134][135] have developed different strain energy dissipation criterion based models. Strain energy dissipation is a parameter related to fatigue damage.

1.6.2 Statistically-based models

Conventional least square fitting based methods

In principle fatigue life/damage of materials used in corrosive environment (e.g., HTW) cannot be precisely predicted by conventional physically-based methods (e.g., Morrow, SWT and strain energy based methods), as they consider only mechanical degradation and corrosive degradation is absent. Thus statistically-based models are commonly applied in this context, where corrosive effects play a significant role and multiple influential factors (e.g., temperature, strain rate, DO) are involved.

Higuchi et al. [64][73][2][136] have firstly introduced F_{en} factor (defined as Equ. 1.26) in their environmental fatigue life correction and which is adopted in JSME Codes.

$$F_{en} = \frac{N_{f,air}}{N_{f,water}} \rightarrow \ln F_{en} = \ln N_{f,air} - \ln N_{f,water} \tag{1.26}$$

where $N_{f,air}$ and $N_{f,water}$ are fatigue life in air at RT and in water (LWR environments) respectively, For austenitic SSs:

$$\epsilon_a = 23.0 N_{f,air}^{-0.457} + 0.11 \tag{1.27}$$

$$\ln F_{en} = \left(C - \dot{\epsilon}^*\right) T^* \tag{1.28}$$

where the constant C, $\dot{\epsilon}^*$ and T^* depends on water chemistry (BWR/PWR), strain rate ($\dot{\epsilon}$) and temperature and more detail can refer to [2].

Analogously, Chopra et al. [3][63][137] have introduced three fitted constants (T^*, $\dot{\epsilon}^*$, O^*) to consider the environmental effects of temperature, strain rate and DO. The fitted relationship for fatigue life of austenitic SSs in RT (25°C) air:

$$\ln N_{f,air} = 6.891 - 1.920 \ln \epsilon_a - 0.112 \tag{1.29}$$

in LWR environments:

$$F_{en} = \exp\left(-T^* \dot{\epsilon}^* O^*\right) \tag{1.30}$$

The F_{en} is defined by Equ. 1.26. The definition of three fitted constants (T^*, $\dot{\epsilon}^*$, O^*) were recently revised in ANL report (NUREG/CR-6909) 2018 [3] on the basis of its first version [63].

Optimization algorithms (machine learning) based methods

Conventional least square fitting used in Higuchi and Chopra methods can only take several influential factors into consideration but is insufficient to describe the non-linear and synergistic effects between influential factors. Optimization algorithms (also called machine learning) such as genetic algorithms, artificial neural network (ANN), support vector machine (SVM) can be applied to deal with such kind of multivariable non-linear problems of fatigue in LWR environments.

Pleune et al. [138] have trained a 4 layers network (6 inputs in first layer, 10, 6 and 1 neurons in subsequent layers) with fatigue life data collected by Chopra in NUREG/CR-6909 [63]. The ANN model predicts better than conventional statistical model (used in [63]) with improving R^2 from 0.86/0/72 to 0.91/0.82 for data in air/water. In addition, the ANN model outweighs conventional statistical models in aspect of interpolation, more influential factor inputs and synergistic effects description. Al-Assadi et al. [139], Vassilopoulos et al. [140], Srinivasan et al. [141] have performed similar research with ANN. However, it is necessary to be aware of the limitation of machine learning techniques, most representative of ANN, that demand of big data set and are subjected to potential of overfitting, which can be reduced by using cross validation, separating training and testing datasets or dropping certain percentage of data in

each training cycle.

The data gained from different institutes would inevitably have some bias, as different testing methods, experimental operators and materials. The situation is most researchers who use statistical models, either machine learning based or conventional least square fitting based, developed/tested their models only with their own data. Inevitably, this will constrain models' generalization property to the situations which is not included in their training datasets.

2 Material and Experimental Methods

2.1 Investigated material

In this work, a 316L low-carbon austenitic SS was studied. The chemical composition is given in Table 2.1. The material was produced as hot finish hollow bar, 219.1 mm in outer diameter (OD), 19.5 mm in wall thickness (WT), 1300 mm in length by Sandvik (marketed as SANMAC 316L) in solution annealed (non-sensitized) and quenched condition.

Table 2.1 – Chemical composition of the investigated material (in wt.%).

Steel	C	Si	Mn	P	S	Cr	Mo	Ni
316L	0.011	0.56	1.77	0.031	0.024	17.20	2.02	11.14

The as-received material was characterized with EBSD and tensile tests to determine its crystallographic grain structure and mechanical properties. In the inverse pole figure (IPF) map (Fig. 2.1), it is observed that the as-received material has a homogeneous texture-free, equi-axed austenitic structure with an mean grain size of about 60 µm and high share of {111} twin grain boundaries (38%) , which are highlighted with black lines. The mechanical properties were characterized by tensile tests (following DIN 50125, using 10 × 50 cm cylindrical B specimens) at RT (≈ 22°C), 100, 200 and 300°C and at a nominal strain rate of 0.1%/s. The measured engineering stress-strain curves are plotted in Fig. 2.2, from which the elastic modulus, 0.2% yield stress and elongation are obtained and plotted against different temperature as Fig. 2.3. Both strength and ductility decrease with temperature. The 0.2% yield stress in Fig. 2.3, derived from the curves in Fig. 2.2 decreases from 260 MPa at 22°C to 150 MPa at 300°C. In the same temperature range, the Young's modulus, which is reported by the material provider, decreases from 200 to 179 GPa.

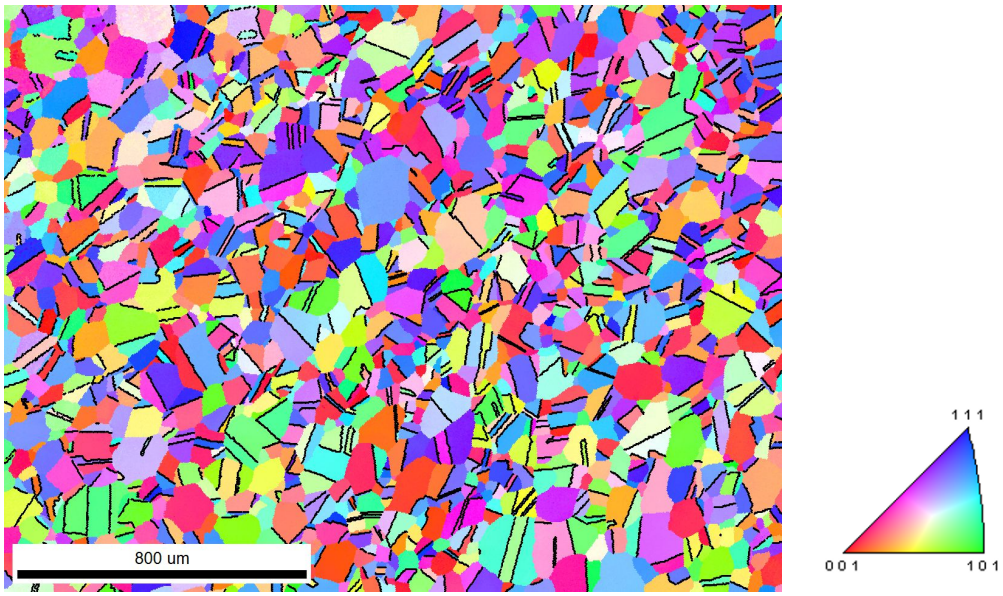

(a) (b)

Figure 2.1 – Inverse pole figure (IPF) of the as-received material. The black lines highlight {111} twin grain boundaries.

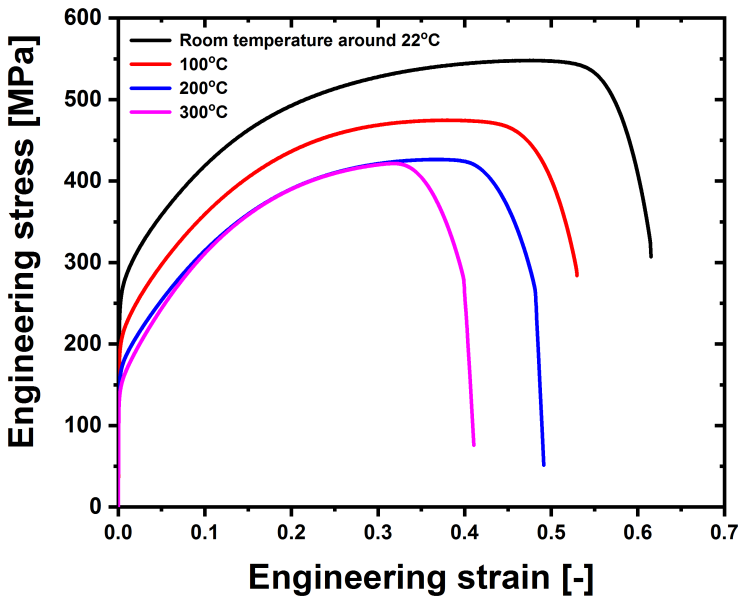

Figure 2.2 – Engineering stress-strain curves of original 316L SS tested at RT, 100, 200 and 300°C.

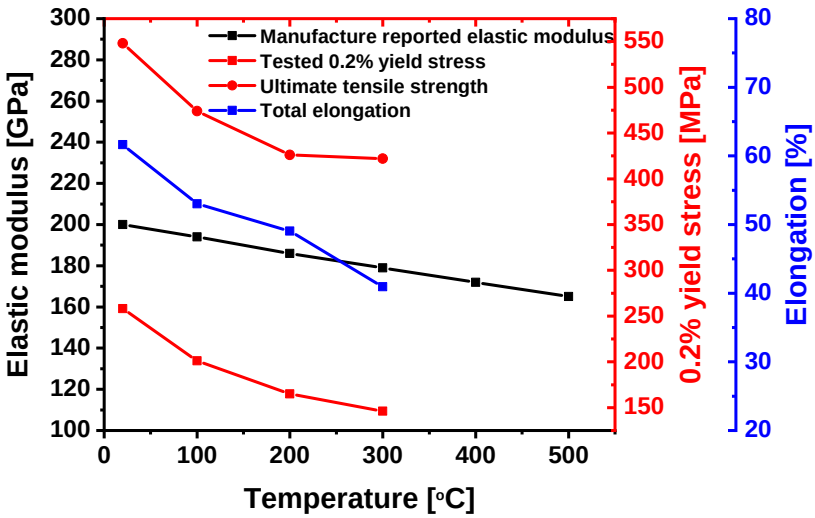

Figure 2.3 – Measured 0.2% yield stress at 22 to 300°C and the elastic modulus from 22 to 500°C as reported by the material provider.

2.2 Specimen preparation

Specimens for fatigue test were cut from the original tube with the loading axis parallel to the longitudinal direction of the tube (see Fig. 2.4). Hollow specimens with outer diameter (OD) of 10 mm and wall thickness (WT) of 2.5, 2.0, 1.5 mm were fabricated for fatigue tests in water and in air (see Table 2.2). The holes of hollow specimen were drilled. Only hollow specimens were applied in this study. The detail geometries are drawn as Fig. 2.5. The gage length is 18 mm. 4 small tubes were welded to the drilled holes at the two heads of hollow specimen to work as the water inlet and outlet.

Table 2.2 – Specimen geometries for fatigue tests in water and in air. All specimens with 10 mm outer diameter and 18 mm gage length.

Specimen wall thickness [mm]	2.5	2.0	1.5
Specimen for test in water	√	√	√
Specimen for test in air	√	√	N.A.

The surface finish of both inner and outer surfaces was controlled by the specimen manufacturer by grinding. The surface roughness of the hollow specimen was characterized by Ra, RzD and Rt values defined as: Ra is the arithmetic average of the profile over the evaluation length; RzD is the average of the successive values of Rti calculated over five sampling length, where Rti is the vertical distance between the highest and lowest points of the profile within a sampling length within the evaluation length; and Rt is the maximum height of the profile, namely the vertical distance between the highest and lowest points within the evaluation length. The measured inner and outer surface roughness values on the inner and outer surfaces are 0.41

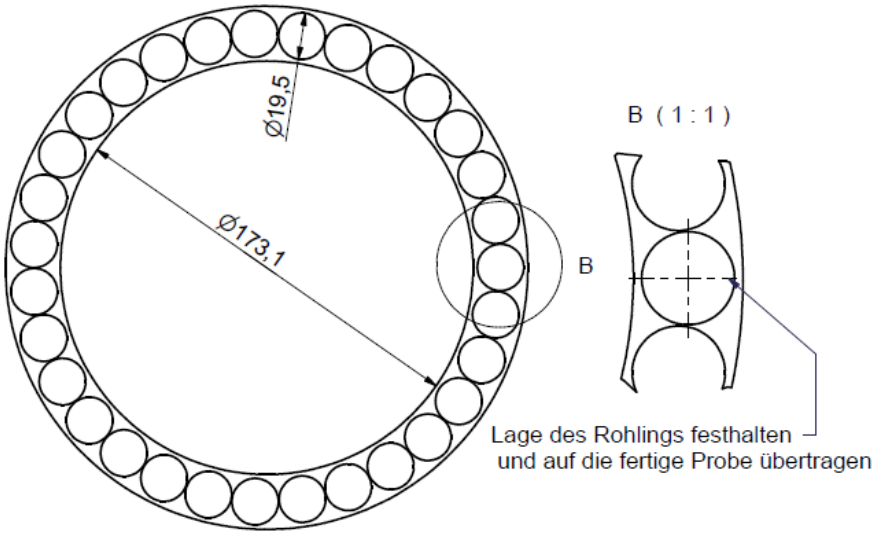

Figure 2.4 – Schematic of cutting plan of specimens for fatigue tests from the original tube, the length unit is mm.

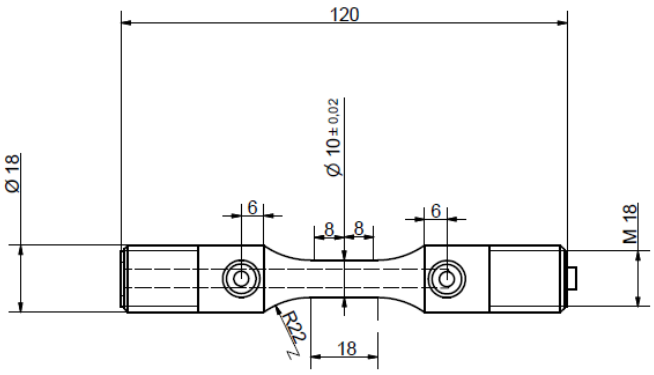

(a)

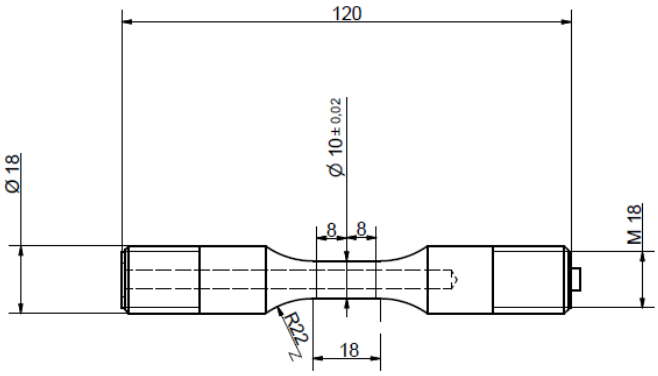

(b)

Figure 2.5 – Drawing of hollow specimens used for the tests (a) in water and (b) in air.

μm of Ra / 3.57 μm of RzD and 0.15 μm of Ra / 1 μm of RzD respectively, as plotted in Fig. 2.6. The grinding scratches on outer surface are parallel to loading axis, however, the scratches on inner surface are tilted at ≈ 45° to the loading axis. Fig. 2.7 shows two representative topographies of outer and inner surface finish. The surface finish of nuclear components must meet some requirements. For instance, according to the RCC-M rules (Règles de Conception et de Construction des Matériels Mécaniques des Ilots Nucléaires PWR", or in English, "Design and Construction Rules for the Mechanical Components of PWR Nuclear Islands), Ra has to be smaller than 6.3 μm in most cases. This value is not specific to fatigue life issues but to facilitate ultrasonic and radiography inspection tests and to avoid trapping of radioactive elements and thus to limit contamination level. Rt value for components in mixing zone and subject to thermal fatigue is to be smaller than 15 μm. The Ra and Rt values of our specimens are in all cases lower than the requirements for actual components.

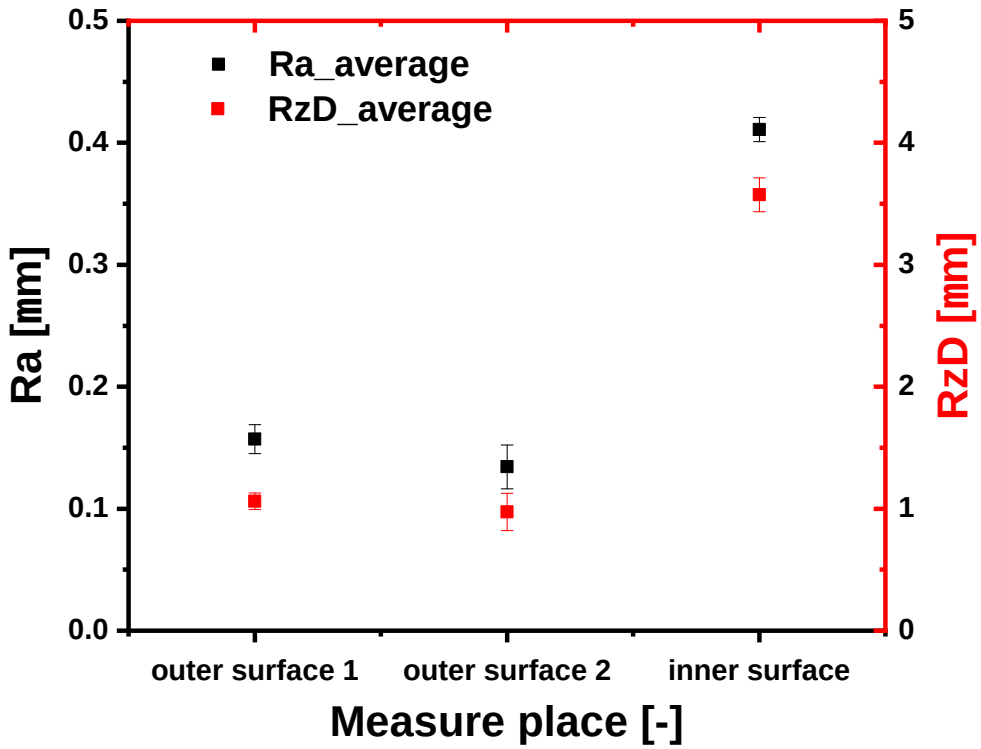

Figure 2.6 – Measured roughness of outer and inner surface of fatigue test specimens.

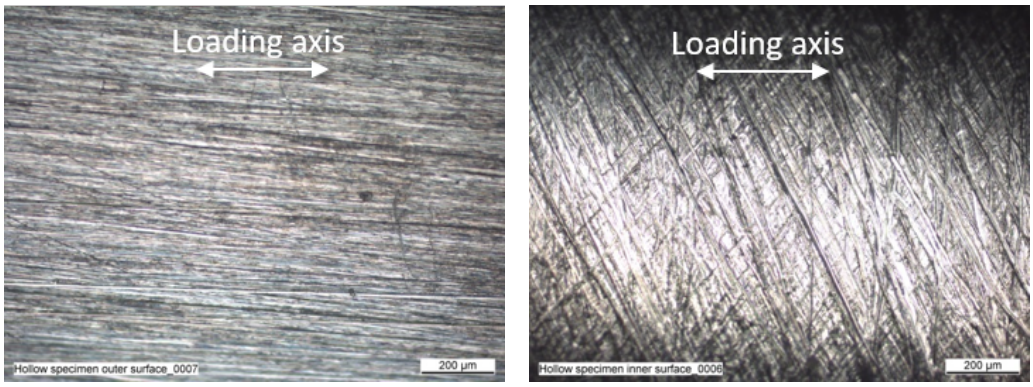

(a) (b)

Figure 2.7 – Specimen surface finish (a) of outer surface and (b) of inner surface.

2.3 Mechanical test facilities and procedures

2.3.1 Fatigue tests in air condition

Fatigue tests in air were performed with a Schenck RMC 100 type electro-mechanical machine. High-temperature air environment was provided by an ATS series 2961 oven, equipped with three heating zones and a EUROTHERM 2704 type thermal controller. The difference between the set point temperature and the real temperature was smaller ± 2°C. The temperature variation along the gage is below ± 3°C. An in-house modified Epsilon model 3648-010M-025-ST extensometer (L_o = 15 mm, with ± 2.5 mm range, relative error within ± 0.02%) was used to measure strain. The extensometer was cooled with liquid cooling by a Huber Minichiller 300, which also provided cooling for the upper and lower grips of the load train, which is equipped with a load cell with capacity of 50 kN.

The test conditions are summarized in Table 2.3. For the sake of consistency with the tests performed in water, hollow specimens were used for tests in air. However, only two different specimen wall thicknesses were investigated. Mean stress of -20, -10, 0, +50 MPa were applied. -10 MPa mean stress was exclusively applied in test in air to mimic the compressive stress (≈ -7 MPa at 100 bar in specimen with 2.5 mm wall thickness) caused by internal pressure. Other testing parameters, such as temperature, waveform, starting scenario, strain rate/frequency, were kept identical for tests in both environments. Fatigue life was defined when the measured elongation was larger than 1.0 mm (for load-controlled tests) and measured load drops 25% from the plateau level (for strain-controlled tests) or when the specimen totally broke into two parts.

Table 2.3 – Fatigue tests conditions in air and water.

Test environments	in air	in water
Materials [-]	SANDVIK 316L	SANDVIK 316L
Specimen geometry [-]	Hollow WT = 2.5 mm WT = 2.0 mm	Hollow WT = 2.5 mm WT = 2.0 mm WT 1.5 mm
Temperature [°C]	288	288
Water pressure [bar]	N.A.	100 *
Signal waveform [-]	sin	sin **
Frequency [Hz]	0.17 (1 Hz after 10^5 cycles)	0.17 (1 Hz after 10^5 cycles) ***
Investigated mean stress [MPa]	-20, 0, 10, +50	-20, -10, 0, +50

* an internal pressure of 200 bar was used for the wall thickness effects study.
** Sawtooth waveform was used for low strain rate study.
*** 60 s in uploading & 6 s in unloading for low rate strain rate study.

2.3.2 Fatigue tests in water condition

Fatigue tests in water were performed with our in-house built fatigue test systems (Fig. 2.8), which consists of an Instron 8862 electro-mechanical machine and a water loop that can provide BWR or PWR water chemistry conditions and allow thermo-mechanical loading. The detailed technical description can be found in [142][143]. The tests were performed in simulated boiling water reactor/hydrogen water chemistry (BWR/HWC) environment. BWR/HWC environment is characterized by a temperature of 288°C with a pressure of 100 or 200 bar, high-purity, deoxygenated (nitrogen purging) water with 150 ppb dissolved hydrogen. The conductivity in the inlet and outlet water was 0.055 μS/cm and smaller than 0.07 μS/cm, respectively. The specimens were heated by the high-temperature water flowing through the hollow specimen with minimal axial and through-wall temperature gradients. A pre-oxidation period of 72 hours was applied before starting the tests. During the pre-oxidation and test, a small compressive offset force, which equals to water pressure times the specimen hollow area, was imposed to balance the tensile force induced by pressurized water. The strain signal was measured with an extensometer attached on the specimen outer surface. A MTS 635.53F-30 type extensometer (L_o = 15 mm, with + 2.4/- 1.2 mm range, relative error smaller than 0.5%) was used for load-controlled tests and a Sandner Sensor EXA15-1u type extensometer (L_o = 15 mm, with ± 1 mm range, relative error within ± 0.2%) was used for strain-controlled tests. The Sandner extensometer was used for strain-controlled tests. As the strain amplitudes were between 0.15% - 0.6%, high sensitivity and accuracy were required, which were guaranteed by this extensometer, which in addition possesses a high eigen frequency thanks to its short arms. Before starting the tests (both in air and water), the extensometer setup was checked (before and after heating) by loading one cycle with a σ_a = 17 MPa (namely force amplitude F_a = 1 kN) to measure the elastic modulus. The measured modulus should be 200 ± 3 GPa at RT and 163 ± 3 GPa at 288°C.

Most fatigue tests were conducted in load-controlled mode but several in strain-controlled mode. Same mean stresses (-20, 0, +50 MPa) were applied, except +10 MPa mean stress was applied for one test to counteract the compressive stress, mentioned above, induced by internal water pressure. Sinusoidal waveform (0.17 Hz before & 1 Hz after 10^5 cycles) was adopted for most tests, only the tests to study slow strain rate were run with a sawtooth profile (60 s uploading time & 6 s in unloading). It has been reported that the environmental reduction of fatigue initiation life in austenitic SS occurs when the strain rate $\leq \approx 7\%/s$, the temperature $\geq \approx 100°C$ and the strain amplitude $\geq \approx 0.1\%$ - 0.15%, are simultaneously satisfied [3]. For the EAF study, the strain amplitude of interest ranges from 0.1% to 0.8%. Our load-controlled tests, carried out at 0.17 Hz, produce average strain rates 0.07%/s to 0.41%/s. For tests running longer than 10^5 cycles (of HCF), where the environment effect is moderate or absent, the frequency was increased to 1 Hz beyond 10^5 cycles to shorten the test duration.

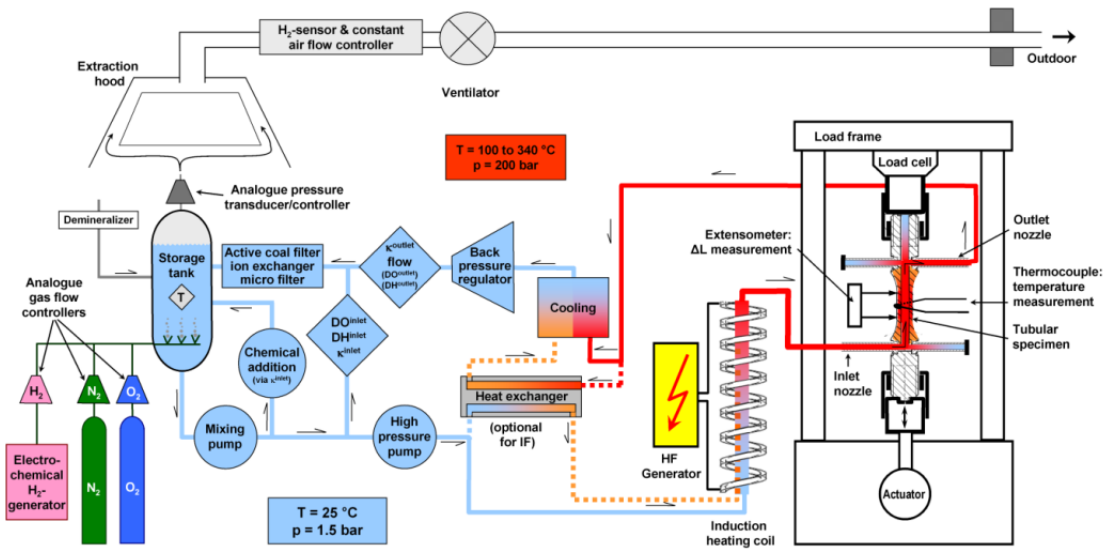

Figure 2.8 – Schematic of facility for fatigue test in water environment [143].

Positive mean stress (as high as +50 MPa) may lead to high plastic deformation (as high as 7-8%) if the maximum stress is reached in the first cycle [13]. For load-controlled tests, a specific starting scenario was implemented to minimize the initial tensile strain. A representative starting procedure of test under load-control with σ_a = 210 MPa & σ_m = -20 MPa in HTW is illustrated in Fig. 2.9. The tests were started by increasing the stress amplitude and mean stress incrementally and successively in tension and compression. For the tests without mean stress, the specimens were loaded according to the following scenario: first cycle starting in tension with σ_a = 17 MPa, second cycle starting in compression with σ_a = 34 MPa, third cycle starting in tension with σ_a = 51 MPa and so on, until the desired stress amplitude was reached. For the tests with mean stress, the stress amplitude was firstly set up as described above and then the mean stress was adjusted by successively increasing the absolute value of mean stress in 10 MPa increment each cycle, but in alternating the tensile and compressive direction, until

the chosen mean stress level was reached. This procedure allows to work harden the material without overstraining the specimens in either tensile or compressive direction. Tests under strain control were started by loading to maximum strain in the first cycle directly.

During the tests, the mechanical loading parameters (including force, strain, travel displacement), the environmental parameters (including specimen temperature, heating water temperature, pressure, flow, dissolved hydrogen (DH), conductivity and etc.) and water leakage and tank water level were monitored. The end of life was determined at the moment of leakage, no matter load or strain is controlled.

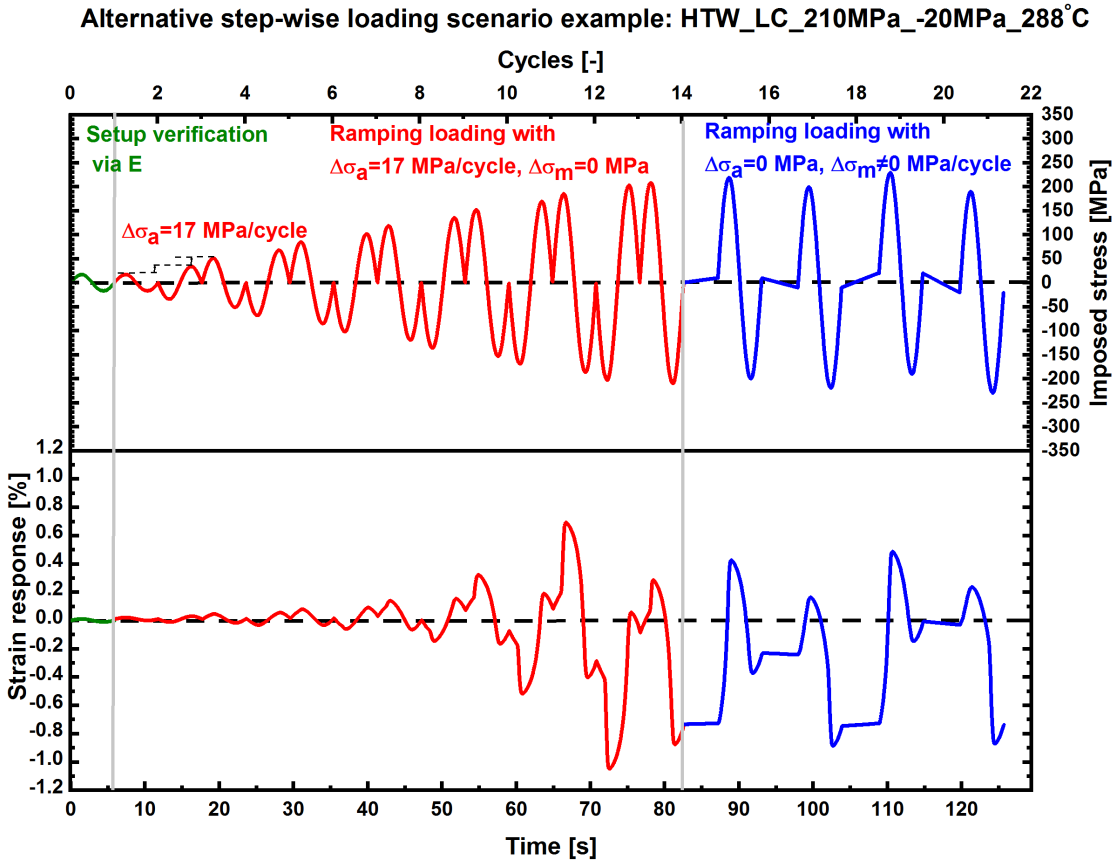

Figure 2.9 – The loading scenario for starting test with σ_a = 210 MPa and σ_m = −20 MPa, during which stress amplitude and mean stress successively increase. Note the alternated direction of loading at the beginning of each cycle.

2.4 Test results data analysis

2.4.1 Data processing

The raw data, with time, cycle number, specimen elongation, force and temperature signals recorded, normally has problem in: identifying the starting point of cyclic loading, exist of

noise data, mismatch between time/cycle and loading signals, holding and interrupted cycles. Thus data processing is required before go to data analysis. Leveraging the open-source tools like $Python$, $Pandas$, $Numpy$, $Scipy$ & $Matplotlib$, a toolkit was developed with the functions of:

- data cleaning
- time/cycle-loading signal mismatch correction
- starting point identification
- holding & interrupted cycles delete
- test data from different file binding
- stress & strain calculation
- maximum & minimum data filter
- and etc.

Detail work flow and script are described in Appendix B.1.

2.4.2 Hysteresis loop analysis

Mechanical parameters were obtained from the hysteresis loop analysis. The tensile (E_t) and compressive (E_c) elastic modulus in hysteresis loop (as Fig. 2.10) are not strictly equal to the material Young's elastic modulus. Once the crack has initiated, the equivalent elastic modulus should decrease theoretically. The E_t and E_c values were calculated by fitting the linear segments of the hysteresis loop with an ad-hoc fitting procedure specially developed for this purpose. First, a section with 45 data points (indicated as the black block between the two short blue lines) was selected starting from 20 points after the maximum/minimum strain (namely the upper right (point C)/lower left (point F) tips of hysteresis loop). Then a subsection composed with 40 data was fitted. After each fitting, the subsection shifts one data point. Once shifted to the end of black block, the subsection is added by one data point, for example to 41 data points. Repeating the fitting and shift over the black block. Finally, the average of the elastic modulus values, which have R^2 larger than 0.99, was applied. More technical detail can refer to the list of codes in Appendix B.2.1.

Once E_c and E_t are calculated, the elastic strain ϵ_e is calculated as $\frac{\sigma_a}{E}$ and the stress at yield point $\sigma_0^{(t)}$ is determined when the loop curve deviates from the linear line (black dash in Fig. 2.10) by 0.05%. The plastic strain range $\triangle\epsilon_p$ is the strain difference between points A and D, where the stresses equal to mean stress. The anelastic strain ϵ_{ane} is calculated as $\triangle\epsilon - \triangle\epsilon_p - \epsilon_e^{(t)} - \epsilon_e^{(c)}$.

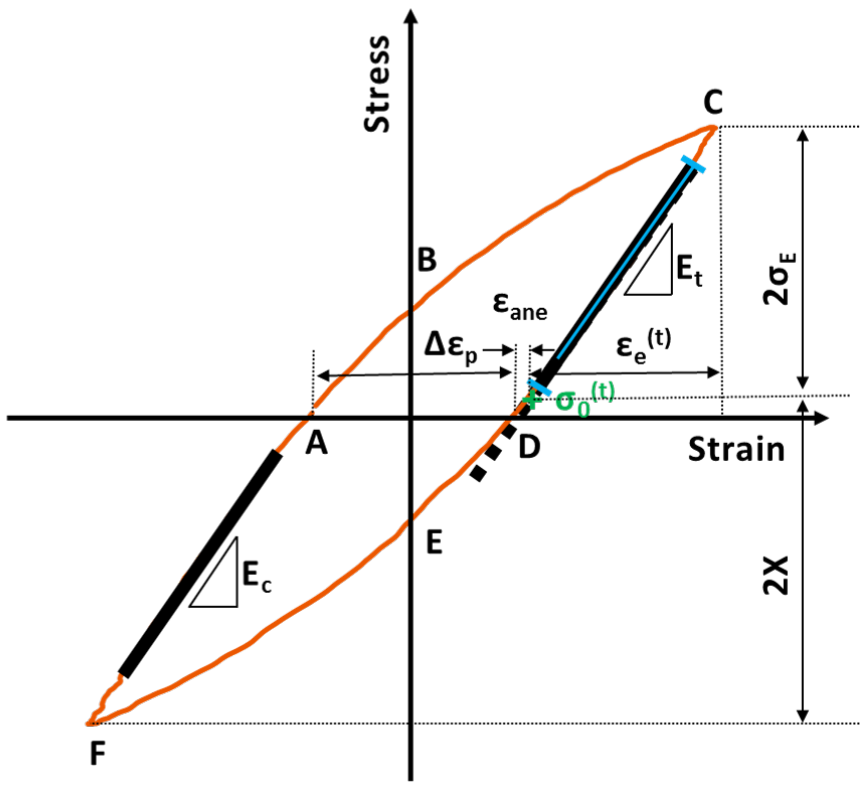

Figure 2.10 – Schematic for hysteresis loop analysis.

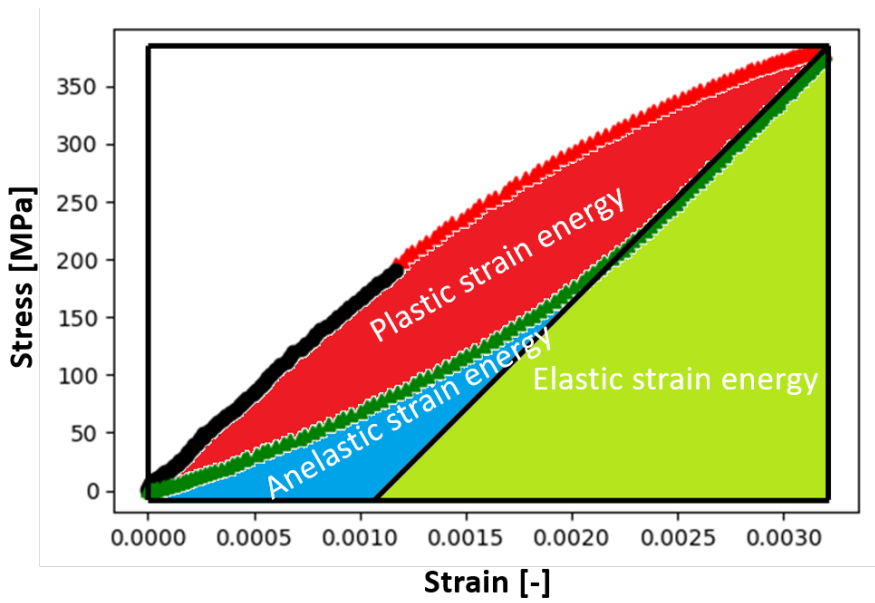

Figure 2.11 – Method for strain energy analysis in each hysteresis loop.

Different components of the strain energy, namely total strain energy density $\triangle W_t$, plastic strain energy density $\triangle W_p$, elastic strain energy density $\triangle W_e$ and anelastic strain energy density $\triangle W_{ane}$, as schematically illustrated in Fig. 2.11 were calculated. The $\triangle W_t$ was calculated by integrating the upper half curve (correspond to the upload) of the loop:

$$\triangle W_t = \int_{\epsilon_{min}}^{\epsilon_{max}} \sigma^{(upload)} d\epsilon \tag{2.1}$$

The plastic strain energy density was calculated:

$$\triangle W_p = \int_{\epsilon_{min}}^{\epsilon_{max}} \sigma^{(upload)} d\epsilon - \int_{\epsilon_{min}}^{\epsilon_{max}} \sigma^{(release)} d\epsilon \tag{2.2}$$

Elastic strain energy density was calculated:

$$\triangle W_e = \frac{1}{2} \triangle \epsilon_e \triangle \sigma = \frac{\triangle \sigma^2}{2E} \tag{2.3}$$

Then the anelastic strain energy density is equal to:

$$\triangle W_{ane} = \triangle W_t - \triangle W_p - \triangle W_e \tag{2.4}$$

Additionally, the hysteresis loop shape parameter [104], defined as the ratio of loop area over square area, was also calculated. Technical detail can refer to the Appendix B.2.2.

2.5 Materials characterization with microscopes

2.5.1 Post-test specimen cutting

Most specimens were broken open at the end of the test, except the specimens tested with small stress amplitude or under strain-control. To break the specimens open, they were fatigued with high frequency cyclic loading (with R > 0, 1 Hz and very limited plastic deformation) until failure.

The fracture surfaces were cut off for fractographic characterizations such as striation measurements in HRSEM. The gage length part was cut, as Fig. 2.12 illustrates, into four pieces along the loading axis. Two thin pieces (highlighted in blue) were used for TEM and ECCI characterization to investigate the microstructures after test in the bulk materials. One from the middle half (highlighted in blue) was used to observe the cracks (highlighted with red squares) on wall cross section (for crack density quantification with OM images, crack around investigation with EBSD and ECCI) and the cracks on the inner & outer surfaces with SEM & EBSD. All cutting were performed with blade saw, except several tiny pieces for TEM specimen were cut with WELL diamond wire saw.

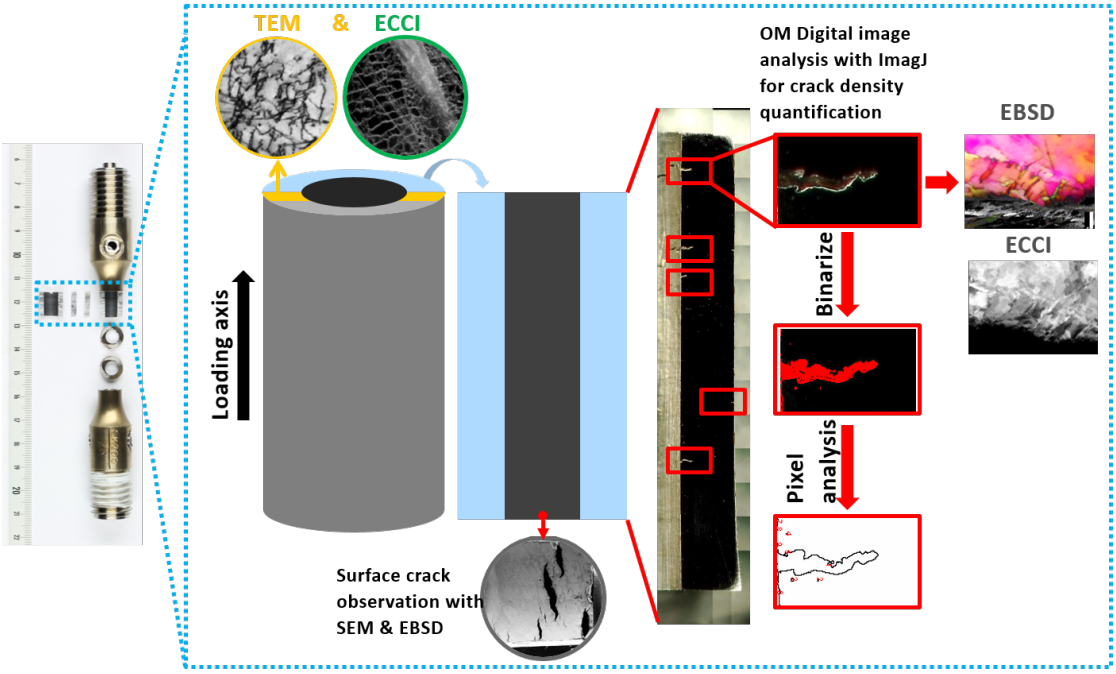

Figure 2.12 – Schematic drawing for post-test specimens cutting and respective usage.

2.5.2 Crack density measurement with optical microscopy and *ImageJ*

As Fig. 2.12 shows, the piece highlighted in blue was used for measuring the crack density. The wall cross section was ground and polished to 0.25 μm and then was photographed with KH-8700 3D digital microscope in mapping mode at a step of around 0.5 mm. The stitched images were analyzed with *ImageJ* to measure crack number density, crack depth and opening for the cracks with depth larger than 50 μm. Fig. 2.12 shows the standard procedure for *ImageJ* analysis.

2.5.3 Fractographic observations with scanning electron microscopy

Fractographic observations were performed to observe crack initiation sites, characterize corrosion oxides and measure striation spacing for crack growth rate.

The fracture surfaces were first cleaned in an ultrasonic bath with ethanol for at least 30 min, then they were photographed with OM. The fatigue cracking zone was identified as oxidized black area following exposure to high-temperature water or high-temperature air.

Before measuring the striation spacing in SEM (Zeiss ULTRA 55), the oxides on the surface were removed or partially removed with cathodic cleaning or pure chemical etching. Cathodic cleaning is an electrochemical process, in which the sample is the cathode and a Pt sheet (or an other inert electrode) is used as a counter electrode and anode. The oxide film on the specimen is removed by galvanostatic reduction. The forming and detaching hydrogen

bubbles during the reduction process help to mechanically clean the surface from debris and deposits. This method effectively removes oxides on ferrous materials without altering the fracture morphology, since the underlying metal matrix is cathodically protected. Chemical etching treats the surface with mild acids or alkaline solutions that dissolve the oxide films. This technique should be used only as a last resort, because it involves possible chemical attack of the fracture surface. In this study both methods were applied.

For cathodic cleaning, the fracture surface of interest was exposed to the electrolyte (the rest of the surface was covered with Teflon). The specimen worked as cathode and a platinum plate as anode in an ultrasonic bath with a commercial ENDOX 214 (sodium cyanide) electrolyte [144]. The cathode was polarized with a current density of 0.15-0.3 A/cm^2 for 10-30 min, depending on reduction efficiency and oxidation level. With this method, oxide particle (most big oxide particles like Fe_3O_4) were removed without altering the fracture morphology.

In chemical etching, the fracture surface was firstly treated in boiling ($\approx 100°C$) $KMnO_4$ (30 g/L) and $NaOH$ (100 g/L) water solution for 15 min, then was treated in boiling ammonium citrate dibasic $C_6H_{14}N_2O_7$ solution (100 g/L) for 15 min. After this treatment, most Fe_3O_4 particles and the spinel oxides were removed, but this may lead to a mild attack of the fracture surface.

The cleaned fracture surfaces were analyzed by HRSEM to determine the striation spacing from the initiation sites along the main crack growth direction with a step size of 0.1 mm as Fig. 2.13 illustrates. Normally, striations were visible starting from 50 μm crack depth. Multiple points were photographed at each step. The striation spacing (average value of several striations = width of striations/number of striations) was gained by manually measuring the width and number of several parallel striations with the help of Imagic^{TM} digital image software. In order to avoid measurement bias, at least five striation spacing data from different sites (within one measuring step) shifting along the horizontal direction in SEM images were acquired for each step. Then the averaged value of striation spacing at different sites was applied for this step.

2.5.4 Surface & crack characterization with SEM and EBSD

The piece cut from the middle half of Fig. 2.12 was used for surface crack observation. A small piece was cut off along the red dash line in Fig. 2.14 using a diamond wire saw. Then its inner and outer surfaces were automatically photographed with SEM in array. Thus all surface profiles (including cracks, scratches, inclusions and slip band markings) were surveyed.

The surfaces were then directly electrochemically polished, without any prior mechanical grinding, to maximally retain surface strain information. Electro-polishing was performed at $\approx$ 40 V in water-cooled perchloric-ethanol electrolyte (800 ml ethanol, 150 ml H_2O, 55 ml $HClO_4$) for 10-20 s. Polishing time, voltage and flow rate may vary with electrolyte quality and specimen surface condition. Well-polished surfaces were characterized with EBSD and the results were analyzed with TSL OIM Analysis 7 software.

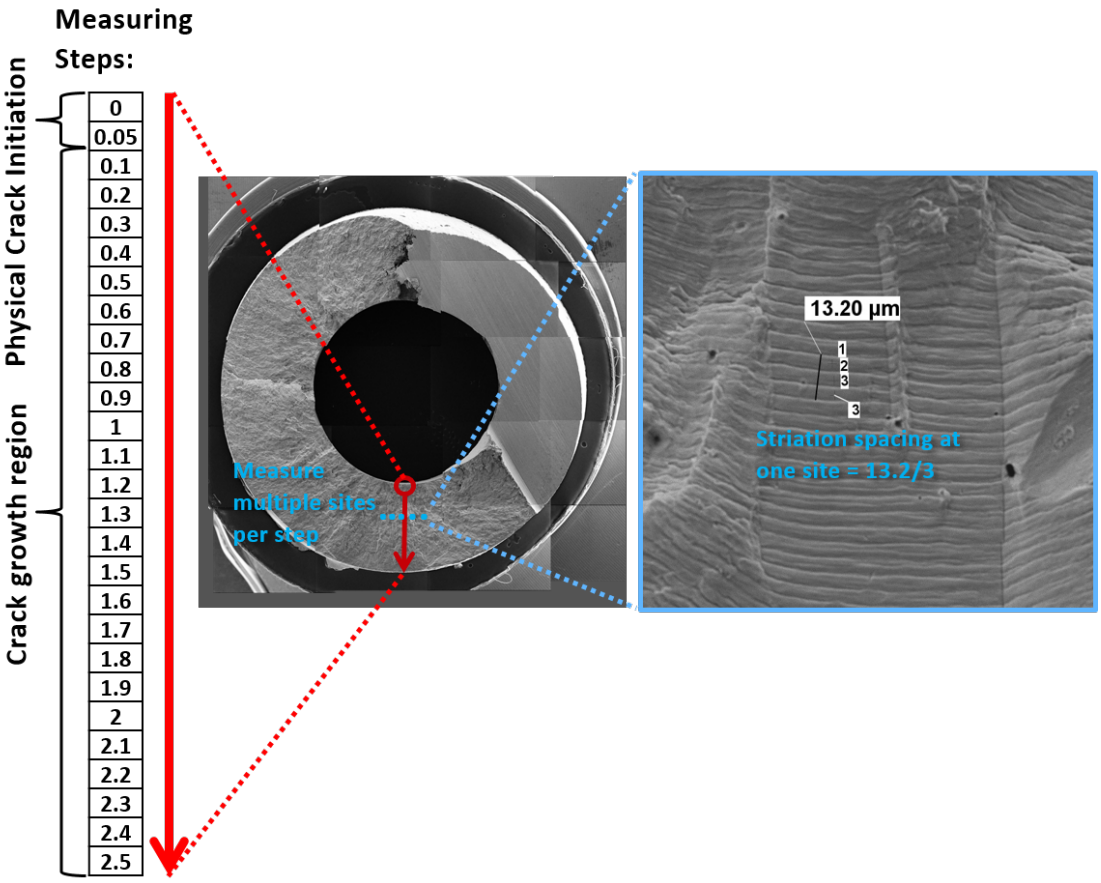

Figure 2.13 – Illustration of striation spacing measurement scenario.

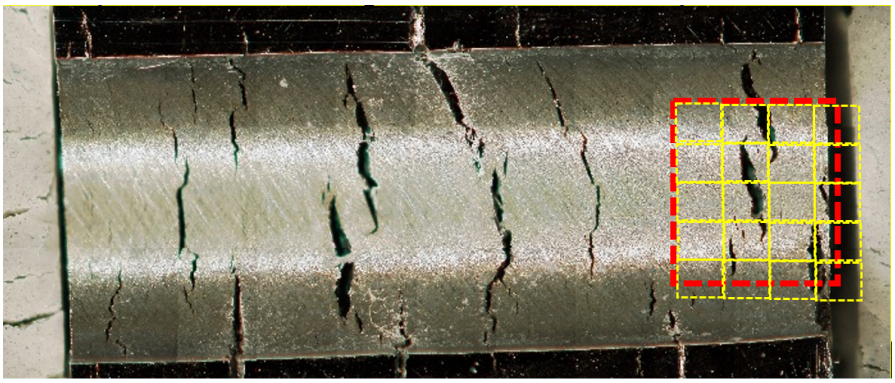

Figure 2.14 – One example of inner surface crack observation. Red dashed area was cut off by diamond saw and yellow dash lines indicate SEM survey array.

2.5.5 Microstructure characterizations with TEM & ECCI

The thin pieces in Fig. 2.12 were thinned to ≈100 μm via grinding with P300, P500, P1200, P2400 sandpaper in sequential order. Then the thin film was punched to 3 mm diameter discs, which were further reduced to thinner than 100 nm via standard JET electro-polishing method with Tenupol-5. The applied electrolyte, which consists of 90% methanol and 10% perchloric acid, was cooled to -20°C and sustained by JULABO Refrigerated Circulator. Typical polishing parameters are ≈ 34 V voltage, ≈ 16 m/s flow rate and automatic light stop. The voltage was adjusted to keep the current in the 100-120 mA range.

TEM JEOL JEM2010 (LaB_6, 200 kV) coupled with double-tilt analytical holder ($T_x or T_y = \pm 30°$) was applied for microstructures characterization. Gatan DigitalMicrograph™software acquired data and images. Loading axis of specimen lined with holder inserting direction. Microstructures (e.g. dislocations, grain boundaries, stacking faults) were observed under bright field in two beam condition. Some weak beam condition observation was performed for better resolution. Diffraction spots and Kikuchi patterns were recorded and analyzed for orientation information of microstructures and individual grains.

3 Results

3.1 Mechanical fatigue test results

As described in Section 2.3, most fatigue tests were performed in load-control mode, but several strain-controlled tests were also conducted. Three environments, room temperature pressurized hydrogenated water, 288°C air and 288°C BWR/HWC, were considered. Besides mean stress, environment and stress/strain amplitude, the specimen wall thickness and loading strain rate were investigated.

3.1.1 Fatigue tests in room temperature hydrogenated water

Before performing the fatigue tests in high temperature environments, several tests in hydrogenated water at room temperature ($\approx 22°C$) with different pressures were carried out, for comparison with the tests in HTW and to quantify the effect of internal water pressure.

The test results in the form of stress amplitude versus fatigue life are plotted in Fig. 3.1. Three stress amplitudes (280, 246 and 204 MPa) were used. At each stress level, three different water pressures (0, 100, 200 bar) were applied, except the one at σ_a = 204 MPa, where the test was interrupted at 10^6 cycles (runout). The data with σ_a = 280 MPa in Fig. 3.2 suggest a very slight increase in fatigue life with pressure, while those with σ_a = 246 MPa do not confirm the trend. In any case, we concluded that the influence of the internal pressure on fatigue life remains smaller than the uncertainty associated with the intrinsic scatter.

Since the tests were done in load-control, each specimen behaves slightly different from the others in terms of the average strain amplitude (average over the cycles) for a given stress amplitude. The relationship between the average strain amplitude and the fatigue life is depicted in Fig. 3.3. As expected, the tests with higher strain amplitude have shorter fatigue life and the tests conducted at higher pressure show a somewhat smaller strain amplitudes (at least the trend is so).

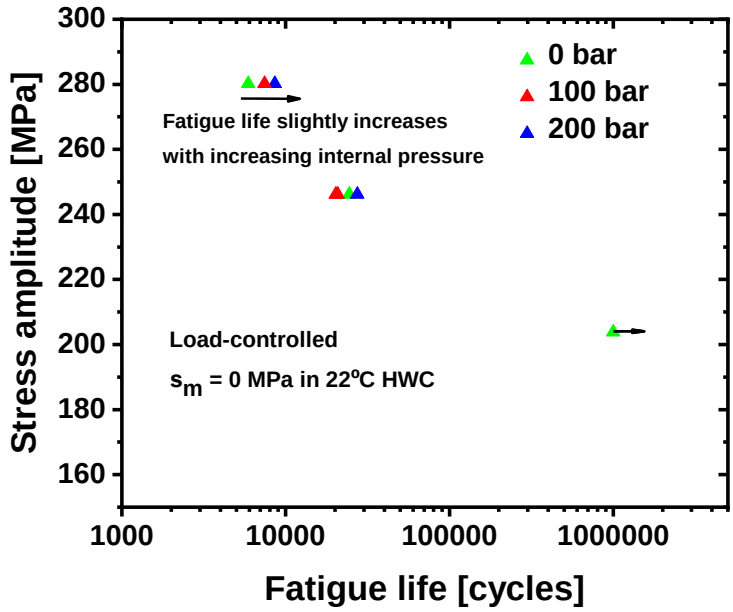

Figure 3.1 – Stress amplitude versus fatigue life of tests at room temperature HWC.

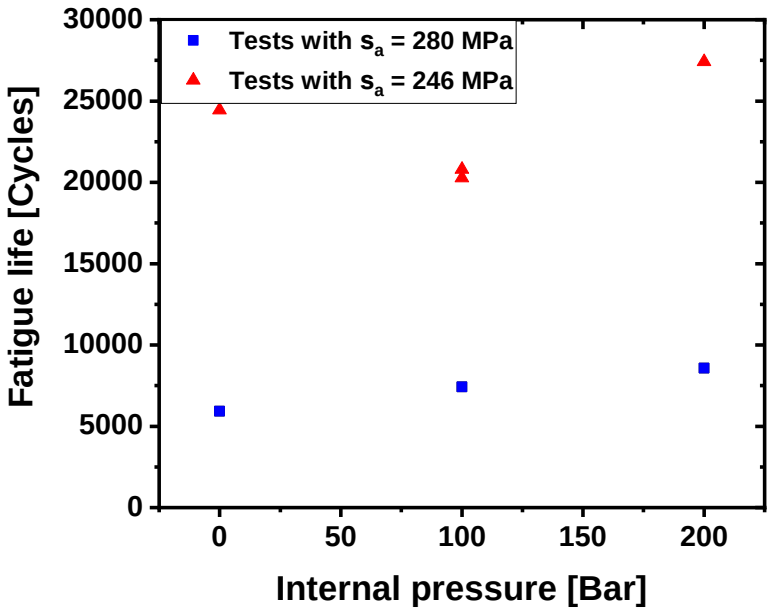

Figure 3.2 – Fatigue life dependence on internal water pressure of tests with σ_a = 280 MPa and 246 MPa.

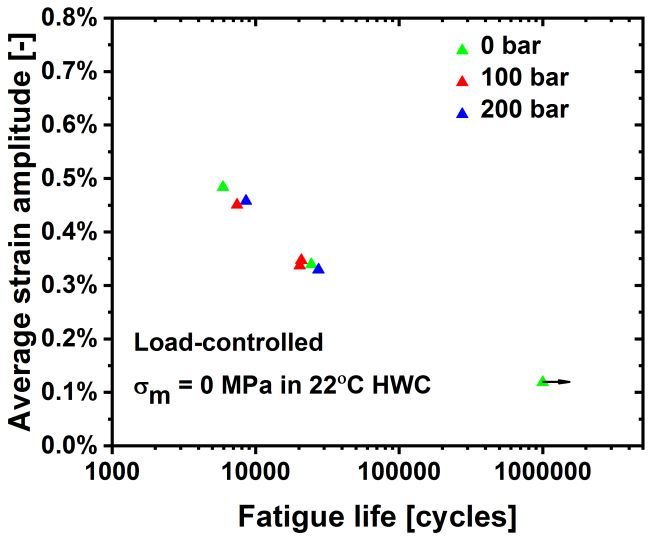

Figure 3.3 – Average strain amplitude versus fatigue life of tests at room temperature in HWC environment.

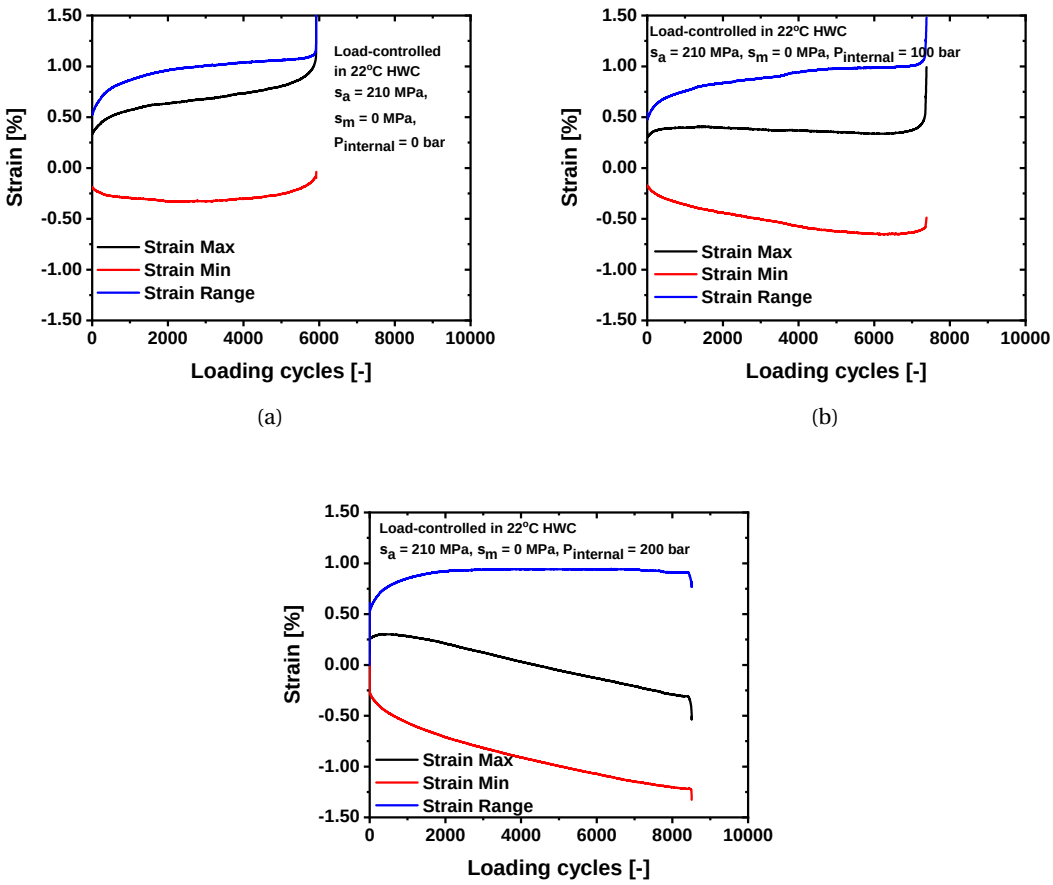

Figure 3.4 – Strain evolution versus cycle with σ_a = 280 MPa, σ_m = 0 MPa in HWC at room temperature with (a) 0 bar, (b) 100 bar, (c) 200 bar.

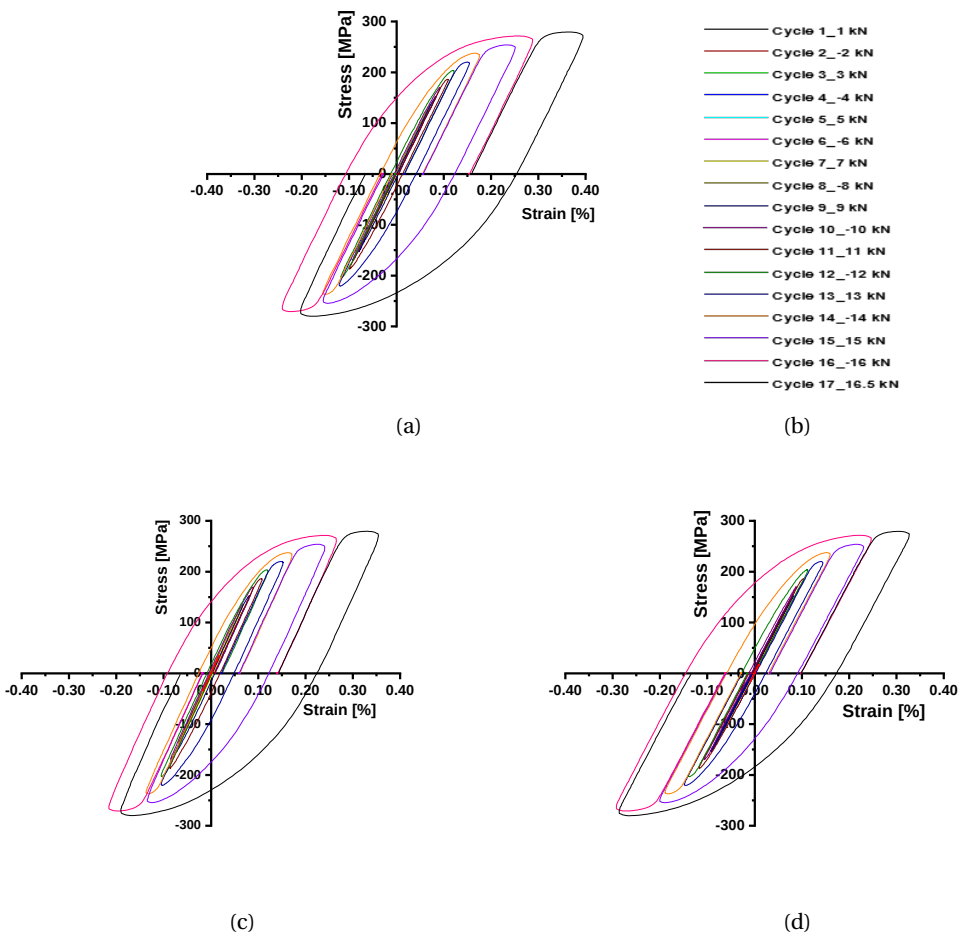

Figure 3.5 – Hysteresis stress-strain loops of the starting cycles in load-controlled tests with σ_a = 280 MPa, σ_m = 0 MPa in HWC at 22°C with (a) 0 bar, (b) 100 bar, (c) 200 bar.

The strain evolution during the fatigue life of the tests with σ_a = 280 MPa is shown in Fig. 3.4, where the maximum, minimum and mean strain are plotted for the tests at different pressures. While the average strain amplitude of the three tests is practically the same, the maximum and minimum strains evolution, and consequently the mean strain, are different. In fact, increasing the internal pressure tends to promote a weak negative ratcheting. Thus, the internal pressure plays a more pronounced effect on mean strain than on strain amplitude. However, if the small difference in fatigue life due to the internal pressure arises from a variation of strain amplitude or from the variation of mean strain remains unclear.

The first stress-strain hysteresis loops of three tests with different internal pressures, started according to the loading procedure described in Section 2.3.2, are plotted in Fig. 3.5. In the first 12 cycles (at 204 MPa), the material deforms linearly. Then, plastic strain occurs at higher stress. At the end of the starting procedure, the stress-strain point (at σ = 0 MPa) is still close to origin. This effectively prevents large positive mean strain from building up as it would be the

case by direct starting procedure. Note that the hysteresis loops with higher pressure develops a larger compressive component. This is consistent with the observation of strain evolution in Fig. 3.4.

3.1.2 Fatigue tests in air at 288°C

Fatigue test results in 288°C air, in the form of stress versus fatigue life, are presented in Fig. 3.6. Only the results of the specimens with a wall thickness (WT) WT = 2.0 mm are shown. For the load-controlled tests in air, the fatigue life was determined when the measured elongation was larger than 1.0 mm or when the specimen had totally failed into two parts.

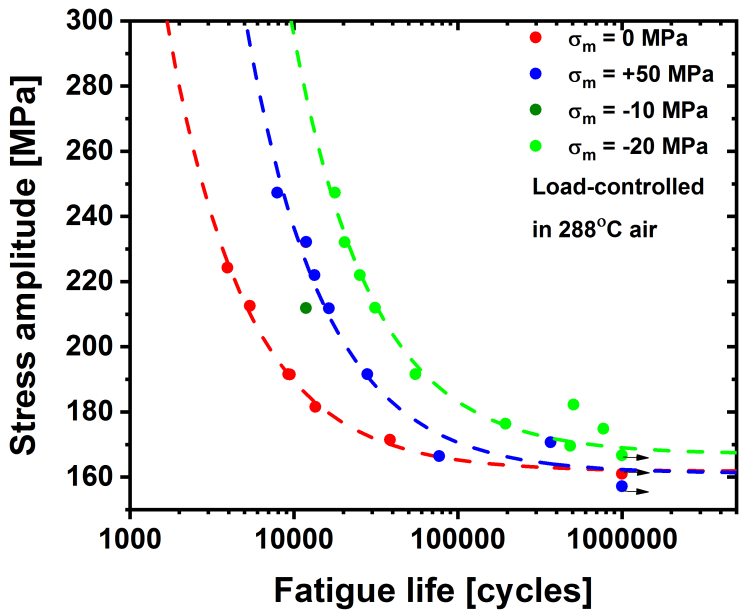

Figure 3.6 – Stress amplitude versus fatigue life with and without mean stress in air at 288°C.

In Fig. 3.6, the most salient results show that both negative (-10, -20 MPa) and positive (+50 MPa) mean stresses increase fatigue life, when $N_f \leq 10^5$ cycles, with respect to the tests with zero mean stress. However, for the tests with $N_f > 10^5$ cycles, +50 MPa mean stress insignificantly modifies fatigue life and -20 MPa mean stress slightly increases the fatigue life and the limit at 10^6 cycles. Actually, we defined the region with $N_f \leq 10^5$ as the LCF region and the regime with $N_f > 10^5$ as the HCF region.

The curves in Fig. 3.6 represent the fits through the points with the same mean stress according to Langer equation:

$$\sigma_a = B(N_f)^{-b} + \sigma_{fs} \tag{3.1}$$

where σ_{fs} stands for fatigue strength/limit, B and b are fitting constants. For mathematical convenience in comparing fatigue life between different mean stresses, the exponent constant b is fixed to be 0.9 in fitting.

Thus the following three equations were obtained:

$$\sigma_m = 0\ MPa: \quad \sigma_a = 110457(N_f)^{-0.9} + 162 \tag{3.2}$$

$$\sigma_m = +50\ MPa: \quad \sigma_a = 300065(N_f)^{-0.9} + 161 \tag{3.3}$$

$$\sigma_m = -20\ MPa: \quad \sigma_a = 510905(N_f)^{-0.9} + 167 \tag{3.4}$$

Similarly to the definition of F_{en} (Equ. 1.26), we defined a F_{σ_m} factor to quantify the effect of mean stress on fatigue life. Combining the Langer equations for zero and non-zero mean stress, we derived:

$$F_{\sigma_m} = \frac{N_{f,\sigma_m \neq 0}}{N_{f,\sigma_m = 0}} = \left(\frac{B_{\sigma_m \neq 0}}{\sigma_{a,\sigma_m \neq 0} - \sigma_{fs,\sigma_m \neq 0}}\right)^{1/b_{\sigma_m \neq 0}} \times \left(\frac{\sigma_{a,\sigma_m = 0} - \sigma_{fs,\sigma_m = 0}}{B_{\sigma_m = 0}}\right)^{1/b_{\sigma_m = 0}} \tag{3.5}$$

As the exponential constant b is fixed, thus:

$$F_{\sigma_m} = \frac{N_{f,\sigma_m \neq 0}}{N_{f,\sigma_m = 0}} = \left(\frac{B_{\sigma_m \neq 0}}{B_{\sigma_m = 0}}\right)^{1/b} \times \left(\frac{\sigma_{a,\sigma_m = 0} - \sigma_{fs,\sigma_m = 0}}{\sigma_{a,\sigma_m \neq 0} - \sigma_{fs,\sigma_m \neq 0}}\right)^{1/b} \tag{3.6}$$

Using the numerical values of Equ.3.2, Equ. 3.3 and Equ. 3.4, and considering that $\sigma_{fs,\sigma_m=0} \approx \sigma_{fs,\sigma_m=+50} \approx 161$ MPa, and that $\sigma_{fs,\sigma_m=-20} = 167$ MPa, one gets $F_{\sigma_m=+50} \approx 3.0$ and $F_{\sigma_m=-20} \approx 6.2$ when $\sigma_a \geq 180$ MPa (namely in LCF regime). This shows a dependence on σ_a of the F_{σ_m} factor.

For comparison purposes, it is interesting to plot all our fatigue life data (with and without mean stress) in terms of the average strain amplitude, see Fig. 3.7. The average strain-life data were also fitted with a Langer equation and then compared with the NUREG/CR-6909 mean curves.

$$Best\ fit\ of\ tests\ in\ 288^\circ C\ air: \quad \overline{\epsilon_a} = 1.239(N_f)^{-0.65} + 0.001 \tag{3.7}$$

$$NUREG/CR-6909\ mean\ curve\ in\ air: \quad ln(N_f) = 6.891 - 1.920 ln(\epsilon_a - 0.112) \tag{3.8}$$

where ϵ_a is expressed in %. In Fig. 3.7, the mean curves of NUREG/CR-6909 Rev. 1 is plotted for comparison with the best fit through our data. Our results are well consistent with NUREG/CR-

6909 predictions.

In Fig. 3.7, positive mean stress data indicate a weak decrease in fatigue life with respect to zero mean stress data, while the opposite is observed for negative mean stress data. Generally speaking, when the fatigue life is represented in terms of the average strain amplitude, any difference induced by mean stress tends to vanish. Thus it is reasonable to fit all the data with different mean stress with a single function. The exponent parameter is fixed for convenience in comparing with the results obtained in HTW.

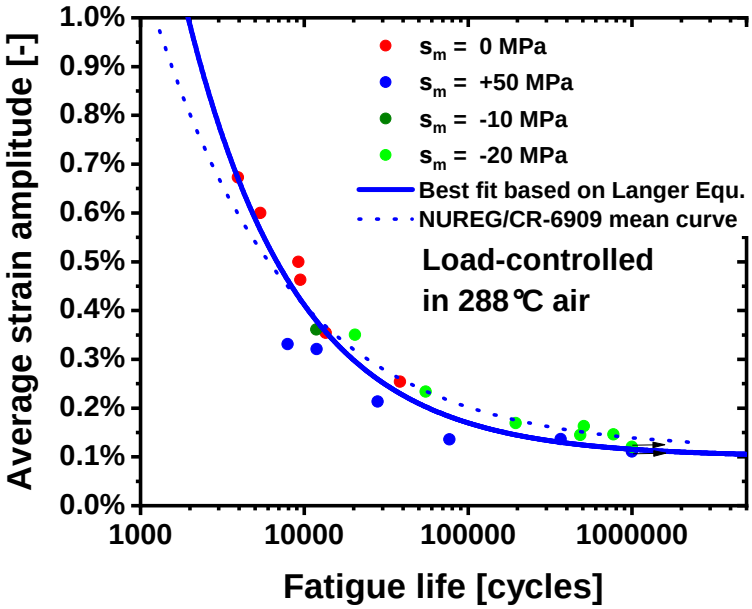

Figure 3.7 – Average strain amplitude versus fatigue life of tests conducted under load control with and without mean stress in air at 288°C.

The strain evolution as a function of the cycle number was recorded and analyzed. Fig. 3.8 presents the strain evolution of the tests with σ_a = 190 MPa and σ_a = 210 MPa under different mean stresses. Evidently, the tests with different mean stresses but with the same stress amplitude start with different strain amplitudes due to the accumulated hardening at the end of the starting procedure (where +50 MPa mean stress hardens more than -20 MPa mean stress does). For all tests, the first hardening stops around 20 cycles. Then the softening stage takes over around 1000 cycles. Then a plateau stage comes, except the tests with negative mean stress, in which the plateau stage is not obvious and secondary hardening comes instead.

3.1.3 Fatigue tests in BWR/HWC at 288°C

The stress-life (S-N) results of the tests carried out at 288°C and 100 bar in BWR/HWC are plotted in Fig. 3.9, where only the results of specimens with a wall thickness of 2.5 mm are

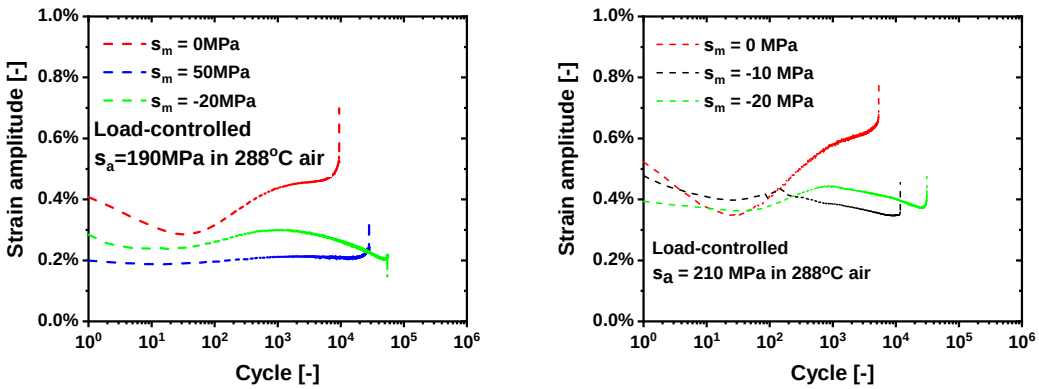

(a) (b)

Figure 3.8 – Strain evolution versus cycle of load-controlled tests with (a) σ_a = 190 MPa, (b) σ_a = 210 MPa in air at 288°C.

presented. The fatigue life was determined when a water leakage occurred, in other words when the crack had grown through the specimen wall. The data points at 10^6 cycles with the arrows indicate run-out tests.

Like for the tests in air, least squares fittings with Langer equation (Equ. 3.1), were done:

$$\sigma_m = 0\ MPa: \quad \sigma_a = 69447(N_f)^{-0.9} + 171 \tag{3.9}$$

$$\sigma_m = +50\ MPa: \quad \sigma_a = 5747(N_f)^{-0.5} + 151 \tag{3.10}$$

$$\sigma_m = -20\ MPa: \quad \sigma_a = 166336(N_f)^{-0.9} + 195 \tag{3.11}$$

Note that for the +50 MPa mean stress data, the exponent coefficient had to be changed to get a good fit quality. Keeping it equal to -0.9 yields indeed a poor fit through the data.

Consistently with the observation of LCF tests in high temperature air, both positive (+50 MPa) and negative (-20 MPa) mean stresses increase fatigue life. In the HCF regime ($N_f > 10^5$), -20 MPa mean stress increases fatigue life and fatigue limit (from 171 to 195 MPa), while +50 MPa mean stress decreases fatigue life and limit (from 171 to 151 MPa). Clearly in HTW environment, mean stress effects on fatigue life are different from those in HTA environment. The synergistic effects of environments and mean stress will be addressed in detail in Chapter 4 of discussion. The fitted curves of σ_m = 0 MPa and σ_m = +50 MPa intersect each other at around 10^5 cycles. This results from a competition between cyclic hardening and environmental degradation effects.

The fatigue life increase in the LCF regime was calculated with the aid of Equ. 3.5. Since the exponent coefficient b and the fatigue limit are not the same in the equations with and without mean stresses, F_{σ_m} is not constant; actually we found: $F_{\sigma_{m=+50}}$ is between 0 and 2.7 and $F_{\sigma_{m=-20}}$ is between 4.0 to 16.0.

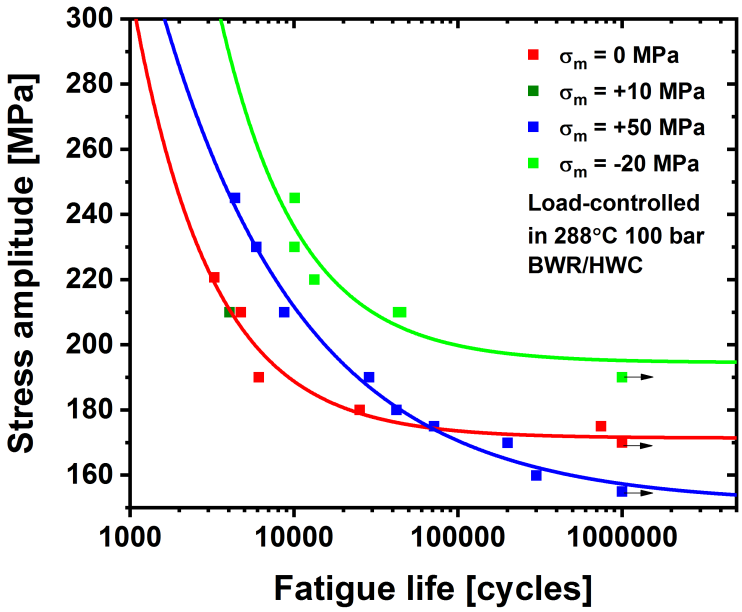

Figure 3.9 – Stress amplitude versus fatigue life of tests with and without mean stress in BWR/HWC environment with 100 bar at 288°C.

The strain-life results are plotted in Fig. 3.10. The best fit equation for test results is:

$$Best\ fit\ for\ tests\ in\ 288^\circ C\ HWC/BWC: \quad \overline{\epsilon_a} = 0.89(N_f)^{-0.65} + 0.001 \tag{3.12}$$

In Equation 3.12, the exponential parameter is fixed. The fatigue ductility is around 0.1%, like in HTA. In this representation, mean stress makes insignificant difference on fatigue life. The NUREG/CR-6909 strain-life curve equation that takes into account of the LWR environments:

$$NUREG/CR-6909\ mean\ curve\ in\ water: ln(N_f) = 6.891 - 1.920 ln(\epsilon_a - 0.112) + T^* \dot{\epsilon}^* O^* \tag{3.13}$$

where ϵ_a is in %. T^*, $\dot{\epsilon}^*$, O^* are transformed parameters of temperature, strain rate and DO level respectively and are defined as:

$$T^* = (T - 100)/250 \qquad when\ 100^\circ C \leq testing\ temperature\ of\ 288^\circ C \leq 325^\circ C \tag{3.14}$$

$$\dot{\epsilon}^* = ln(\dot{\epsilon}/7) \qquad when\ 0.0004\%/s \leq \dot{\epsilon} = \frac{4\epsilon_a}{period} \leq 7\%/s \tag{3.15}$$

$$O^* = 0.29 \qquad when\ DO \leq 0.1ppm \tag{3.16}$$

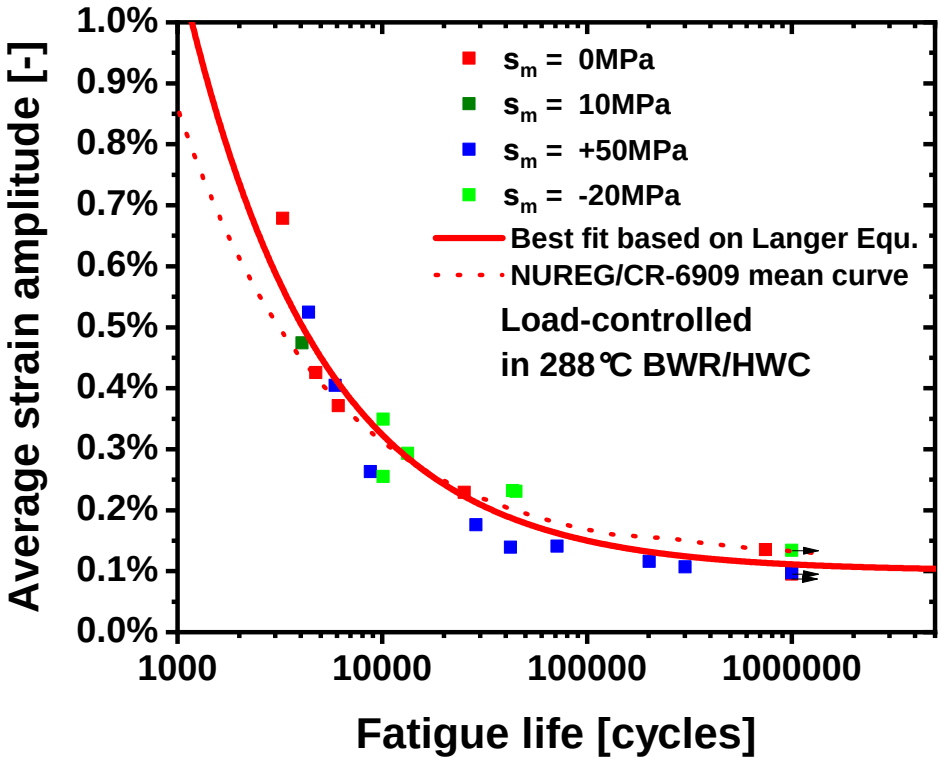

Figure 3.10 – Average strain amplitude versus fatigue life with and without mean stress in BWR/HWC environment with 100 bar at 288°C.

In Fig. 3.10, our test results well agree with NUREG/CR-6909 predictions, except the section with very high strain amplitude. Here different experimental strategies, in material, mean stress, control mode, waveform (saw tooth waveform in NUREG/CR-6909), loading history, specimen surface finish and geometry, should be considered.

Two sets of strain amplitude versus cycle are plotted in Fig. 3.11. These curves present the same characteristics as the strain evolution in Fig. 3.8 of the tests in HTA: all undergo first hardening in the first 20 cycles, then comes a softening stage, which is followed by a plateau stage, except

for the tests with negative mean stress. In Fig. 3.8a, we observed that the secondary hardening occurs after 1000 cycles for the tests with σ_m = +50 MPa and σ_a = 190 MPa. Under these conditions, the specimen ran longer than 1000 cycles with small plastic strain (but normally the N_f is between 10^4 and 10^5 cycles) and thus accumulated a significant amount of damage required for triggering secondary hardening.

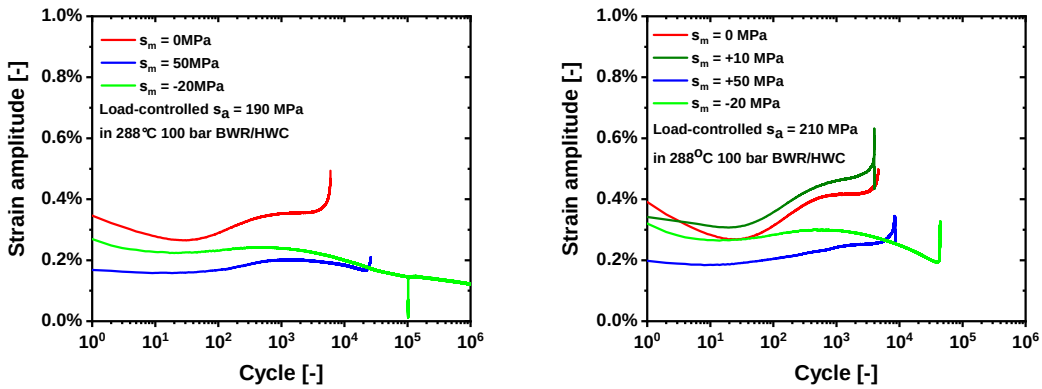

(a) (b)

Figure 3.11 – Strain evolution versus cycles with (a) σ_a = 190 MPa, (b) σ_a = 210 MPa in BWR/HWC environment with 100 bar at 288°C.

3.1.4 Fatigue tests under strain-control

Four strain-controlled tests, with ϵ_a = 0.15%, 0.2%, 0.4%, 0.6%, were conducted in each environment. The results in the form of stress-life and strain-life were plotted in Fig. 3.12 and Fig. 3.13 for the tests in HTA and in Fig. 3.14 and Fig. 3.15 for the tests in HTW. For the strain-controlled tests, the stress amplitude parameter represents the average value; analogously, the strain amplitude is the average value of strain amplitude for load-controlled tests. For strain-controlled tests in water, the fatigue life was determined when water leaks; For strain-controlled tests in air, the fatigue life was determined at the moment stress amplitude drops 25% respect to the plateau level if the specimen did not totally fail before that.

In both stress-life and strain-life forms, the green stars (data from the strain-controlled experiments) drop around the fitting curves of load-controlled test results. So the load-controlled test results correlate well with the results of strain-controlled tests. Nonetheless, it has to be recognized from Fig. 3.13 that strain-controlled tests tend to have longer fatigue lives than that of the load-controlled tests for a given strain amplitude. In addition, in all four figures (Fig. 3.12 to Fig. 3.15), materials have higher fatigue life/limit in HCF regime under strain-controlled condition than under load-controlled condition.

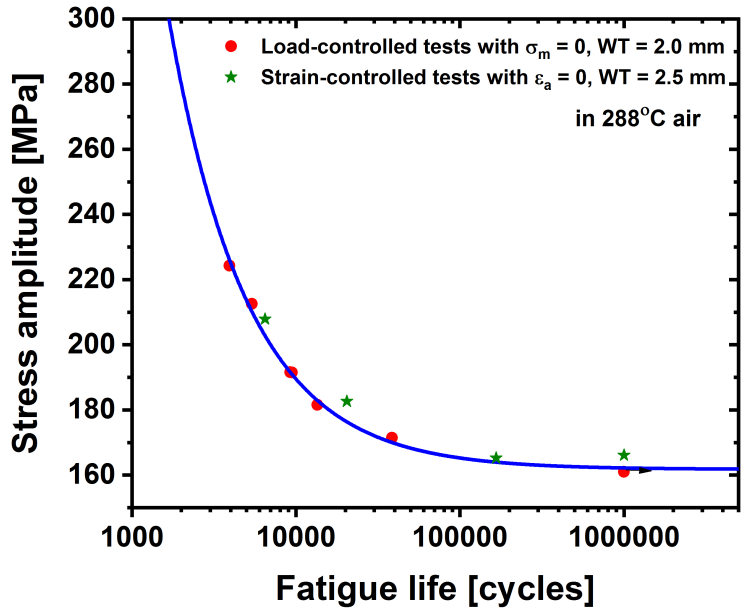

Figure 3.12 – Stress-life (S-N) of tests conducted under strain and load control in air at 288°C. The curve is fitted only with the load-controlled data.

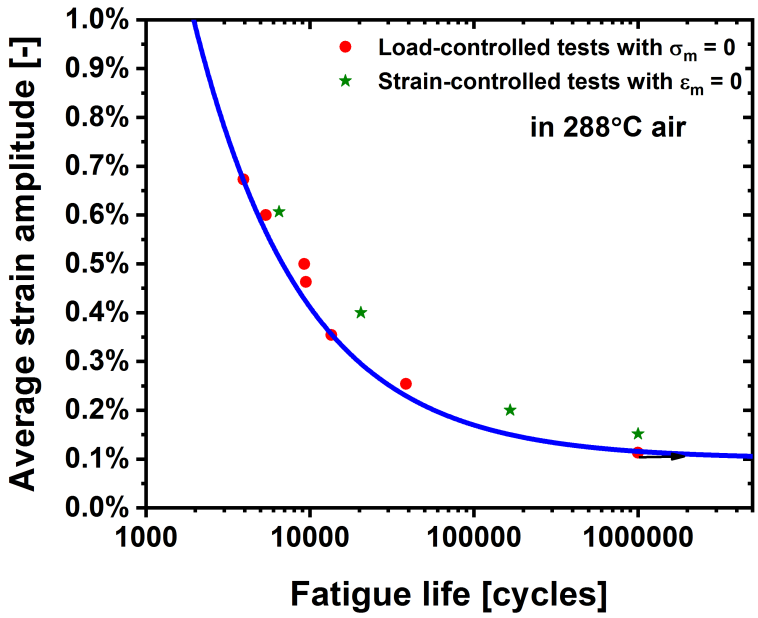

Figure 3.13 – Strain-life of tests conducted under strain and load control in air 288°C. The curve is fitted only with the load-controlled data.

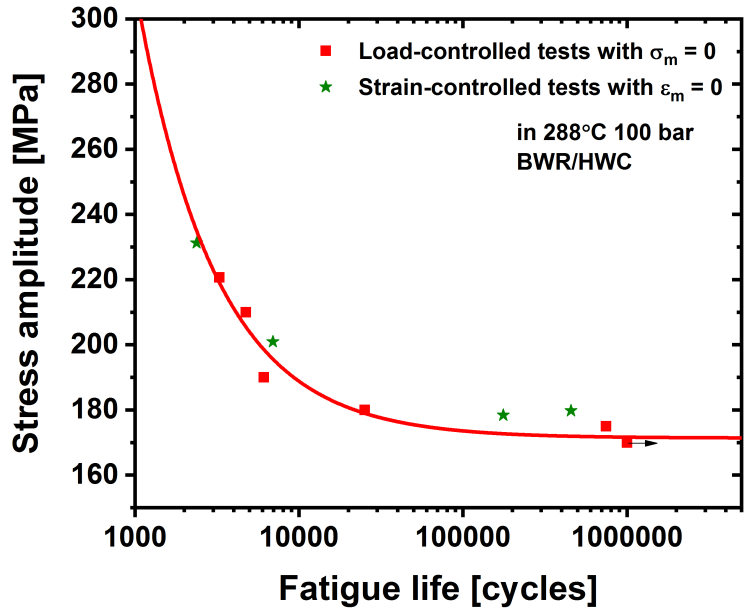

Figure 3.14 – Stress-life of tests conducted under strain and load control in BWR/HWC environment with 100 bar at 288°C. The curve is fitted only with the load-controlled data.

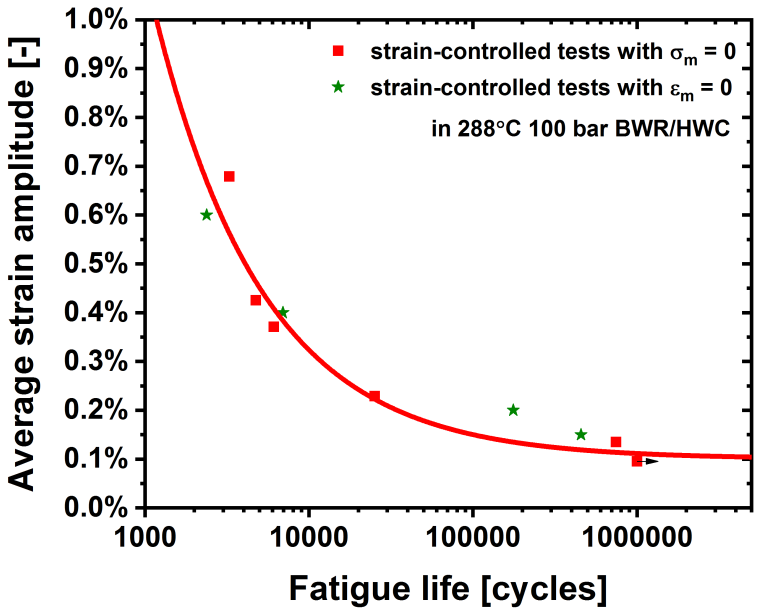

Figure 3.15 – Strain-life of tests conducted under strain and load control in BWR/HWC with 100 bar environment at 288°C. The curve is fitted only with the load-controlled data.

The stress amplitude evolution against the loading cycle number for tests in HTA and HTW is plotted in Fig. 3.16 and Fig. 3.17 respectively. Tests in both environments show a similar stress evolution profile when considering same strain amplitude condition, except the one for ϵ_a = 0.15% in HTW, whose stress amplitude appears too high. This may reflect either some intrinsic scatter or possible technical issues like misalignement for instance. Similarly to the cyclic deformation response in load control, the strain-controlled tests also undergo first hardening, softening, stable plateau or secondary hardening at low strain amplitude. For all strain-controlled tests, the first hardening lasts for fewer than 100 cycles, which lasts longer than in the situation in load control. For tests of ϵ_a = 0.6%, the stable plateau is absent, indicating that softening mechanisms (like formation of channel and wall structures) may outweigh hardening factors (like dislocation density increase, dislocation cells). Secondary hardening was observed in the tests with ϵ_a = 0.15% and ϵ_a = 0.2% after 1000 cycles loading. The softening stage is relatively small. Secondary hardening initiates much earlier than in the situation of load-control. This is possibly attributed to a faster accumulation of point and planar dislocation defects in strain-control condition.

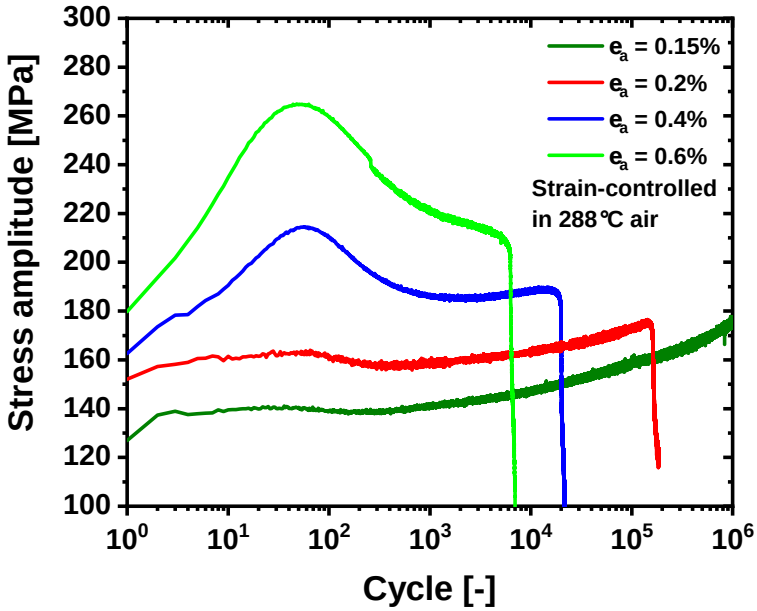

Figure 3.16 – Stress evolution versus cycle of tests conducted under strain control in air at 288°C.

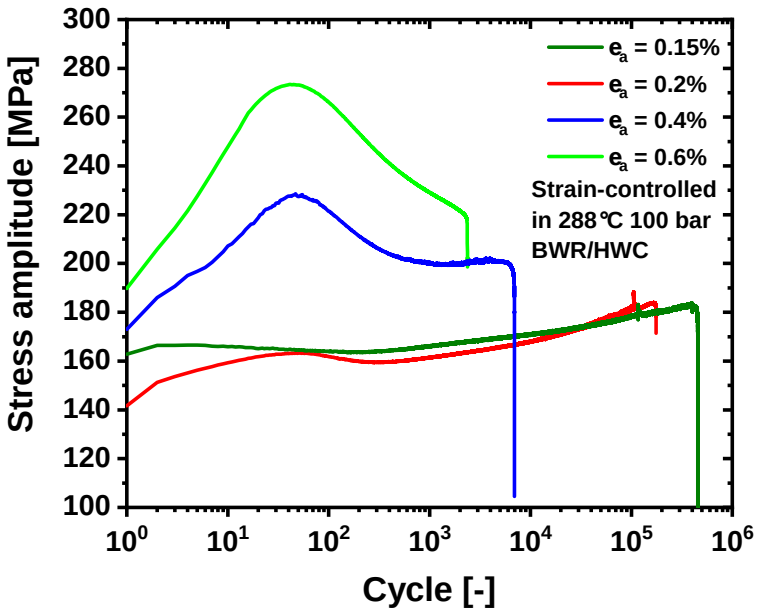

Figure 3.17 – Stress evolution versus cycle of tests conducted under strain control in BWR/HWC environment with 100 bar at 288°C.

3.1.5 Fatigue tests with different specimen geometries and internal pressures

As mentioned above, different specimen geometries were used for the tests in HTA and HTW. Actually, only variations of the specimen wall thickness (WT) were considered. Two WTs (2.0, 2.5 mm) and three WTs (1.5, 2.0, 2.5 mm) were chosen for the tests in HTA and HTW respectively (see Table 2.3). In addition, for the tests in HTW, the specimens were pressurized with either 100 or 200 bar. The idea was to modify the level of the hoop stress with modifications of WT and pressure to change the stress state in the specimens to reveal relevant effects on the fatigue life. In Fig. 3.18, the stress-life results obtained in HTA with the two specimen geometries are plotted together. The curves represent the best fits of results of specimens having a WT of 2.0 mm while the dots correspond to the specimens with WT = 2.5 mm. As can be seen, there is no notable difference in the results between the specimens with WT = 2.0 mm and WT = 2.5 mm in HTA, independently of the control mode and mean stress.

More influence of the specimen geometry was evidenced with the tests in HTW, as can be seen in Fig. 3.19 where a more pronounced effect of WT on fatigue life is observed. The underlying reason resides in the fact that the specimens are pressurized, which leads to a triaxial stress state in the specimen wall and to a WT dependent hoop stress. For the tests without mean stress, the specimens with the thinnest WTs (2.0 and 1.5 mm) tend to have a longer fatigue life. Indeed, among the four combinations of WT and pressure, the two with the thinnest WT and the highest pressure (200 bar) deviate notably from the best fit curve obtained with WT = 2.5 mm and 100 bar. This is likely to be due to the high level of the hoop stress reached

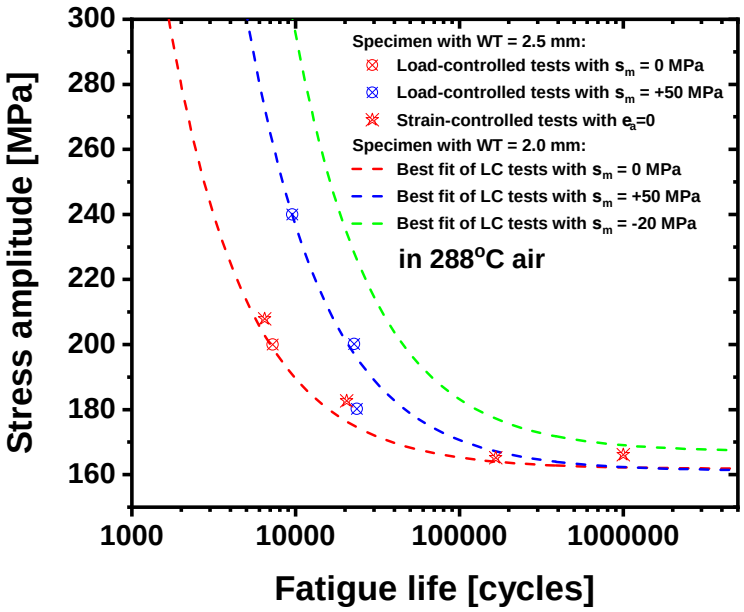

Figure 3.18 – Stress-life curves of specimens with different wall thicknesses in air at 288°C.

in these last cases. This point will be further discussed in the next chapter. Note however, this observation is not confirmed for the specimen with +50 MPa mean stress, suggesting an additional effect of mean stress.

The evolution of the strain amplitude for all the specimens tested in HTW is reported in Fig. 3.21, Fig. 3.22 and Fig. 3.23. From the strain amplitude at the first cycle, one observes first that the specimens with different WT underwent different levels of hardening during the starting procedure. Secondly, there is a significant difference in the strain amplitude between the various conditions (WT and pressure), which have a significant impact on the triaxial stress state. Nonetheless, these results indicate that for the specimens WT of 2.5 mm the pressure plays a minor role on fatigue life.

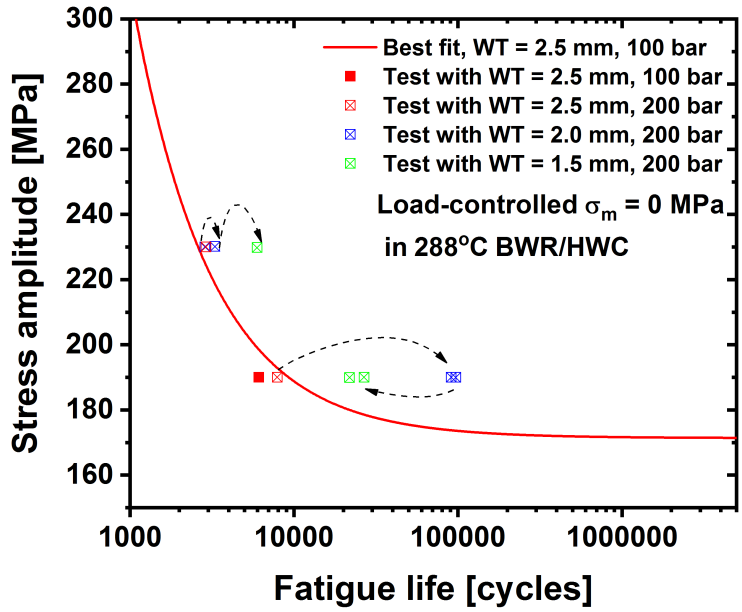

Figure 3.19 – Stress-life of specimens with different wall thicknesses in BWR/HWC at 288°C, (σ_m = 0 MPa).

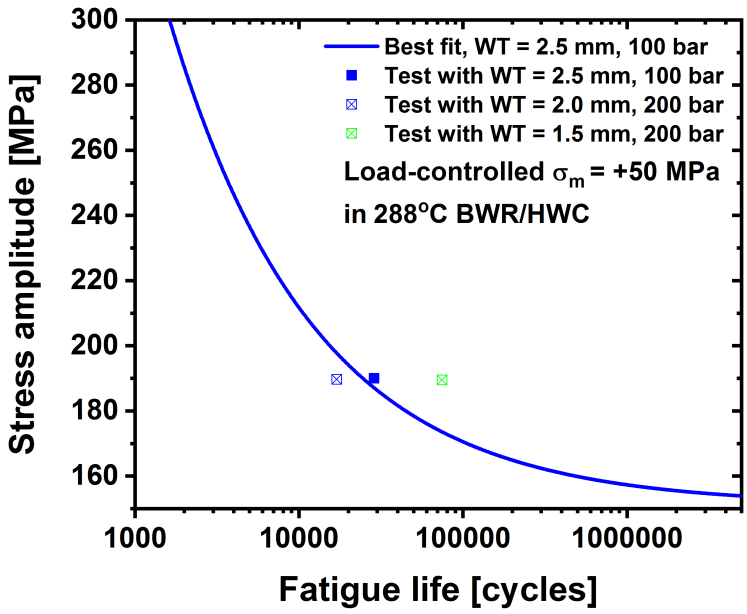

Figure 3.20 – Stress-life of specimens with different wall thicknesses in BWR/HWC at 288°C, (σ_m = +50 MPa).

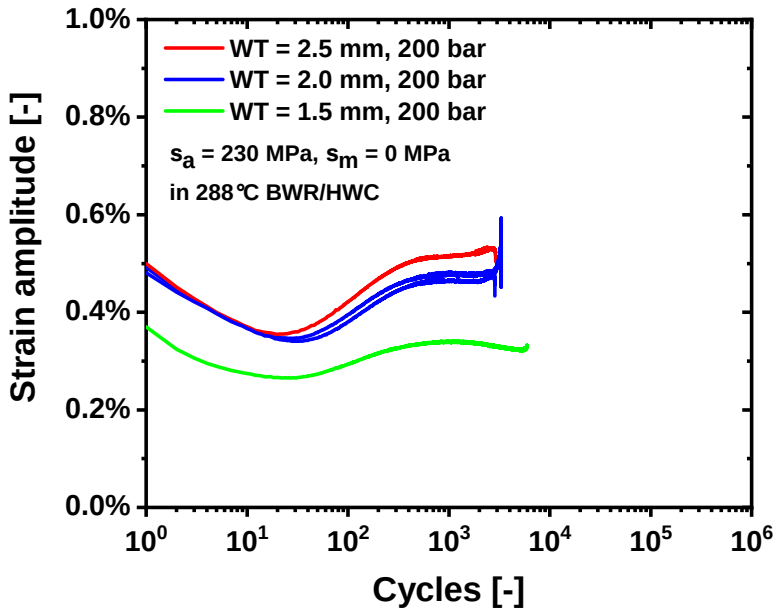

Figure 3.21 – Strain amplitude versus cycle of specimens with different wall thicknesses σ_a = 230 MPa in BWR/HWC environment with 200 bar at 288°C.

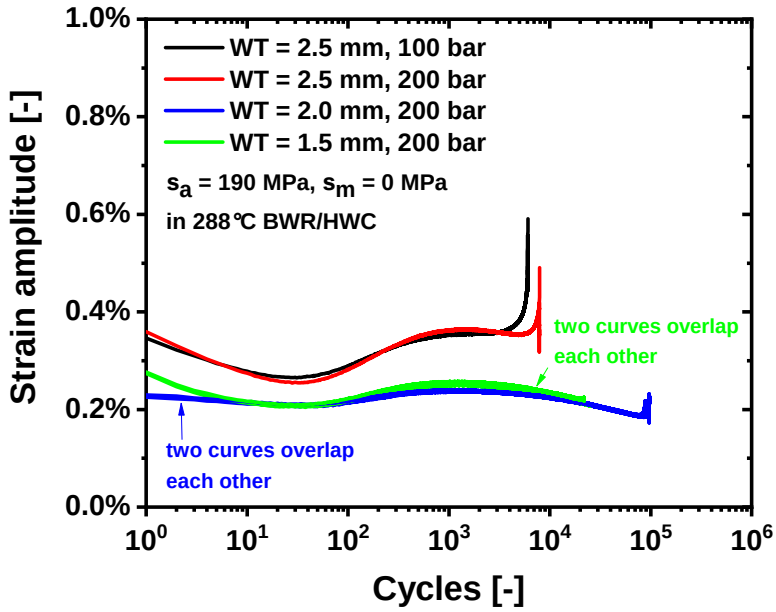

(a)

Figure 3.22 – Strain amplitude versus cycle of specimens with different wall thicknesses σ_a = 190 MPa in BWR/HWC environment at 288°C.

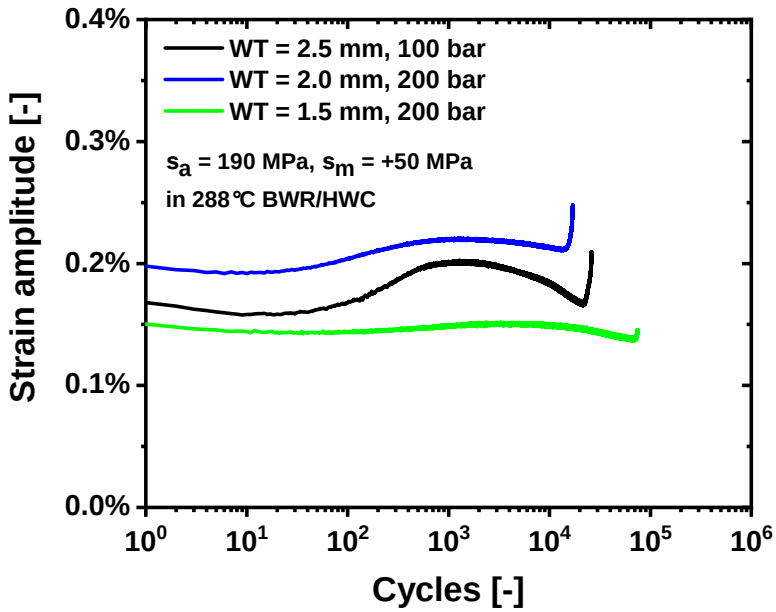

Figure 3.23 – Strain amplitude versus cycle of specimens with different wall thicknesses under σ_a = 190 MPa, σ_m = +50 MPa in BWR/HWC environment at 288°C.

3.1.6 Fatigue tests with different strain rates

Strain rate effect was investigated with four tests performed with a strain rate of ≈ 0.01%/s, i.e. one order of magnitude smaller than all the other tests that were done at ≈ 0.1%/s. As described in Table 2.3, asymmetrical saw-tooth waveform, 60 s in loading and 6 s in unloading, was applied for the lower strain rate tests to ensure a constant rate; however, sinusoidal waveform was applied for higher stain rate tests. The average strain rate (2*strain range/period) was used for tests with sinusoidal waveform.

The stress-life results of the low strain rate (0.01%/s) are plotted in Fig. 3.24. Lower strain rate decreases fatigue life under both positive (+50 MPa) and zero mean stress conditions. The life reduction factors $F_{\dot{\epsilon}}$ are between 1.33 and 2.07 with an average value of 1.61. Considering the F_{en} theory:

$$\frac{F_{en}^{0.01\%/s}}{F_{en}^{0.1\%/s}} = \frac{N_f^{air}/N_f^{water,0.01\%/s}}{N_f^{air}/N_f^{water,0.1\%/s}} = \frac{N_f^{water,0.1\%/s}}{N_f^{water,0.01\%/s}} = F_{\dot{\epsilon}} \tag{3.17}$$

Based on the F_{en} defined in NUREG/CR-6909 Rev.1 [3]:

$$\begin{aligned}\frac{F_{en}^{0.01\%/s}}{F_{en}^{0.1\%/s}} &= exp(T^*_{0.01\%/s}\dot{\epsilon}^*_{0.01\%/s}O^*_{0.01\%/s} - T^*_{0.1\%/s}\dot{\epsilon}^*_{0.1\%/s}O^*_{0.1\%/s}) \\ &= exp(T^*O^*(\dot{\epsilon}^*_{0.01\%/s} - \dot{\epsilon}^*_{0.1\%/s}))\end{aligned} \tag{3.18}$$

with the transformed parameters T^*, $\dot{\epsilon}^*$, O^* in Equation 3.14, Equation 3.15 and Equation 3.16, we get:

$$\frac{F_{en}^{0.01\%/s}}{F_{en}^{0.1\%/s}} = exp\left(\frac{288-100}{250} \times 0.29 \times \left(ln\frac{0.1}{7} - ln\frac{0.01}{7}\right)\right) = 1.65 \tag{3.19}$$

Our test results are well consistent with the prediction based on NUREG method, even if it was derived from saw tooth waveform of strain-controlled tests. Additionally, based on our observation described in Section 3.1.4, control-mode, either strain control or load control, does not make significant difference on fatigue life.

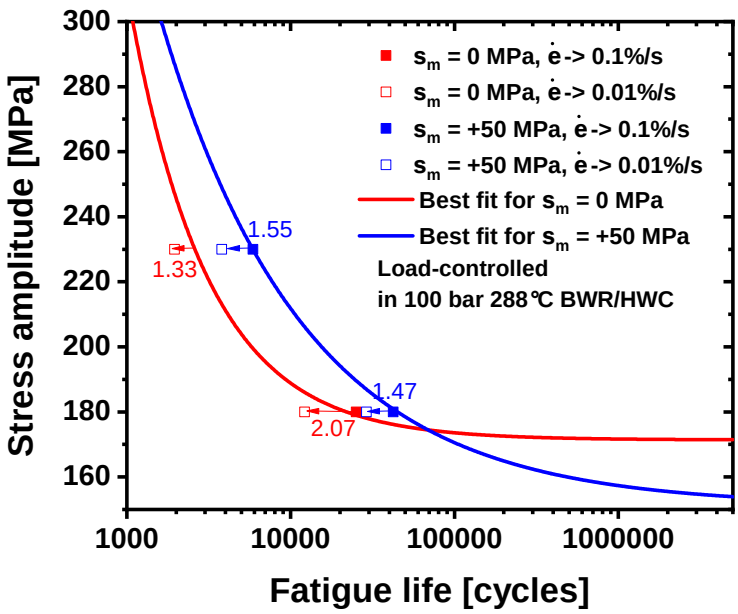

Figure 3.24 – Stress-life of tests with strain rate of $\dot{\epsilon} \approx 0.1\%/s$ and $\dot{\epsilon} \approx 0.01\%/s$ in BWR/HWC environment with 100 bar at 288°C.

In Fig. 3.25, the tests with slower stain rate have larger strain amplitude and result in shorter fatigue life. This is consistent with the common understanding: higher strain means higher plastic damage per cycle and results in short fatigue life; faster loading strain rate leads to stronger stress-strain response (namely a smaller strain amplitude at the same stress amplitude). Besides the effect of strain rate on the mechanical response, slower strain rate, if lower than a certain value and if temperature and DO meet their corresponding threshold concomitantly, can accelerate crack grow. Observations regarding strain rate effect on crack growth rate in HTW will be described in Section 3.5. There, strain rate is speculated having effects on both crack initiation (as induce higher/lower strain/stress) or crack growth for fatigue of austenitic SSs in HTW.

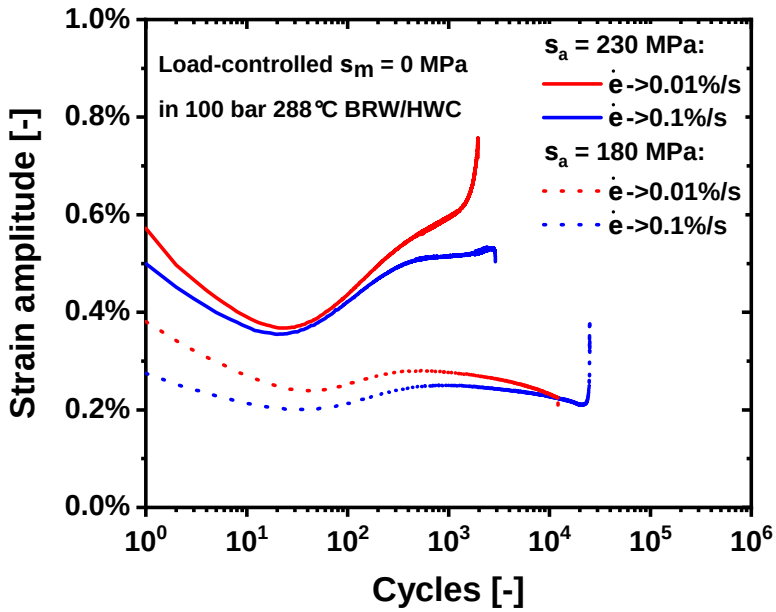

Figure 3.25 – Strain amplitude versus cycle of tests with strain rate of $\dot{\epsilon} \approx 0.1\%/s$ and $\dot{\epsilon} \approx 0.01\%/s$ in BWR/HWC environment with 100 bar at 288°C.

3.2 Fractographic observations

Optical microscopy (OM) observations of selected fracture surfaces are shown in Fig. 3.26, with the stress amplitude along the horizontal axis and the mean stress along the vertical one. The black areas observed on the OM pictures correspond to the oxides formed in HTW. They indicate the fatigue cracked zones, which were exposed to the HTW during crack propagation. For the tests in HTW, cracks initiated at multiple sites on the inner surface. Higher stress amplitude produces more crack initiation sites. This is in good agreement with the specimen surface observations, where a higher surface crack density is observed for higher stress amplitudes (see below in Section 3.3). Higher crack density corresponds to a larger number of secondary cracks and results in bigger fatigue cracked zone.

For all investigated mean stresses (+10, +50, 0, -20 MPa), the number of cracks at the condition with -20 MPa mean stress is reduced with respect to that with zero or positive mean stresses. This is also verified with the observation of surface cracks and cracks on wall cross-section (see below in Section 3.3). For example, it was found that the test with σ_a = 210 MPa, σ_m = +50 MPa and the test with σ_a = 230 MPa, σ_m = -20 MPa had a similar average strain amplitude of around 0.25%. However, comparing the fracture surfaces of these two tests, one observes that the test with σ_m = -20 MPa presents a smaller cracked area than the test with σ_m = +50 MPa. This indicates that the crack density does not only depends on the strain/stress amplitude but also on the mean strain/stress.

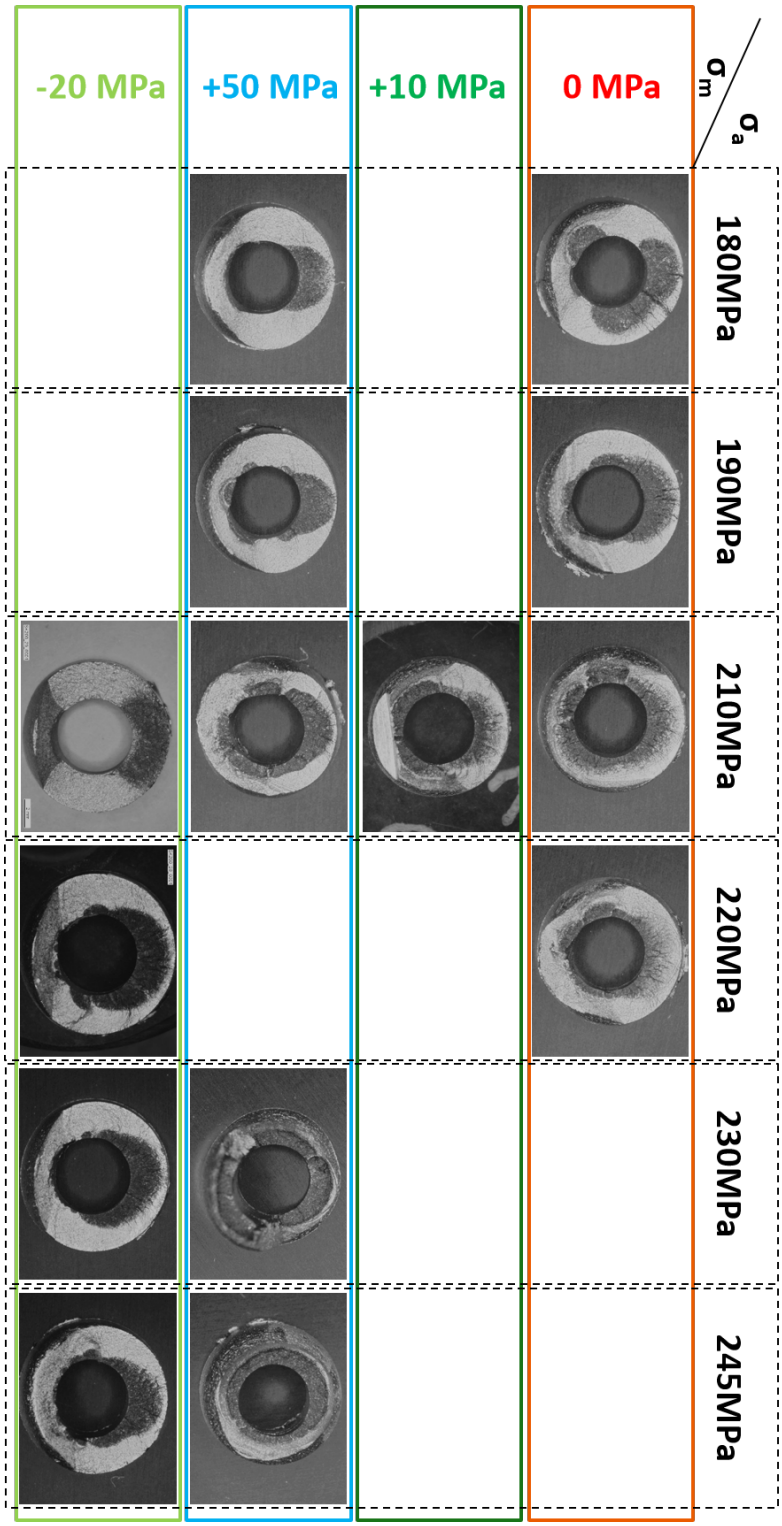

Figure 3.26 – Fracture surfaces observed with OM of specimens tested at 288°C in BWR/HWC environment at 100 bar.

A typical fracture surface is presented in Fig. 3.27. The whole surface can be divided into three areas: fatigue crack area, transition area and ductile fracture area. Multiple cracks initiated on the inner surface (Fig. 3.27c). The fatigue cracked area is the area over which the crack propagates during stress cycling, from the inner surface where it initiates to the outer surface. The crack propagates perpendicularly to the specimen axis and its path can be assessed from the river-flow pattern (Fig. 3.27e) [72]. The so-called transition area (Fig. 3.27g) is the region adjacent to the fatigue crack where no striation was observed but where voids are formed (Fig. 3.27a). This area is formed after the main crack has grown through the wall and is created during a few cycles. Ultimately, the ductile area corresponds to the final loading of the very last cycle where the controller of the testing machine tries to impose the maximum stress. This region is typical of ductile fracture, characterized as honey-comb (Fig. 3.27d).

The fracture mode of the specimens tested in 288°C air is generally similar to the mode in 288°C BWR/HWC. The only main difference observed for several tests is that the main cracks initiated on the outer surface and minor cracks initiated from inner surface (Fig. 3.28).

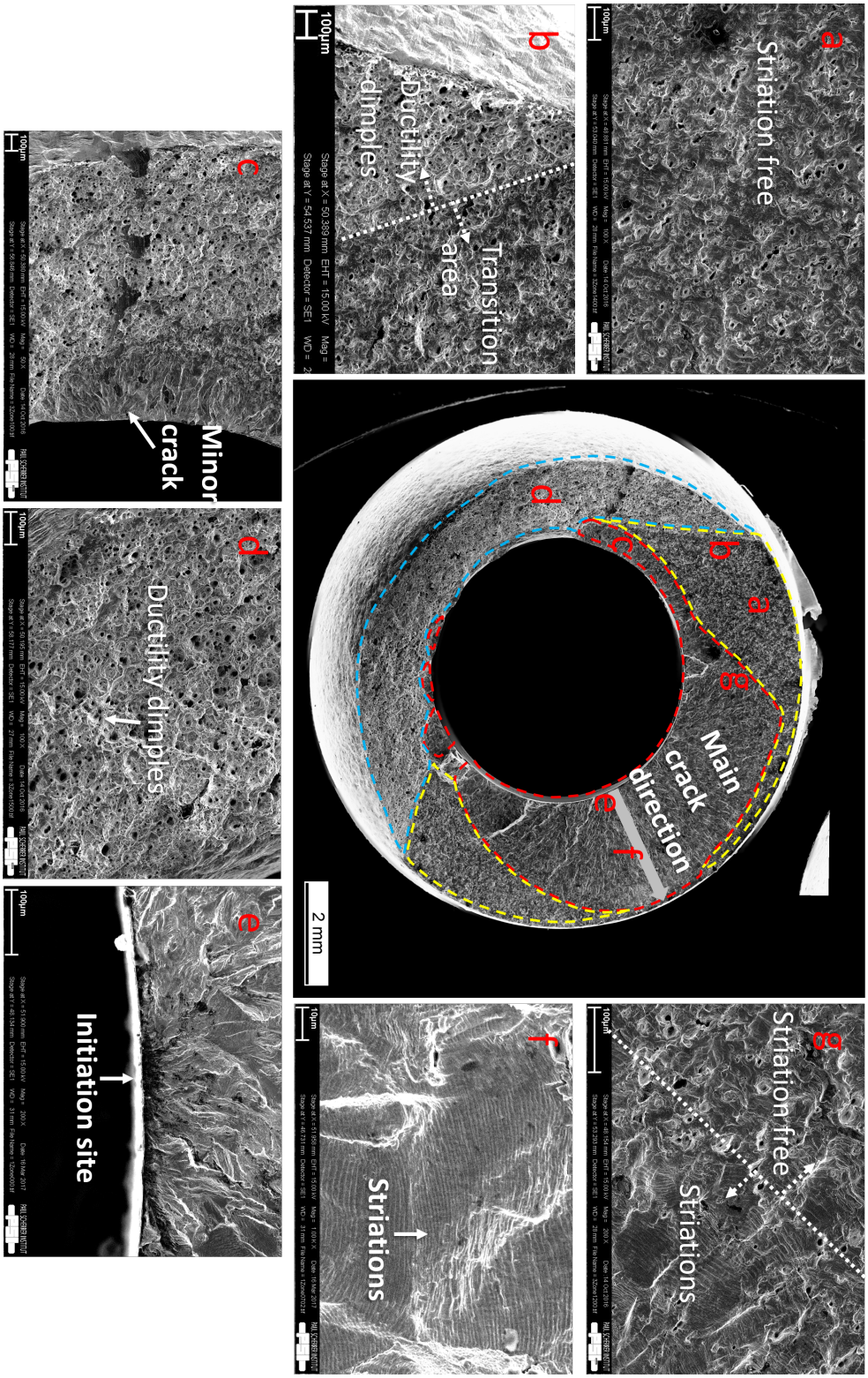

Figure 3.27 – Details of one representative fracture surface observed with SEM. The red line indicates the fatigue cracked area; the yellow line indicates the transition area; the blue line indicates the ductile fracture area.

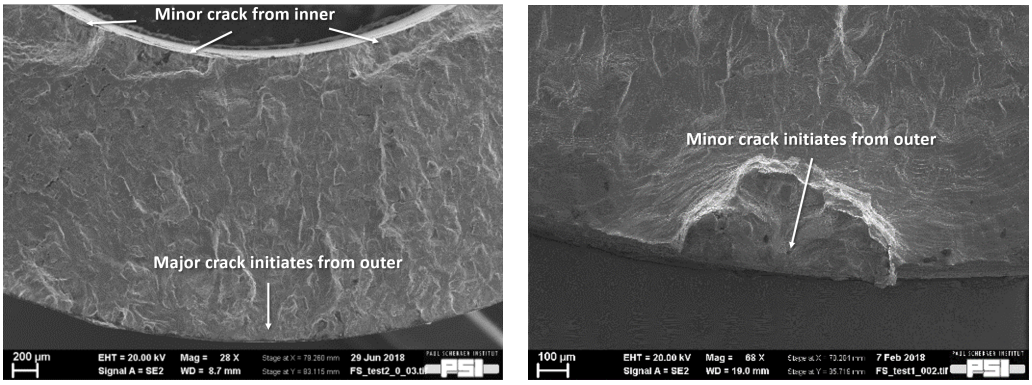

(a) (b)

Figure 3.28 – Fracture surfaces of specimens after tested in air at 288°C, (a) main crack from outer surface, (b) main crack from inner surface and minor crack from outer surface.

3.3 Crack density measurement

All tested specimens were cut and photographed following the method described in Section 2.5.1 and Section 2.5.2. Only some representative observations are shown to outline the correlation between fatigue crack initiation/growth and imposed mechanical loading as well as environmental conditions. Fig. 3.29 presents the OM observations of polished wall cross-sections of tested specimens with different mean stresses. We observed that, in the wall cross-sections of the specimens with higher mean stress, the crack opening of the secondary cracks is larger. In Fig. 3.29d, no crack was observed for -20 MPa mean stress. In addition, significant necking was observed in the specimen with +50 MPa mean stress.

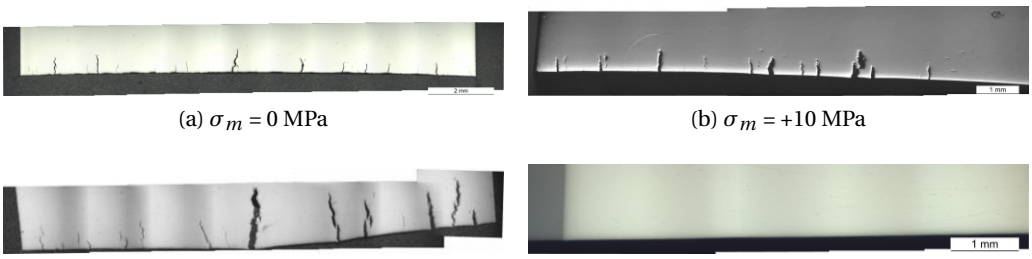

(a) σ_m = 0 MPa (b) σ_m = +10 MPa

(c) σ_m = +50 MPa (d) σ_m = -20 MPa

Figure 3.29 – OM observations of specimens wall cross-sections cut along the loading axis. The specimens were tested with σ_a = 210 MPa, (a) σ_m = 0 MPa, (b) +10 MPa, (c) +50 MPa, (d) -20 MPa.

Quantitative measurement was performed to determine the crack density on polished wall cross-sections. Fig. 3.30 describes the measured crack number density on wall cross sections. Higher positive mean stress causes higher crack number density in both environments. Note that no obvious crack number density difference between the two environments was observed.

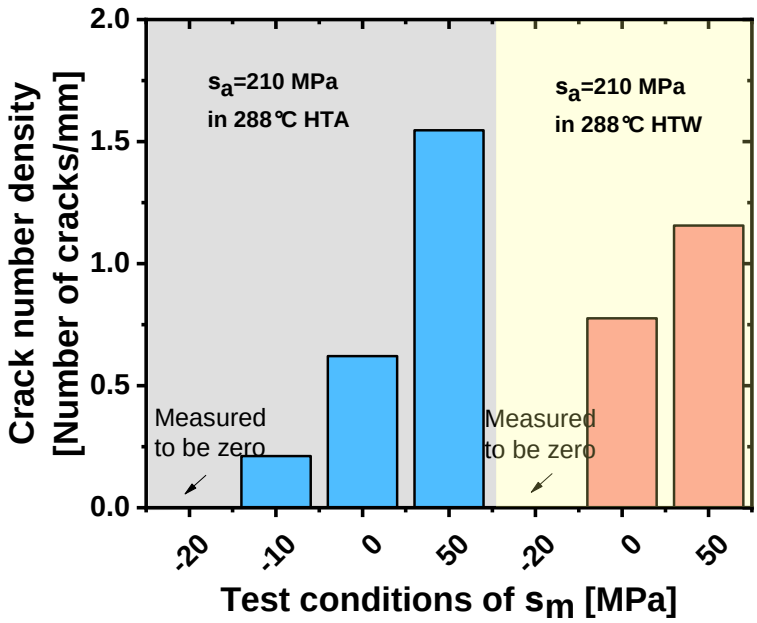

Figure 3.30 – Measured crack number density (number of cracks/length along the loading direction) on wall cross-section of each specimen with σ_a = 210 MPa and different σ_m in air and BWR/HWC at 288°C.

The crack opening was also quantified by the ratio of the cracked open area (black area in Fig. 3.29) over the area of wall cross-section. The method is schematically described in Fig. 2.12. It has to be recognized that the crack opening so defined is a just straightforward way to compare the general trend in cracking behavior under different conditions. As described in Fig. 3.29 and Fig. 3.30, the crack opening and number density are related to mean stress, which in turn is correlated with mean strain. The crack opening dependence on test conditions (different mean stresses and environments) is described in Fig. 3.31, which shows that larger positive mean stress induces higher crack opening.

In Fig. 3.32, the OM observations of inner surfaces are presented along with the mean strain average over the entire fatigue test. The mean strain-stress amplitude plots show that larger mean stress induces higher mean strain. Correspondingly, higher mean stress/strain induces larger crack opening and number density as observed on inner surfaces, even if only qualitative observations were performed in this case. Again, the crack opening and number density are positively correlated with mean strain. This is consistent with the observation on wall cross-section in Fig. 3.29, Fig. 3.30 and Fig. 3.31.

Additionally, higher crack opening was observed in specimens tested in HTW than in HTA. The OM observations in Fig. 3.33 indicate higher crack opening and number density on the surfaces of specimens tested with +50 MPa mean stress or in HTW.

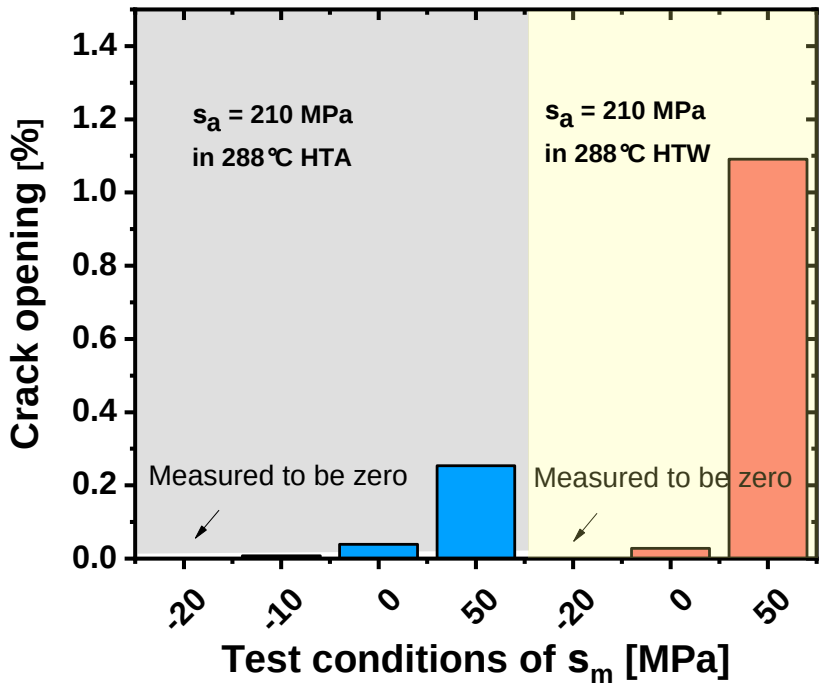

Figure 3.31 – Measured crack opening (area of crack opening/area of wall cross section) of specimens with σ_a = 210 MPa and different σ_m in air and BWR/HWC at 288°C.

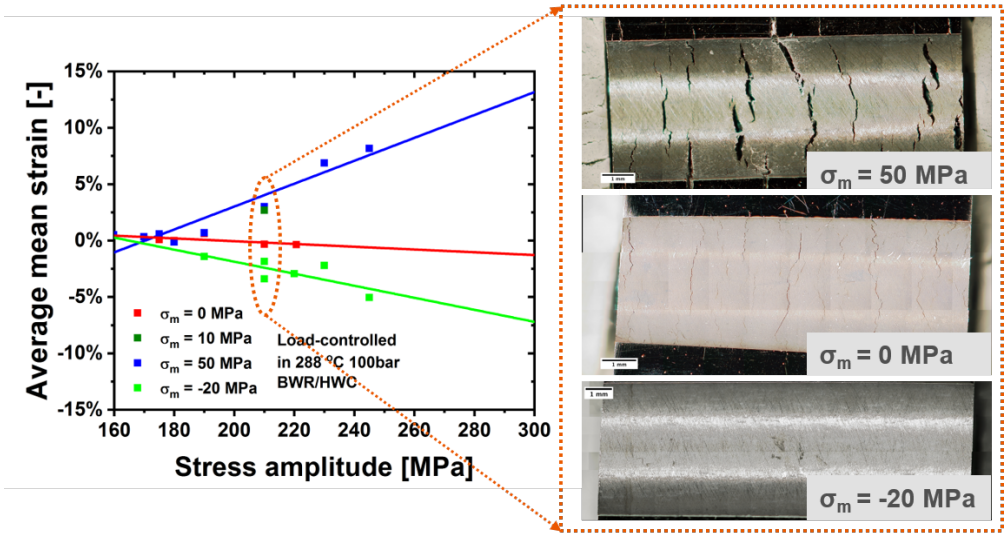

Figure 3.32 – Inner surface observation of specimens after-test with σ_a = 210 MPa and variant σ_m in 288°C BWR/HWC. Left plot presents their mean strain value achieved in fatigue tests.

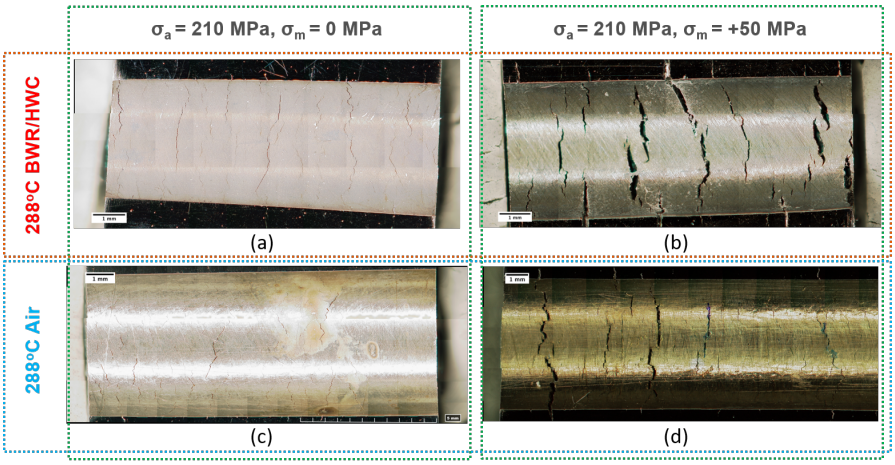

Figure 3.33 – Inner surface OM observations of specimens with σ_a = 210 MPa and different σ_m of 0 MPa and +50 MPa in air and in BWR/HWC at 288°C.

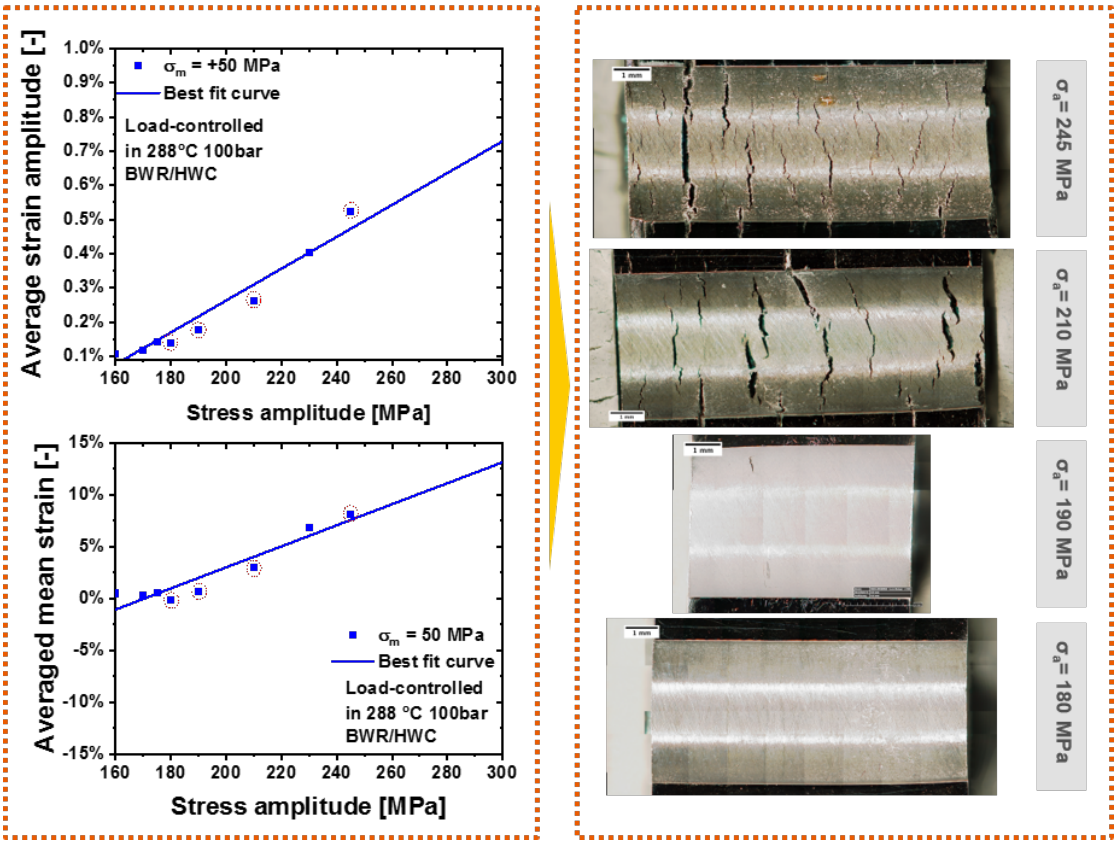

Figure 3.34 – Inner surface observations of specimens with different σ_a and their corresponding strain amplitudes (upper left plot) and average mean strain (lower left plot) during fatigue tests.

Besides the influence of mean stress, the stress amplitude was found to affect the cracking

behavior as Fig. 3.34 illustrates. The inner surface of four specimens with the same mean stress but different stress amplitudes were observed. The surface with higher stress amplitude, with corresponding higher strain amplitude and mean strain, has larger opening and number of cracks.

3.4 Crack initiation sites

Following the method described in Section 2.5.4, the inner and outer surfaces of some specimens were characterized with SEM and EBSD to identify the with and without mean stress in HTA and HTW environments. Again, no secondary cracks were observed on the inner and outer surfaces of the specimens tested with -20 MPa mean stress. For the tests without and with +50 MPa mean stresses, no significant difference in the crack initiation sites was observed. Therefore, only the results of two tests with the same σ_a and σ_m (210 MPa and +50 MPa respectively) in HTA and HTW are presented here (Fig. 3.35 to Fig. 3.38).

Fig. 3.35a and 3.37a are the inner surface images (taken with SEM automatic survey mode, as described in Fig. 2.14) of specimen tests in HTW and HTA environments respectively. For both environments, the main cracks initiated on the inner surface. In HTW, around 80% of cracks initiated at scratches and initially grew along them. Beyond a certain crack length, the cracks reoriented to grow perpendicularly to the loading direction. For the test in air at 288°C, almost all cracks initiated and grew along scratches (see Fig. 3.37a).

We observed many fewer and smaller cracks on the outer surfaces of the specimens tested in both environments (Fig. 3.36a and Fig. 3.38a). External cracks mainly initiated at the surface slip markings for the specimen tested in HTW (Fig. 3.36b). All external surface cracks are perpendicular to the loading direction (LD) for the specimen tested in HTA (Fig. 3.38b). The surface slip markings formed as a consequence of high mean strain attained in tests with σ_m = +50 MPa. No slip markings were observed in tests with σ_m = 0 MPa or -20 MPa.

We characterized the surface strain distribution, local strain and microstructures around the cracks on electro-polished surfaces via EBSD. In Fig. 3.36c, all surface cracks were erased after electro-polishing. This indicates that the external cracks were very shallow. However, in Fig. 3.38c, it is observed that most external cracks remained after electro-polishing. This is also validated with observations of cracks on specimen wall cross section, where longer external cracks exit in specimens tested in HTA than in HTW. By analyzing IPF images (Fig. 3.35e, Fig. 3.37e, Fig. 3.36e and Fig. 3.38e), the inner surfaces revealed that larger deformation than on the outer surfaces occurred. Indeed, the IPF images show higher misorientation contrast in inner surface EBSD images and relatively homogeneous strain distribution in outer surface EBSD images. From Fig. 3.35e and Fig. 3.37e, we deduced that cracks initiated neither at slip markings nor at microstructural defects. This observation confirmed that crack initiates at the root of surface scratch.

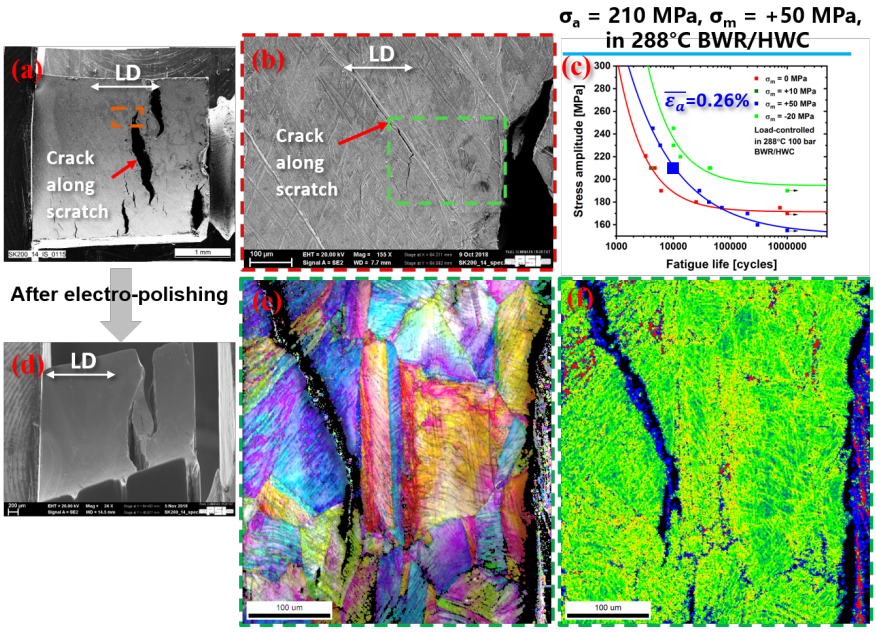

Figure 3.35 – Observation of crack initiation sites on inner surface of specimen tested with σ_a = 210 MPa, σ_m = +50 MPa in BWR/HWC at 288°C. (a-b) SEM images of inner surface with cracks and grinding scratches, (c) observed test in stress-fatigue plot, (d) SEM image of inner surface after electro-polishing, (e) EBSD IQ + IPF image (f) strain analysis of selected area with cracks.

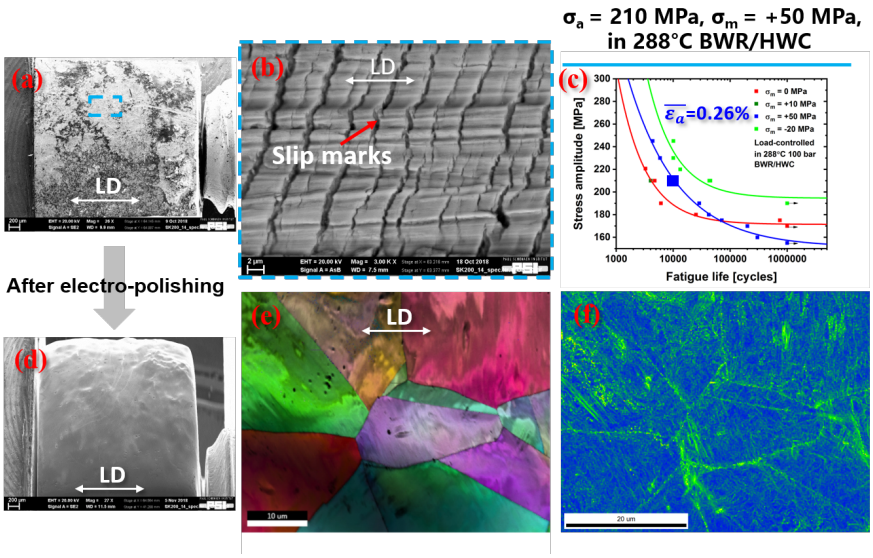

Figure 3.36 – Observation of crack initiation sites on outer surface of specimen tested with σ_a = 210 MPa, σ_m = +50 MPa in BWR/HWC at 288°C. (a-b) SEM images of outer surface with cracks and grinding scratches, (c) observed test in stress-fatigue plot, (d) SEM image of inner surface after electro-polishing, (e) EBSD IQ + IPF image (f) strain analysis of selected area with cracks.

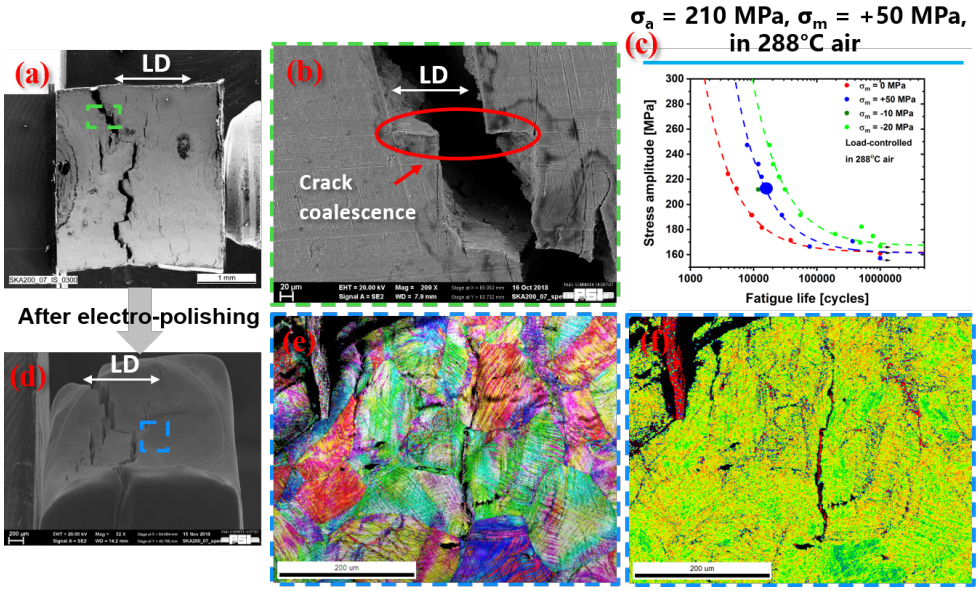

Figure 3.37 – Observation of crack initiation sites on inner surface of specimen tested with σ_a = 210 MPa, σ_m = +50 MPa in air at 288°C. (a-b) SEM images of inner surface with cracks and grinding scratches, (c) observed test in stress-fatigue plot, (d) SEM image of inner surface after electro-polishing, (e) EBSD IQ + IPF image (f) strain analysis of selected area with cracks.

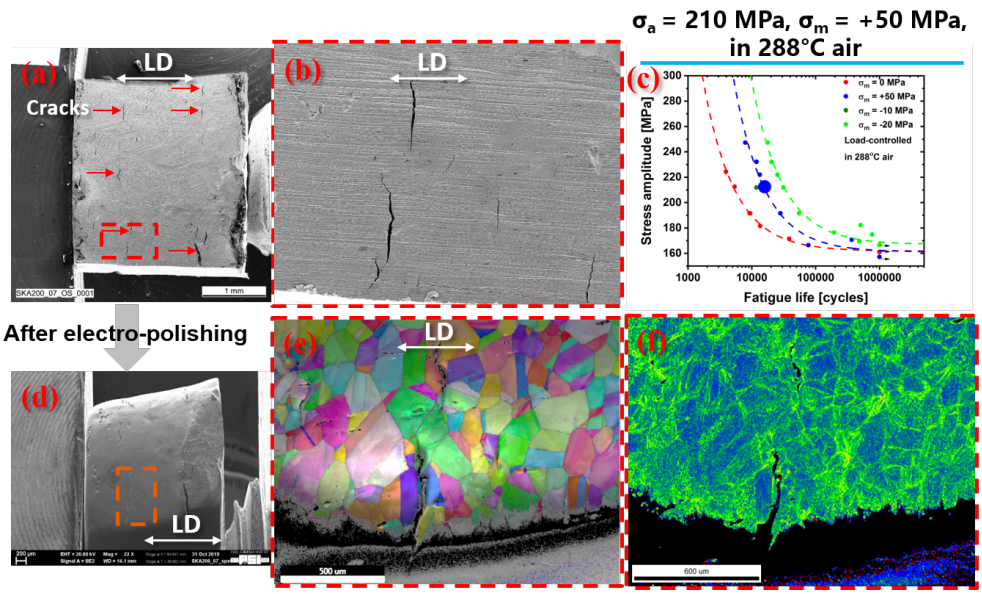

Figure 3.38 – Observation of crack initiation sites on outer surface of specimen tested with σ_a = 210 MPa, σ_m = +50 MPa in air at 288°C. (a-b) SEM images of outer surface with cracks and grinding scratches, (c) observed test in stress-fatigue plot, (d) SEM image of inner surface after electro-polishing, (e) EBSD IQ + IPF image (f) strain analysis of selected area with cracks.

3.5 Crack growth rate

3.5.1 Striation spacing measurement methodology

Oxide layer removal

The striations on the fracture surfaces, even at 50 μm crack depth, were well visible and countable in HRSEM images. This implies that crack growth is not dominated by dissolution processes but rather by mechanical mechanisms, otherwise the striations would not be visible [63]. Unfortunately, HTW environment leads to massive oxides covering on the fracture surfaces making the observations of the striations at short crack depth (normally < 0.5 mm) very difficult. Thus, it was necessary to apply a surface treatment to remove the oxides.

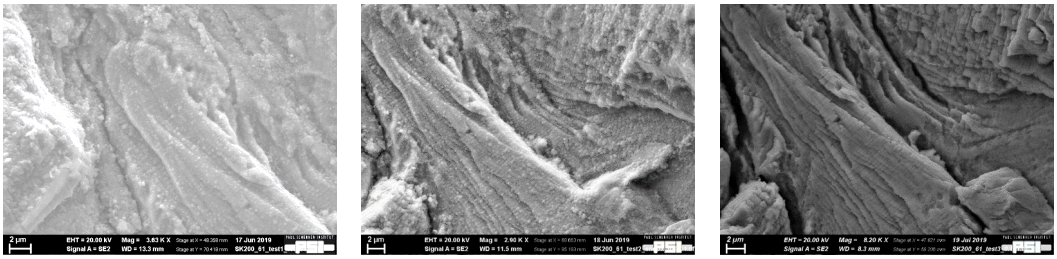

(a) (b) (c)

Figure 3.39 – SEM images of fracture surface at 0.1 mm crack depth of specimens tested in 288°C BWR/HWC with σ_a = 230 MPa, σ_m = 0 MPa: (a) without surface treatment, (b) after electrochemical treatment in ENDOX solution, (c) after chemical etching treatment in KMO_4 + NaOH water solution and then in ammonium citrate dibasic water solution. The details of the procedure are described in Section 2.5.3.

Fig. 3.39b and Fig. 3.39c show the fracture surface at 0.1 mm crack depth after electrochemical treatment in ENDOX solution and after chemical etching treatment respectively. The surface without any treatment looks like Fig. 3.39a, in which the striation is barely distinguishable. After treatment in ENDOX solution, a large part of the big debris was removed. However, most dense oxides were still present. This cathodic cleaning relies on mechanical removal by generated hydrogen bubbles at cathodic probe. It works well on low-alloy steels, where surface most loose iron oxides are formed. For austenitic stainless steels, more dense oxides (e.g., spinels, chromium rich oxides layer) are formed. This increases the difficulty for mechanical removal in cathodic cleaning. Although striation is distinguishable with the help of HRSEM, cathodic cleaning can not provide us a fully satisfying surface for striation measurement. Thus we considered a more aggressive treatment in KMO_4 + NaOH water solution and then in ammonium citrate dibasic water solution. The post-treated surface is shown in Fig. 3.39c, where one can seen that most oxides were removed and the identification of striations has significantly improved. This treatment may introduce chemical attack on surface morphology. Therefore, the treatment duration should be controlled with caution according to oxides layer

thickness, which depends on testing temperature, environment and duration.

In order to assess the effects of different treatment methods on striation spacing measurement, the spacing after cathodic cleaning surface and after chemical etching surface are found almost identical. This confirms that the measured results with the two different oxides removal treatments are valid. Nevertheless, the chemical etching save us a lot of efforts on spacing counting if the chemical attack is properly controlled.

Verification of striation/cycle ratio with cycling block test

The purpose of striation spacing measurement is to determine the crack growth rate (da/dN) along the crack depth. De Baglion [145] and Poulain [72] estimated that the striation spacing equals the local crack growth rate, namely one striation corresponds to one cycle for 304L, for the tests in PWR environment but a different striation spacing over crack growth rate ratio (around 2) was reported for the tests in air. In general, they claim that a relation exists between striation spacing and crack growth rate in a given environment.

In order to verify the ratio between striation number and cycle number in HTW and in HTA, ad-hoc cycling block tests were designed and performed. First, block tests for several tests in HTW were successively performed with a stress amplitude of 190 MPa and with two different frequencies of 0.17 Hz (for 900 cycles) and 0.008 Hz (for 100 cycles). The loading protocol is schematically described in Fig. 3.40. The two frequencies were used alternatively until specimen failure. Block tests in HTW were designed based on the assumption that the striations formed during cyclic loading with the slower strain rate would be more widely spaced. Thus, it is possible to distinguish the striations, which formed during slower loading rate (smaller frequency), and to determine the ratio striations/cycle.

The fracture surface after the block test in HTW was observed under HRSEM and the striation spacing and number in the 0.008 Hz blocks were measured with the help of digital image analysis software. Several 0.008 Hz blocks were found along the main crack. Fig. 3.41 is a typical one, in which the boundaries between blocks with different frequencies are easily recognized and highlighted with red dash lines. Striations in the 0.008 Hz block are wider spaced than those in the 0.17 Hz block and the measured spacing was $\approx$ 1.15 μm and $\approx$ 0.43-0.52 μm respectively. This is consistent with our assumption that lower strain rate leads to larger crack growth rate per cycle due to more severe corrosion attack. Striation number in 0.008 Hz block (area between the dash lines) was counted, one by one, to be $\approx$ 100, which perfectly matches the imposed loading cycles of 100. This confirms that one striation corresponds to one loading cycle for tests in HTW; in other words, the striation spacing equals the local crack growth rate per cycle (da/dN) at least at the condition of σ_a = 190 MPa with frequency of 0.008 Hz. The observations of other blocks confirmed this conclusion. Thus we generalized this rule, striation spacing equals to local crack growth per cycle, to other loading conditions in HTW.

Analogously, the ratio between striation spacing and crack growth per cycle in HTA was verified

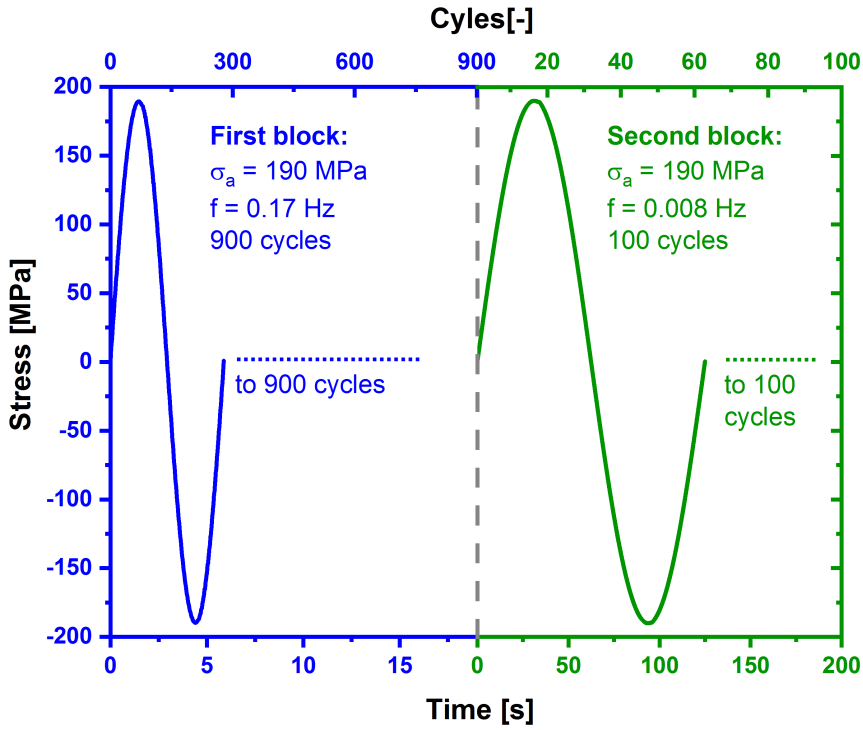

Figure 3.40 – Designed loading protocol for block tests in HTW.

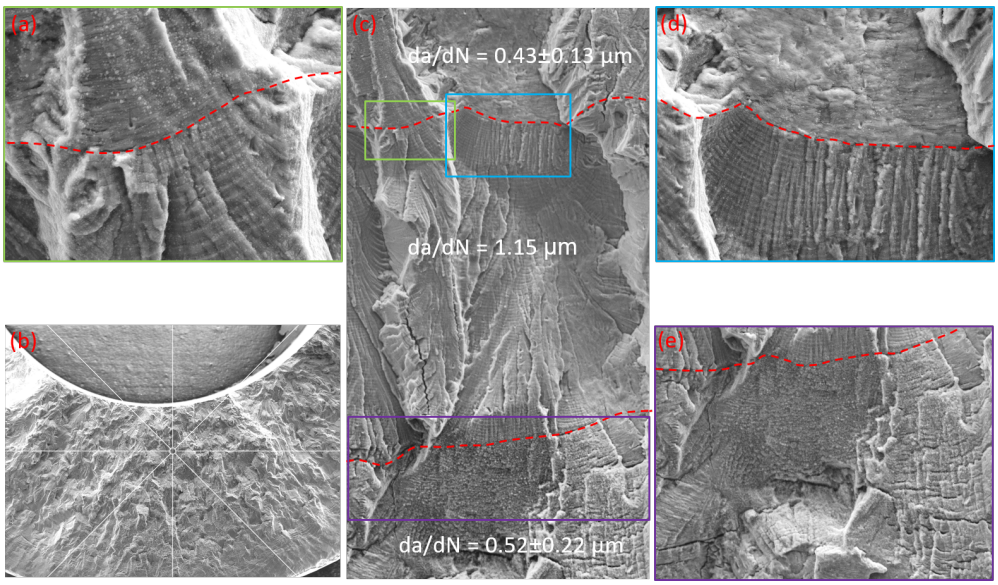

Figure 3.41 – Striation measurement of specimen after block test with σ_a = 190 MPa 0.17 Hz (900 cycles) & 0.008 Hz (100 cycles) in BWR/HWC at 288°C.

with block test. The testing protocol is described in Fig. 3.42. Three different stress amplitudes of 200 MPa (0.17 Hz), 175 MPa (0.17 Hz) and 160 MPa (0.5 Hz) are loaded for 100, 900 and 1000 cycles respectively. Unlike the tests in HTW, strain rate would not significantly affect crack growth rate. Thus we generate striations with different spacings by varying the stress amplitude.

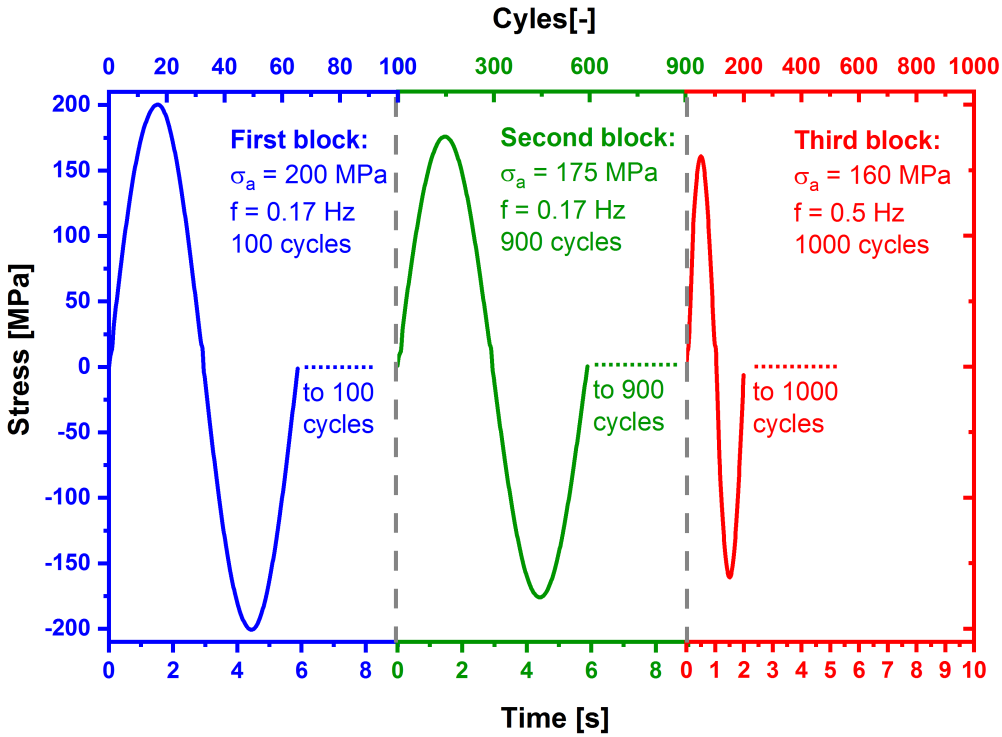

Figure 3.42 – Designed loading protocol for block tests in HTA.

Along the main crack, several blocks with different striation spacing were identified. For example, the blocks for σ_a = 200 MPa and for σ_a = 160 MPa are indicated as the areas between dash lines in Fig. 3.43a and Fig. 3.44a respectively. In Fig. 3.43a, three different striation spacings were measured: 0.21 ± 0.02 μm for the block with σ_a = 160 MPa, 1.06 ± 0.34 μm for the block with σ_a = 200 MPa, 0.75 ± 0.04 μm for block with σ_a = 175 MPa. Higher stress amplitude induces larger striation spacing. The largest striation spacing is around 5 times the spacing of the smallest one. This provides sufficient size contrast between the different blocks. For example, the boundaries (highlighted with red dash lines) between the different blocks are visible in Fig. 3.43b and Fig. 3.43c. 94 striations were counted in the block of σ_a = 200 MPa, at which 100 cycles were loaded.

For the block with σ_a = 160 MPa in Fig. 3.44, number of striations (942 striations) was calculated by dividing crack length (194 μm in this block) by average striation spacing (0.2059 ± 0.0409 μm).

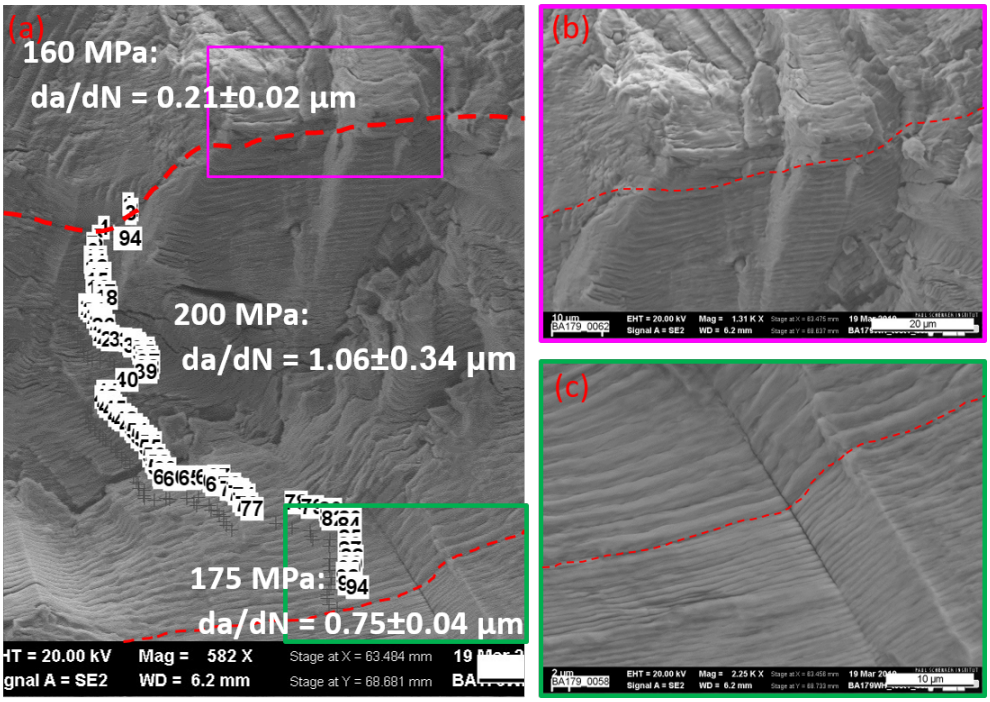

Figure 3.43 – Striation measurement of specimen after block test with σ_a = 200 MPa, 0.17 Hz (for 100 cycles), σ_a = 175 MPa, 0.17 Hz (for 900 cycles), σ_a = 160 MPa, 0.5 Hz (for 1000 cycles) in air at 288°C. Area between dash lines indicates the block of σ_a = 200 MPa.

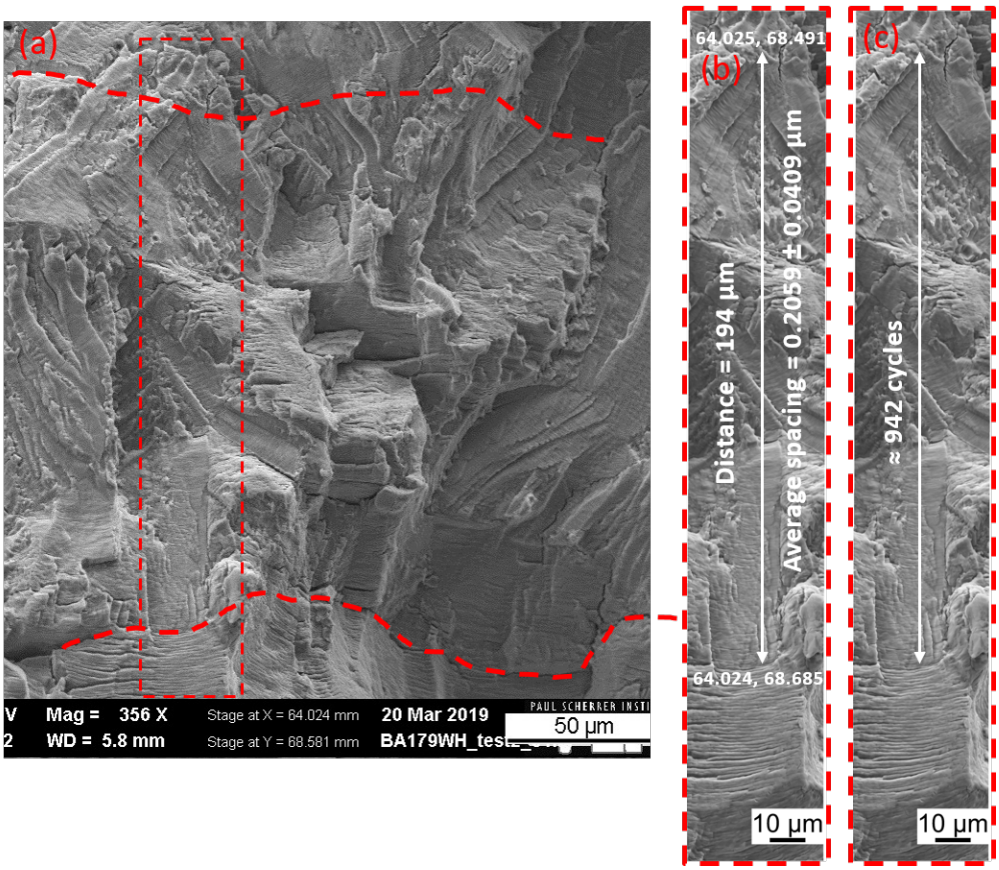

Figure 3.44 – Striation measurement of specimen after a block test with σ_a = 200 MPa 0.17 Hz (100 cycles), σ_a = 175 MPa 0.17 Hz (900 cycles), σ_a = 160 MPa 0.5 Hz (1000 cycles) in air at 288°C. Area between dash lines indicates block of σ_a = 160 MPa.

With the analysis of the block tests in HTA, we confirmed again that the striations/cycle ratio is approximately equal to one. Hence, the crack growth per cycle (da/dN) can be easily inferred from the striation spacing. For the locations, where the striation was impossible to be counted, interpolation values were applied. Striations in the crack initiation region, where the crack depth is shorter than 50 μm, are invisible, In the following, the crack growth region is defined as the region where the cracks grows from 50 μm to the end of life. In this region the striation spacing is physically measurable. Correspondingly, the number of cycles to create physical crack (crack <50 μm) is defined as physical crack initiation life.

3.5.2 Striation spacing measurement on specimens tested in HWC at room temperature

The crack growth rates of three specimens tested under similar condition, but with different internal water pressures, are compared in Fig. 3.45. The results of striation spacing/crack growth rate da/dN almost align with each other, even if a slight difference can be observed beyond 1.0 mm crack depth. This may stem from the modest difference in ϵ_a and ϵ_m among the three specimens. As a whole, the striation measurement method was considered to be reliable to measure the growth rate of cracks in hollow specimens tested in high-temperature water or air.

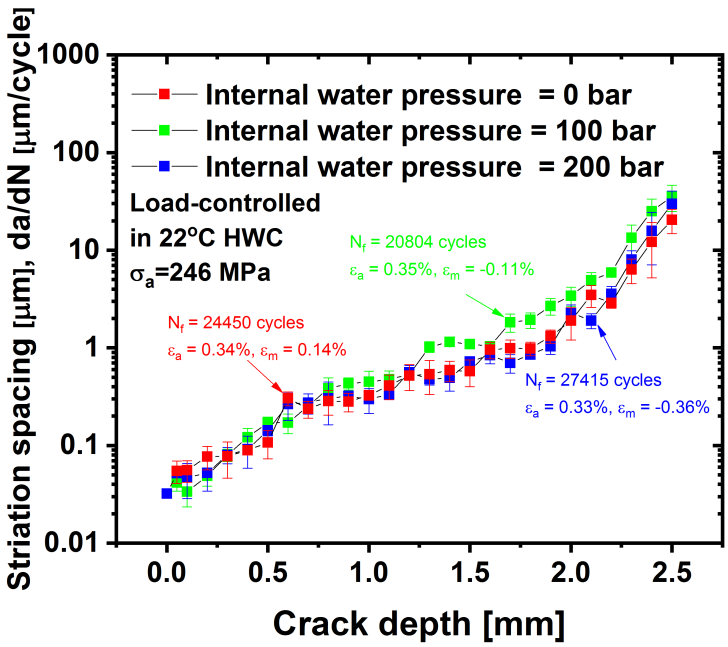

Figure 3.45 – Measured striation spacing along the main cracks of three specimens tested under similar condition: σ_a = 246 MPa, σ_m = 0 MPa, hydrogenated water at 20°C.

3.5.3 Crack growth rate law and correlation with macroscopic mechanical parameters

In this section we present first the measured crack growth rate as a function of the stress intensity factor calculated within the frame of linear elastic mechanics. For the smooth specimens, we have to consider corrections of the actual crack length to taken into account the fact that the linear elastic fracture mechanics is not applicable for very small cracks and the entire ligament is plastically deformed in smooth specimens. So we present then the crack growth rate laws in terms of a strain intensity factor and of the J-integral, which are more appropriate parameters to measure the driving force for crack growth in the case of smooth specimens that are elastically-plastically deformed.

Correlation with stress intensity factor

The stress intensity factor K_I was calculated with the formula (Equation 3.20) proposed by Chapuliot for pipes containing different crack geometries and loadings configurations [146]:

$$K_I = \left[\sigma_0 i_0 + \sigma_1 i_1 \left(\frac{a}{t}\right) + \sigma_2 i_2 \left(\frac{a}{t}\right)^2 + \sigma_3 i_3 \left(\frac{a}{t}\right)^3 + \sigma_4 i_4 \left(\frac{a}{t}\right)^4 + \sigma_{gb} F_b\right] \sqrt{\pi a} \tag{3.20}$$

where a is the crack depth, t is the wall thickness of the hollow specimen; σ_0, σ_1, σ_2, σ_3, σ_4 are polynomial the components describing the imposed axisymmetric loadings; σ_{gb} is the global bending components; i_0, i_1, i_2, i_3, i_4 are the axisymmetric shape functions that allow a non-uniform axisymmetric loading in the wall; and F_b is the shape function associated with global inflexion loading. For uniform uniaxial cyclic loading, $\sigma_1 = \sigma_2 = \sigma_3 = \sigma_4 = \sigma_{gb} = 0$, as no inflexion is involved and the temperature gradient is negligible. For an internal and external circumferential defect as shown in Fig. 3.46a and Fig. 3.46b respectively, σ_a is given by [146]:

$$\sigma_0 = \frac{F_{max}}{\pi\left(r_e^2 - r_i^2\right)} + \frac{P_{internal} \times r_i^2}{r_e^2 - r_i^2} \tag{3.21}$$

where F_{max} is the maximum imposed loading force. The maximum value is assumed to represent better the driving force for crack growth than the amplitude value in case of asymmetrical cyclic loading. $P_{internal}$ is the internal pressure, r_e is the external radius and r_i is the internal radius. $P_{internal}$ = 10 MPa, r_e = 5 mm, r_i = 2.5 mm for the tests in high-temperature water and $P_{internal}$ = 0 MPa, r_e = 5 mm, r_i = 3 mm for the tests in high-temperature air.

Finally, the shape function i_0 is derived by fitting the values of i_0 versus a/t, which were calculated by Chapuliot [147][146]. We assume a/c = 1 for both internal and external semi-elliptical cracks as Kamaya did [148]. Here 2c is the surface crack length.

For semi-elliptical crack initiated from the inner surface (Fig. 3.46a), i_0 is given by:

$$i_0 = 0.6571 + 0.0106\left(\frac{a}{t}\right) + 0.3331\left(\frac{a}{t}\right)^2 - 0.8364\left(\frac{a}{t}\right)^3 + 0.929\left(\frac{a}{t}\right)^4 \tag{3.22}$$

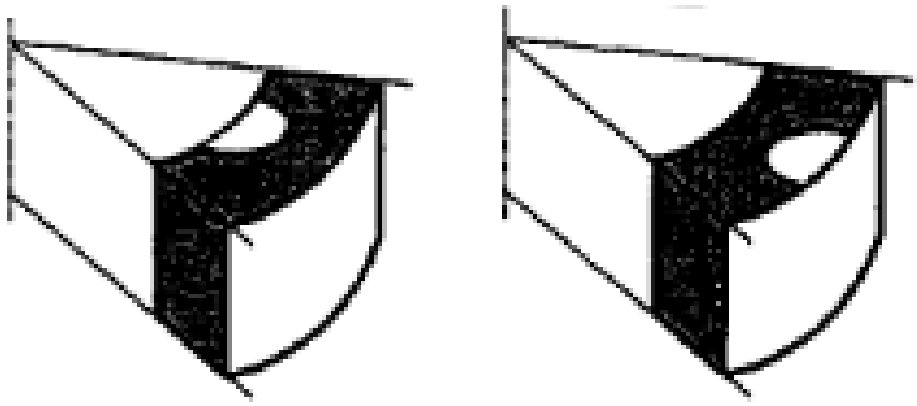

(a) (b)

Figure 3.46 – Internal (left) and external (right) circumferential semi-elliptical fault in a tube [147][146]

.

For semi-elliptical crack initiated from outer surface (Fig. 3.46b), i_0 is given by:

$$i_0 = 0.8831 + 0.0290\left(\frac{a}{t}\right) + 0.6858\left(\frac{a}{t}\right)^2 - 0.2934\left(\frac{a}{t}\right)^3 + 0.2782\left(\frac{a}{t}\right)^4 \tag{3.23}$$

Therefore, the K_I can be calculated by combining the previous equations.

$$K_I = \sigma_0 i_0 \sqrt{\pi a} \tag{3.24}$$

From the former equations, we can see the K_I is related to the σ_{max} and the tensile stress caused by internal pressure. The range of stress intensity factor ΔK is commonly applied to correlate crack growth rate in stage II.

$$\Delta K = K_{max} - K_{min} = f(\sigma_{max}) - f(\sigma_{min}) \tag{3.25}$$

The K_{min} is taken as zero if σ_{min} is negative (in compression), as stress intensity factor is undefined in compression and compression loading is generally considered to be of little influence on crack propagation. This is consistent with our application of K_I concept.

Fig. 3.47 shows the crack growth rate against the crack depth at different stress amplitudes. As expected, the crack growth rate strongly increases with the stress amplitude. Fig. 3.48 presents the correlation between the crack growth rates in HTW without mean stress and the calculated K_I. While the correlation looks somewhat better than in Fig. 3.47 (da/dN versus crack depth), it is unsatisfactory in two points. First, the crack growth rate at low stress amplitude (180 MPa) is not in line with that of the higher stress amplitudes, which is attributed

to the higher cyclic hardening at 180 MPa stress amplitude than at the other larger stress amplitudes. The hardening exponent was calculated with the method described in Section 3.5.3 with the Equation 3.41) (see in Table 3.1). The cyclic hardening level is indeed higher at the lower stress amplitude of 180 MPa. Second, the crack growth rates in the short-crack region (a ≤ 0.5 mm) do not follow the trend of those in the region of a > 0.5 mm. The short crack effect was commonly observed and reported [149][150][36] as a phenomenon of plastic strain controlled crack growth. In short-crack region, the linear elastic △K concept is not applicable as the crack size is of the order of the plastic zone size. In the mechanically short-crack region, crack closure effect may occur as a results of the build-up of plasticity, roughness and oxides.

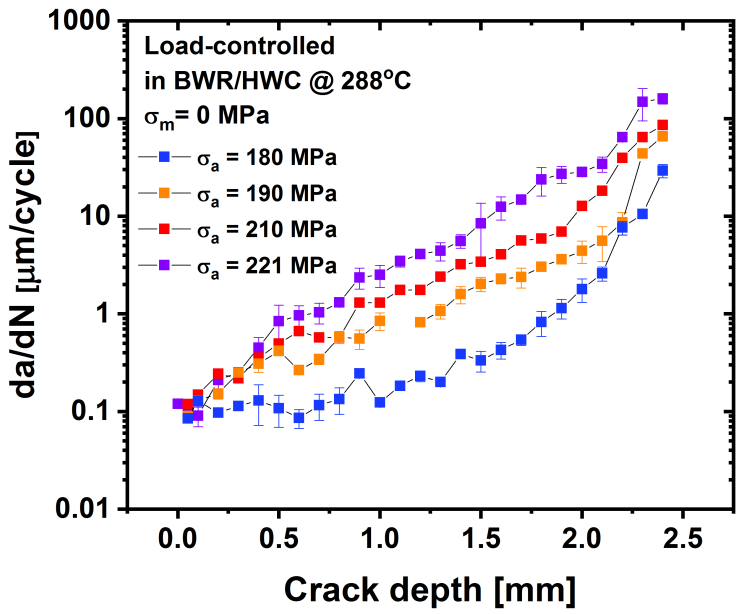

Figure 3.47 – crack growth rate versus crack depth of tests without mean stress in BWR/HWC environment at 288°C.

Haddad et al. [149][36] have introduced a concept of effective crack length in SIF calculation. The effective crack length is a constant characteristic of material (grain size) and accounts for non-continuum behavior of very small crack. With the knowledge of threshold stress intensity $\triangle K_{th}$ and fatigue limit σ_f, effective crack length (a_0) can be calculated:

$$a_0 = \left(\frac{\triangle K_{th}}{\sigma_f}\right)^2 \frac{1}{\pi} \tag{3.26}$$

In our case, the effective crack length is calculated to be ≈ 0.275 mm, given the $\triangle K_{th} \approx 5$ $MPa\sqrt{m}$ and $\sigma_f \approx 170$ MPa. Similarly, we considered the short crack correction by introducing

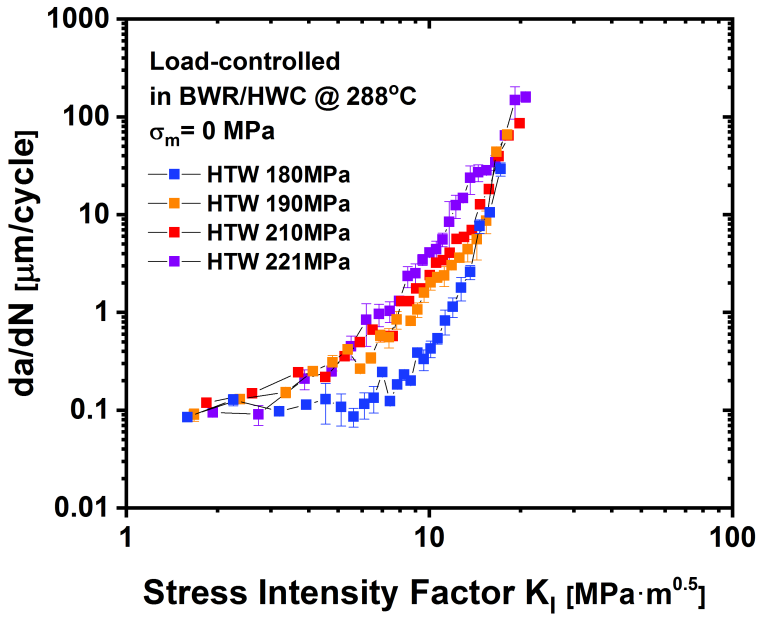

Figure 3.48 – Correlation between crack growth rate and stress intensity factor of tests without mean stress in BWR/HWC environment at 288°C.

the effective crack length a_0 into the calculation of K_I in Equation 3.24:

$$K_I = \sigma_0 i_0 \sqrt{\pi (a + a_0)} \tag{3.27}$$

Fig. 3.49 presents the correlations of da/dN versus K_I, which is with short crack effect corrected via Equation 3.27.

From Fig. 3.49, one observes that K_I fairly correlates the crack growth rates without mean stress, provided that the induced cyclic hardening is approximately at same level, i.e. for the stress amplitude 190, 210 and 220 MPa (see Table 3.1). However, with different mean stresses (in Fig. 3.50) the correlation between K_I and the crack growth rates is not satisfactory. As discussed in Section 3.1, austenitic stainless steels undergo hardening as well as softening during cyclic loading. The cyclic hardening shows a strong dependence on mean stress but a weaker one on stress/strain amplitude. The calculated hardening exponent as well as average strain range, plastic strain range are listed in Table 3.1. The calculation for hardening exponent is presented in Section 3.5.3.

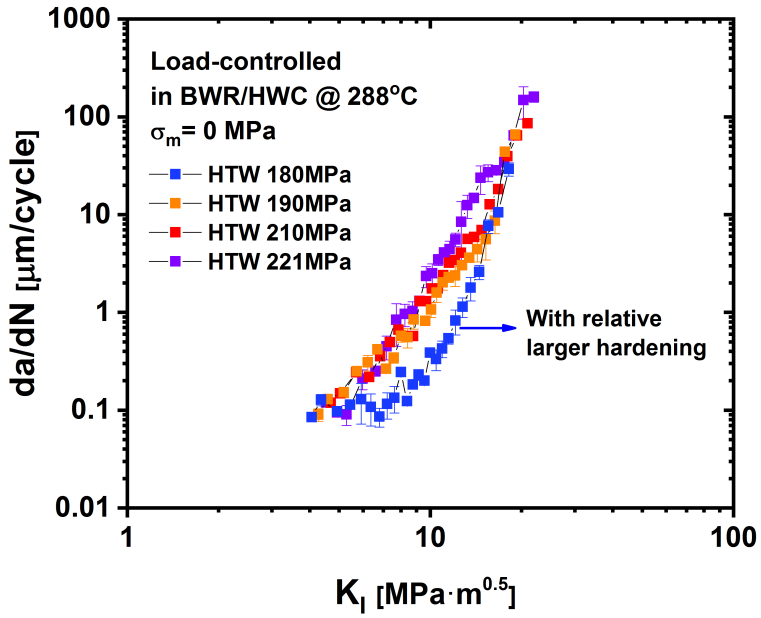

Figure 3.49 – Crack growth rate of tests without mean stress in BWR/HWC environment at 288°C correlated with K_I given by Equation 3.24 with correction of short-crack effect.

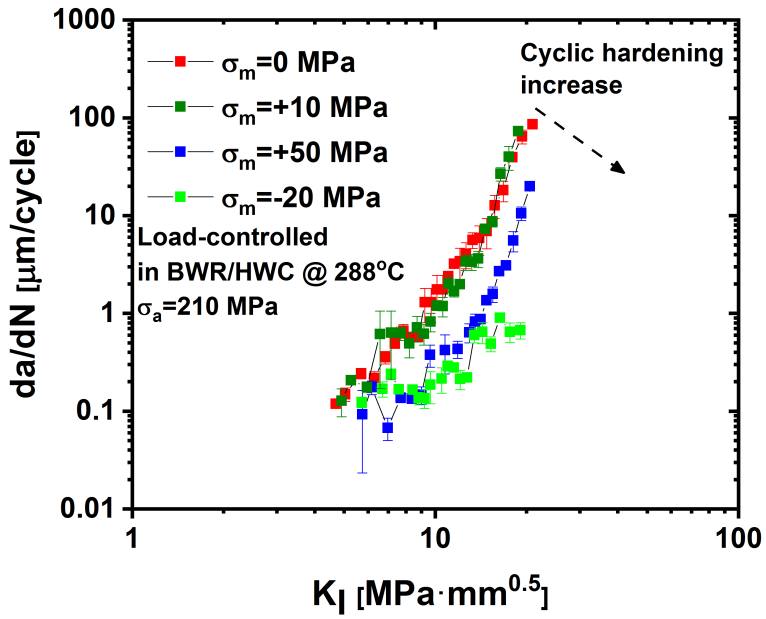

Figure 3.50 – Correlation between crack growth rate and K_I of tests with σ_a = 210 MPa and different mean stresses (0, +10, +50, -20 MPa) in BWR/HWC environment at 288°C.

Correlation with strain intensity factor

Haddad [36], Haigh [151], Kamaya [80], Zhang et al. [152] have proposed to use a strain based approach—here we call it strain intensity factor (K_ϵ) for convenience—to correlate the crack growth rates in elastoplastic condition, where the strain field at crack tip acts as the dominant driving force for crack growth. Being analogous to the tress intensity factor in Equation 3.27, strain intensity factor in Equation 3.28 uses strain range $\triangle\epsilon$ to replace σ_0. The geometry factor i_0 is kept unchanged.

$$\triangle K_\epsilon = \triangle\epsilon\sqrt{i_0}\pi\,(a + a_0) \tag{3.28}$$

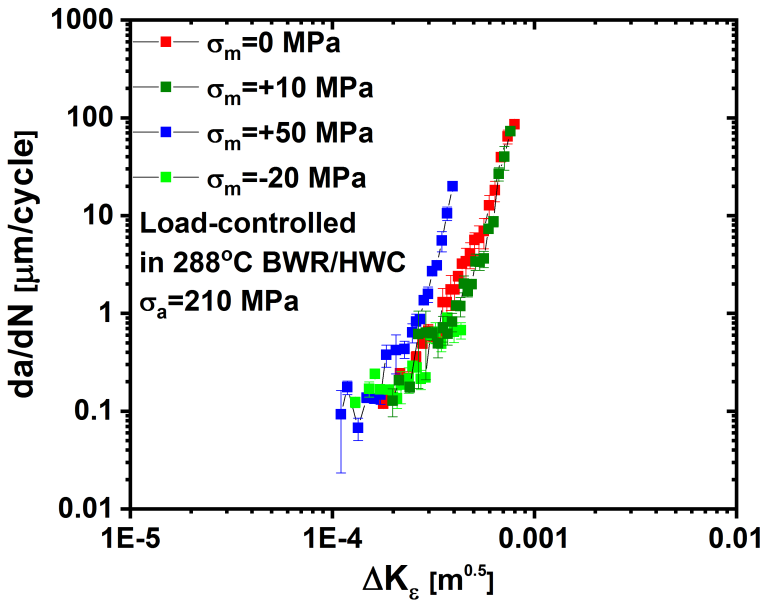

Figure 3.51 – Correlation between crack growth rates and strain intensity factor of tests with σ_a = 210 MPa and different mean stresses (0, +10, +50, -20 MPa) in BWR/HWC at 288°C.

Then, the crack growth rates are correlated with strain intensity factor $\triangle K_\epsilon$ given in Equation 3.28 and are plotted in Fig. 3.51, which shows a significant improvement in comparison to the correlations with the stress intensity factor, except for the specimen loaded with +50 MPa mean stress where the crack grows faster than the others with mean stresses given similar $\triangle K_\epsilon$ in Fig. 3.51. The much larger σ_{max} is likely to be the cause. This suggests that neither stress nor strain intensity factor alone can satisfactorily correlates the crack growth of 316L steel tested with mean stress. Strain intensity factor is also applied to the cracks loaded with different mean stress in 288°C air. Their correlation is plotted as Fig. 3.52.

The strain intensity factor is a simplified approach to represent the driving force for crack growth. However, strain is not the sole driving factor in the situation with co-occurrence of

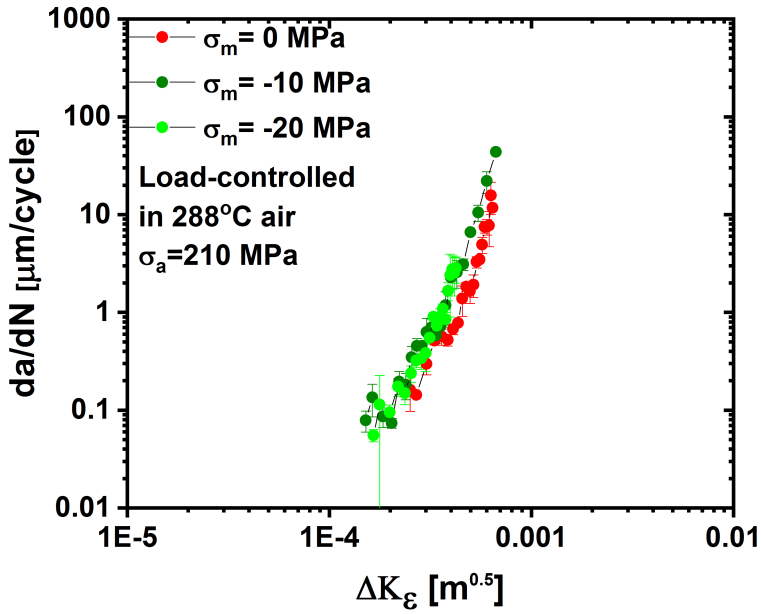

Figure 3.52 – Correlation between crack growth rates and strain intensity factor of tests with σ_a = 210 MPa and different mean stresses (0, -10, -20 MPa) in air at 288°C .

elastic-plastic and linear elastic fracture mechanics. J-integral approach may provide us a better solution [153].

Correlation with J-integral

The concept of "J-integral" was originally proposed by Rice [154] to measure the intensity of the stress and strain fields at the crack tip of elastic-plastic materials [153]. The value of J depends on the load as well as on the plastic deformation. Dowling [34][35] and Haddad et al. [36][149] have modified the J-integral approach for applications with short fatigue cracks in notches. Then, Chen [155] and Mann [156] have applied the modified J-integral approach for crack growth in stainless steels at elevated temperatures, by considering the J-integral range $\triangle J$.

$$\triangle J = \triangle J_e + \triangle J_p \tag{3.29}$$

where the $\triangle J_e$ is assumed to be equal to the strain energy release rate G under plane stress, which is related to $\triangle K$ and E:

$$\triangle J_e = G = \frac{\triangle K^2}{E} \tag{3.30}$$

with the stress intensity range $\triangle K$:

$$\triangle K = \triangle\sigma\, i_0 \sqrt{\pi\,(a+a_0)} \tag{3.31}$$

thus, $\triangle J_e$ can be written as:

$$\triangle J_e = \frac{\triangle\sigma^2 i_0^2 \pi\,(a+a_0)}{E} = 2\pi i_0^2 \triangle W_e\,(a+a_0) \tag{3.32}$$

with the elastic strain energy density $\triangle W_e$:

$$\triangle W_e = \frac{\triangle\sigma^2}{2E} \tag{3.33}$$

An approximation solution for J_p for the exponential hardening plastic case was obtained based on the work of Shih and Hutchinson [34][36][150][157].

$$\triangle J_p = 2\pi i_0^2 f(n) \triangle W_p\,(a+a_0) \tag{3.34}$$

here $f(n)$ is a function of cyclic hardening exponent n:

$$f(n) = (n+1)\left[3.85\frac{1-n}{\sqrt{n}} + \pi n\right] / (2\pi) \tag{3.35}$$

the strain hardening exponent n is defined in Ramberg-Osgood relationship:

$$\epsilon = \epsilon_e + \epsilon_p = \frac{\sigma}{E} + \left(\frac{\sigma}{A}\right)^{1/n} \tag{3.36}$$

$$\sigma = A(\epsilon_p)^n \tag{3.37}$$

where E is the elastic modulus and A is the strength coefficient.

The plastic strain energy density $\triangle W_p$ can be expressed empirically as [34]:

$$\triangle W_p = \frac{\triangle\sigma \triangle\epsilon_p}{n+1} \tag{3.38}$$

Combining the expression of $\triangle J_e$ (Equation 3.32, Equation 3.33) and that of $\triangle J_p$ (Equation 3.34, Equation 3.38) with Equation 3.29, one gets:

$$\triangle J = 2\pi i_0^2\,(a+a_0)\left\{\triangle W_e + f(n)\triangle W_p\right\} = 2\pi i_0^2\,(a+a_0)\left\{\left[\frac{\triangle\sigma^2}{2E}\right] + f(n)\left[\frac{\triangle\sigma\triangle\epsilon_p}{n+1}\right]\right\} \tag{3.39}$$

combined with Equation 3.42, Equation 3.39 is reduced to:

$$\triangle J = 2\pi i_0^2\,(a+a_0)\left\{\frac{f(n)}{n+1}\triangle\sigma\triangle\epsilon - \frac{\triangle\sigma^2}{2E}\left[\frac{2f(n)}{n+1} - 1\right]\right\} \tag{3.40}$$

This equation gives an approximation of J-integral for a cracked smooth axial specimen. i_0 is the geometrical factor for semi-circular cracks; $\triangle\sigma$, $\triangle\epsilon$ are known for a given test. In the following, we use the average value $\overline{\triangle\sigma}$ and $\overline{\triangle\epsilon}$ for strain-controlled and load-controlled test respectively. a_0, n, $f(n)$, E are constants for a given material. a_0 is calculated to be 0.275 mm, E equals 165 GPa at 288°C. The hardening exponent is normally obtained through a series of cyclic loading with different amplitudes for mastering materials. However, we found that the cyclic strain hardening depends on mean stress and stress/strain amplitude for 316L material. Only a very large amount of strain hardening characterization tests can yield the hardening exponent at various condition. Alternatively, according to Equation 3.38 we get:

$$n = \frac{\triangle\sigma\triangle\epsilon}{\triangle W_p} - 1 \tag{3.41}$$

The plastic strain $\triangle\epsilon_p$ and strain energy $\triangle W_p$ are deduced from the hysteresis loop analysis (described in Section 2.4.2) using Python coded programs (codes are listed in Appendix B.2) instead of using Equation 3.42, as the true stress imposed by controlled load increases with crack growth when cross-section area decreases. This phenomenon is amplified when necking occurs, when the specimen normally has big crack opening and large mean strain. Tests with positive mean stress or large stress amplitude are all in this case.

$$\epsilon_p = \triangle\epsilon - \epsilon_e = \triangle\epsilon - \frac{\triangle\sigma}{E} \tag{3.42}$$

A schematic illustration of hysteresis loop analysis is shown in Fig. 3.53. $\triangle\epsilon_p$ is measured by detecting length of AD. $\triangle W_p$ is calculated with the area of hysteresis loop (ABCDEF) via integral function in Equation 2.2.

The measured average value of $\triangle\epsilon_p$ and $\triangle W_p$ over cycles of selected tests are listed in Table 3.1. The exponent n is calculated according to Equation 3.41. For the condition of σ_m = 0 MPa, the tests with σ_a = 190, 210, and 221 MPa have similar hardening exponents, which agree with the experimental measuring results of 0.271 at 300°C reported by other peers [155]. The test with lower stress amplitude of 180 MPa has a larger hardening exponent, which may be attributed to the occurrence of different material hardening mechanism, such as occurrence of secondary cyclic hardening. Among the tests with different mean stresses, +10 MPa mean stress slightly enhanced the cyclic hardening (exponential parameter n slightly increases). +50 MPa leads to the most pronounce enhancement on cyclic hardening (increases parameter n the most). The calculated hardening exponent n is consistent with the experimental observation that mean stress enhances cyclic hardening, thus leading to smaller strain response given similar stress amplitude. This consequently contributes to longer fatigue life. The underlying mechanism of mean stress effect on cyclic hardening from microstructural side will be discussed in Section 3.7 and Section 4.6.

The correlation between the crack growth rates (with different mean stresses) and J-integral (given in Equation 3.40) is shown in Fig. 3.54 and Fig. 3.55. Compared with the correlation in Fig. 3.51 and Fig. 3.52, J-integral shows slightly better performance in correlating the crack

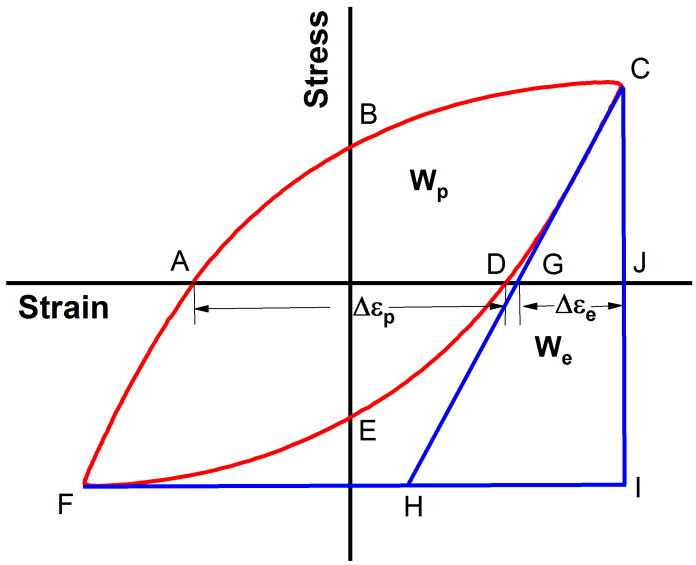

Figure 3.53 – Schematic of hysteresis loop analysis and corresponding mechanical parameters.

Table 3.1 – Calculated average strain amplitude $\overline{\epsilon_a}$, average plastic strain range $\overline{\Delta\epsilon_p}$, plastic strain energy density ΔW_p and cyclic hardening exponent n of seleted tests in 288°C BWR/HWC.

σ_a [MPa]	σ_m [MPa]	$\overline{\epsilon_a}$ [%]	$\overline{\Delta\epsilon_p}$ [MPa]	$\overline{\Delta W_p}$ [MJ/m^3]	n
180	0	0.23	0.24	0.63	0.34 *
190	0	0.37	0.47	1.39	0.29
210	0	0.43	0.60	2.00	0.26
221	0	0.68	0.98	3.44	0.25
210	+10	0.47	0.62	2.00	0.29 **
210	+50	0.26	0.20	0.61	0.40 **
210	-20	0.23	0.20	0.62	0.36 **

* Relatively higher hardening exponent compared with the cases of σ_a = 190, 210, and 221 MPa may be attributed to the dependence on stress amplitude, which may induce different hardening mechanism (e.g., secondary hardening). This was also observed for different crack growth laws in Fig. 3.49.

** Higher cyclic hardening exponent for the tests with mean stress. This implies mean stress enhances cyclic hardening.

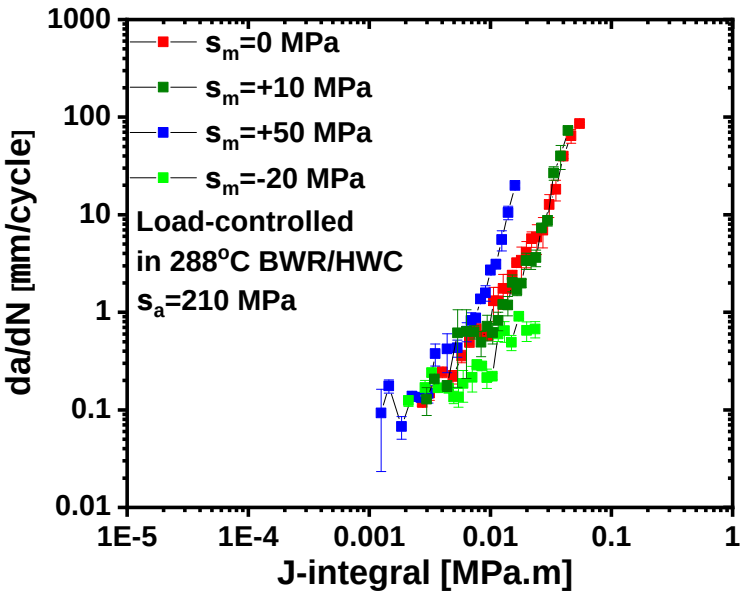

Figure 3.54 – Correlation between the crack growth rates of tests with different mean stresses and same stress amplitude of 210 MPa in 288°C BWR/HWC and the J-integral given in Equation 3.40.

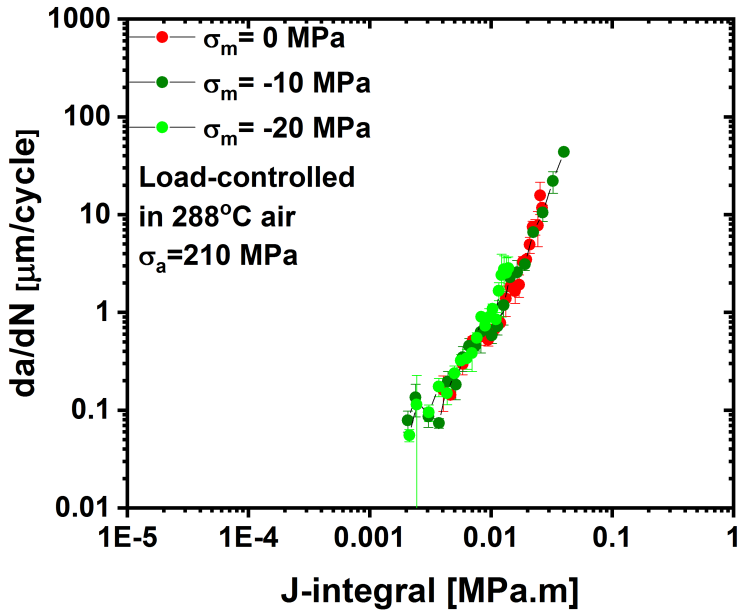

Figure 3.55 – Correlation between the crack growth rates of tests with different mean stresses (without +50 MPa, as strong ratcheting resulting in strain out of extensometer measure range) and same stress amplitude of 210 MPa in 288°C air and the J-integral given in Equation 3.40.

growth rates than $\triangle K_\epsilon$ does. However, there still has some insufficiency in correlating the last stage of crack for the test with +50 MPa mean stress. In this case, strong necking was observed, the local true strain may be much higher than our evaluated average strain or stabilized strain. Thus, the true J-integral of the last stage of crack is underestimated by our calculation with average plastic strain and energy values.

3.5.4 Mean stress effect on crack growth rate

As a combination of different influential factors (e.g., σ_a, σ_m, σ_{max}, ϵ_a, ϵ_m, environment, crack shape) influences fatigue life, it is difficult to convincingly separate their individual and synergistic influence on fatigue behavior. For this reason, in the following we focus on the effect of a single parameter on crack growth rather than on the effect of combination of several parameters. To unify the crack growth driving force, the stress intensity factor (K_I), strain intensity factor ($\triangle K_\epsilon$) and J-integral were applied to correlate the measured crack growth rates.

To evaluate mean stress effects, the stress amplitude and environment conditions were controlled being unchanged. A representative data of crack growth rates tested with same stress amplitude of σ_a = 210 MPa, but different mean stresses in BWR/HWC at 288°C and in air at 288°C, is plotted in Fig. 3.56 and Fig. 3.57 respectively. In BWR/HWC at 288°C, tests with mean stress (+50 MPa or -20 MPa) show lower crack growth rate than the tests without mean stress. Tests with +10 MPa mean stress and without mean stress did not show a large difference in crack growth rate. Tests in air at 288°C show similar effects of mean stress on crack growth rate, except for the test with -20 MPa mean stress shows higher crack growth rate. After looking for the initiation sites of the measured main cracks, the main cracks of the tests with σ_m = -20 MPa and 0 MPa in air at 288°C were found to have exceptionally originated from the outer surface. For the other tests, either in air or in water, the main cracks originated exclusively from the inner surface. Different crack originating sites and growing directions result in different crack shapes and stress/strain fields in front of the crack. Necking happens for the tests with positive mean stress (+10 and +50 MPa), thus in which mean stress condition the crack depth is much shorter than wall thickness.

The crack growth rates of tests with different mean stresses were correlated with the parameters of SIF (in Fig. 3.50 and Fig. 3.58), strain intensity factor (in Fig. 3.51 and Fig. 3.52)) and J-integral (in Fig. 3.54 and Fig. 3.55) as well. Calculation of K_I considered mean stress through σ_0 in the Equation 3.24. However, the mean stress effect on crack growth rate remains clearly visible in the correlation with K_I in Fig. 3.50 and Fig. 3.58. Thus mean stress does not have only an impact on crack growth via the maximum stress but also through the corresponding mean strain and strain amplitude (via impact on strain hardening) it generates. In correlation with $\triangle K_\epsilon$ and J-integral, the effect of mean stress on crack growth rate disappears or is much weaker. This is consistent with our deduction.

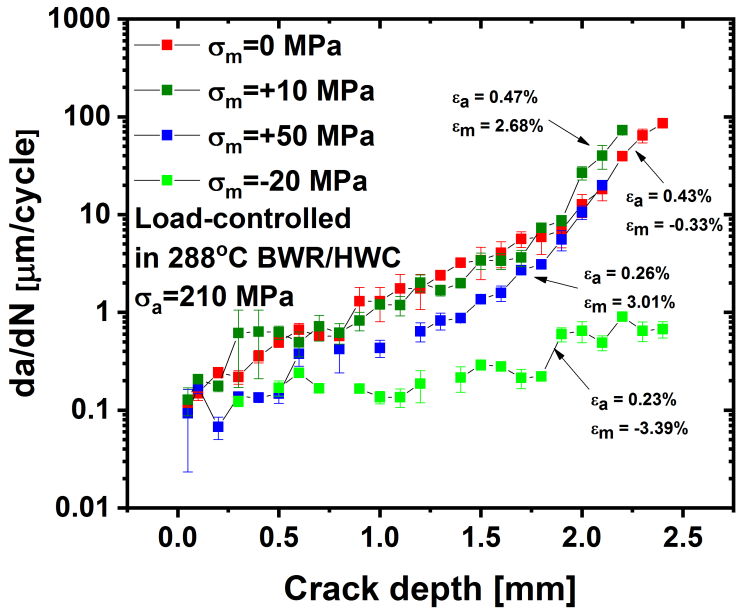

Figure 3.56 – Measured striation spacing along the main crack depth of specimens tested with σ_a = 210 MPa and different mean stresses (0, +10, +50, -20 MPa) in BWR/HWC at 288°C.

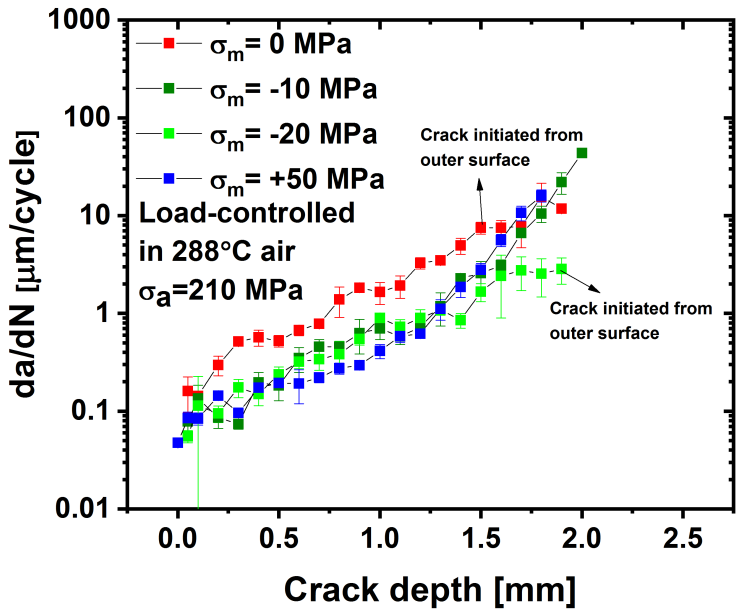

Figure 3.57 – Measured striation spacing along the main crack depth of specimens tested with σ_a = 210 MPa and different mean stresses (0, +10, +50, -20 MPa) in air at 288°C.

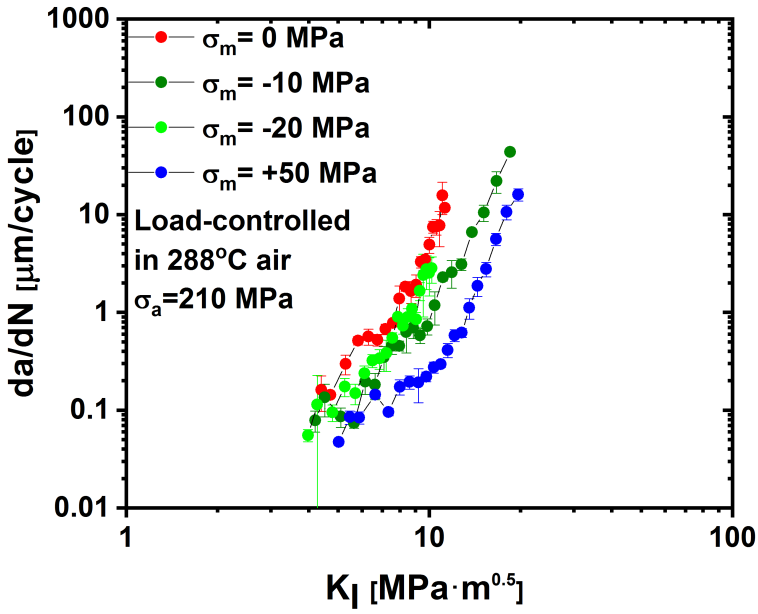

Figure 3.58 – Correlation between crack growth rates and K_I (given in Equation 3.27 of tests with σ_A = 210 MPa under different mean stresses (0, +10, +50, -20 MPa) in air at 288°C.

3.5.5 Environmental effect on crack growth rate

Based on the discussion in previous subsections, J-integral appears to be the best parameter to represent the mechanical driving force for crack growth under conditions with different σ_a, σ_m, and $\triangle\epsilon$.

The environmental effects were firstly investigated without mean stress. The correlations between crack growth rates and J-integral of tests without mean stress in both environments are plotted in Fig. 3.59. In this figure, no significant effect of environment on crack growth rate is observed.

Synergistic effects of environment and mean stress were observed in tested fatigue lives, especially in HCF region ($N_f \geq 10^5$ cycles), where BWR/HWC environment has different effects on fatigue life for different mean stress condition. In addition, slower crack growth rates were observed for tests in HTW, when compared with growth rates in HTA, as Fig. 3.60 shows. This phenomenon is systematically observed for other stress amplitude condition (such as 220 MPa) with -20 MPa mean stress. This is not in line with the common understanding, that aggressive environments accelerate crack growth rate. This may not apply for the condition with compressive asymmetrical loading and massive oxides formation in HTW, when the crack closure effect is active.

Crack growth rates of tests with +50 MPa mean stress in both environments are plotted in Fig.

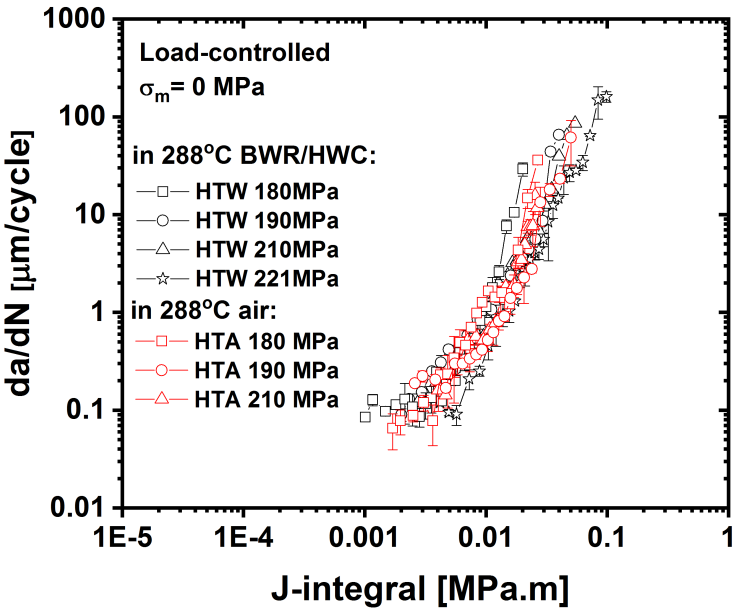

Figure 3.59 – crack growth rate versus J-integral of tests with σ_m = 0 MPa in both environments.

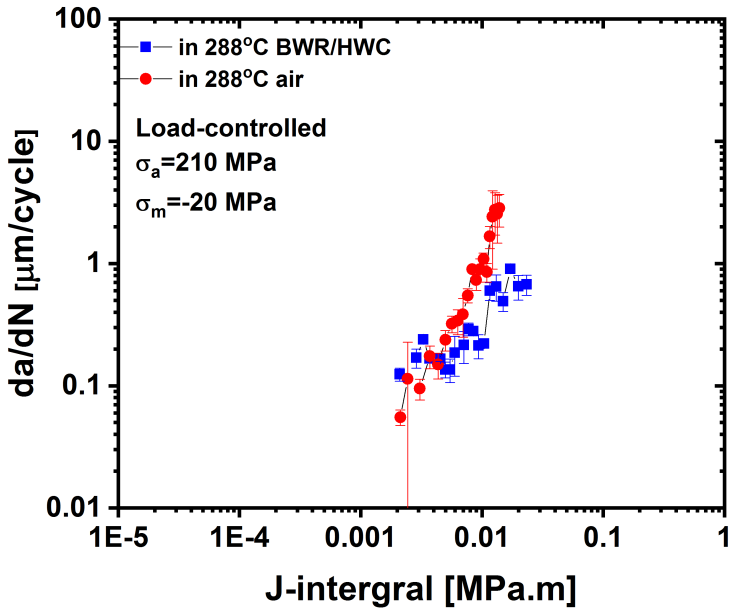

Figure 3.60 – Comparison of crack growth rate in BWR/HWC and air environment with σ_a = 210 MPa and σ_m = -20 MPa.

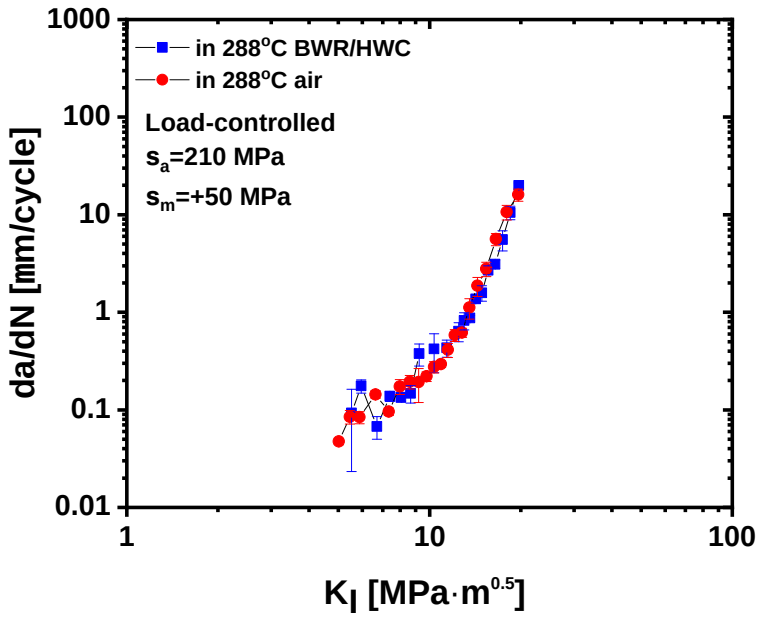

Figure 3.61 – crack growth rate versus stress intensity factor of tests with σ_a = 210 MPa, σ_m = +50 MPa in both environments.

3.61, in which only the correlations with K_I are presented, due to an incomplete recording of the strain signal, which exceeded the measure range of the extensometer. Thus we compare the growth rates of tests with same stress amplitude (σ_a = 210 MPa in Fig. 3.61). We assume that the cracks undergo similar mechanical loading. In Fig. 3.61, tests in both environments show no significant difference in growth rates.

3.5.6 Specimen wall thickness effect on crack growth rate

In section 3.1.5, different fatigue lives were observed for specimens with different wall thicknesses for tests in BWC/HWC at 288°C. The reason is likely to result from different stress triaxiality levels depending on the wall thickness and on the internal pressure. How wall thickness will affect crack growth and crack initiation? Fig. 3.62 highlights the wall thickness effects on crack growth rate and on the crack growth life and physical crack initiation life (cycles for 0.05 mm depth crack formation). A slight difference was observed between the specimens with different wall thicknesses in Fig. 3.62a. However, the difference disappears if the crack growth rate is plotted against the strain intensity factor in Fig. 3.62b, where the mechanical driving factors (such as stress, strain) are unified by $\triangle K_\epsilon$. From Fig. 3.62c, it is concluded that the wall thickness has a bigger effect on crack initiation life than on crack growth life. Different stress triaxility levels at the specimen inner surface result in distinct von Mises stress and damage to materials, which determines the number of cycles needed to initiate a crack. However, crack growth is more dependent on the local stress/strain.

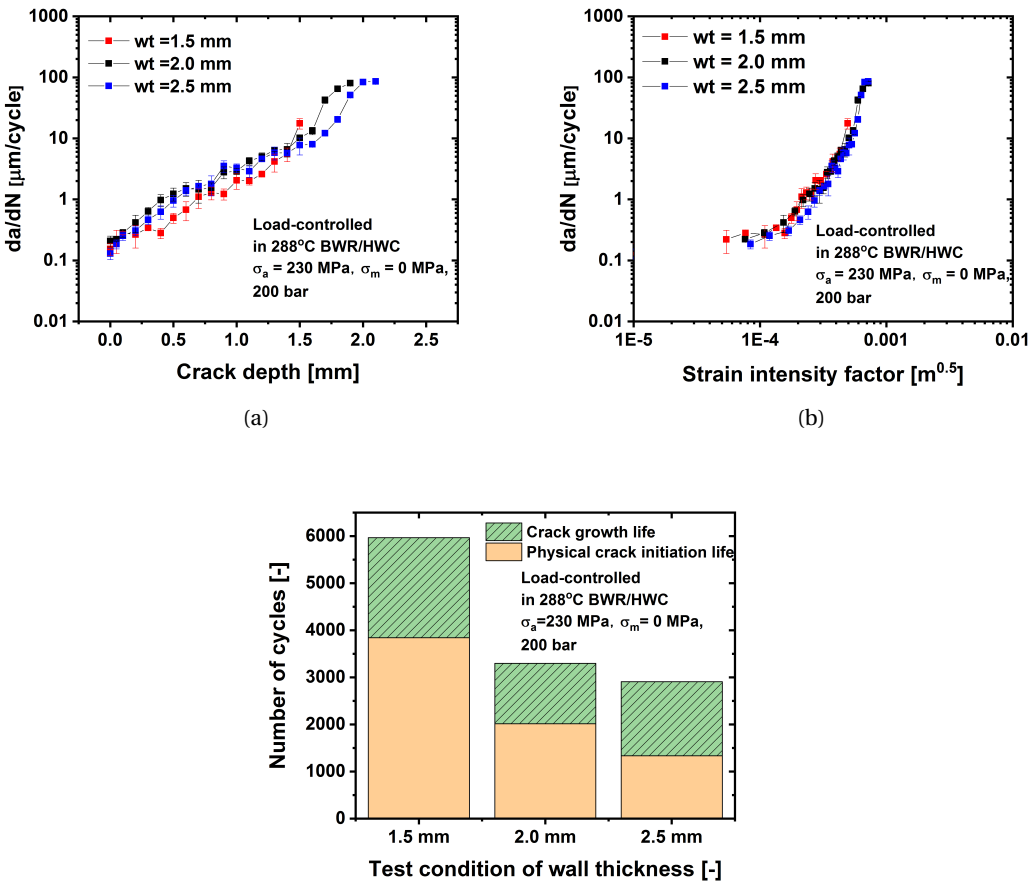

Figure 3.62 – Specimen wall thickness effect on crack growth for tests with σ_a = 230 MPa, σ_m = 0 MPa, (a) da/dN vs. crack depth, (b) da/dN vs. strain intensity factor, (c) measured crack initiation life and crack growth life for different specimen wall thicknesses.

3.5.7 Strain rate effect on crack growth rate

Decreasing strain rate accelerates crack growth in LWR environments. When the crack growth period dominates the whole fatigue life, the reduction of fatigue life mainly originates from the acceleration of crack growth induced by slower strain rate [158]. In our study, strain rate effects on fatigue life (as Fig. 3.24 shows) and on crack growth were investigated with and without mean stress to determine whether the crack propagation period or the crack initiation period dominates.

Fig. 3.63 and Fig. 3.64 present the observation of strain rate effects on crack growth rate and on crack growth life/physical crack initiation life, under the conditions with σ_m = 0 MPa and σ_m = +50 MPa respectively. In Fig. 3.63b and Fig. 3.64b, the short crack effect was not corrected. For the conditions without mean stress, no significant difference, in the correlations between

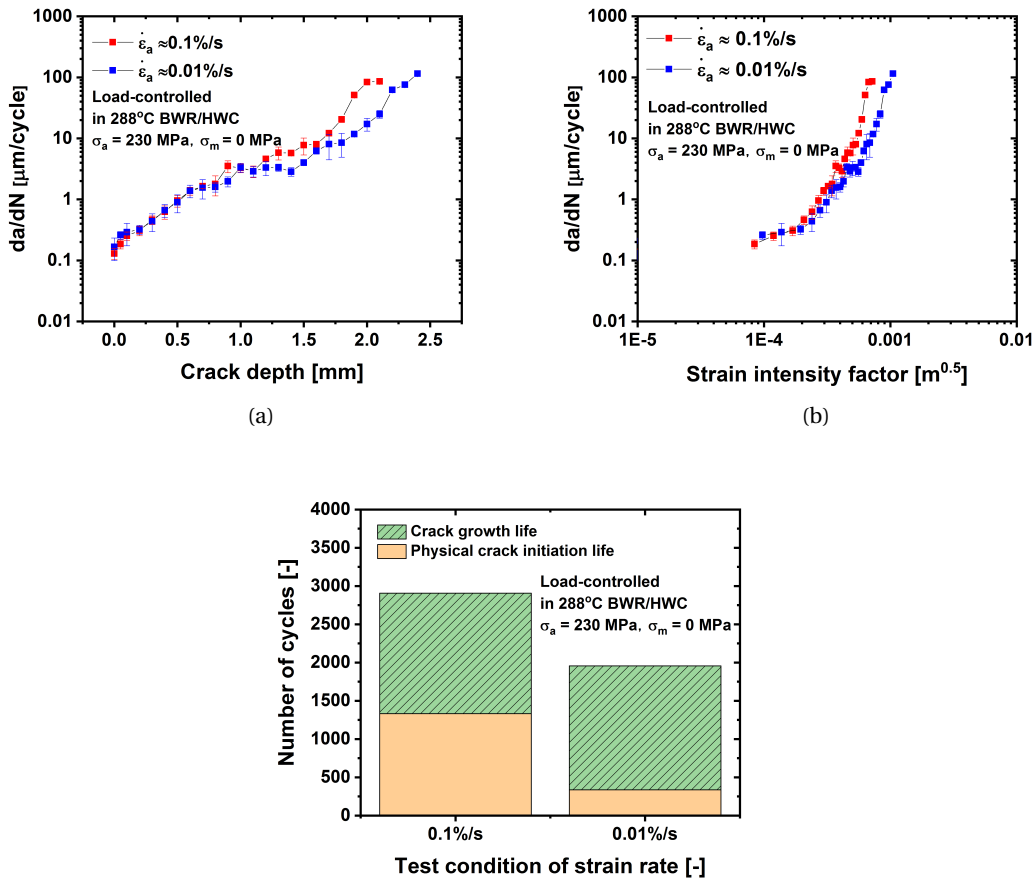

Figure 3.63 – Strain rate effect on crack growth for tests with σ_a = 230 MPa, σ_m = 0 MPa, (a) da/dN versus crack depth, (b) da/dN versus strain intensity factor, (c) measured physical crack initiation life and crack growth life at different strain rate conditions.

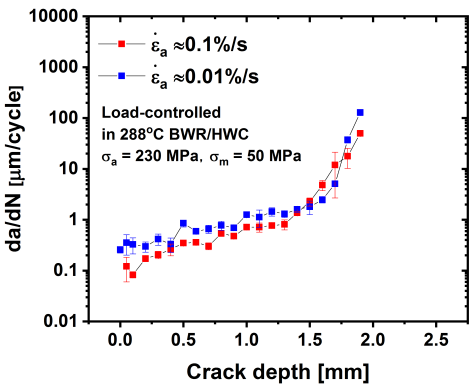

(a)

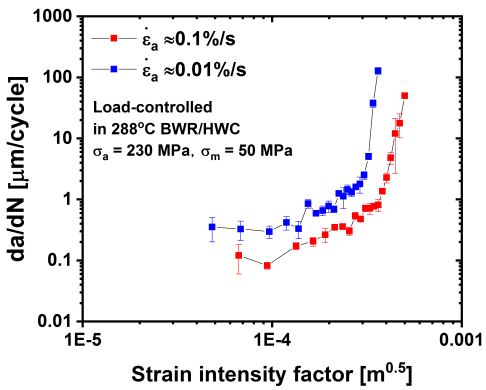

(b)

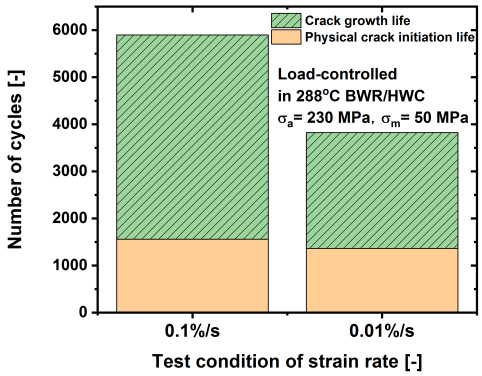

(c)

Figure 3.64 – Investigation of strain rate effect on crack growth for tests with σ_a = 230 MPa, σ_m = +50 MPa, (a) da/dN versus crack depth, (b) da/dN versus strain intensity factor, (c) measured physical crack initiation life and crack growth life at different strain rate conditions.

crack growth rate and crack depth/strain intensity factor, was observed between the tests with different strain rates (higher one: $\dot{\epsilon} \approx 0.1\%/s$ and lower one: $\dot{\epsilon} \approx 0.01\%/s$) in Fig. 3.63a and Fig. 3.63b. This is reflected by similar number of cycles of the crack growth period for the two tests in Fig. 3.63c. However, the test with lower strain rate has much shorter initiation life. This might be cause by the higher strain amplitude in the tests with lower strain rate as observed in Fig. 3.25. For the condition with +50 MPa mean stress, lower strain rate leads to faster crack growth rate, given the same crack depth or same strain intensity factor. In the correlation with strain intensity factor, the strain rate effects on the mechanical side should be already considered in the parameter of $\triangle K_\epsilon$. Thus judging from Fig. 3.64b, the acceleration of crack growth mainly originates from the enhanced environmental degradation imposed by lower strain rate. In Fig. 3.64b, the test with slower strain rate has similar physical crack initiation life but shorter crack growth life compared with the test with standard loading rate (of ≈ 0.1%/s). The crack growth period dominates and crack initiates early for the tests with +50 MPa mean stress (in Fig. 3.64).

Besides above mentioned factors, such as mean stress, environment, specimen geometry (WT), strain rate, the effects of stress amplitude, strain amplitude (under strain control) and control mode on crack growth were also investigated, but they are not be presented in detail here. Briefly. we mention that higher stress/strain amplitude leads to faster crack growth, at similar mean stress and environment, when correlated with crack depth. However, the effects of stress/strain amplitude on crack growth disappear when correlating with J-integral, which is recognized as a more effective parameter to represent the mechanical driving factors. As far as the control mode is concerned, no significant effects on crack growth was observed.

3.6 Physical crack initiation life and crack growth life

With the measured fatigue lives and crack growth data, the physical crack initiation life, defined as the number of cycles to create a crack with a depth a = 0.05 mm, and crack growth life were calculated with the following equations:

$$N_{cg} = \sum_{k=1}^{n} \rho_k \triangle a_k \tag{3.43}$$

$$N_{ci} = N_f - N_{cg} \tag{3.44}$$

where n is the total number of striation measuring segments/steps. k is the subscript for the kth segment. $\triangle a_k$ is the crack length in the kth segment. ρ_k is the average striation number density ($\frac{N_k}{\triangle a_k}$).

In both environments, the mean stresses (+50, -20 MPa) increase the physical crack initiation life and crack growth life in the tests with σ_a = 210 MPa and σ_a = 190 MPa in Fig. 3.65 and Fig. 3.66 respectively. -20 MPa mean stress has obviously the most important effect in

delaying the formation of physical crack. Our results show that BWR/HWC environment shortens both crack initiation life and crack growth life, at least for the tests with 0 or +50 MPa mean stress. Since the ratio of crack initiation life over growth life is smaller in BWR/HWC at 288°C environment than in air at 288°C, the HTW environmental effect on crack initiation contributes more to the decrease of total fatigue life than the effect on crack growth. We emphasize again that main cracks on the specimens tested with σ_a = 210 MPa and σ_m = 0 or -20 MPa in air initiated from the specimen outer surface. This is likely to reduce the crack growth life, owing to larger values of K_I and $\triangle K_\epsilon$ at a given stress/strain amplitude.

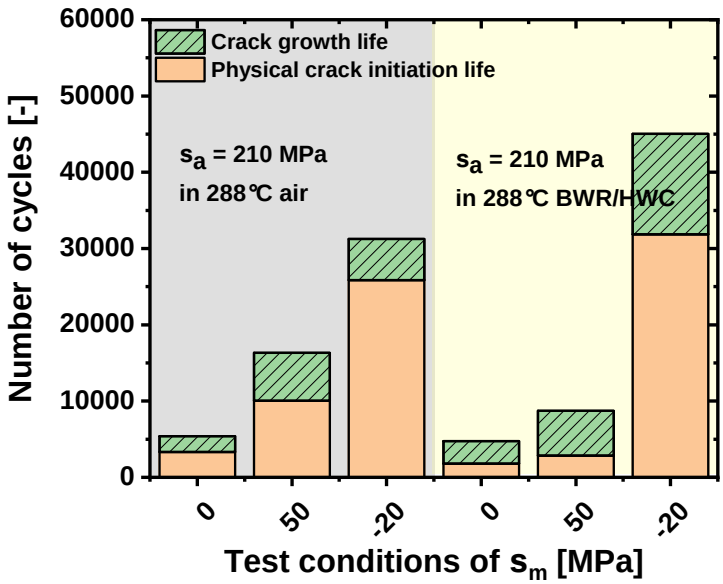

Figure 3.65 – Physical crack initiation life and crack growth life with σ_a = 210 MPa and different mean stresses in both environments.

Acceleration of crack growth in BWR/HWC can be quantified based on da/dN versus $\triangle K_\epsilon$ correlation. The corresponding mechanisms were thoroughly discussed in the former research works [4][5][142][159]. However, the reason for reduction of initiation period remains unclear. The LWR environmental effects on different possible mechanisms (e.g., initiation sites at intrusions of persistent slip bands [23][26][160], grain boundary decoherence [70][161], surface scratch grooves, inclusions) are still open issues.

In Fig. 3.67, the number of cycles for physical crack initiation and crack growth were compared between tests with different stress amplitudes for identical mean stress and environment conditions in each plot. The column diagrams show that the specimens loaded with smaller stress amplitudes have larger fatigue life. At first glance, the life difference comes mainly from physical crack initiation. Stress amplitude has much less influence on crack growth life than on physical crack initiation life.

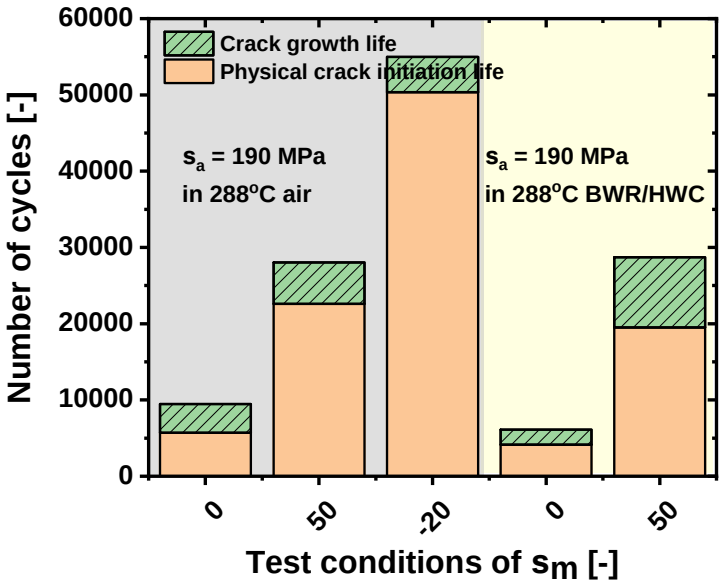

Figure 3.66 – Physical crack initiation life and crack growth life with σ_a = 190 MPa and different mean stresses in both environments.

The data of crack initiation life and crack growth life depicted in Fig. 3.67 are plotted in the form of stress-life in Fig. 3.68, where the lives of crack initiation and crack growth show both a dependence on stress amplitude and mean stress. Higher stress amplitude leads to shorter life. +50 MPa and -20 MPa mean stresses increase both lives. This is well consistent with the observation of total fatigue life in Fig. 3.9. In Fig. 3.68b, the red and blue lines intersect each other around 180 MPa. Similar phenomenon was observed in Fig. 3.9 but is absent in Fig. 3.68a. This implies synergistic effect of mean stress and HTW mainly occurs during the crack growth period. Looking at 3.68a and 3.68b, it is clear that stress amplitude and mean stress influences are more pronounced on initiation life than on growth life. In other words, the fatigue life difference mainly originates from the change in crack initiation life.

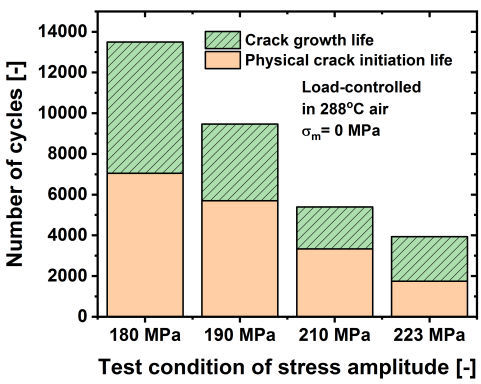

(a) σ_m = 0 MPa in HTA

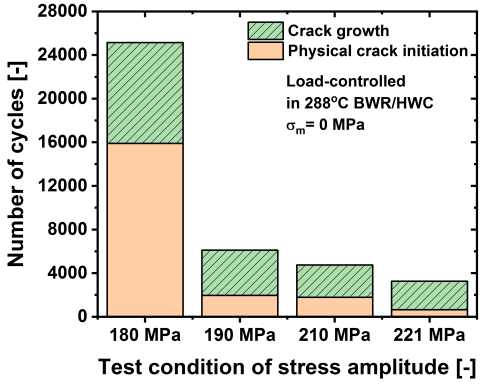

(b) σ_m = 0 MPa in HTW

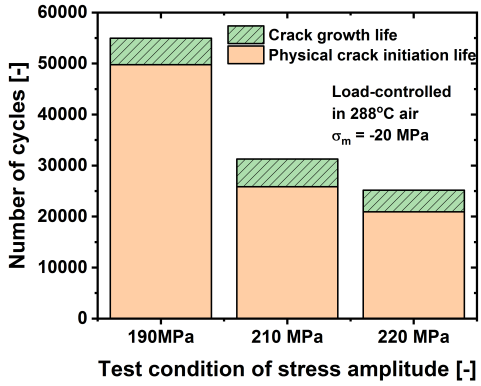

(c) σ_m = -20 MPa in HTA

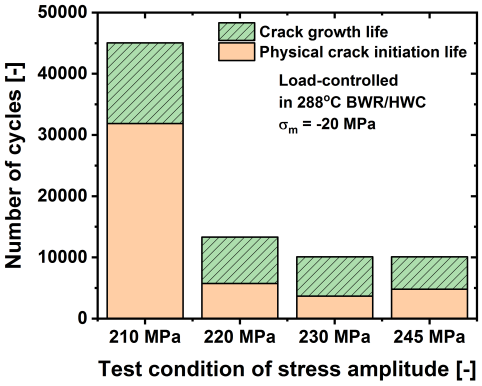

(d) σ_m = -20 MPa in HTW

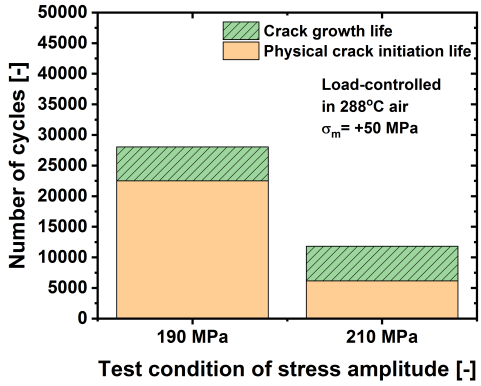

(e) σ_m = +50 MPa in HTA

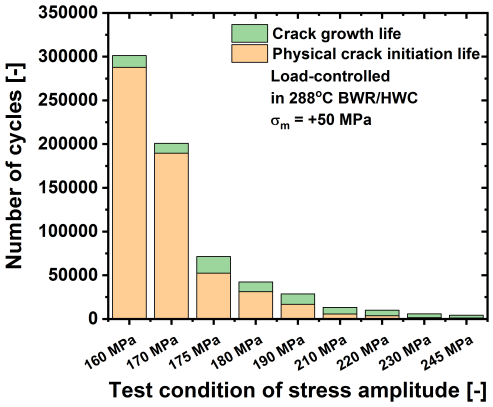

(f) σ_m = +50 MPa in HTW

Figure 3.67 – Physical crack initiation life and crack growth life of tests with (a) σ_m = 0 MPa in HTA, (b) σ_m = 0 MPa in HTW, (c) σ_m = -20 MPa in HTA, (d) σ_m = -20 MPa in HTW, (e) σ_m = +50 MPa in HTA and (f) σ_m = +50 MPa in HTW.

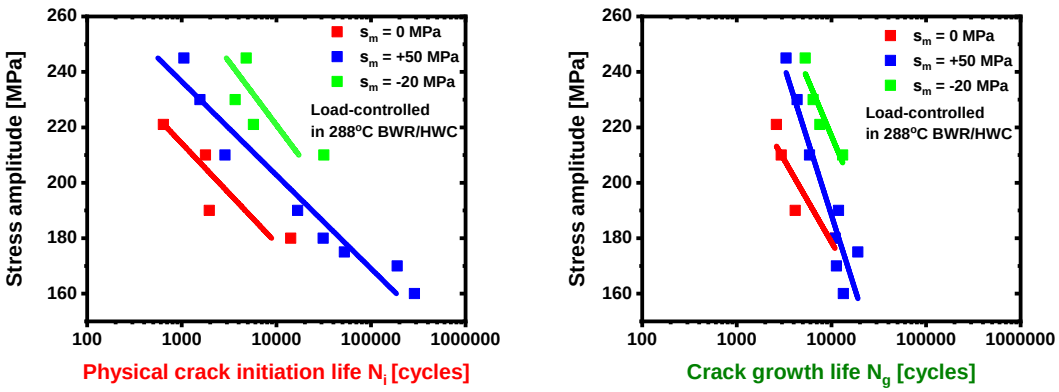

(a) (b)

Figure 3.68 – Measured crack initiation life & crack growth life of tests in HTW in the form of (a) stress versus crack initiation life, (b) stress versus crack growth life.

3.7 Microstructures characterization

3.7.1 Microstructures at end of life

We just recall that the as-received material was characterized with EBSD in Fig. 2.1, which shows that the solution annealed material has randomly oriented grains and high share of twin boundaries. Typical microstructures of a tested specimen are presented in Fig. 3.69, which shows significantly heterogeneity intra and inter grains. As discussed in Section 1.5, the dislocation structures developed during cyclic loading depend on grain orientation, resolved stress/strain, stacking fault energy, loading cycles, temperature and distance to grain boundaries, which act as obstacles to dislocation movement (local stress/strain riser) but also as source of dislocation generation. In the region highlighted with the red square in Fig. 3.69d (magnified in Fig. 3.69a), persistent slip bands (PSBs) were generated. In the blue square area in Fig. 3.69d (magnified in Fig. 3.69b and Fig. 3.69c), massive dislocation cells were formed around the triple junctions and along GBs. A large mount of dislocations were impeded at the GBs and high stress/strain was raised. This leads to dislocation cells formation. The inverse pole figure (IPF) in Fig. 3.69e qualitatively illustrates the strain magnitude of the blue square area (Fig. 3.69b). Observation in Fig. 3.69 confirms that the polycrystalline material deforms inhomogeneously in micro-scale and that the types of developed microstructures depend on observed locations. Characterizing the microstructures of deformed material is the key method to understand the deformation mechanism. However, the local microstructures observed in TEM do not necessarily yield a complete view and understanding of the overall deformation mechanisms occurring on a more global length scale [97]. Thus, we applied ECCI (large field of view, lower resolution, worse contrast) as a complementary tool of TEM (small field of view, high resolution and better contrast).

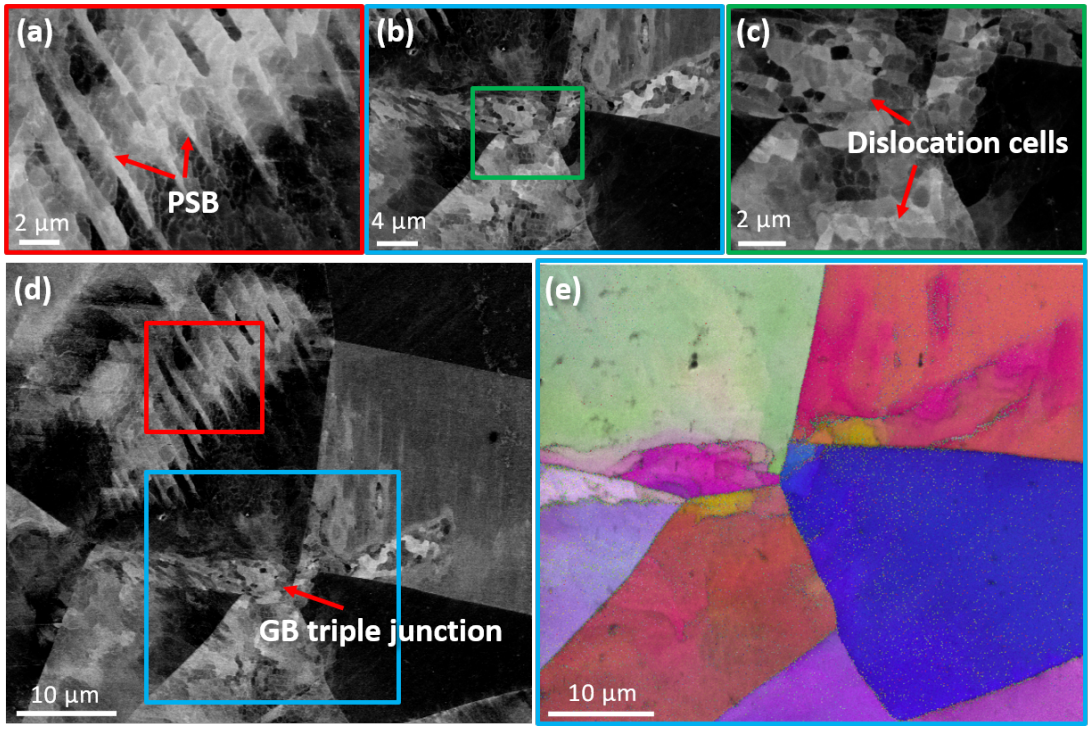

Figure 3.69 – Microstructures of a specimen tested with σ_a = 210 MPa, σ_m = 0 MPa under load control in HTW. The test results in $\overline{\epsilon_a}$ = 0.425% and $\overline{\epsilon_m}$ = -0.33%. (d) ECCI image and microstructures of PSB within grain are showed in (a), dislocation cells at GB triple junction are showed in (b) and (c) in detail. (e) is the IPF + IQ image at the GB triple junction.

The as-received material was delivered after solution annealing treatment. Low dislocation density was observed in TEM (see Fig. 3.70b). Only several dislocation pile-ups close to the grain boundaries (GB) (Fig. 3.70a) were observed. Fig. 3.70 also shows the observations of microstructures at the end of life of specimens tested with different mean stresses (0, +10, +50, -20 MPa) but with the same stress amplitude (210 MPa) in BWR/HWC at 288°C. As already mentioned, the tests with different mean stresses result in different strain amplitudes and mean strains.

For the specimen tested without mean stress, large dislocation densities were observed as shown in Fig. 3.70d and Fig. 3.70e, where most dislocations slipped on the primary slip plan $\{\bar{1}11\}$. At several locations, dislocations lock each other in the form of sessile junctions or dislocation tangles. In the ECCI image (Fig. 3.70f), dislocation walls and channel structures were also observed at locations close to GBs in several grains. In Fig. 3.69, even spatial structures like dislocation cells, which requires higher plastic strain to form, were developed at the GB triple junction area. For the test with σ_m = +10 MPa, dislocation cells were observed close to GBs (Fig. 3.70g), where stacking faults (in the $(00\bar{2})$ trace) were observed as well (in Fig. 3.70h). In ECCI observation (in Fig. 3.70i), PSBs and dislocation channel and walls were found close to the GBs. However, in most grains the dislocation structures are planar as observed by

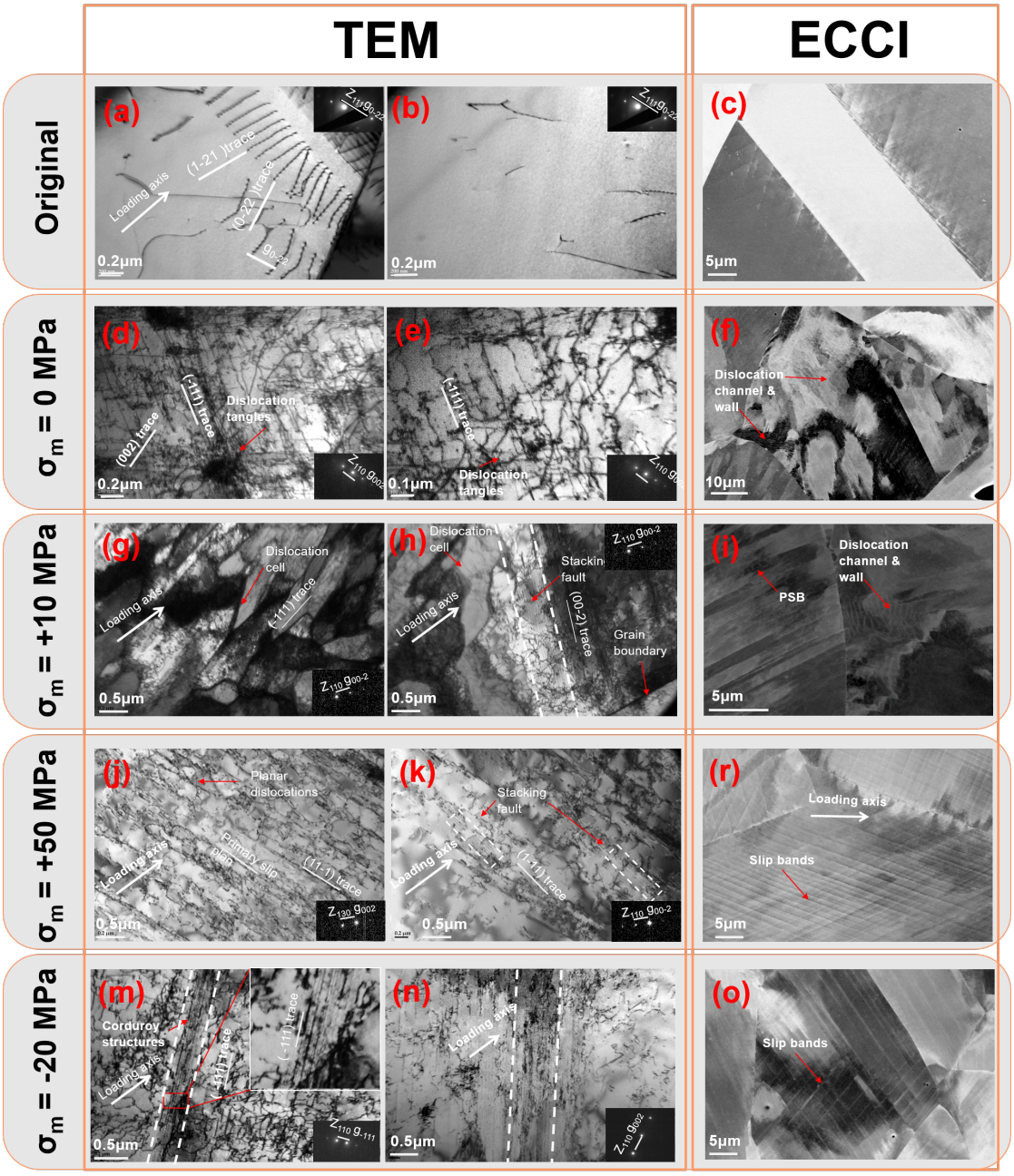

Figure 3.70 – Microstructures of (a-c) original material and deformed materials under load control in BWR/HWC at 288°C with σ_a = 210 MPa, (d-f) σ_m = 0 MPa (test results in $\overline{\epsilon_a}$ = 0.43% and $\overline{\epsilon_m}$ = -0.33%, N_f = 4741 cycles), (g-i) σ_m = +10 MPa (the test results in $\overline{\epsilon_a}$ = 0.47%, $\overline{\epsilon_m}$ = 2.68% and N_f = 4053 cycles), (j-r) σ_m = +50 MPa (the test results in $\overline{\epsilon_a}$ = 0.26%, $\overline{\epsilon_m}$ = 3.01% and N_f = 8735 cycles) and (m-o) σ_m = -20 MPa (the test results in $\overline{\epsilon_a}$ = 0.26%, $\overline{\epsilon_m}$ = -0.96% and N_f = 45047 cycles).

ECCI. For the test with σ_m = +50 MPa, which results in the smallest $\overline{\epsilon_a}$ among the investigated tests in Fig. 3.70, only planar dislocations in the primary slip $\{\bar{1}11\}$ plans were observed (in Fig. 3.70j and Fig. 3.70k). The ECCI results (in Fig. 3.70r) also confirmed that. A small number of stacking faults were observed as well. For the test with σ_m = -20 MPa, which results in the same $\overline{\epsilon_a}$ as that of test with σ_m = +50 MPa but with a much longer fatigue life, only planar dislocation structures in primary slip planes were activated [97]. Furthermore, structures, which are of the order of ≈ 15 nm line spacing, aligning in {111}<112> were evidenced. The corduroy contrast is visible when observed with $g_{\bar{1}11}$ and is invisible when g_{002} is activated. Corduroy structures were assumed to originate from point defect coalescence or superjogs and multiple slip activity [114].

3.7.2 Microstructures at interrupted cycles

In order to gain insight into the dislocation structure evolution during the fatigue life, a series of interrupted tests at 10, 100, 1000, 10000 cycles were performed and their microstructures were investigated.

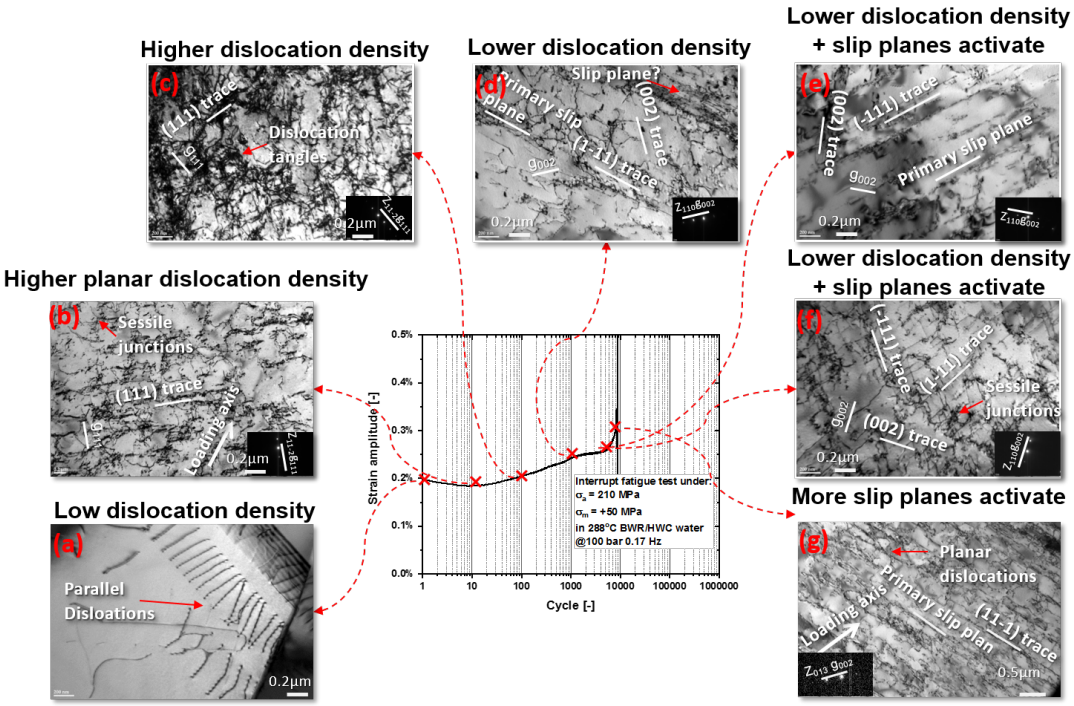

Figure 3.71 – TEM observations of microstructures of specimens tested to (a) 0 cycle, (b) 10 cycles, (c) 100 cycles, (d) 1000 cycles, (e-f) 5000 cycles and (g) 8735 cycles at the end of life under the condition of σ_a = 210 MPa, σ_m = +50 MPa, load control in BWR/HWC at 288°C.

Fig. 3.71 presents the microstructures of specimens loaded to the predefined cycles with σ_a = 210 MPa and σ_m = +50 MPa under load control. The middle plot illustrates the strain

amplitude evolution with loading cycles. In the first 10 cycles, the strain amplitude decreases as the material hardens and the planar dislocation density increases with accumulation of dislocation interactions in the form of sessile junctions (in Fig. 3.71b). At 100 cycles, numerous dislocation tangles were formed. This is accompanied with a softening stage (strain amplitude increases), but the dislocation density remains high and the dislocations are randomly and homogeneously arranged. Up to 1000 cycles at the end of the softening stage, the dislocation density was observed to decrease with indications of activation of primary slip plan. Beyond 1000 cycles, the strain amplitude comes to a plateau, which means that the hardening mechanisms counteract and balance the softening mechanisms. The microstructures show lower dislocation density and multiple primary slip planes activated. At the end of life, the dislocations remain in planar configuration and more slip planes are activated. However, in the last stage of life the steep increase of the strain amplitude mainly originates from the deformation around the main crack. Thus, in the last several cycles, the measured strain of the whole specimen should not be correlated with the microstructure of the massive material.

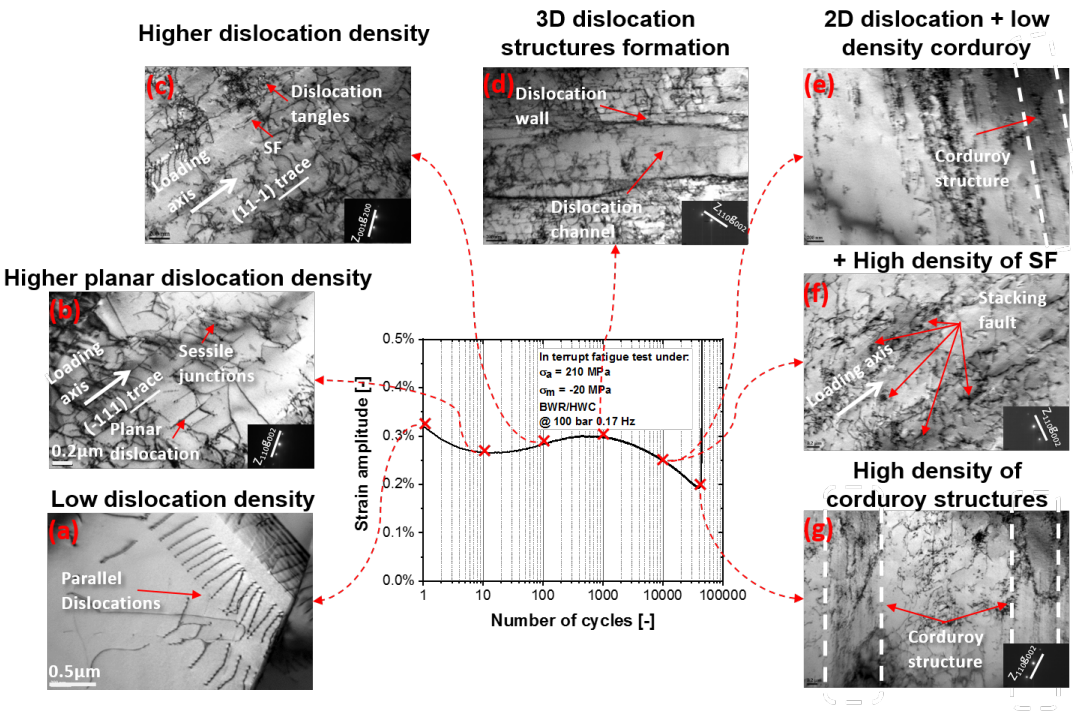

Figure 3.72 – TEM observations of specimens tested to (a) 0 cycle, (b) 10 cycles, (c) 100 cycles, (d) 1000 cycles, (e-f) 10000 cyles and (g) 45047 cycles at the end of life under the condition of σ_a = 210 MPa, σ_m = -20 MPa, load control in BWR/HWC at 288°C.

Fig. 3.72 depicts the microstructures after 10, 100, 1000 and 10000 cycles with σ_a = 210 MPa and σ_m = -20 MPa under load control. Accordingly, the strain evolution with the loading cycles is presented as the plot at the middle. Similarly to the observations with σ_m = +50 MPa (in Fig. 3.71), the material undergoes first hardening at the beginning cycles and achieves the

peak at 10 cycles, where we observed an increased dislocation density in planar configuration with dislocations interacting each other in the form of sessile junctions (in Fig. 3.72b). After 10 cycles, the material softening starts until 1000 cycles, where the material has the largest strain response. At the middle of the softening stage of 100 cycles (in Fig. 3.72c), even denser dislocations were developed, compared with the state at 10 cycles, but most in the form of dislocation tangles. A small number of stacking faults were also formed. At 1000 cycles of the most soften point, as observed in Fig. 3.72d, dislocation walls and channel structures were formed, which act as path for the moving dislocations and result in material softening. Then secondary hardening stage takes over without occurrence of a plateau stage. Appearance of corduroy structure (in Fig. 3.72e and Fig. 3.72g) in the secondary hardening stage confirms that corduroy structures may responsible for the active secondary hardening. With further loading, the material was harder and more corduroy structures were observed. Massive stacking faults were also observed as an example in Fig. 3.72f. Corduroy structures are reported as strong obstacle to dislocation motion. Alike structure was observed as well in our specimens at the end of life in Fig. 3.73.

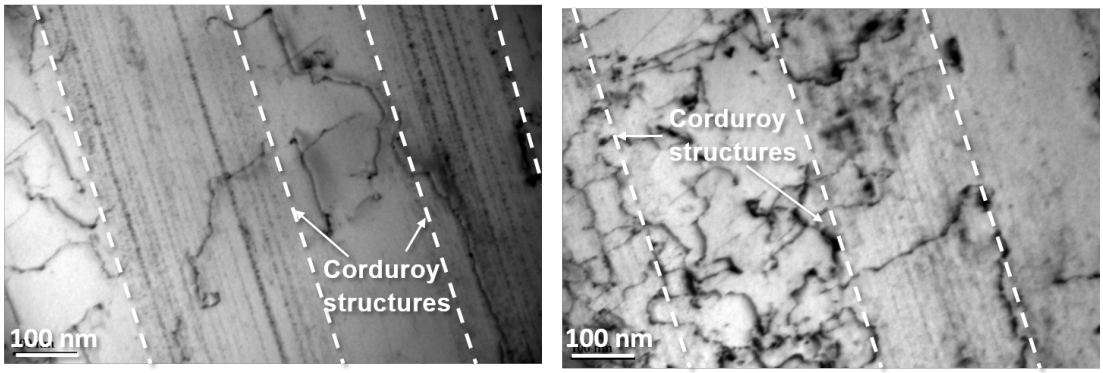

(a) (b)

Figure 3.73 – TEM observation of microstructures (dislocations and corduroy structures) of post-test material (at end of life) with σ_a = 245 MPa and σ_m = -20 MPa under load control in BWR/HWC at 288°C.

3.7.3 Microstructures around the cracks

In the microstructurally short crack region (stage I/mode II), which is shorter than 50 μm and within one grain, cracks normally propagate ≈ 45° to loading direction following crystallographic planes. Afterwards, in mechanically short crack and long crack regions, cracks propagate transgranularly and perpendicularly to the loading direction. It is commonly recognized that massive plasticity will be built up in front of crack tip. The footprints of plasticity, in form of microstructures with high dislocation density, are left behind the crack propagation. In Fig. 3.74, the microstructures along cracks were characterized with ECCI. A large mount of dislocation cells (around 400 nm in diameter) were developed along the cracks. The dislocation cells were formed in highly localized plasticity. When analyzed with EBSD, the strain

magnitude can be roughly estimated by detecting the misorientation. The wall of dislocation cells, which consists of dense dislocations structure, can be recognized as low angle boundary.

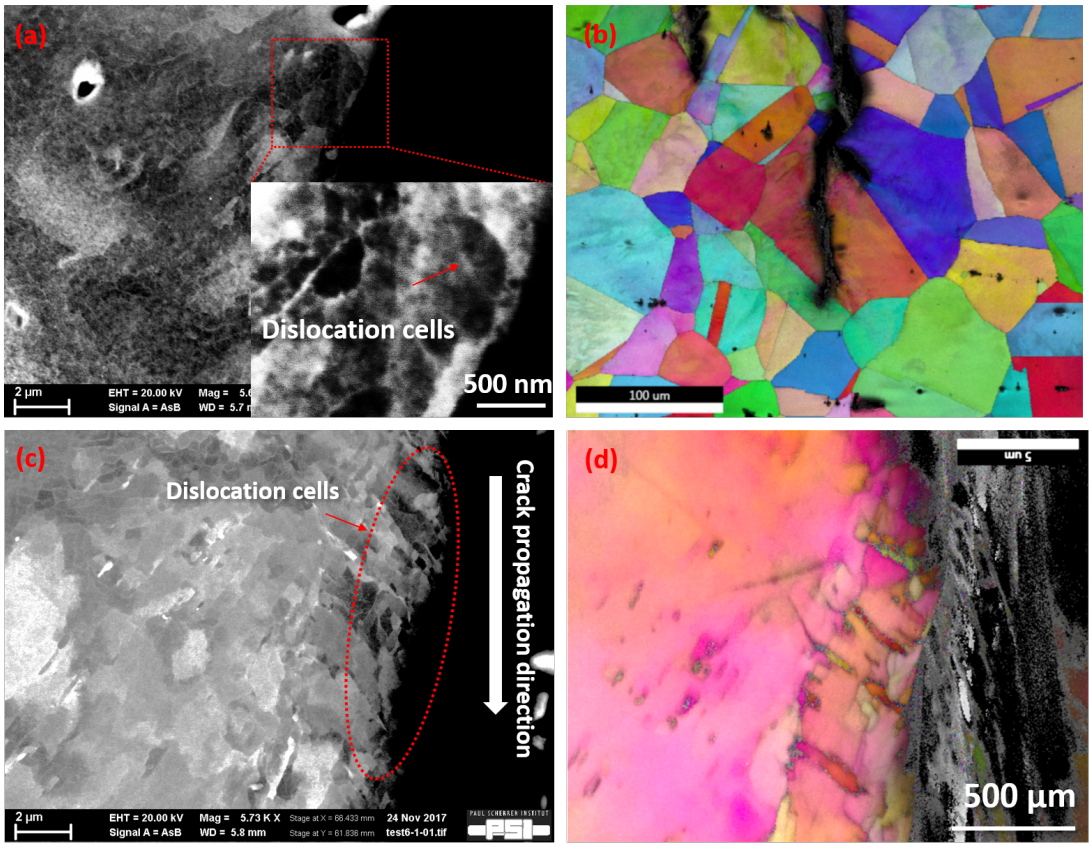

Figure 3.74 – (a) and (c) ECCI images of microstructures along cracks, (b) and (d) EBSD images of area around cracks. The specimen was tested with σ_a = 210 MPa, σ_m = 0 MPa in BWR/HWC at 288°C.

3.8 Fatigue life correlation and prediction

3.8.1 Modified Smith-Watson-Topper method

As mentioned above, both positive (+50 MPa) and negative (-20 MPa) mean stresses increase fatigue life, regardless the environment (HTW or HTA). This behavior is not consistent with the conventional mean stress correction models, such as Morrow, Geber, Goodmann and Sonderberg models, which all predict a decrease of fatigue life with increasing tensile mean stress. However, the approach proposed by Smith, Watson and Topper (SWT), which is based on a stress-strain function (Equation 3.45) composed of the maximum stress (σ_{max}), the strain amplitude (ϵ_a) and the elastic modulus (E), was proven to well predict the fatigue lives of

austenitic steels with mean stress [124].

$$SWT = \sqrt{\sigma_{max}\epsilon_a E} = f(N_f) \tag{3.45}$$

where the σ_{max} is the value at middle-life for strain-controlled tests.

Considering our load-controlled tests, we slightly modified the Equation 3.45 by replacing ϵ_a and σ_{max} with their average values over the cycles $\overline{\epsilon_a}$ and $\overline{\sigma_{max}}$. In load-controlled tests, ϵ_a varies and σ_{max} is constant, however, in strain-controlled tests, vice versa. Thus Equation 3.46 can be applied to tests performed under both control modes.

$$SWT_{mod} = \sqrt{\overline{\sigma_{max}}\,\overline{\epsilon_a} E} = f(N_f) \tag{3.46}$$

In Fig. 3.75 and Fig. 3.76, the SWT_{mod} parameter predicts well the fatigue lives with Equation 3.47 and Equation 3.48, derived with the data in air and BWR/HWC at 288°C respectively. The test results fall well around the fitting curves (predicted fatigue lives).

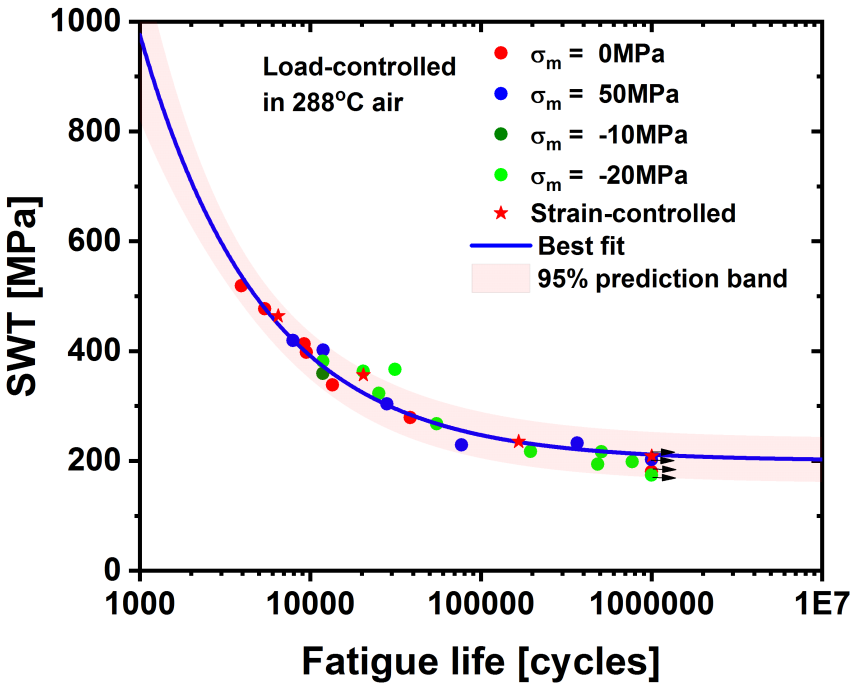

Figure 3.75 – Modified SWT parameter versus fatigue life in air at 288°C.

$$288^\circ C\ air: \quad \sqrt{\overline{\sigma_{max}}\,\overline{\epsilon_a} E} = 75524(N_f)^{-0.65} + 200 \tag{3.47}$$

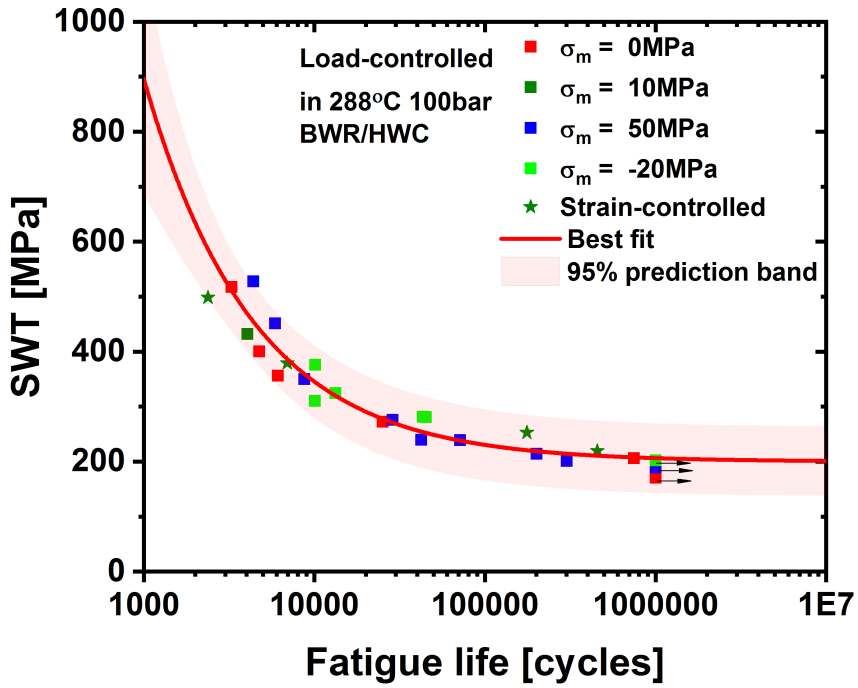

Figure 3.76 – Modified SWT parameter versus fatigue life in BWR/HWC at 288°C.

$$288^{\circ}C\ BWR/HWC: \quad \sqrt{\sigma_{max}\epsilon_a E} = 58921(N_f)^{-0.65} + 200 \tag{3.48}$$

The modified SWT approach properly corrected the effect of mean stress on fatigue life. The fitting functions indicate that the material has similar SWT_{mod} limit of 200 MPa for the tests in the two environments. The environmental effect is also manifested by a reduction of life in this SWT representation as illustrated in Fig. 3.77. Analogously with F_{en} environmental effect evaluation method, the environment effect could also be evaluated by the modified SWT parameter:

$$F_{en}^{SWT_{mod}} = \frac{N_f^{288^{\circ}C\ air}}{N_f^{288^{\circ}C\ BWR/HWC}} \tag{3.49}$$

The $F_{en}^{SWT_{mod}}$ was calculated with the equations of the two curves in Fig. 3.77. Analytically, the equation of Langer fit as:

$$SWT_{mod} = A \times N_f^{-B} + C \tag{3.50}$$

Thus we can derive:

$$F_{en}^{SWT_{mod}} = \frac{N_f^{288°C\ air}}{N_f^{288°C\ BWR/HWC}} = \left(\frac{A^{air}}{SWT_{mod} - C^{air}}\right)^{1/B^{air}} \times \left(\frac{SWT_{mod} - C^{water}}{A^{water}}\right)^{1/B^{water}} \tag{3.51}$$

From Equation 3.47 and Equation 3.48, we have $B^{air} = B^{water}$ and $C^{air} = C^{water}$. Thus Equation 3.51 can be simplified as:

$$F_{en}^{SWT_{mod}} = \frac{N_f^{288°C\ air}}{N_f^{288°C\ BWR/HWC}} = \left(\frac{A^{air}}{A^{water}}\right)^{(1/B)} \tag{3.52}$$

where A^{air} = 75524, A^{water} = 58921 and B = 0.65. Thus $F_{en}^{SWT_{mod}}$ is calculated around 1.47 for a strain rate of about 0.1%/s.

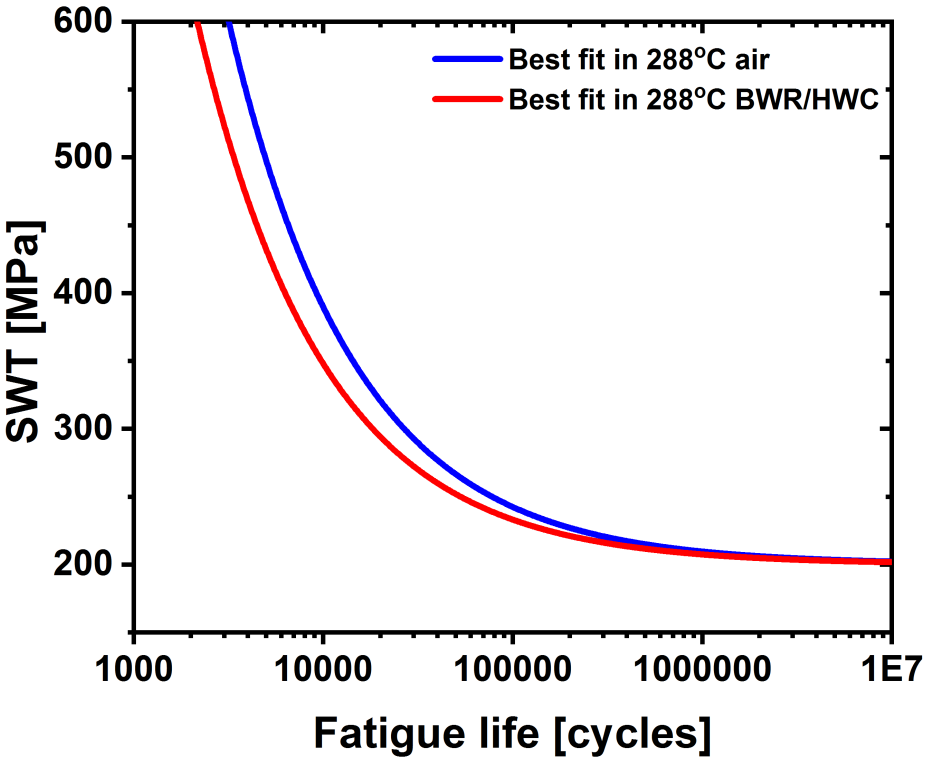

Figure 3.77 – The best fits of modified SWT versus fatigue life in air and BWR/HWC at 288°C.

3.8.2 Strain Energy based method

Hysteresis strain energy is related to the number of cycles to failure. In HCF, $\triangle\epsilon_p$ -> 0, the elastic strain energy controls the fatigue damage; in LCF, plastic strain energy controls the

fatigue damage [131][129]. A number of relationships were developed to correlate the strain energies per cycle (in different form) with fatigue life. In this study, the average values of total cyclic strain energy density and plastic strain energy density ($\overline{\triangle W_t}$ & $\overline{\triangle W_p}$) over all cycles appear to be promising parameters to correlate both LCF and HCF data with/without mean stress tested under strain- or load-controlled conditions, as shown Fig. 3.78 and Fig. 3.79. In both load- and strain-controlled tests, the plateau/stabilized stage accounts the most cycles in whole life. Thus the average values approximately equal to the middle-life or stabilized values. The $\overline{\triangle W_t}$ and $\overline{\triangle W_p}$ was calculated by analyzing each hysteresis loop with our in-house coded program. $\triangle W_t = \triangle w_p + \triangle W_e + \triangle W_{ane}$ as Fig. 2.11 describes.

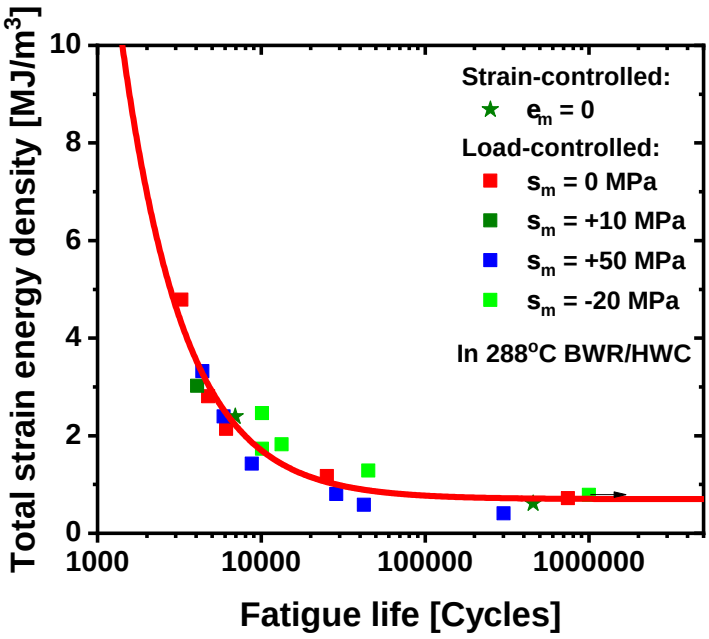

Figure 3.78 – The average total strain energy density $\overline{\triangle W_t}$ versus fatigue life N_f.

The relationships between $\overline{\triangle W_t}$, $\overline{\triangle W_p}$ and N_f in Fig. 3.78 and Fig. 3.79 can be described by a power law [131][162], which is in the similar form of Langer equation:

$$\triangle W = W_f (2N_f)^d + \triangle W_{end} \tag{3.53}$$

Where W_f and d are the fitting parameters and W_{end} is the strain energy density associated with the material endurance.

The best fit equations are:

$$\overline{\triangle W_t} = 36780(N_f)^{-1.14} + 0.7 \tag{3.54}$$

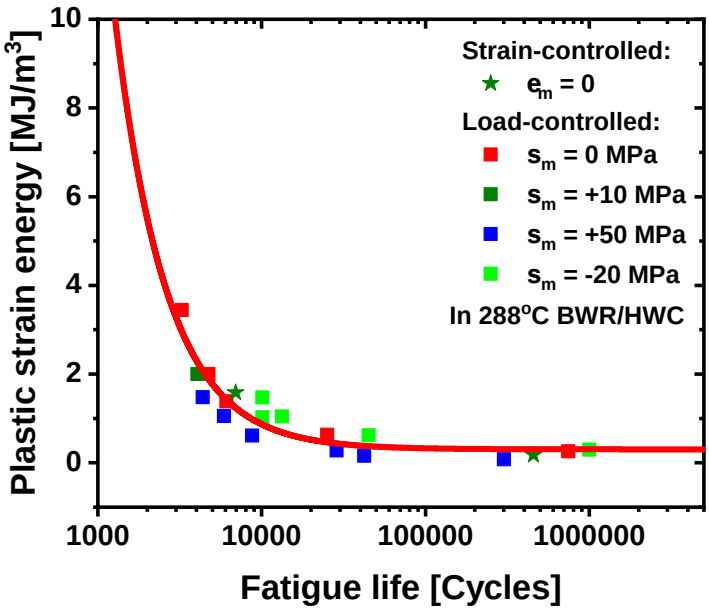

Figure 3.79 – The average plastic strain energy density $\overline{\triangle W_p}$ versus fatigue life N_f.

$$\overline{\triangle W_p} = 186357(N_f)^{-1.38} + 0.3 \tag{3.55}$$

3.8.3 Machine learning based method

Predicting the life of EAF is a multi-factor nonlinear problem, which may involve factors from mechanical loading, material properties and environments. In tackling this kind of problem, machine learning based methods may outweigh physically or phenomenologically based or least square fitting based methods.

In this study, we have tried different kinds of networks. The one that has the best performance is illustrated in Fig. 3.80. The four layers network has 9 neurons in the input layer, one neuron in output layer and 10 neurons in each hidden layer. Nine features, six from mechanical loading factors, two from material properties and one from environmental factors, were selected as inputs. In this case, a data set made up with 48 test results from our lab were used. Before neuron network training, the data set was separated into two parts in a way to have 70% data for training and 30% data for validation and test. The dropout function (which is a regularization technique patented by Google for reducing overfitting and improve generalization in neural networks by preventing complex co-adaptations on training data by by randomly dropping out nodes during training. It is a computationally cheap and remarkably effective regularization method to neural networks) was applied with drop rate of 0.3 in each

layer to minimize the possible overfitting. Training steps are up to 50000 with a train rate of 0.3.

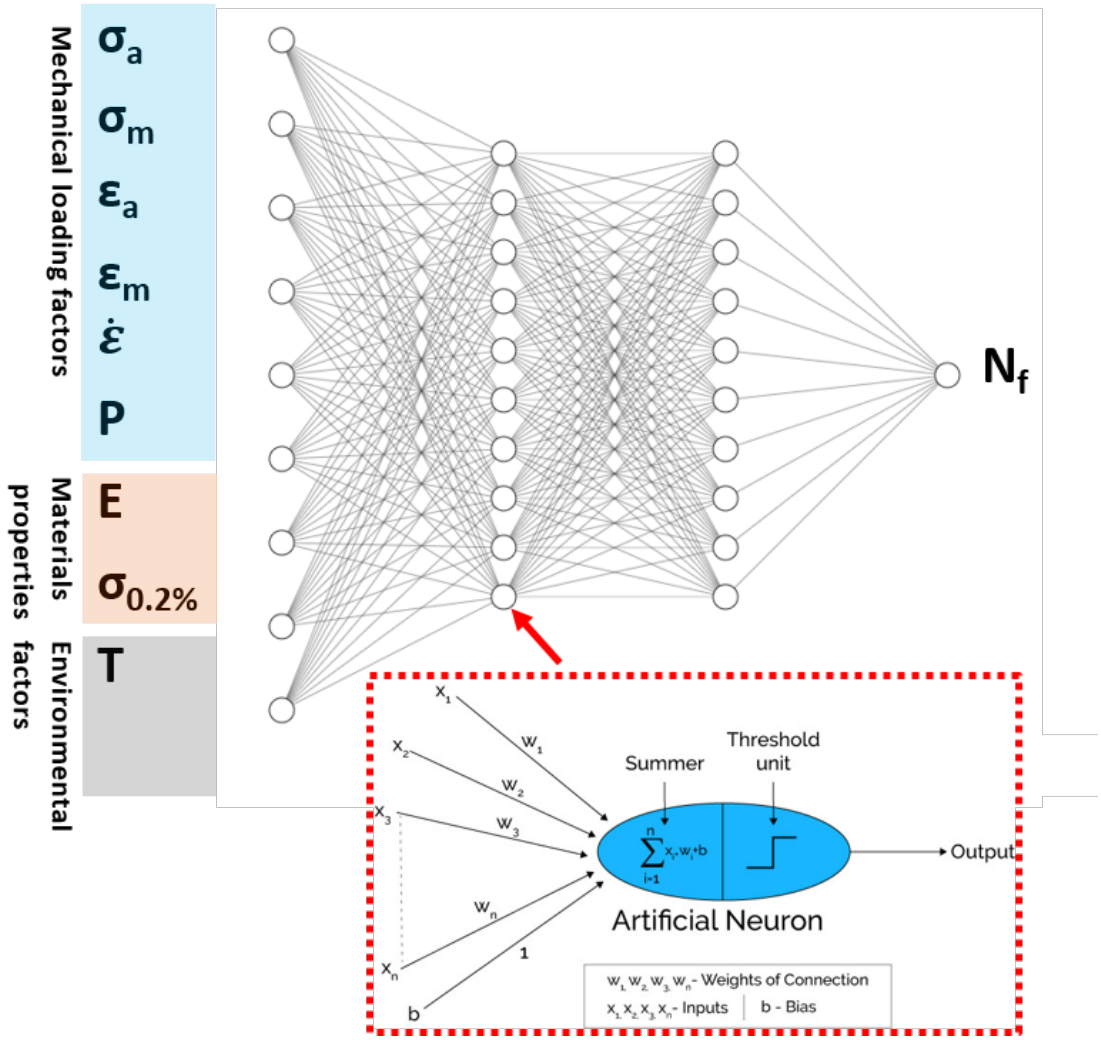

Figure 3.80 – Schematic illustration of the ANN architecture and its input features.

Fig. 3.81 presents the predicted lives versus experimental lives from the artificail neural network (ANN) training prediction and test validation, comparing with SWT method prediction (for HTW as Equation 3.48 describes) and NUREG/CR-6909 Rev.1 prediction [3]. For the training, the network optimizes the weighting matrix $\boldsymbol{M}$ and bias matrix $\boldsymbol{B}$ in $\boldsymbol{X} \cdot \boldsymbol{M} + \boldsymbol{B} = \boldsymbol{Y}$ to minimize the loss function (or called cross entropy) of sum of squares errors, which is equal to $\sum_{i=1}^{n}(y-\hat{y})^2$, where y is the experimental life and $\hat{y}$ is the predicted life in training. A test data set, which does not appear in the training data set, was used to validate the predictive accuracy of well-trained network. The predicted lives for the test validation are plotted in red dots in Fig. 3.81. The prediction accuracy for a test dataset, instead of the prediction accuracy of a training dataset, more correctly represents the predictive ability of a well-trained neural network, as the neural network with bad generalization can have very nice prediction accuracy

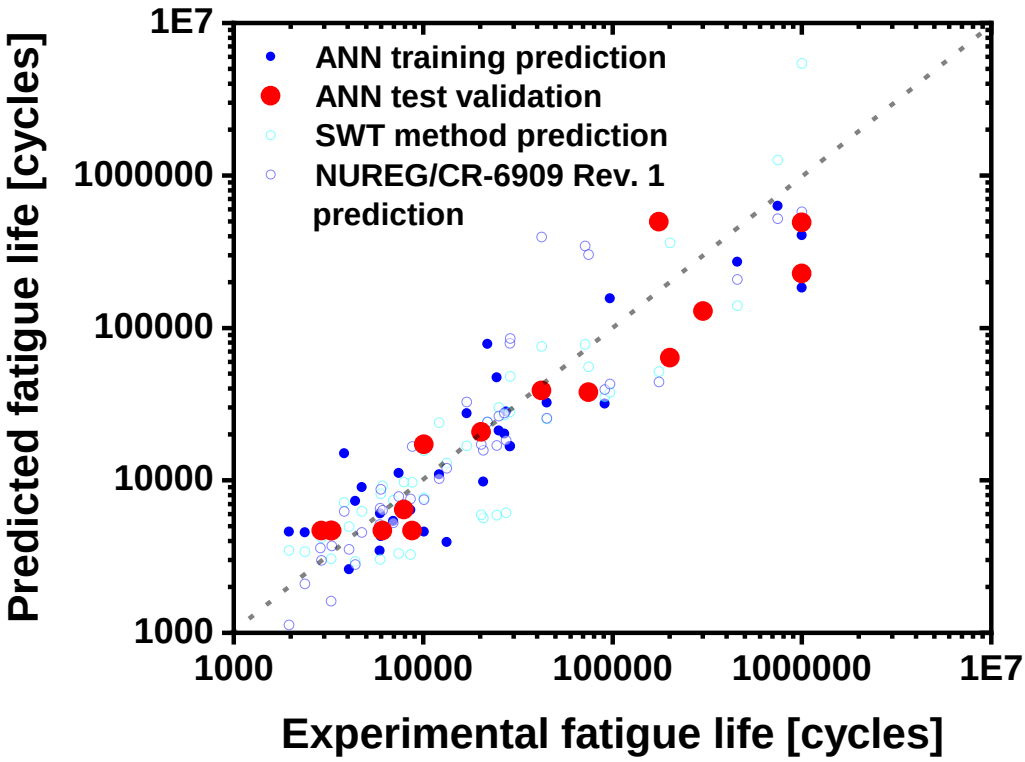

Figure 3.81 – Experimental fatigue life versus predicted fatigue life from ANN training, ANN test validation, SWT method and NUREG/CR-6909 Rev.1 model. The data is our test results in water with variable factors of temperature, stress/strain amplitude, mean stress/strain, wall thickness and strain rate.

for training dataset but bad prediction accuracy for test dataset. Such situation results from overfitting.

In Fig. 3.81, the well-trained neural network shows better predictive performance in accuracy and generalization than the SWT method developed in this thesis and newest NUREG method by showing R^2 of 0.83 for ANN training prediction, 0.90 for ANN test validation, 0.75 for SWT method and 0.79 for NUREG Method. The R^2 value was calculated based on the logarithm of fatigue lives. No deterioration of R^2 in ANN test validation comparing with the one in ANN training implies that the neural network has nice generalization. The neural network has better prediction in LCF regime than in HCF regime. For run-out tests, we took their fatigue lives as 10^6 while they are not the actual lives. Bigger uncertainty in fatigue life exist and many fewer data points were gathered in HCF regime than in LCF regime. These factors may lead to worse prediction in HCF.

4 Discussion

4.1 Mean stress effects on fatigue behavior

4.1.1 Phenomenologically-based interpretation of the fatigue test results

It is commonly recognized that positive mean stress is detrimental and negative mean stress is beneficial to fatigue life. This is true for carbon steels and low alloy steels, whose fatigue limits are lower than the yield stresses, but not for austenitic stainless steels.

In Fig. 3.6 and Fig. 3.9, we observed that both positive (+50 MPa) and negative (-10 & -20 MPa) mean stresses increase fatigue life at a given stress amplitude. However, when the fatigue life is reported against the average strain amplitude (in Fig. 3.7 and Fig. 3.10) or against the proposed modified SWT parameter (in Fig. 3.75 and Fig. 3.76), all data were well correlated with each other.

The observed beneficial mean stress effects on fatigue life is attributed to the enhanced cyclic hardening by mean stress, which results in smaller strain amplitude in comparison with zero-mean stress cases at a given stress amplitude. The plastic deformation per cycle is a key criterion to determine how many cycles the material can sustained. Fig. 4.1 and Fig. 4.2 describes the relationships between the average strain amplitude and the stress amplitude with different mean stresses in air and BWR/HWC at 288°C respectively. Both figures show that mean stress strengthens material during cyclic loading, which again is reflected by a decrease of strain amplitude. The Table 3.1 with the mechanical parameters obtained from the hysteresis analysis shows that the tests with mean stress have larger hardening exponent as well. Interestingly, we found a linear relationship between the average strain amplitude and stress amplitude, which depends on the mean stress in a given environment. Furthermore, different slopes of the fits in air and BWR/HWC at 288°C reveal an influence of the environment, mostly probably related to the internal water pressure, on cyclic mechanical behavior. The strain-stress relations are expressed mathematically as:

$$In\ 288^{\circ}C\ air: \quad \overline{\epsilon_a} = A(\sigma_a - \sigma_o) + 0.001 \tag{4.1}$$

$$In\ 288^{\circ}C\ BWR/HWC: \quad \overline{\epsilon_a} = B(\sigma_a - \sigma_o) + 0.001 \tag{4.2}$$

For the fitted average strain amplitude-stress amplitude relationships in 288°C air, the stress amplitude σ_o at 0.1% strain amplitude is 155 MPa independent of mean stress. In 288°C BWC/HWC, σ_o depends on mean stress: σ_o = 160 MPa for +50 MPa mean stress, σ_o = 170 MPa without mean stress and σ_o = 175 MPa for -20 MPa mean stress. The A and B coefficients depend on mean stress in a non-linear manner and are presented in Table 4.1.

Table 4.1 – The dependence of strain-stress slope (A & B) on mean stress.

Mean stress $[MPa]$	slope parameter A in HTA $[MPa^{-1}]$	slope parameter B in HTW $[MPa^{-1}]$
0	8.97×10^{-5}	10.49×10^{-5}
+50	2.69×10^{-5}	4.26×10^{-5}
-20	3.16×10^{-5}	3.51×10^{-5}

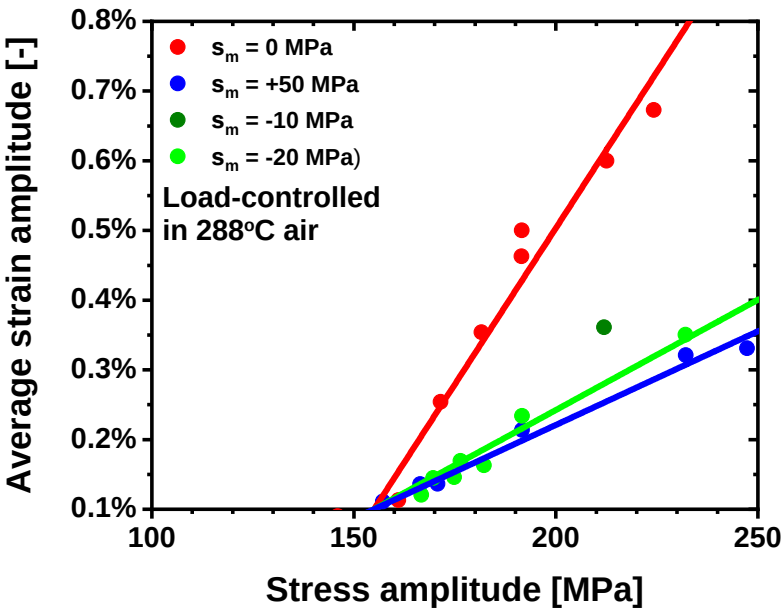

Figure 4.1 – Average strain amplitude dependence on stress amplitude with different mean stresses in air at 288°C.

Mean stress under load-controlled condition induces mean strain, either in positive or in negative direction, as presented in Fig. 4.3 and Fig. 4.4. The evolution of mean strain (also called racheting or cyclic creep) represents directional progressive accumulation of plastic deformation of a material in the direction of mean stress [163]. Higher stress amplitude leads to larger accumulation of plastic strain in the mean stress direction per cycle for materials that deform elasto-plastically ($\epsilon_a > \approx 0.1\%$). This was experimentally verified that larger mean

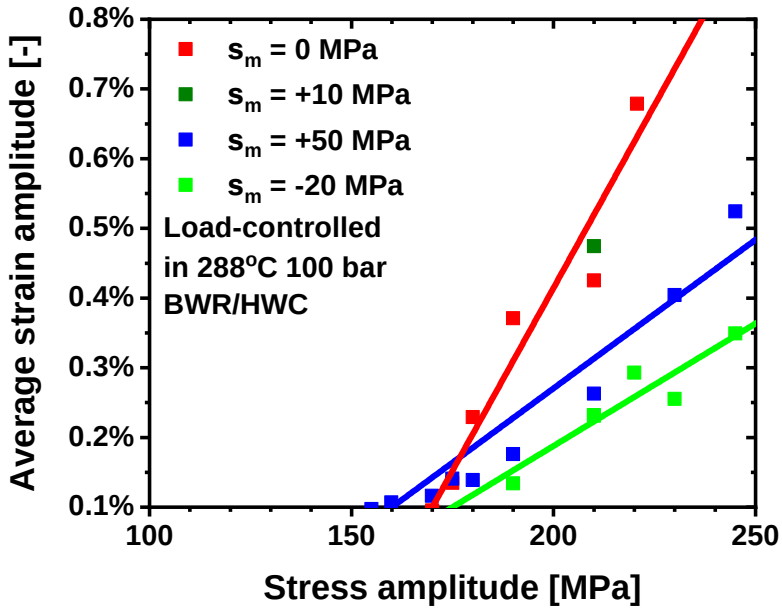

Figure 4.2 – Average strain amplitude dependence on stress amplitude with different mean stresses in 100 bar HWC/BWR environment at 288°C.

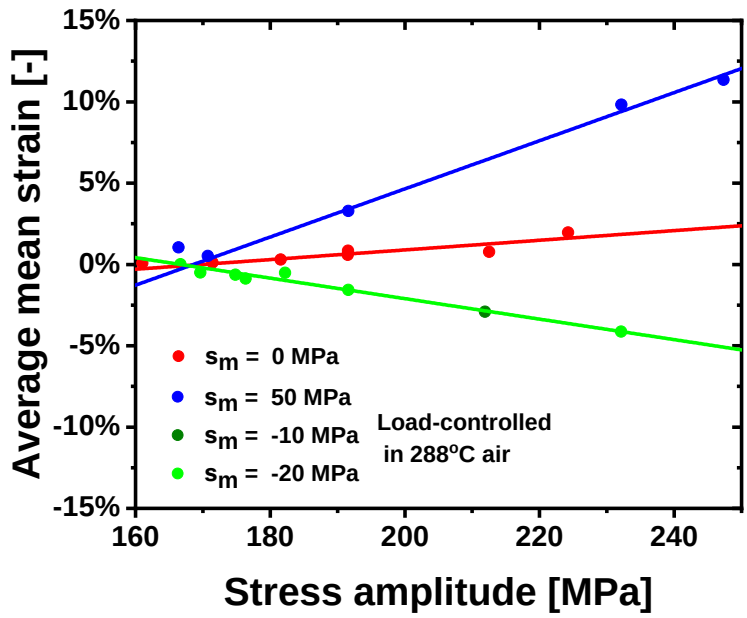

Figure 4.3 – Average mean strain dependence on stress amplitude with different mean stresses in air at 288°C.

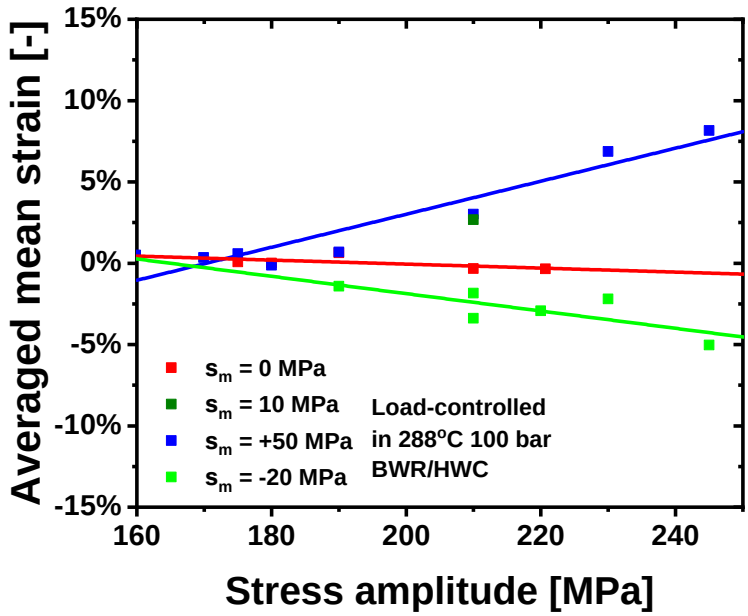

Figure 4.4 – Average mean strain dependence on stress amplitude with different mean stresses in 100 bar BWR/HWC environment at 288°C.

strains were found for the tests with larger stress amplitudes in Fig. 4.3 and Fig. 4.4. Mean strain was reported to have minor effect on fatigue life, but it can affect the crack density and opening (due to the larger maximum plastic strain). Fig. 3.32 and Fig. 3.34 show that the specimens with higher mean strain, which is positively related to mean stress, have a greater crack number density and opening on the inner surfaces.

In Fig. 3.7 and Fig. 3.10, we see that the measured fatigue strain limit is around 0.1%. In Fig. 4.1, the fitted relationships have almost the same stress amplitude of σ_o = 150 MPa at the fatigue limit of $\overline{\epsilon_a}$ = 0.1%. However, in Fig. 4.2, the fitted relationships have different σ_a (160 MPa for σ_m = +50 MPa, 170 MPa for σ_m = 0 MPa and 175 MPa for σ_m = -20 MPa) at the fatigue limit of $\overline{\epsilon_a}$ = 0.1%. This is consistent with our S-N results in Fig. 3.6 and Fig. 3.9 where the tests with different mean stresses have practically the same fatigue stress limit in HTA, but different stress limits (151 MPa for σ_m = +50 MPa, 171 MPa for σ_m = 0 MPa and 195 MPa for σ_m = -20 MPa) in HTW, although fatigue limits σ_f are not the same as the stress amplitude values σ_o in Fig. 4.1 and Fig. 4.2. These Figures describe the cyclic stress-strain from mechanical point of view. In principle, the mean stress should not affect much the average strain amplitude relationship at the fatigue limit (0.1%), where only small plastic strain is induced and where mean stress only slightly influences the material hardening. This is consistent with the cyclic stress-strain relationships in HTA of Fig. 4.1. However, different σ_o (higher for negative mean stress and lower for positive mean stress) were observed at $\overline{\epsilon_a}$ = 0.1% in BWR/HWC environment. Analogously, different stress limits were observed for tests with different mean

stresses in BWR/HWC environment in Fig. 3.9. The synergistic effect between mean stress and BWR/HWC environment in HCF regime (discussed in Section 4.3) may responsible for this. The fitting lines in Fig. 4.3 and Fig. 4.4 intersect at $\overline{\epsilon_m}$ = 0%. This shows that mean stress barely contributes to ratcheting (neither in tension nor in compression) in the HCF region, where slight plastic strain is induced.

4.1.2 Physically-based interpretation with microstructures observations of the fatigue test results

The microstructures at the end of life and at interrupted cycles of tests with σ_a = 210 MPa and σ_m = +10, +50, -20 MPa were presented in Fig. 3.70, 3.71 and 3.72 respectively. In Fig. 3.70, neither spatial (3D) dislocation structures nor strong strain localization (like at GBs) were observed at the conditions with σ_m = +50 MPa or -20 MPa. The microstructures configuration and magnitude of strain localization at the end of life are highly dependent on plastic strain ($\overline{\triangle\epsilon_p}$), as the cyclic stress-strain curve (CSS) illustrates in Fig. 1.25. The established $\overline{\triangle\epsilon_p}$ equals 0.60%, 0.62%, 0.20%, 0.20% for the conditions with σ_m = 0, +10, +50, -20 MPa at σ_a = 210 MPa respectively. Given the SFE of 316L SS, larger plastic strain stimulates more wavy slips, which result in persistent slip bands, cells or structures between these two structures [98][30][93][104][105][108][25][97]. Planar arrays of dislocations were formed for tests with lower plastic strain. During cyclic loading, the dislocations move towards and accumulate at GBs generating high observed local strain and high stress and dislocation density rises locally to preserve the continuity of material. High strain will lead to formation of spatial microstrcutures. The local strain determines how many cycles are need to initiate a crack, although cracks initiate merely on the surfaces in our tests. Thus the materials tested with mean stress, which have only planar dislocations and less strain localization, have longer fatigue lives (at least the cycles need to form a crack, for example a stage I crack of microstructurally small crack) at the same stress amplitude.

Mean stress was observed to enhance cyclic hardening and weaken cyclic softening when comparing the curves of strain versus loading cycles in Fig. 3.8 and Fig. 3.11. Tests with mean stress have larger drop of strain (with respect to the material original state) in the first hardening stage and smaller rise of strain in the softening stage. Additionally, secondary hardening often occurs in tests with mean stress (+50 MPa and -20 MPa), if the tests run longer than 10^4 to 10^5 cycles.

During the first hardening stage, including the starting cycles, accumulation of plastic strain in the direction of mean stress (compressive or tensile) occurs for each cycle and lead to a corresponding mean strain. This accumulation of plastic strain induces extra lattice defects and dislocations. During the first hardening stage (< 20 cycles), we have seen that materials tested with mean stress developed higher dislocation (in planar configuration) density, and had higher strength, which then results in smaller strain amplitude response at the same level of stress amplitude.

During the softening stage, occurence of wavy dislocations, dislocation wall/channels and veins is observed promoting dislocation motion. Based on the CSS theory, formation of wavy structures needs relatively high plastic strain range [97][98][93]; however, the established plastic strain range in materials loaded with mean stress is relatively low, owing to a stronger hardening in the former hardening stage. Thus in these materials planar dislocations are formed preferentially, instead of wavy dislocations. This is confirmed by our TEM observations in Fig. 3.71c-d and Fig. 3.72c-d. However, with increasing dislocation density, dislocation tangles were formed, which is a lower energy structure and can decrease the resistance to dislocation motion, but which still retains a higher resistance than wavy structures. Thus, materials loaded with mean stress have weaker softening.

In our case, secondary hardening appears only if a large amount of damage is accumulated, in other words if the specimen is loaded with small stress/plastic strain amplitude. This requires two conditions: (a) the damage (represented by plastic strain amplitude) induced in one cycle is low enough; (b) no severe strain/stress localization takes place. During the secondary hardening stage, the corduroy structures were exclusively observed. These microstructures are arrays of point defects or nano-size dislocation loops. As discussed in the above paragraphs, materials loaded with mean stress at 288°C have relatively smaller plastic strain amplitude and homogeneous strain/strain distribution in the last two stages. This provides the conditions for corduroy structures formation, which is directly related to occurrence of secondary hardening.

4.1.3 Physically-based interpretation with strain energy-based analysis of the fatigue test results

The modified SWT parameter can be regarded as an energy-based criterion for fatigue life prediction. Indeed, we just recall that the modified SWT parameter is equal to $\sqrt{\overline{\epsilon_a}\,\overline{\sigma_{max}}\,E}$. The product $(\overline{\epsilon_a}\,\overline{\sigma_{max}})$ has the dimension of a strain energy density and is actually the sum of the strain energy and the complementary energy for the zero mean stress case. As such, it does not correspond to the dissipated energy during one cycle. The plastic and total strain energies calculated from the hysteresis loop analysis are then more physically based than the SWT parameter itself. In Fig. 3.75, Fig. 3.76, Fig. 3.79 and Fig. 3.78, we showed that the modified SWT parameter and the average strain energy density correlates all the fatigue life data with and without mean stresses. This implies that mean stress effects are well taken into account by these criteria. For the modified SWT parameter and total strain energy density $\triangle W_t$ (which is equal to $\int_{\epsilon_{min}}^{\epsilon_{max}} \sigma^{upload} d\epsilon$), the strain amplitude depends on mean stress and stress amplitude: $\epsilon_a = f(\sigma_a, \sigma_m)$. The strain energy density represents the damage induced in each loading cycle. In another words, the correlations between the energy-based criteria (SWT parameter or $\triangle W$) and fatigue life is related to the material tolerance to cyclic damage. No obvious mean stress influence on these correlations imply that mean stress does not change the damage resistance of materials when considering strain energy-based criteria.

To conclude this section, mean stress is beneficial to fatigue life of austenitic stainless steels in

load-controlled tests by enhancing cyclic hardening and weakening cyclic softening, which result in smaller strain deformation for a given stress level. From a microstructurally-based interpretation, mean stress promotes planar dislocation configurations, which are formed in the first ≈ 20 cycles, and hinders wavy dislocations and strain localization in the softening stages. A strong material hardening corduroy structure, which relates to secondary hardening, was often observed in the end-life materials loaded with mean stress. Mean stress increases fatigue life by decreasing plastic damage in each cycle but does not affect the damage resistance of material.

4.2 Fatigue degradation in LWR environments

4.2.1 Stress-life representation analysis

The stress amplitude versus fatigue life (S-N) results with 0, +50, -20 MPa mean stress in both environments (air and BWR/HWC at 288°C) are plotted in Fig. 4.5, Fig. 4.6 and Fig. 4.7 respectively. Unlike the environment effect discussed in strain-life plots and quantified by the environmental factor independent of the the strain amplitude $F_{en} = N_f^{air}/N_f^{water}$, the environmental factor varies with stress amplitude in the stress-life representation. Larger N_f^{air}/N_f^{water} ratio is observed at higher stress amplitude. The fitting curves of the two environments intersect each other indicating that the BWR/HWC environment does not necessary decrease the fatigue life or fatigue limit. The BWR/HWC environment does not significantly change the fatigue limit with +50 MPa mean stress either. The BWR/HWC environment slightly increases the fatigue limit (from ≈ 161 MPa to ≈ 171 MPa) under zero mean stress condition and significantly increases the fatigue limit (from ≈ 167 MPa to ≈ 195 MPa) under -20 MPa mean stress condition. In the HCF region, LWR environmental effects would vanish when the strain amplitude is below the threshold level. In Fig. 4.6, the plot with +50 MPa mean stress, the situation is still consistent with the conventional understanding. The beneficial effect of HTW in HCF regime in Fig. 4.5 and Fig. 4.7 could be tentatively attributed to internal water pressure that induces a larger von Mises stress in compression than in tension [11] (≈ -7 MPa mean stress in our pressurized hollow specimen, which would increase the fatigue limit in HCF region, where the detrimentally environmental effect is negligible), or to oxide-induced crack closure effect under negative mean stress or to crack tip blunting by oxide layer. Corrosion formed oxides can blunt crack tips resulting in lower driving force for crack growth. This could retard crack growth and contribute to fatigue life & limit increase. A more plausible explanation is the build-up plasticity, roughness and oxide-induced crack closure effects, which can cause crack arrest [31].

$N_f^{air}/N_f^{BWR/HWC}$ dependence on stress amplitude was calculated for different mean stresses and is plotted in Fig. 4.8, where the data points correspond to the experimental results and the curves to the best fit predictions. In the plot for σ_m = 0 MPa in Fig. 4.5, the fatigue life in air starts to outstrip the fatigue life in BWR/HWC around 190 MPa, where the corresponding average strain amplitude ($\overline{\epsilon_a}$) are 0.37% in HTW and 0.46% in HTA. Above this strain/stress

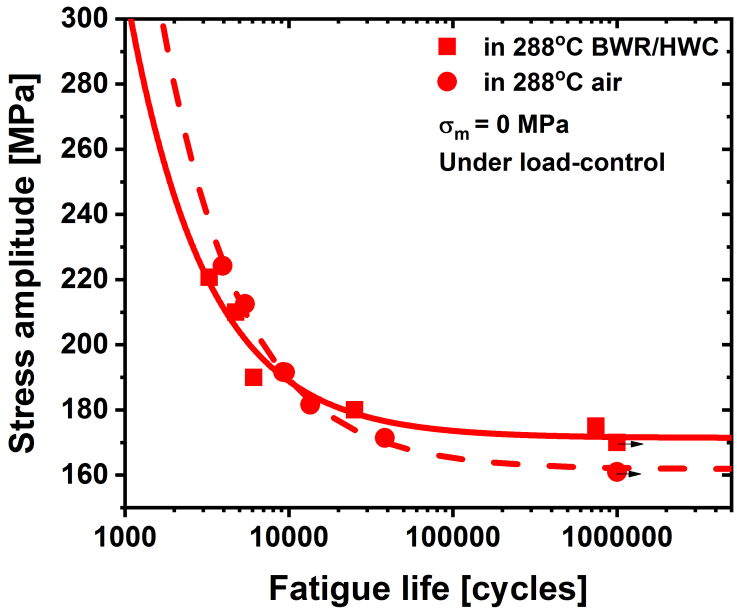

Figure 4.5 – Stress amplitude versus fatigue lives of tests without mean stress in air and BWR/HWC at 288°C.

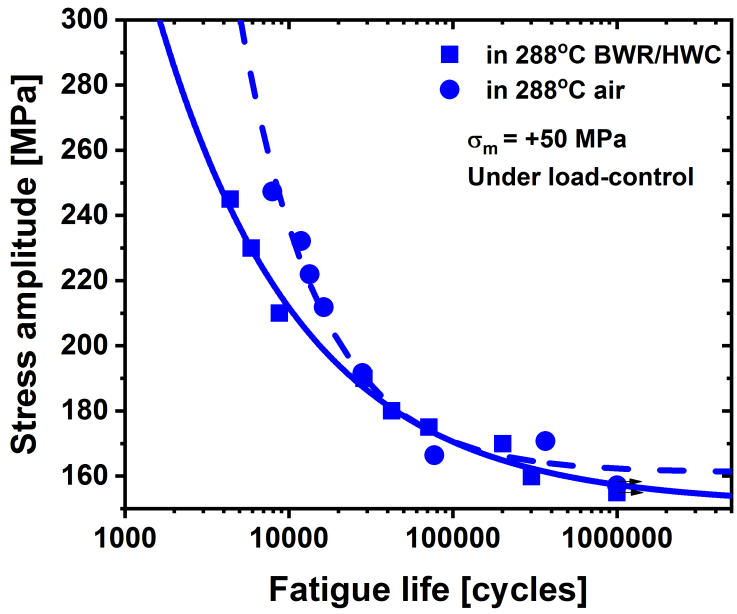

Figure 4.6 – Stress amplitude versus fatigue lives results of tests with +50 MPa mean stress in air and BWR/HWC at 288°C.

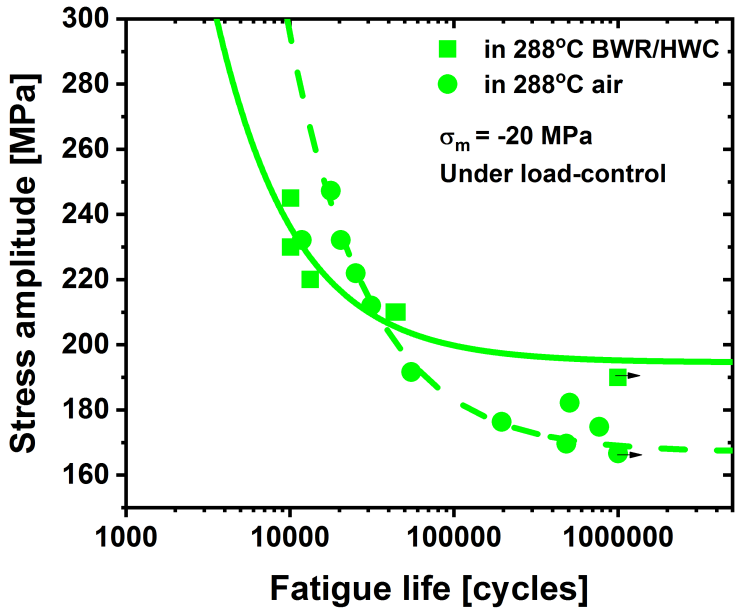

Figure 4.7 – Stress amplitude versus fatigue lives results of tests with -20 MPa mean stress in air and BWR/HWC at 288°C.

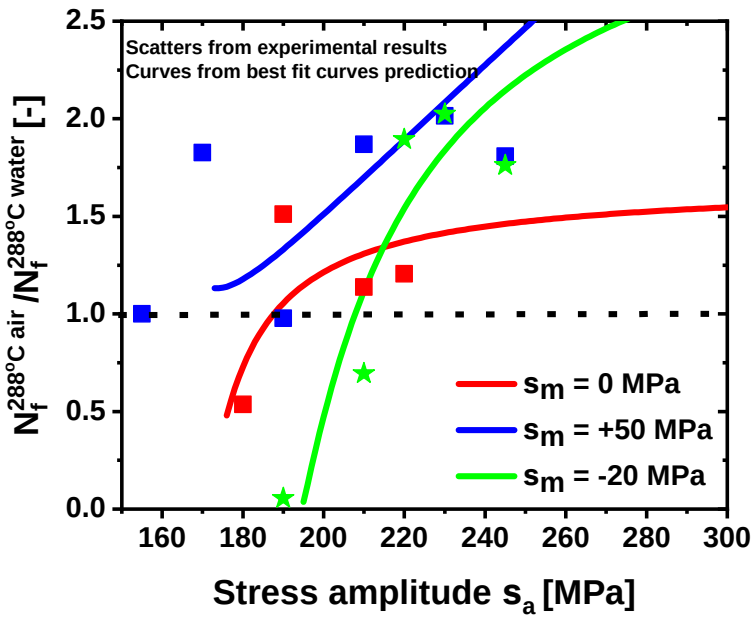

Figure 4.8 – The environmental factor ($N_f^{288°C\ air}/N_f^{288°C\ BWR/HWC}$) versus σ_a under different mean stresses. To be notice: the scatters are from experimental test results and curves are calculated from the prediction of best fits in Fig. 4.5-4.6, not the fitting of the scatters.

level, the detrimental effects of HTW environment outweigh the possible beneficial effects of internal water pressure or crack closure. For tests with σ_m = +50 MPa, $N_f^{air}/N_f^{BWR/HWC}$ is always larger than 1. For σ_m = -20 MPa, N_f^{air} starts to outstrip $N_f^{BWR/HWC}$ around σ_a = 210 MPa. Above this stress amplitude, the HTW detrimental effects prevail resulting in shorter fatigue life in HTW; below this stress amplitude a longer fatigue life in HTW is found. Analyzing the data points with $N_f^{air}/N_f^{BWR/HWC} > 1$ in Fig. 4.8, both +50 MPa and -20 MPa mean stresses suggest similar environmental factors, which are larger than those of without mean stress condition. This means both positive and negative mean stress amplifies the degradation effect of high-temperature water environment when considered in stress-life plots. Positive mean stress amplifies environmental influence was commonly recognized. However, the exact reason for the observed non-standard phenomenon of -20 MPa mean stress is unclear. The synergistic effects of environment and mean stress are addressed in detail in Section 4.3.

4.2.2 Strain-life representation analysis

As already mentioned, LWR environments significantly accelerate fatigue degradation when temperature and strain amplitude are larger than their respective critical values (150°C, ≈0.15%) , and the strain rate is lower than 0.4%/s [4][5]. However, in NUREG-CR-6909 Rev. 1, HTW environmental degradation occurs for austenitic SSs when ϵ_a > 0.112%, T > 100°C, $\dot{\epsilon}$ < 7%/s and DO < 0.1 ppm [3]. The F_{en} (= N_f^{air}/N_f^{water}) concept was first adopted in JSME code to correct the environmental effects, which are not explicitly addressed in the ASME Code Section III [63]. Then NRC codes, ASME Code Cases and some European Codes adopted similar methodologies to evaluate the environmental effects on fatigue life. The F_{en} factor was reported to depend on temperature, strain-rate and dissolved oxygen content for austenitic stainless steels [70][2][137][7][3]. A dependence of F_{en} on strain range was reported by Kamaya based on the tested fatigue lives of 316L steel in PWR water environment [147]. He also observed that the environmental effect was insignificant at a strain amplitude of 0.25% and 0.22%. This is not consistent with JSME Code's claim that there is no dependence of F_{en} factor on strain amplitude larger than 0.11% and no environment effect when strain amplitude is equal or less than 0.11%.

All above mentioned statements are based on the results of strain-controlled tests with constant strain rate (normally saw tooth waveform was applied) and using solid specimens with smooth surface. In our case, we performed load-controlled tests using sinusoidal waveform (mathematical expression as Equation 4.3), resulting in non-constant strain rate, as Fig. 4.9 shows.

$$\sigma = \sigma_0 \sin \omega t \tag{4.3}$$

where the ω equals to $\frac{2\pi}{1/0.17Hz}$. 0.17 Hz is the frequency we applied for sinusoidal waveform.

We take the mid-life cycle (at the stabilized plateau) of one test with σ_a = 210 MPa, $\overline{\epsilon_a}$ = 0.425% without mean stress as an example (in Fig. 4.9) to explain the F_{en} calculation. As introduced

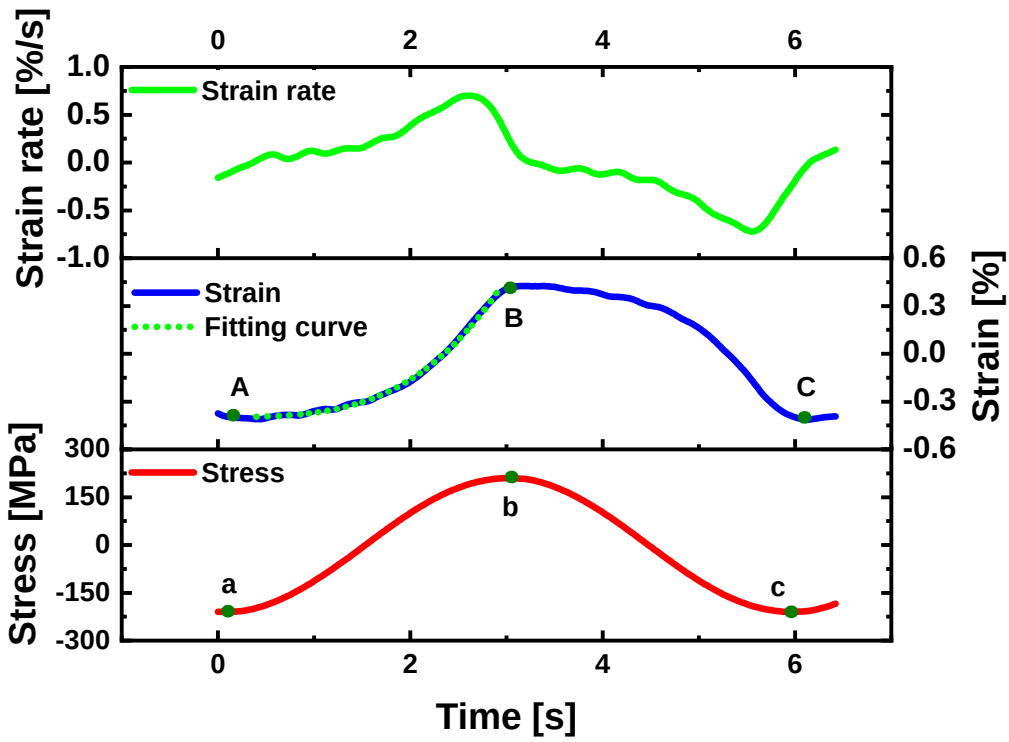

Figure 4.9 – Stress, strain and strain rate versus time (correspond to the loading signal and specimen deformation signals) of the 3250th cycle at the mid-life of test with $\sigma_a = 210$ MPa without mean stress under load-control in BWR/HWC at 288°C.

in the experimental Section 2.3.2, the test was conducted under load-control with sinusoidal waveform in a frequency of 0.17 Hz. As Fig. 4.9 illustrates, the corresponding strain signal is neither in sinusoidal waveform nor in saw tooth waveform. The strain rate is not constant either, so we fitted the strain-time curve of upload part with a power law:

$$\epsilon(t) = \left(\frac{\alpha}{n}\right) t^n + B \tag{4.4}$$

We get:

$$\epsilon(t) = 0.02484\, t^{3.23778} - 0.39584 \tag{4.5}$$

Through derivation of Equation 4.4, the strain rate function is expressed as:

$$\dot{\epsilon} = \alpha\, t^{(n-1)} \tag{4.6}$$

Based on the modified rate approach described in NUREG/CR-6909 Rev.1 [3], the F_{en} for the

total strain transient is given by:

$$\begin{aligned} F_{en} &= \frac{1}{\epsilon_{max}-\epsilon_{min}}\int_{\epsilon_{min}}^{\epsilon_{max}} F_{en}(T,\dot{\epsilon},O)d\epsilon \\ &= \frac{1}{\epsilon_{max}-\epsilon_{min}}\int_{\epsilon_{min}}^{\epsilon_{max}} exp(-T^*\dot{\epsilon}^*O^*)d\epsilon \\ &= \frac{1}{\epsilon_{max}-\epsilon_{min}}\int_{t_{min}}^{t_{max}} exp(-T^*\dot{\epsilon}^*O^*)\dot{\epsilon}dt \end{aligned} \tag{4.7}$$

T^*, $\dot{\epsilon}^*$, O^* are the transformed parameters of temperature, instant strain rate and DO level respectively. T^* and O^* are constant and calculated to be 0.752 and 0.29 respectively, based on Equation 3.14 and Equation 3.16. Based on Equation 3.15:

$$\dot{\epsilon}^* = ln\left(\frac{\dot{\epsilon}}{7}\right) = ln\left(\frac{\alpha t^{(n-1)}}{7}\right) \tag{4.8}$$

Taking Equation 4.8 and values of T^* and O^* into Equation 4.7, get:

$$F_{en} = \frac{1.529\alpha^{-0.21808}}{\epsilon_{max}-\epsilon_{min}}\cdot\alpha\cdot\frac{t^{0.78192(n-1)+1}}{0.78192(n-1)+1}\Bigg|_{t_{max}}^{t_{min}} \tag{4.9}$$

For the mid-life cycle in Fig. 4.9, ϵ_{max} = 0.425%, ϵ_{min} = -0.425%, t_{max} = 2.9 s, t_{max} = 0 s, the fitting parameters α = 0.08142 and n = 3.2778 from Equation 4.5, then we calculated the F_{en} = 1.78.

On the other hand, in our average strain rate F_{en} calculation, we used average strain rate $\bar{\dot{\epsilon}}$, which equals $\frac{\epsilon_a}{1/(0.17\times4)}$:

$$F_{en} = exp(-T^*\bar{\dot{\epsilon}}^*O^*) \tag{4.10}$$

The average strain rate F_{en} is calculated to be 2.0.

Comparing the calculated F_{en} factors with the modified rate approach and our average strain rate approach, we found their difference is smaller than 15%. Thus we use the average strain rate F_{en} approach in this thesis.

We plotted the two best fits from Fig. 3.7 and Fig. 3.10 together in Fig. 4.10. The F_{en} factor, which was calculated from the two best fits of HTA (Equation 3.7) and HTW (Equation 3.12), is independent of ϵ_a and equal to 1.66. The F_{en} was also calculated with average strain rate approach (expressed in Equation 4.10) is from 1.66 to 2.4 varying with strain rate in the strain amplitude range of 0.1% to 1.0%. The F_{en} factor of 1.66 calculated from the two best fits well agrees with the prediction from NUREG/CR 6909 Rev. 1. The fatigue limit in strain is around 0.1% in both environments, showing no environment effect when $\epsilon_a \leq$ 0.1%. This implies that environment as well as mean stress, which was discussed in last section, do not significantly change the fatigue limit in strain amplitude.

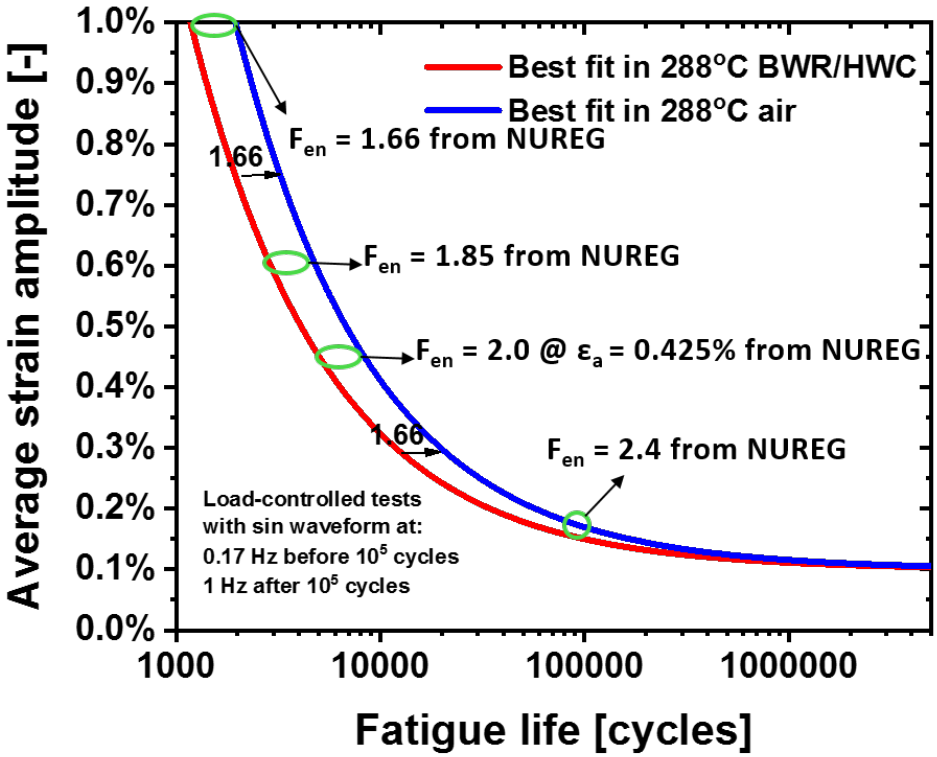

Figure 4.10 – Comparison of the best fits of (average) strain-life in air and BWR/HWC at 288°C. The F_{en} factors at different strain amplitudes (with different strain rates) are calculated based on the average strain rate F_{en} approach described in Equation 4.10 [3].

4.3 Synergistic effects of environments and mean stresses

Environmental degradation effects of HTW have been studied by the community for many years. Mean stress effects have been addressed by various authors: Goodman [119], Gerber [118], Soderberg [122], SWT [123]. In real conditions, both factors of HTW and mean stresses (originating from dead weight, residual stress, thermal gradient and stratification) exist in LWR components. However, the environmental effects and mean stress effects are investigated separately in most cases. Understanding their synergistic effects is required to correctly evaluate environmentally-assisted fatigue (EAF) in LWR water environments.

Fatigue life consists of periods of crack nucleation and growth:, short crack (microstructurally in stage I/mode II + mechanically short crack in stage I/mode I) and long crack (stage II/mode I) or consider the unstable crack (stage III/mode I) in the last stage. The environment plays a different role in each period. Nucleation and short crack phases account for a larger portion of fatigue life at low stress/strain amplitude (high cycles regime) than at high stress/strain amplitude (low cycles regime), where long crack growth life is more dominant. Thus we discuss

the environmental effect and mean stress effect on LCF and HCF separately.

4.3.1 LCF regime

We plotted the stress-life data in LCF regime of tests in both environments in Fig. 4.11, where only the data with 0 and +50 MPa mean stresses are reported. HTW decreases fatigue life with or without mean stress. +50 MPa mean stress increases fatigue life no matter in HTW or in HTA. On first glance on Fig. 4.11 we see that the environmental degradation (red arrows) is greater when with +50 MPa mean stress than without mean stress and the beneficial factor of +50 MPa stress (blue arrows) is smaller in HTW than in HTA by comparing the width of gaps/length of arrows between the fitting curves.

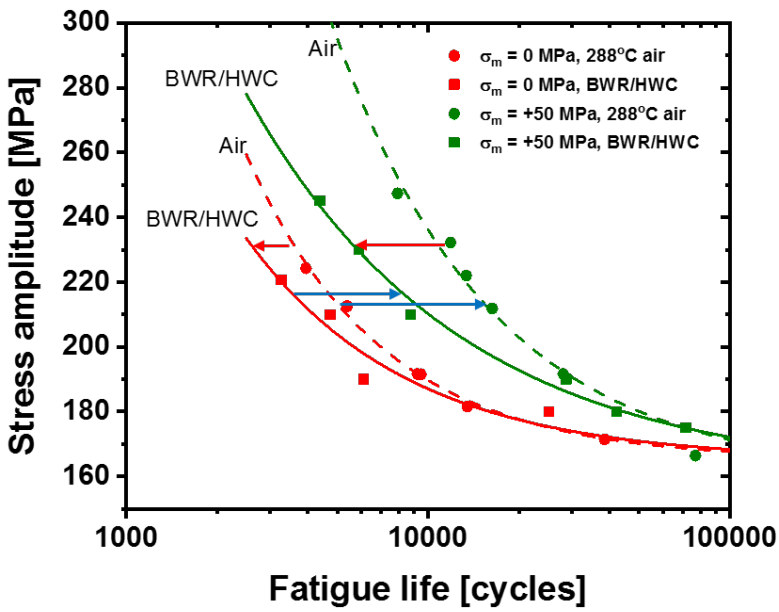

Figure 4.11 – Stress amplitude versus fatigue life in LCF regime ($N_f < 10^5$) of tests in air and BWR/HWC at 288°C.

For a more quantitative analysis, we defined the environmental factors, which are calculated from the stress-life data, as:

$$F_{en,0} = \frac{N^0_{air}}{N^0_{water}}|_{\sigma_m=0} \tag{4.11}$$

$$F_{en,50} = \frac{N_{air}^{50}}{N_{water}^{50}}|_{\sigma_m=50} \tag{4.12}$$

The environmental factors of σ_m = 0 MPa and σ_m = +50 MPa at different stress amplitudes are presented in Table 4.2, where the F_{en} are always larger than 1 and $\frac{F_{en,0}}{F_{en,50}}$ are always smaller than 1.

Table 4.2 – Environmental factors at different mean stress conditions based on stress-life data.

$\sigma_a[MPa]$	$F_{en,0}$	$F_{en,50}$	$\frac{F_{en,0}}{F_{en,50}}$
250	1.44	2.17	0.66
220	1.37	1.75	0.78
190	1.08	2.30	0.83

By combining Equ. 4.11 and Equ. 4.12, we get:

$$\frac{N_{water}^{50}}{N_{water}^{0}} = \frac{N_{air}^{50}}{N_{air}^{0}} \times \frac{F_{en,0}}{F_{en,50}} \tag{4.13}$$

where $\frac{F_{en,0}}{F_{en,50}} < 1$, thus $\frac{N_{water}^{50}}{N_{water}^{0}} < \frac{N_{air}^{50}}{N_{air}^{0}}$. In other words, the beneficial factors of +50 MPa mean stress is smaller in HTW than those in HTA.

It has already been shown that positive mean stress enhances the environmental degradation of HTW during cyclic loading in stress-life representation [13][11][12]. Our results confirmed this observation and show negative correlation between σ_a and $\frac{F_{en,0}}{F_{en,50}}$ as seen in Fig. 4.8. Tests with positive mean stress lead obviously to a longer exposure time of the crack tip to HTW environment during the tensile loading. All possible HTW degradation mechanisms, which include the slip oxidation/dissolution and the hydrogen-induced cracking mechanisms, are favored by the loading condition with positive mean stress, reflected by a higher K_I and higher $\epsilon_{p,max}$. The investigation of inner surfaces of post-test specimens tested with +50 MPa mean stress in HTW (Fig. 3.35) and HTA (Fig. 3.37) indicates that higher strain and more wavy dislocation structures were formed at the surface in HTW than in HTA. Thus HTW exerts bigger degradation impact with positive mean stress, the impact of +50 MPa mean stress on fatigue life is smaller in HTW than in HTA.

4.3.2 HCF regime

In the HCF regime (as Fig. 4.12 shows), tests with -20 MPa and 0 MPa mean stresses have significantly higher fatigue limit in HTW than in HTA. The fatigue limit difference at +50 MPa

mean stress condition is insignificant and is still in the range of uncertainty in determining the fatigue limit. The comparison between the fatigue limits in HTW (grey curve) and in HTA (red curve) shows that in HTW the fatigue limit is much more sensitive to the mean stress. From a mean stress of -20 MPa to +50 MPa, the fatigue limit decreases by ≈ 6 MPa in air while it drops by ≈ 43 MPa in BWR/HWC. All fatigue limits are attained at an average strain amplitude of ≈ 0.1%, as Fig. 3.7 and Fig. 3.10 show, at which the environmental effects disappear. This is true when $\sigma_m \geq 0$ but it is not necessary the case for the tests with $\sigma_m < 0$, when the oxide-induced crack closure effect is more pronounced. This is also reported by Zerbst [31] in studying compressive residual stress effects on crack closure of welds working in corrosive environment.

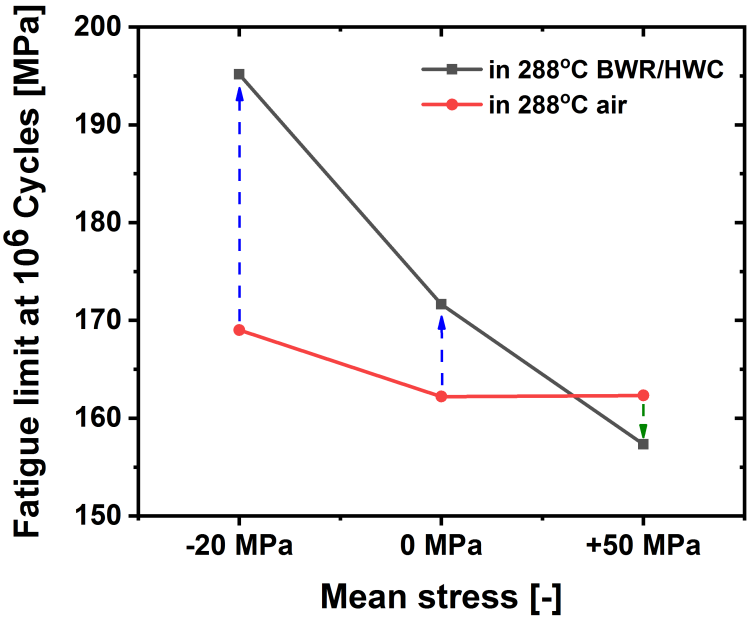

Figure 4.12 – Fatigue limit of stress amplitude at 10^6 cycles versus mean stress of tests in air and BWR/HWC at 288°C.

In order to verify the hypothesis that oxide-induced crack closure happens in HCF regime with negative mean stress, the cracks on the specimen wall cross sections of specimens tested in HCF regime were investigated. For the run-out specimens ($N_f \leq 10^6$), almost no crack on the polished wall cross sections was observed with HRSEM. For the specimens with higher stress amplitudes, cracks growing parallel to loading axis were exclusively observed for the specimens tested with -20 MPa mean stress, as Fig. 4.13 shows. The SEM observation of Fig. 4.14a shows that the crack is filled with particles and different phases from the steel matrix, which were identified as iron- and chromium- oxides through EDX characterization. This indicates the cracks may be arrested, but the exact reason is still unclear. Some SEM and EDX observations revealed that the cracks, formed with -20 MPa mean stress, coalesce with elongated MnS inclusions, which are normally aligned parallel to loading axis.

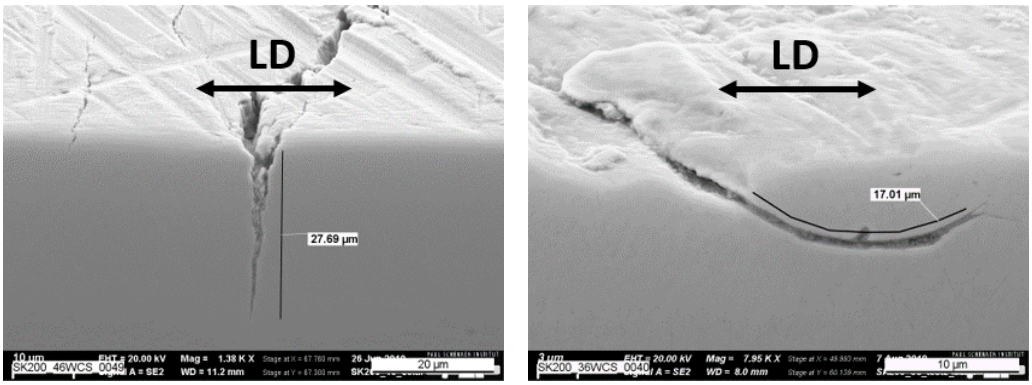

(a) (b)

Figure 4.13 – Observed cracks on wall cross section of after-test specimens with σ_a = 210 MPa (a) +50 MPa mean stress and 1000 cycles loading, (b) -20 MPa mean stress and 10000 cycles loading in BWR/HWC at 288°C.

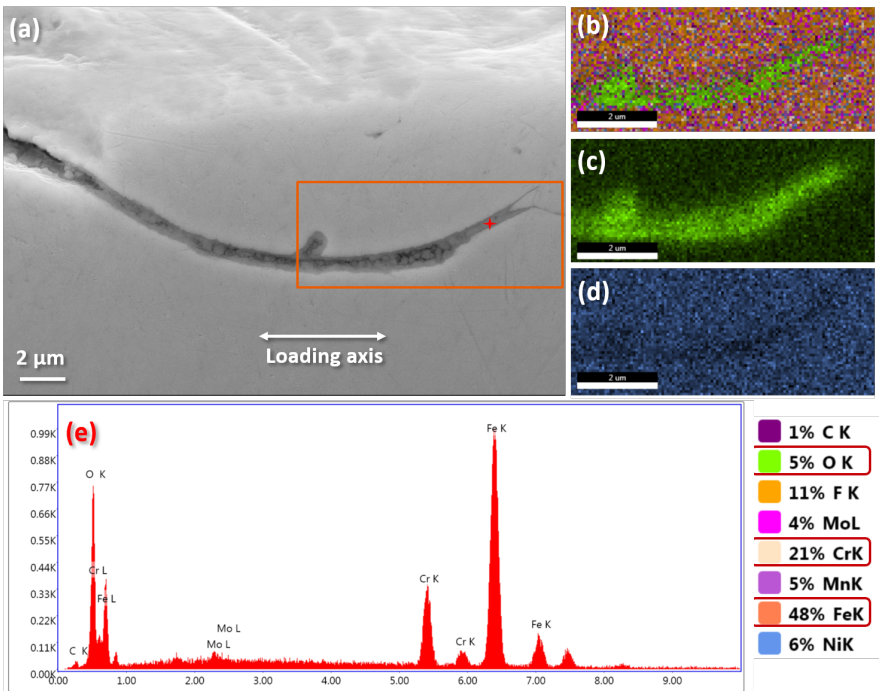

Figure 4.14 – EDX characterization of crack on wall cross section of after-test specimen with σ_a = 210 MPa, σ_m = -20 MPa loaded to 10000 cycles in BWR/HWC at 288°C. (a) is the SEM image of the crack, (b-d) are element mapping images, (e) is the spectroscopy at the location marked with red star in SEM image.

4.4 Specimen geometry and pressurized water effects on fatigue

Hollow specimens have already been used by many authors to assess fatigue life in LWR environments or in air [164][165][166][167][147][168][169]. This type of specimen presents several advantages. In particular, it is more easily mounted in a standard testing machine than in an autoclave device and the measurement of the strain is done directly with a clip extensometer on the straight segment of the specimen gage length. This yields a very precise strain measurement and control. However, the main drawbacks of pressurized hollow specimens reside in the fact that there is a certain degree of uncertainty regarding their fatigue behavior when compared with that of solid specimens or with other hollow specimen geometries and/or different internal pressure. Any difference in fatigue behavior is likely to stem from the triaxial stress state in the pressurized specimens. Other influencing factors can also come into play such as: temperature gradient through the wall thickness and surface preparation difference between the inner and outer surface. For the time being, despite a number of investigations carried out by several authors on this topic, there is no clear experimental evidence indicating whether a direct comparison between various geometries of pressurized hollow specimens with unpressurized and solid specimens can be done or if some fatigue life adjustment factor have to be taken into account. The individual conclusions of these studies are somewhat contradictory, incomplete and difficult to reconcile. Only an extended and well-designed experimental program to evaluate the effect of specimen geometry and internal pressure on fatigue life of hollow specimens tested in load-controlled and strain-controlled mode can alleviate all the uncertainities regarding difference in fatigue behavior. Nevertheless, the results of the limited number of tests we performed on various hollow specimen geometries reveal some trend that are discusses hereafter.

Fig. 4.15 illustrates the stress state in a pressurized specimen at 200 bar and presents the corresponding values calculated by finite elements of the hoop stresses on the internal surface of unloaded specimens for different values of the wall thickness and pressure. Fig. 4.15a shows a higher von Mises stress at the inner surface. Table in Fig. 4.15b shows that higher pressure or thinner wall thickness lead to larger von Mises stress. During cyclic loading, the hoop and radial stresses are practically constant while the axial stress varies. In this typical situation, the von Mises stress is larger in compression than in tension [11] for a given absolute value of the axial stress. As a consequence the plastic strain is correspondingly larger in compression, which provides a reasonable explanation of the behavior observed in Fig. 3.2 and in Fig. 3.4. Indeed for these tests, we saw that higher internal pressure produces larger fatigue life and that the minimum strain (in compression) is correspondingly larger. However, the internal pressure change is insufficient to make significant effect on fatigue life.

Besides the investigation of internal pressure effect, fatigue lives of specimens with different (2.5, 2.0, 1.5 mm) wall thickness are plotted in Fig. 3.18 for tests in HTA, Fig. 3.19 and Fig. 3.20 for tests in HTW. For the tests in HTA, the specimen wall thickness does not systematically shift the fatigue life neither without mean stress nor with mean stress at least in the LCF regime. For the tests in HTW, specimen wall thickness has a significant impact on fatigue life and show

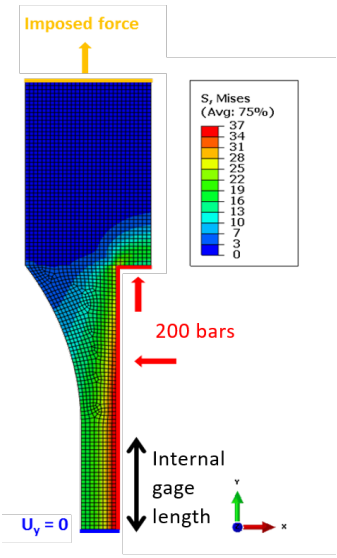

(a)

Stress state on the internal surface, unloaded specimen (axial stress = 0 MPa)				
Pressure (bars)	Specimen wall thickness (mm)	Hoop stress (MPa)	Radial stress(MPa)	Mises (MPa)
100	2.5	17	10	23
200	2.5	33	20	47
200	2.0	42	20	55
200	1.5	58	20	70

(b)

Figure 4.15 – (a) FEA analysis of stress state of pressurized hollow specimen, (b) stress triaxiality dependence of internal pressure and specimen wall thickness [11].

complex synergistic effects with stress amplitude and mean stress. From this analysis of the distinct fatigue life response in HTA and HTW to different wall thickness, we conclude that the wall thickness itself is not the only reason for the difference in fatigue life, but it is due to concomitant effects.

At least in load-controlled fatigue tests, the internal pressure affects the overall strain evolution during an experiment. Different strain amplitudes (in Fig. 3.21-Fig. 3.23) and mean strain (in Fig. 4.16-Fig. 4.18) were developed in specimen with different thickness and pressure. Smaller strain amplitude was found in the specimens with thinner wall thickness, as stronger cyclic hardening occurs. However, it is not necessary the specimen with the thinnest WT (1.5 mm) has the lowest strain amplitude, such as the tests in Fig. 3.22, where the specimen with 2.0 mm WT has the lowest strain amplitude and longest life. When the mean strain developed in specimens with different WTs, we found that the specimens with 2.0 mm WT have less mean strain in the compressive direction and are closer to 0%. Looking at the ramping starting cycles of tests with σ_a = 190 MPa, whose strain amplitude and mean strain evolution is plotted in Fig. 3.22 and Fig. 4.17, we see that the specimens with 2.5 and 1.5 mm WT develop more plastic strain in the compressive direction, while specimens with 2.0 mm WT has the lowest strain amplitude and ratcheting. The pressurized water induced stress triaxiality must affect materials elasto-plastic behavior, which is synergistically affected by stress amplitude and mean stress. The complex relationship behind the elasto-plastic behavior is still unclear, a systematic FEM constitutive modeling may help to reveal it.

The internal pressure and specimen wall thickness effect (namely stress triaxiality effect) seem more relevant in HTW than at room temperature. This may because of lower yield strength at

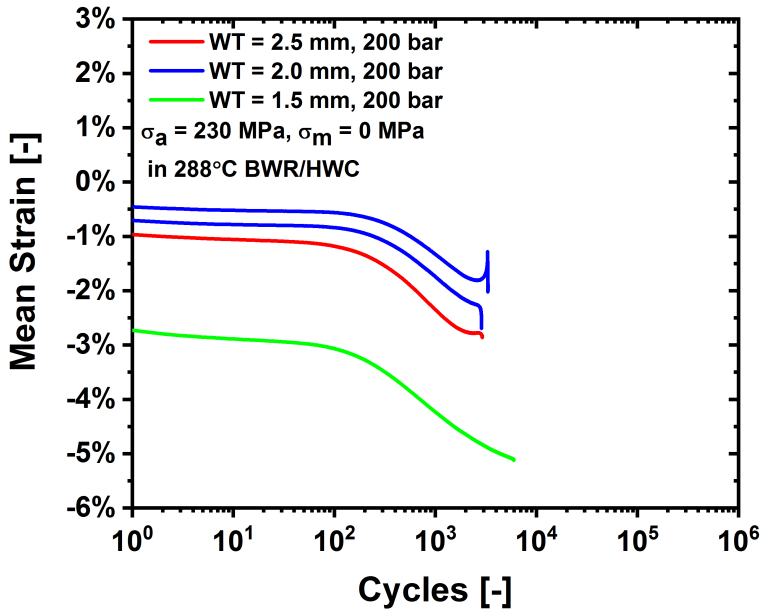

Figure 4.16 – Mean strain evolution along loading cycles of tests for specimens with different WT, σ_a = 230 MPa and σ_m = 0 MPa in 100/200 bar BWR/HWC environment at 288°C.

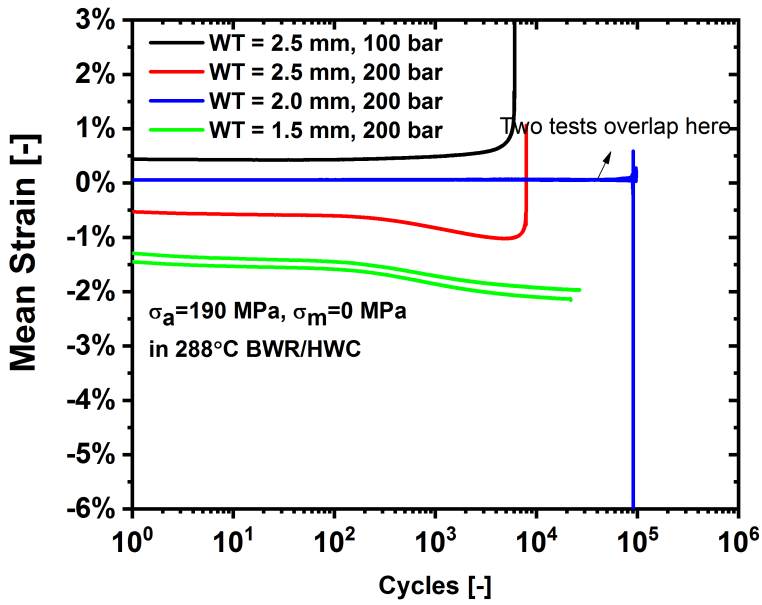

Figure 4.17 – Mean strain evolution along loading cycles of tests for specimens with different WT, σ_a = 190 MPa and σ_m = 0 MPa in 100/200 bar BWR/HWC environment at 288°C.

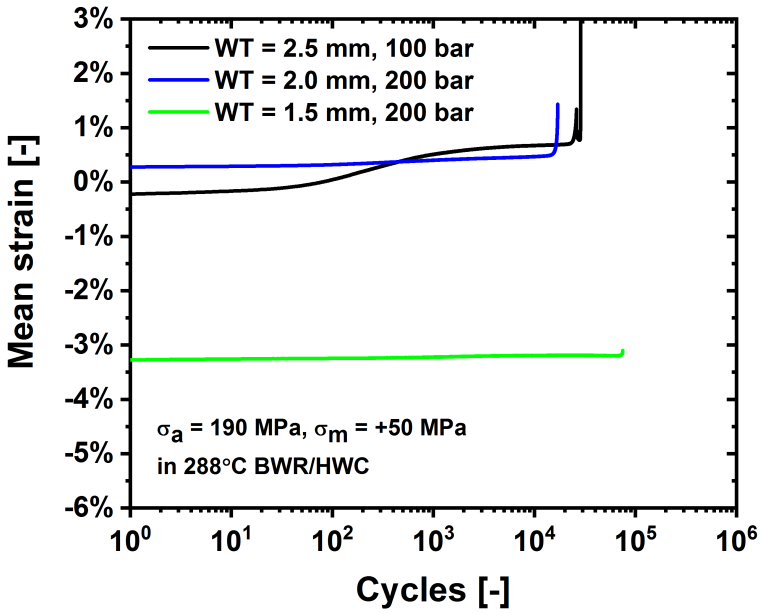

Figure 4.18 – Mean strain evolution along loading cycles of tests for specimens with different WT, σ_a = 190 MPa and σ_m = +50 MPa in 100/200 bar BWR/HWC environment at 288°C.

high temperature (260 MPa at 22∘C and 150 MPa at 300∘C for 0.2% yield strength), where the triaxiality difference may trigger more pronounce effect on plastic deformation, which is the main factor determines fatigue (initiation) life.

The stress state analysis in Fig. 4.15a shows higher stress at locations close to inner surface. Accordingly, we observed that almost all cracks initiated from the inner side of specimens tested in HTW. Higher strain and more wavy dislocation structures were developed at inner surface in HTW than the surface in HTA or outer surface, as depicted in Fig. 3.35-Fig. 3.38. The scratches on specimen surface may act as stress raisers. We also observed more than 80% cracks initiated at/grew along the scratch grooves (presented in Section 3.4). Thus we assumed surface roughness, corrosive environment and higher stress at inner surface cooperatively affect the crack initiation in HTW, which contributes most to the fatigue life difference in HTW and HTA.

Nano-hardness measurements were carried out to possibly reveal inhomogeneity in the accumulated plastic strain through the specimen wall. The contour profile of hardness results plotted in Fig. 4.19. Fig. 4.19b shows higher hardness at inner and outer surfaces of original material, which is a clear indication that compressive residual stress were introduced during specimen manufacture. The scales of hardness are unified for analysis convenience. We get two insights: (1) generally higher hardness was determined in the tested specimens, but without significant difference between materials tested with different mean stresses; (2) higher hardness values were found at locations close to inner surface. This is consistent with FEA

analysis and the deformation characterization of inner surface of the tested specimens, which is presented in Section 3.4.

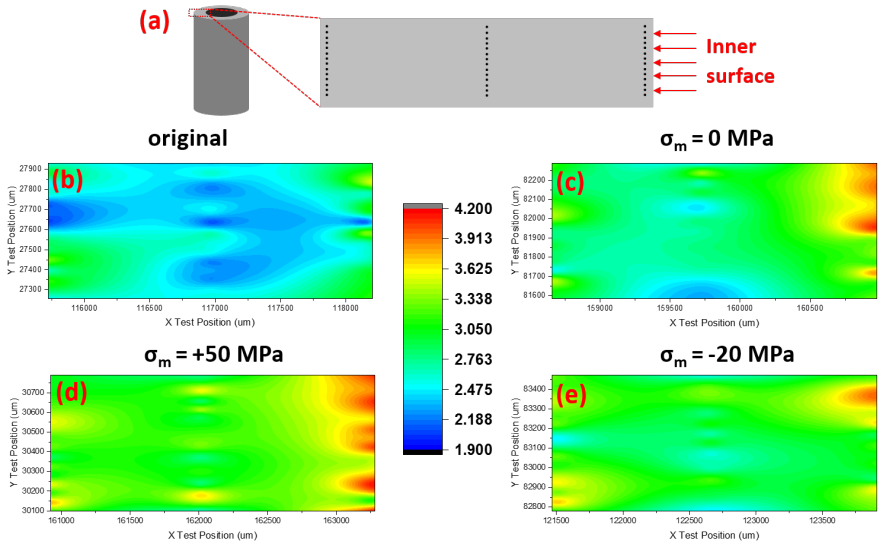

Figure 4.19 – Hardness measured with G200 nanoindentor along the wall radial direction. (a) schematic illustration of specimen cutting and hardness measurement. Locations close to surfaces within 20 μm are measured. (b) for original material, (c) for after-test specimen with σ_a = 210 MPa & σ_m = 0 MPa, (d) for after-test specimen with σ_a = 210 MPa & σ_m = +50 MPa, (e) for after-test specimen with σ_a = 210 MPa & σ_m = -20 MPa.

4.5 Control mode effects on fatigue

In section 3.1.4, the tests performed under strain-control and load-control mode are compared. If one considers the average strain amplitude (for load-controlled tests) or the average stress amplitude (for strain-controlled tests) to predict the fatigue life, these two different control modes yield the same fatigue life curve, only a slight difference can be seen in the HCF regime.

Although multiple cracks were developed during cyclic loading in both control modes, more cracks in load-controlled specimens than in strain-controlled specimens were observed from the post-test observation of cracks on inner surfaces, as shown in Fig. 4.20. Under load-control, the whole gage section undergoes the same stress before crack initiation. Once cracks have been initiated, locations with cracks have higher true stress than at other locations, where the stress is unchanged. Minor cracks (at other locations excluded the location of main crack) initiate once the damage threshold is achieved. Under strain control, the whole gage section deforms homogeneously before crack initiate. After crack initiation, the local deformation around the main crack contributes more to the measured strain so that the strain at other locations will be relaxed and the number of secondary cracks is lower. Although we observed that a different number of cracks were formed and different local stress/strain of main crack in load-/strain-controlled tests given same macro stress/strain amplitude, the fatigue lives

and stress-strain relationships of load-/strain-controlled tests show good consistence. As discussed in Section 4.7 below, the number of cycles to create a long crack (> 0.6 μm/10 grains) account only for about 20% of fatigue life in the tests presented in Fig. 4.28. Thus ≈ 80% of fatigue life is spent for crack initiation, microstructurally short crack and mechanically short crack, where the above described phenomenon is not pronounced because the main crack is still short. The phenomenon leading to a difference in crack density between the two modes occurs during the growth of long crack, which only accounts for small percentage of fatigue life. This is why we still observed consistent fatigue lives (in Fig. 3.12-Fig. 3.15) and macro stress-strain relationships (in Fig. 4.22 and Fig. 4.23) obtained under both control modes.

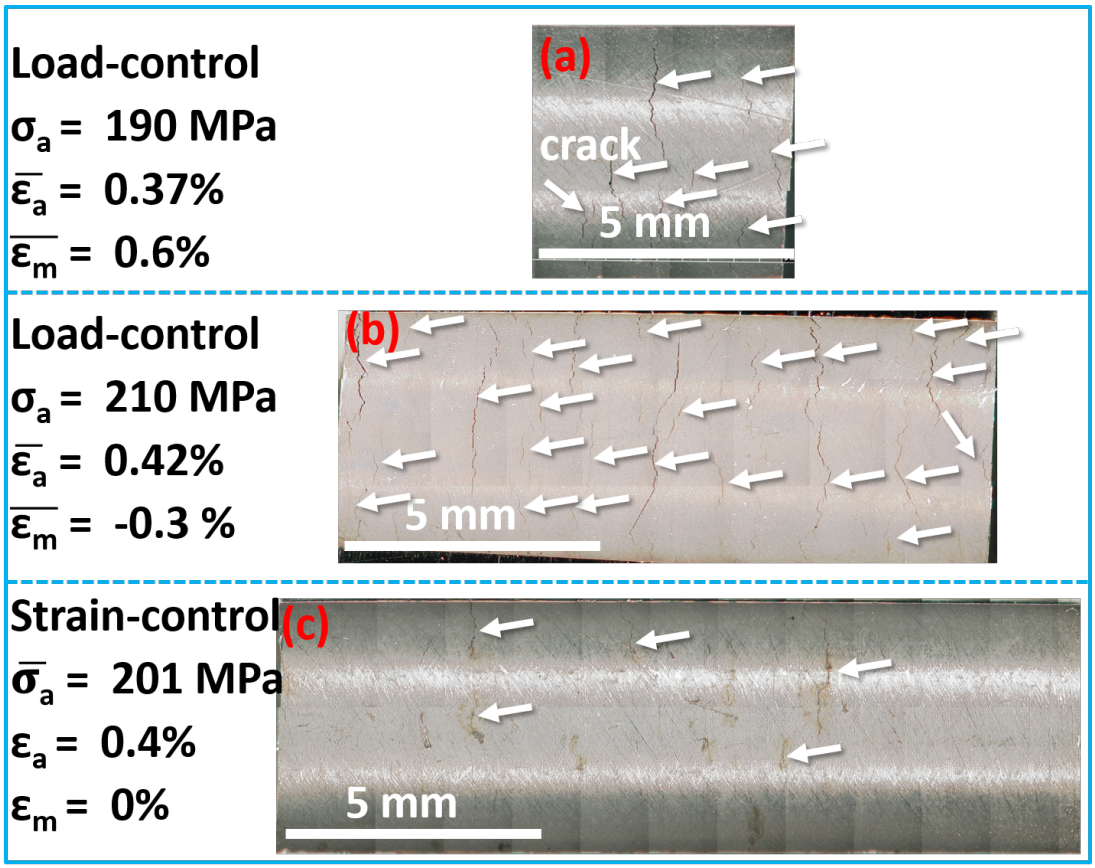

Figure 4.20 – Observation of the cracks on specimen inner surfaces, (a) and (b) tested under load-control, (c) tested under strain-control. For comparison, the three specimens with similar σ_a, ϵ_a and ϵ_m are selected. The arrows highlights the cracks.

The measured strain, both in strain control and load control, is the macro strain of the measured gage section, which consists of the strain of main crack and minor cracks. Thus, under the same strain amplitude, the main crack in strain control should undergo bigger deformation than the main crack in load control for which more cracks open and contribute to the measured strain. Nevertheless, we observed almost a similar crack growth rate of main crack when two tests loaded with similar (average)stress/(average)strain, even though they

are loaded under different control modes, as Fig. 4.21 shows. Thus, it appears that the control mode does not significantly affect the crack growth rate. Given that the material is deformed homogeneously along the gage length before crack initiation, no matter in load control or in strain control, the control mode should not affect crack nucleation phase if loaded with the same stress/strain level.

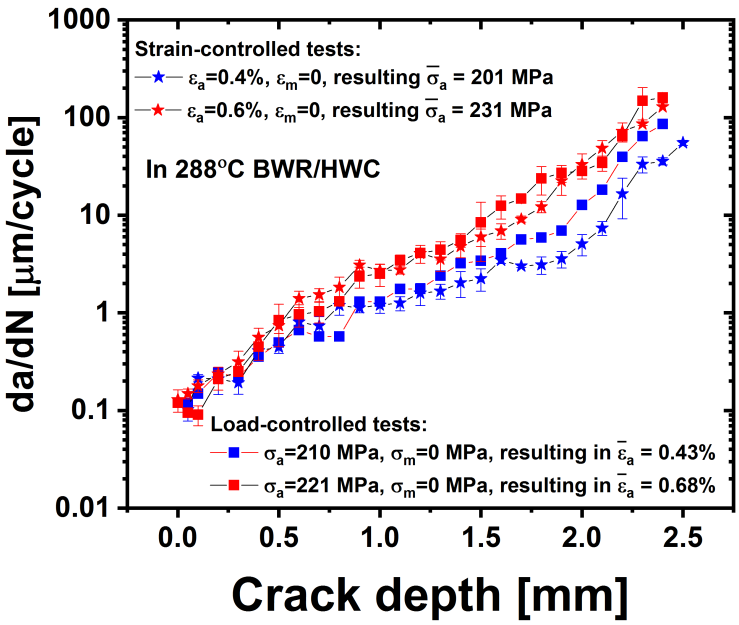

Figure 4.21 – Crack growth rate versus crack depth of two pairs of tests. The two tests marked with square are under load control, the other two tests marked with stars are under strain control.

Observation of similar fatigue lives in both control modes in stress-life and strain-life representations (in Fig. 3.12-Fig. 3.15) supports our interpretation. In addition, consistent cyclic stress-strain relationships of tests in both control modes, as Fig. 4.22 and Fig. 4.23 support it as well.

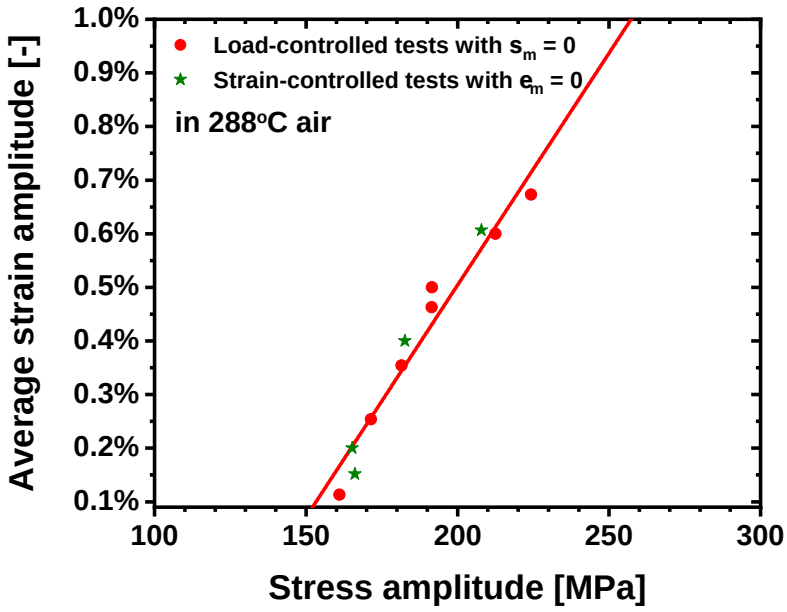

Figure 4.22 – Strain-stress of tests conducted under strain- and load-control in air at 288°C.

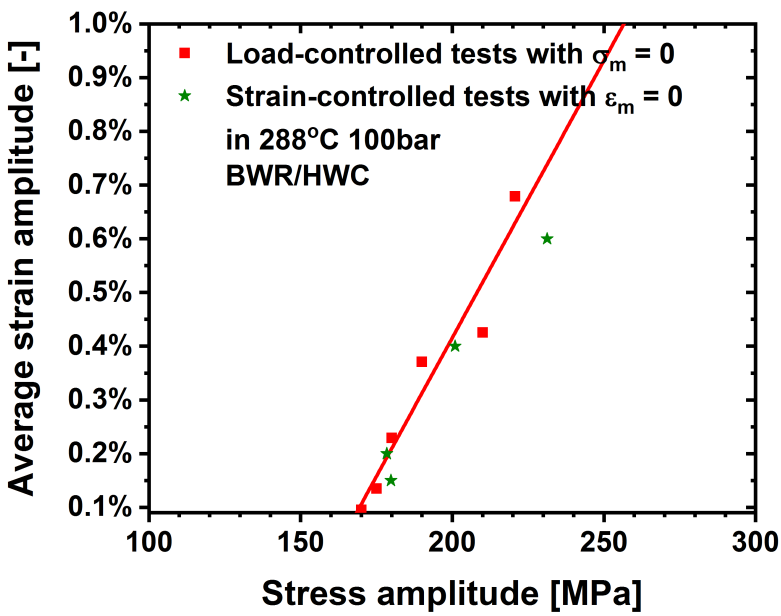

Figure 4.23 – Strain-stress of tests conducted under strain- and load-control in 100 bar BWR/HWC environment at 288°C.

4.6 Correlation between microstructures and fatigue behavior with-/without mean stress

In fatigue tests of austenitic SSs, mean stress was observed to extend fatigue life, as a result of smaller strain amplitude at a given stress amplitude. In symmetrical cyclic loading, correlation between microstructures and cyclic stress-strain behavior, for single and polycrystals, has been studied by many authors at room and high temperature over a wide range of strain amplitudes [89][98][93][104][101][25][97]. This was reviewed in Section 1.5. The unconventional fatigue behavior of SSs with mean stress is ultimately related to the development of dislocation microstructures during cyclic deformation.

Normally, only few dislocations in planar configuration exist in the solution annealed as-received materials. In the first cycles, the dislocation density increases and is responsible for primary cyclic hardening, as Lomer-Cottrell locks impede dislocation motion [103][170][104]. With higher local stress/strain, cross slip and secondary slip is activated. Formation of dislocation tangles lowers the activation energy for cross slip. Cross-slip enhances screw dislocations annihilation and shortens edge dislocations. This results in dislocation-rich and -poor structures. With further loading, these structures transform into dislocation-free regions (channels) and dislocation dense walls. Cross-slip, dislocation annihilation and formation of dislocation-free regions are related to cyclic softening [171] [104]. Dislocation channel/wall structures create high plastic incompatibilities that increase local strain and activate dislocation slips on the secondary slip systems. These systems interconnect with dislocation walls and further transform the wall/channel structure into cellular structures, which finally constrain dislocation motion responsible for to the plateau stage [104]. This provides a general picture of the correlation between microstructures and cyclic stress-strain response. The formation, onset of appearance and amount of typical microstructure depend on material properties, e.g. SFE, temperature, stress/strain level, and stain rate [16][104].

Correlation between microstructures and mean stress was investigated with TEM and ECCI for specimens at the end life or loaded to a certain number of cycles. The microstructure observations are presented in Fig. 3.70 and Fig. 3.71 and Fig. 3.72. As described in Section 3.7, only planar dislocation structures were observed in the materials tested with either +50 MPa or -20 MPa mean stress, even for stress amplitude as high as 245 MPa. Conversely, more spatial dislocation structures (e.g. cells, channels/walls) were observed in materials tested without mean stress, even at the same average strain amplitude level. Without mean stress, localized high stress/strain promotes cross slip and activation of secondary slip systems, which are the foundations for spatial structures formation. The rearrangement of dislocations forms lower and more stable energetic structures (i.e., dislocation high/low density regions) which relieve the grain-grain plastic incompatibilities. On the other hand, formation of spatial structures raises other plastic incompatibilities between dislocation high/low density regions on a finer scale [104][172]. In the case of non-zero mean stress, observation of rare spatial structures reflects less strain localization. The key point here is to understand why fewer spatial dislocation structures and strain localization develop in the cases with mean stress.

In the first cycles of our tests, which include the special starting procedure with ramping loading cycles, material hardens due to an increase of dislocation density leading to decrease of strain amplitude with the cycle number. In the first cycles, only dislocations on primary slip plans are activated and dislocation multiplication is positively related to plastic deformation in the starting cycles. All specimens have the same initial microstructure. However, specimens tested with mean stress accumulate a larger plastic strain during the starting cycles as we have reported in Fig. 4.24. In other words, more dislocations were multiplied in the starting cycles with mean stress (this point was not experimentally verified with TEM observations). Anyway, the stress-strain response and microstructure observations at the later cycles agree well with this assumption. Since higher dislocation density produces more hardening in material, the tests with +50 MPa and -20 MPa mean stress have smaller strain in the first testing cycle and at the end of primary hardening, as Fig. 3.11 and Fig. 3.8 show. Tests with/without mean stress reach the saturation of dislocation density at almost the same number of cycles around 20 cycles.

The stacking fault energy (SFE) of 316L SS is quite low, lower than 0.02 Jm^{-2}. Consequently, the dissociation distance between Shockley partial dislocations is large, which does not favor cross-slip. Thus, relatively high local strain is necessary to activate cross-slip and activate secondary slips. As relatively low strain was induced for specimens with mean stress in the primary hardening stage, cross-slip is less probable. Cross-slip is the main reason of dislocation annihilation, formation of dislocation free/dense structures, which is related to cyclic softening. In the strain versus cycles figures (Fig. 3.11 and Fig. 3.8), we see that the specimens tested with mean stress have slighter cyclic softening and rare dislocation veins or dislocation channels/walls are observed in the materials tested with mean stress (as Fig. 3.70, Fig. 3.71 and Fig. 3.72 show). Multiple slip systems interconnection forms dislocation cells, which is seldom observed in the materials tested with mean stress.

In this work, the tests with low strain amplitude at high temperature with a fatigue life longer than 10^4 to 10^5 cycles showed that secondary hardening can occur. As discussed above, tests with mean stress harden materials more in the first hardening stage by producing denser dislocations and weaken material softening in the coming stage via less probable cross-slip and less formation of dislocation moving relaxation structures (e.g. veins, channels/walls). This results in materials tested with mean stress having smaller strain and less strain localization, which ensure the material could be loaded to bigger number of cycles and trigger secondary hardening happening. Thus secondary hardening was often observed in the tests with mean stress, which could run $N_f > \approx 10^4$ to 10^5 cycles. Secondary hardening further strengthens the material and contributes to longer fatigue life. However, no sufficient and necessary condition between occurrence of secondary hardening and mean stress was found. Mean stress may work as a favorable factor to promote occurrence of secondary hardening through sustaining planar configuration of dislocations and preventing formation of relaxed dislocation structures. Corduroy structures were formed exceptionally in the secondary hardening stage. It is composed of lines of small point defect clusters and regular alignments of faulted dislocation loops in $\{111\} < 112 >$ according to [104]. Corduroy structure impedes dislocation movement

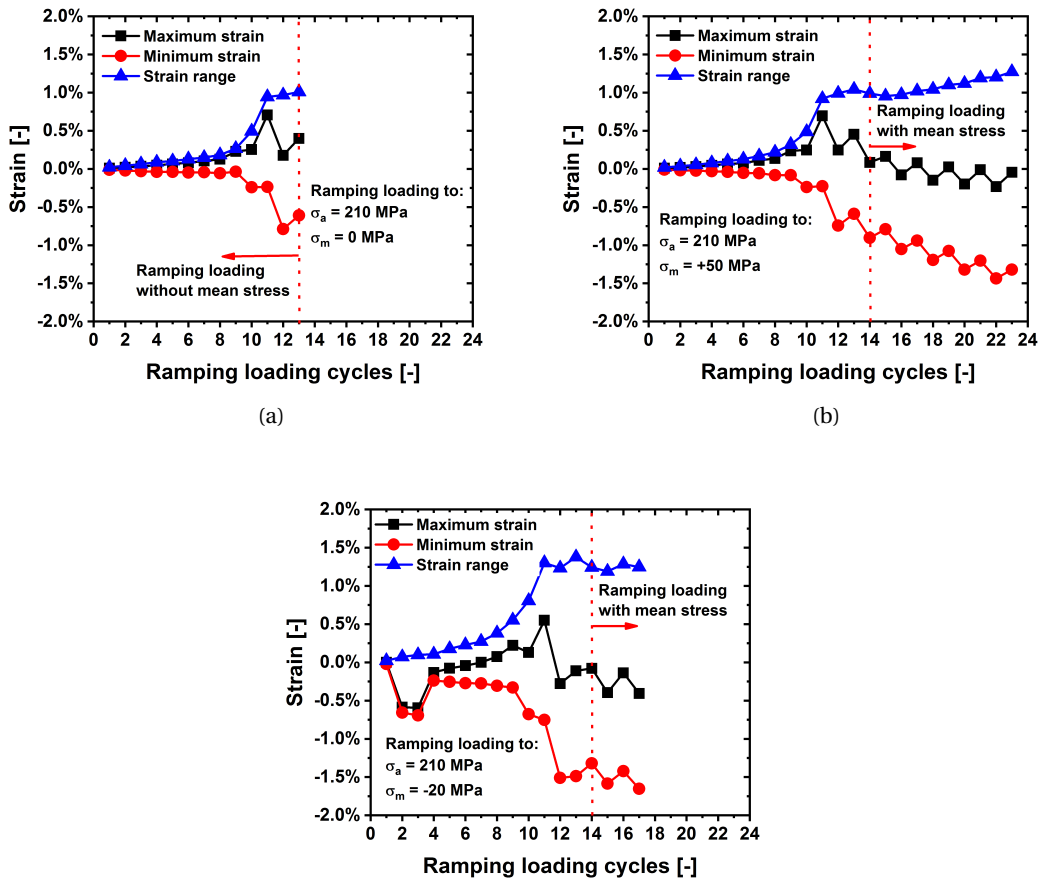

Figure 4.24 – The strain values (maximum, minimum and range) during the ramping loading cycles at the beginning of tests (a) σ_a = 210 MPa, σ_m = 0 MPa, (b) σ_a = 210 MPa, σ_m = +50 MPa, (c) σ_a = 210 MPa, σ_m = -20 MPa. Details of ramping loading procedure are described in Section 2.3.2.

(as Fig. 3.73) and leads to significant hardening behavior.

4.7 Crack growth

4.7.1 Crack growth rate correlation

The stress intensity factor (SIF) K_I is commonly correlated with the crack growth rate. This approach is valid only for small scale yielding conditions (SSY), i.e., when the plastic zone size is very small with respect to any other characteristic specimen and crack dimensions, as it is usually the case with large compact tension specimens. Such SSY-conditions are evidently not met in smooth specimens where the entire ligament is plastically deformed. Thus, the concept of stress intensity factor to derive crack growth laws cannot be justified on a sound basis for smooth specimens. One option is to consider the strain intensity factor K_ϵ, which was recently shown by Kamaya [147] to be useful to study the crack grow rate. Kamaya [147][80] as well as Zhang et al. [152] showed that the strain intensity factor ($\triangle K_\epsilon$) yields better correlation with crack growth rate than SIF for austenitic stainless steels. The physical meaning of the strain intensity factor was discussed in [148][80] but is not be universally accepted. Another physically-based possiblity is to take into account the stress, the plastic deformation and cyclic hardening parameters by using the approximate expression of the J-integral. Dowling [35] [34], Haddad [149], Findley [37], Chen [155], Polak [150], Hutař [153] and Mann [156] have used the J-integral but with different expressions to correlate crack growth rate in cylindrical specimens. This modified J-integral (described by Equation 3.40) takes into account the strain, the stress and the hardening. The above mentioned K_I and $\triangle K_\epsilon$ can only be applied to limited condition, either elastic deformation dominates or plastic deformation dominates. The modified J-integral approach provides a generalized solution for studying crack growth law in the situation with co-occurrence of elastic-plastic fracture mechanics.

4.7.2 Crack growth stages

We found that mean stress, stress amplitude and environments have influence on the different crack growth stages. Thus, it is necessary to precise first the adopted classification of the different crack growth stages we chose, as no universal definition of crack growth and initiation stages is to be found in literature.

As described in Fig. 4.25, a fatigue crack experiences three phases of growth: microstructurally short crack (stage I shear crack), mechanically short crack (stage I tensile crack) and long crack (stage II tensile crack) [31]. Normally, most microstructurally short cracks, which grow along their slip plane, will be arrested at grain boundaries or other obstacles. For the short crack growth stage, linear elastic $\triangle K$ concept is not applicable. In long crack growth stage, the $\triangle K$ concept shows a power law correlation with crack growth rate, which corresponds the well-known Paris law valid in SSY.

Fig. 4.26 shows two representative correlations between the crack growth rate and K_I of tests performed in air. The linear relationship segment, starting from $\approx 0.6\ \mu m/10$ grains, is referred as to long crack stage. The section between 50 μm and 0.6 mm is the so-called mechanically

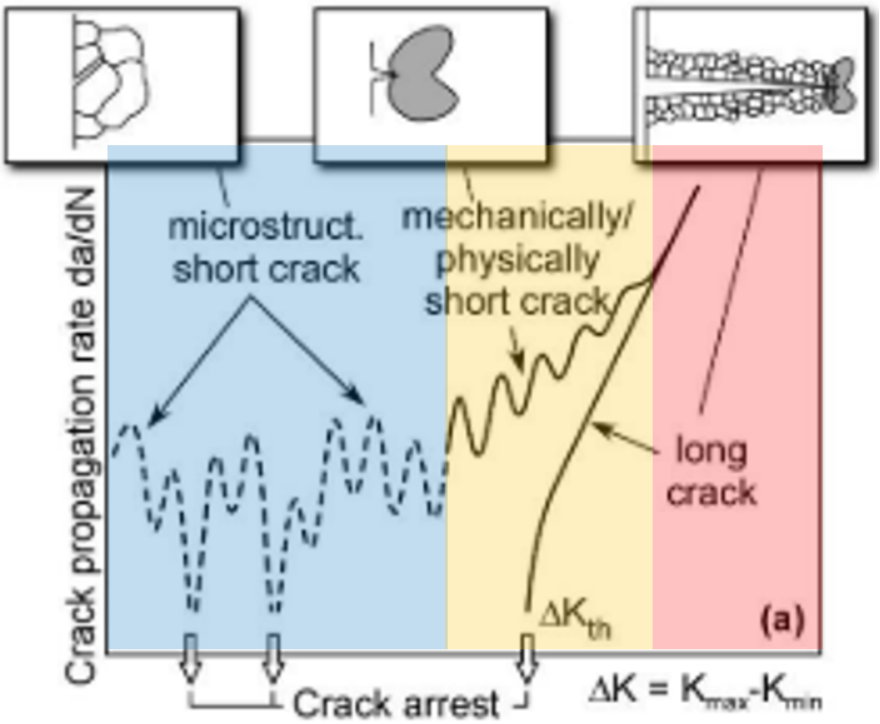

Figure 4.25 – Description of the different stages of fatigue crack growth, considering crack growth rate versus stress intensity factor.

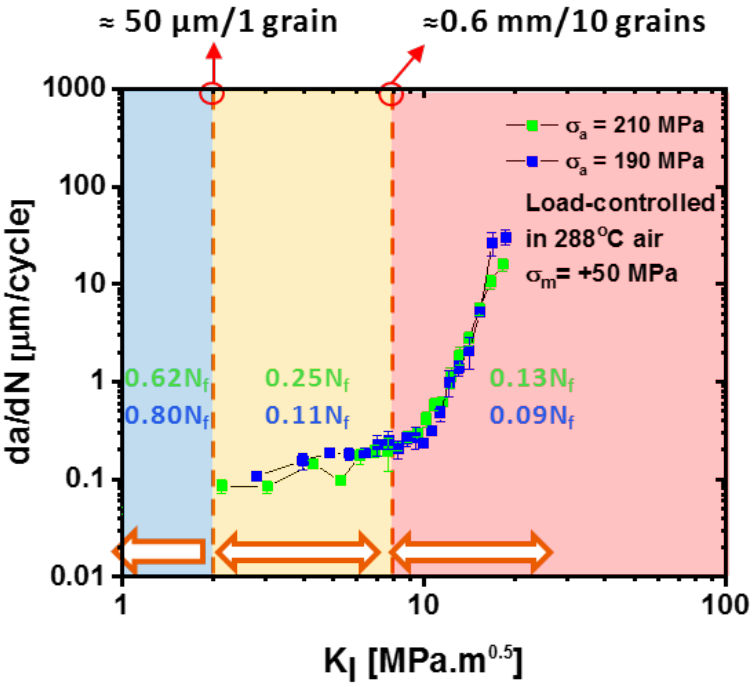

Figure 4.26 – Crack growth rate versus stress intensity factor.

short crack, where the $\triangle K$ concept does not apply and is mostly driven by the plastic strain field. The different crack growth laws in short crack ($< \approx 0.6$ mm) and long crack ($\geq \approx 0.6$ mm) regimes were corrected by introducing an effective crack length in the Equation 3.27. The microstructurally short crack within one grain/microstructure ($\leq 50\ \mu m$) usually grows along its slip plane as a type of shear crack. If stress concentrators such as scratches, pits, inclusion exist, the stage I of microstructurally short crack may vanish. In our case, striation spacing/crack growth rate within the first 50 μm of crack length was difficult to measure. Thus no crack growth data was presented for this stage.

4.7.3 Influential factors on crack growth

Mean stress effect

The correlation between crack growth rates and K_I of tests in HTW and HTA are plotted in Fig. 3.50 and Fig. 3.58 respectively. From the two figures, we see that K_I does not correlate the crack growth rates with different mean stresses well. Cracks with mean stress — no matter if positive or negative — present larger propagation resistance against K_I. This implies that K_I alone does not represent the driving force for crack growth in smooth specimens with mean stress. Therefore, we chose $\triangle K_\epsilon$ and J-Integral as the parameters to correlate the crack growth rates with mean stress. Fig. 3.51 and Fig. 3.52 illustrate the correlations with $\triangle K_\epsilon$ and Fig. 3.55 and Fig. 3.54 illustrate the correlations with J-Integral. Comparing with the correlations with K_I, the mean stress effect is much better taken into account by the correlations with $\triangle K_\epsilon$ and J-Integral. This implies the main driving force for crack growth is related to the strain factors. As discussed in Section 3.1, mean stress enhances cyclic hardening. The degree of hardening, which can be related to the hardening exponent n, depends on mean stress. In light of the correlations with $\triangle K_\epsilon$ and J-Integral, mean stress does not have a significant influence on the resistance to crack growth.

Environmental effect

The dependence of crack depth on loading cycles and on life fraction are plotted in Fig. 4.27 and Fig. 4.28 respectively. Based on the above mentioned classification of crack growth phases, the crack growth showed in Fig. 4.27 and Fig. 4.28 are divided into three phases as well, whose corresponding loading cycles are calculated. From the crack growth and initiation life analysis, most life difference between two environments comes from the difference in cycles needed to form a 0.05 mm depth crack, which is indicated as the region under blue dash line. In mechanically short crack region, the blue and red curves have approximately a similar shape and tangents. This suggests that they have a similar crack growth rate. In the last phase of long crack, both cracks experience very close number of cycles (1878 cycles in water and 2151 cycles in air). However, a higher life fraction for the test in HTW (0.22 N_f) than in HTA (0.13 N_f) is required at the end of life. The life fractions accounted by each phase are shown in Fig. 4.28 in detail. For the test in HTW, the mechanically short crack and long crack phases account

for a relatively larger fraction of fatigue life. Tests in HTA need larger fraction of life to form a physical short crack (0.5 mm depth).

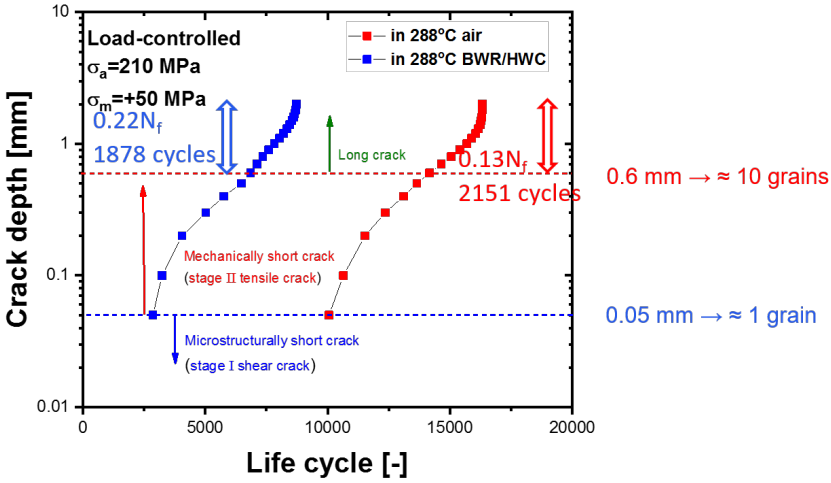

Figure 4.27 – Dependence of crack depth on loading cycles for the load-controlled tests with σ_a = 210 MPa and σ_m = +50 MPa in air and BWR/HWC at 288°C.

As described in Fig. 4.27 and Fig. 4.28, HTW environment affects mostly the phases before the formation of physical short crack. Fig. 4.29 was plotted to see how environment affects the physical crack initiation life and the crack growth life respectively. Analyzed in combination of Fig. 4.10, environment does not significantly change crack growth life and the decrease of total fatigue lives in HTW mainly comes from their shorter physical crack initiation life, given Fig. 4.29 shows 1.6 factor of total fatigue life decrease and around 1.7 factor of crack initiation life decrease between the tests in HTW and HTA.

LWR environments were well known to accelerate crack growth in corrosion fatigue [4][5] and EAF [3][27]. Most of these studies were performed with pre-cracked CT specimens or at severe mechanical loading condition (higher strain amplitude and slower strain rate) and environmental condition (PWR). In high strain amplitude condition, crack initiates very early and crack propagation accounts for almost total fatigue life. In slow strain rate condition, HTW has longer contact with crack during opening and environmental degradation plays big role in crack growth. The strain rate of the tests in this work resulted in only slight reductions in fatigue lives. The crack-tip strain rate for the main cracks is one to two magnitudes higher than the nominal strain rate of the test and thus potentially above the strain rate threshold for EAF. The absence of any environmental effects on crack growth in the late phase of fatigue life is thus not surprising in this context.

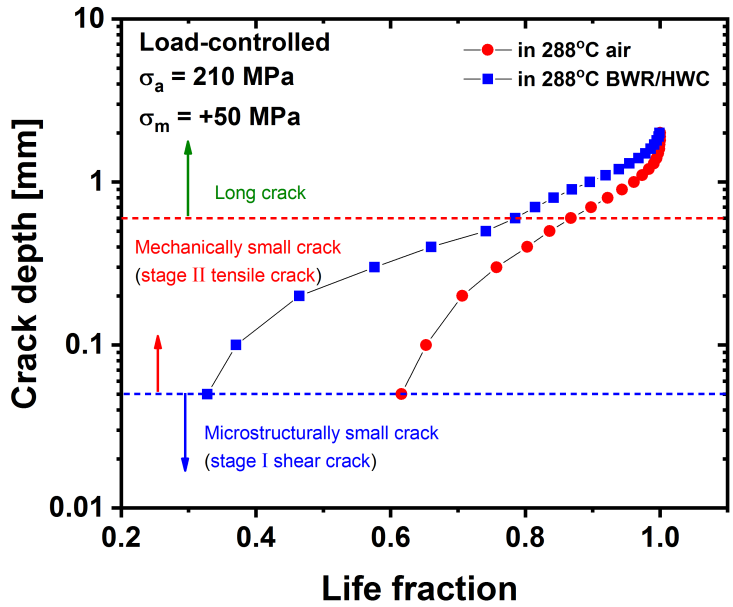

Figure 4.28 – Dependence of crack depth on life fraction (loading cycles/fatigue life).

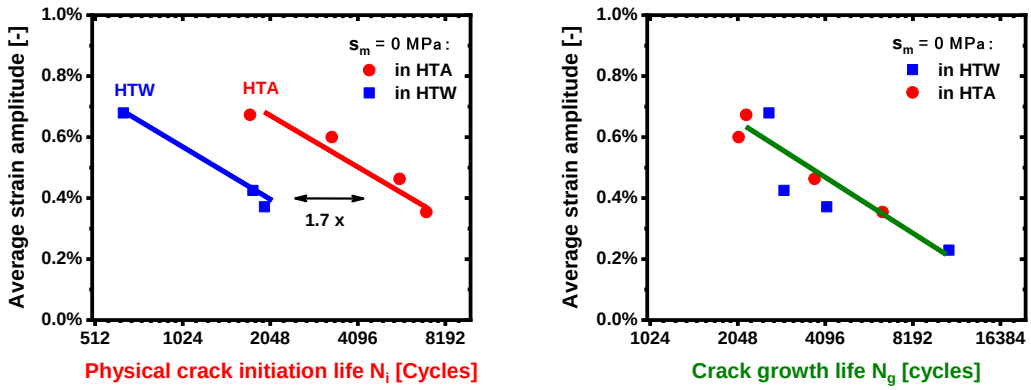

(a) (b)

Figure 4.29 – Relationship between average strain amplitude and (a) Physical crack initiation life, (b) Crack growth life of tests performed with $\sigma_m = 0$ MPa under load-control in air and HWC/BWR at 288°C.

4.8 Different fatigue life correlation and prediction methods

4.8.1 Modified SWT methods

We just recall here the definition of the Smith-Watson-Topper (SWT) parameter :

$$SWT = \sqrt{\sigma_{max}\epsilon_a E} \tag{4.14}$$

which can also be written as:

$$SWT = \sqrt{(\sigma_a\epsilon_a + \sigma_m\epsilon_a)E} \tag{4.15}$$

The SWT parameter as well as the different modified versions of it have been successfully used to take into account mean stress effects on fatigue life of various materials [130][83][81][128][173][12][86]. Since we have performed both load-controlled and strain-controlled experiments that we compared with one another, we had to consider the average quantities over the cycles ($\overline{\sigma_{max}}\,\overline{\epsilon_a}$). However, the definition of SWT is such that it is possible to draw an infinity of hysteresis loops, with distinct shape and area, but with the same values of σ_a, ϵ_a and σ_m. Therefore, a direct correlation between the SWT parameter and the strain energy density or the accumulated damage in the material is not straightforward. However, a correlation between the SWT parameter and the strain energy dissipated or the accumulated damage is likely to exist. In all case, it remains that the modified SWT parameter considered in this work predicts very well the fatigue life of the tests with and without mean stress. In addition, the environmental degradation factor $F_{en}^{\overline{\epsilon_a}}$ calculated from the average strain amplitude ($\overline{\epsilon_a}$) in Fig. 4.10 is equal to 1.66 and the environmental degradation factor calculated from the modified SWT parameter $F_{en}^{SWT_{mod}}$ in Fig. 3.77 is equal to 1.47. Both values are close to each other and consistent with the predictions of NUREG-6909. Thus, SWT_{mod} and $\overline{\epsilon_a}$ are useful parameters to predict the fatigue life under load-control. SWT_{mod} shows a relatively better performance in correlating the fatigue life data with different mean stresses, as it merges σ_a and σ_m and not only $\overline{\epsilon_a}$. However, the method using the modified SWT as the criterion to predict fatigue life may be inconvenient to be implemented in real situations, as both stress and strain signals are needed. Using $\overline{\epsilon_a}$ is a more convenient and easier criterion to implement to predict fatigue.

4.8.2 Strain energy based methods

To correlate the fatigue to strain energy density methods, we considered different forms of strain energy density, such as the elastic strain energy ($\triangle W_e$ for HCF), the plastic strain energy

($\triangle W_p$ for LCF), the total strain energy ($\triangle W_t$) and other forms of their combinations (e.g. $\triangle W_p$ + $\triangle W_{e^+}$), among which $\triangle W_t$ and $\triangle W_p$ show the most promising performance in correlating fatigue lives, either in LCF or HCF, tested with different mean stresses and control modes. The relationships could be described by Langer equation. $\triangle W_t$ or $\triangle W_p$ describes the damage induced per cycle, which determines how many cycles the tested material can endure.

For non-Masing material, like 316L, tested with mean stress, the cyclic constitutive behavior is not easily described analytically and the cyclic hardening behavior depends strongly on mean stress and mildly on stress/strain amplitude. Only if the constitutive relationship is exactly known, can the $\triangle W_t$ or the SWT parameter be correctly calculated and the corresponding life be predicted. Thus the SWT and strain energy based parameters ($\triangle W_t$ and $\triangle W_p$) are not the most convenient ones to be applied in an industrial context. However, the strain energy based methods may provide insight to understand the mechanism which driven material cyclic damage.

4.8.3 Machine learning based methods

The artificial neural network (ANN) shows better performance in predicting the fatigue life of our results than the physically-based method (SWT method) and statistically-based method (NUREG method) as Fig. 3.81 illustrates. Even a small dataset made of 48 points was used to train the neural network. Normally complex network, with multiple input features and deep layers, trained with small dataset can be easily over fitted. This would lead to poor generalization showing a much worse predictive accuracy in test than in training. However, our network achieves a relatively good predictive accuracy without obvious overfitting, possibly because of application of dropout in each layer. The NUREG functions are derived by fitting data mostly from NRC and Japan, which are totally irrelevant with our tested data. However, the SWT method and neural network are developed with our data. Thus it is unfair to compare their performance just using the data from our source, as the fatigue life data from different sources may have certain bias.

The ANN can be trained with a large amount of data from different sources, obtained with different facilities, mechanical and environmental parameters, and materials. The main advantage of an ANN is that it can take into account multiple influential factors simultaneously as input features. This is impossible for methods like SWT method and NUREG method. Thus ANN can converge the data from different sources with considering the most influential factors. Methods like NUREG method, however, only consider several key factors, such as strain amplitude, temperature, strain rate, DO, in their models. ANN may fill the gaps induced by other unconsidered factors, such as material properties, specimen geometry, pressure, which contribute to apparent inconsistency and bias among the data sets from different sources. However, quality and completeness of training data are the key challenges constrain the performance and application of ANN.

ANN can make continuous prediction by interpolation. This fits the industrial real situation,

where almost all influential factors are dynamic. In the case of online monitoring, ANN makes continuous prediction by feeding dynamic influential parameters. However, ANN is a black box for most users and the physical relationships between inputs and output is hidden in the massive matrix and can not be easily illustrated. This tends to refrain the application and acceptance in academic area. ANN gives a new opportunity to analyze the multi-factor nonlinear problems like in EAF.

5 Summary, Conclusions and Perspectives

This chapter is divided in two sections; 1) a summary where the main results are compiled in the form of bullet points, 2) the conclusions and perspectives highlight the main implications of our results and mentioned different open issues and questions to be addressed in a near future.

5.1 Summary

In this PhD work, 62 fatigue tests (58 in load-control and 4 in strain-control) in boiling water reactor/hydrogen water chemistry (BWR/HWC) environment at 288°C and 38 fatigue tests (34 in load-control and 4 in strain-control) in high-temperature air (HTA) environment at 288°C were performed to investigate the effects of mean stress, those of BWR/HWC and HTA environments and to a lesser extend to assess the influence of the control mode, specimen wall thickness and strain rate on the fatigue behavior of a 316L austenitic stainless steel. Extensive post-test characterizations were conducted with optical microscopy (for crack density and opening), scanning electron microscopy (crack initiation and growth), electron back scattered diffraction (fracture mode and local deformation) and transmission electron microscopy/electron channeling contrast imaging (dislocation microstructures) to understand the underlying mechanisms mediating fatigue failure. Data analysis and modeling were performed to analyze and interpret the experimental results and consequently to predict the fatigue life of austenitic stainless steels in the context of environmentally-assisted fatigue. The summaries drawn from the above mentioned work are as follow:

5.1.1 Mean stress effects

When analyzed in stress-life representation (σ_a versus N_f), the experimental results obtained in load-control showed that:

- Negative mean stress is always beneficial for fatigue life and fatigue limit.

- Positive mean stress always increases the fatigue life in the LCF regime ($N_f < 10^5$). In the HCF regime, the fatigue limit (with positive mean stress) is almost identical to that with zero mean stress in HTA, but lower in HTW.

When analyzed in strain-life representation ($\overline{\epsilon_a}$ versus N_f), the following observations were done:

- Mean stress has practically no impact on fatigue life. This is exactly true in LCF regime. In HCF regime, a very small influence was observed. Thus, σ_m does not appear to be an aggravating factor on N_f.
- The conversion of the $\sigma_a(N_f)$ curves into $\overline{\epsilon_a}(N_f)$ curves appears as a straightforward and powerful approach to include σ_m within the framework of NUREG-CR/6909.
- In BWR/HWC and air at 288°C, $\overline{\epsilon_a}(N_f)$ curves are consistent with NUREG-CR/6909 mean curves.

Fractographic observations were carried out. In particular striations spacing was used to determine the crack growth rate in order to evaluate the BWR/HWC environment and mean stress effects on the crack initiation and growth rate.

- Special loading protocols with block sequences were designed to determine the striations/cycle ratio in BWR/HWC and air environments. It was found that this ratio is essential equal to 1 in both environments.
- Mean stress affects mainly the crack initiation phase of a physical crack defined as the number of cycles to create a crack < 50 μm, i.e., crack initiation + microstructurally short crack. The physical initiation phase contributes most to fatigue life change.
- Negative mean stress extends the crack initiation phase. Positive mean stress leads to a bigger crack density and opening.
- Both positive and negative mean stresses decrease the crack growth rate, when considered at the same crack depth or at the same stress intensity factor K_I. However, mean stress shows no effect on crack growth when analyzed against the strain intensity factor $\triangle K_c$ or the J-integral.

Transmission electron microscopy observations were done to gain some insight into the underlying mechanisms controlling the mechanical response:

- From a phenomenological point of view, the beneficial effects of mean stress are attributed to the enhanced cyclic hardening resulting from mean stress, which is manifested by smaller strain amplitude at a given stress amplitude.

- The enhanced cyclic hardening in the primary hardening stage (the first ≈ 20 cycles) results from a larger dislocation density accumulated in the material when tested with mean stress, even though we do not have direct confirmation from dislocation density measurement. A larger dislocation (in planar configuration) density can be induced by larger plastic deformation as we have observed in Fig. 4.24 for the starting cycles (namely the ramping loading cycles in the specific starting procedure) for the materials tested with mean stress.

- In the softening stage, the tests with mean stress have smaller strain amplitude and less strain localization, which hinder cross slip, dislocation annihilation and formation of dislocation relaxed structures (e.g., dislocation wall/channels, veins), thus results in slighter materials softening.

- Secondary hardening was often observed in the tests with mean stress, which run to N_f greater than ≈ 10^4 to ≈ 10^5 cycles. Secondary hardening further strengthens the material and contributes to longer fatigue life. However, no sufficient and necessary condition between the occurrence of secondary hardening and mean stress was found. Mean stress promotes the occurrence of secondary hardening through sustaining planar configuration of dislocations and preventing formation relaxing dislocation structures.

5.1.2 LWR water environmental effects

- In LCF regime, the BWR/HWC environment systematically decreases fatigue life.

- In HCF regime, the fatigue life and fatigue limit are unaffected for σ_m = +50 MPa, slightly increases for σ_m = 0 MPa and obviously increases for σ_m = -20 MPa in BWR/HWC environment, when compared with the fatigue lives in air. Even if LWR water environment does not affect fatigue life in HCF regime, when studied with strain-controlled tests or analyzed in strain-life relationships, there is no contradiction with our findings.

- The BWR/HWC environment affects mainly the physical crack initiation and slightly the crack growth phase, at least for the the test condition with ≈ 0.1%/s strain rate used in this work. In other words, the fatigue life reduction in HTW reflects essentially a reduction of the crack initiation phase.

- From the best fits of $\overline{\epsilon_a}(N_f)$, the calculated F_{en} was found to be equal to 1.66, which is in line with NUREG-CR/6909 prediction, provided that the average strain rate over all cycles is considered.

- An additional life reduction of ≈ × 1.60 was seen for tests performed at an average strain rate of ≈ 0.01%/s, with respect to tests at ≈ 0.1%/s . This is consistent with estimates based on NUREG/CR-6909 formula F_{en}.

- Our tests were performed under load-control with 0.17 Hz sin waveform that induces a variable strain rate. The F_{en} was calculated using the so-called modified rate approach,

which takes into account the variable strain rate. We showed that the calculated F_{en} is consistent the the fatigue life reduction measured form experiments, consistent with the average strain rate approach, and consistent with F_{en} of standard strain-controlled tests with saw tooth waveform (constant strain rate).

5.1.3 Synergistic effects of mean stress and LWR environment

From our data, it was possible to draw some conclusions about the interactions between mean stress effects and LWR environments:

In LCF regime

- Considering the curves $\sigma_a(N_f)$ with positive (+50 MPa) mean stress, it was found that the effects of HTW environment are amplified, which is reflected by an increase of the environmental factor with respect to zero-mean stress ($F_{en} \uparrow$).
- HTW environment weakens the beneficial effect of positive mean stress ($\frac{N^{50}_{water}}{N^{0}_{water}} < \frac{N^{50}_{air}}{N^{0}_{air}}$).

In HCF regime

- When tested with negative (-20 MPa) mean stress, the fatigue life and fatigue limit are significantly higher in HTW than in HTA. Crack closure effect caused by corrosive oxides and compressive stress was tentatively attributed as the reason.

In all cases, the negative impact of mean stress in the LCF regime in BWR/HWC environment on fatigue life is outweighed by the positive results from cyclic hardening. This is at least the case for the mean stress considered in the work, which are representative of those that exist in pipes.

5.1.4 Hollow specimens

The use of hollow specimens to assess LWR environment influence on fatigue behavior is still the subject of discussion on whether adjustment factors have to be considered to compare them with standard solid bar specimens. While this issue was not among the main objective of this work, the limited amount of tests we performed with different geometries (different wall thicknesses), internal pressure and temperature indicate:

- For tests in HTA, the wall thickness (WT) does not affect fatigue life. This is definitely confirmed in LCF regime.
- The effect of pressure on specimen with a 2.5 mm WT at room temperature shows that

the internal pressure, from 0 to 200 bar, on fatigue life remains small, typically of the order of the uncertainty associated with the intrinsic scatter.

- For tests in HTW, the geometry effect of the hollow specimen is more critical to quantify because the internal pressure creates a stress triaxiality within the specimen wall that depends on both the wall thickness and pressure, where the yield strength is relatively low and thus triggers bigger effect on plastic strain, compared with the tests at room temperature.

5.1.5 Data analysis and modeling

- Among the various existing empirically based correction methods for mean stress effects, we proposed to slightly modify the Smith-Watson-Topper stress-strain parameter and showed that a unique curve with all the data with zero, negative and positive mean stress data can be obtained. This method was satisfactory in both environments.When evaluate with modified SWT parameter versus life, the F_{en} is 1.47. In addition, we also demonstrated that life prediction based on the strain and plastic strain energy energy density yield very good predictions.

- The artificial neural network (ANN) method outperforms the modified SWT and NUREG methods in predicting the fatigue lives from our test data set. ANN shows superior performance in being able to take multiple influential factors into considering and make continuous prediction, thus being possible to predict the usage factor with dynamic monitored signals.

5.2 Conclusions and Perspectives

Enough mechanical tests were carried out and analyzed to show what are the effect of mean stress on fatigue life in BWR/HWC environments. It appears that for mean stresses up to +50 MPa, which is representative of the stress level in pressurized pipes, the fatigue life reduction is not significantly affected. This conclusion is drawn from the analysis of the load-controlled in terms of average strain-amplitude, which is a straightforward way to compare the results with strain-controlled data. When so reported, the fatigue data with mean stress are consisted with the fatigue life mean curve in LWR environment, indicating that mean stresses are not an aggravating factor for life reduction. Similarly, the more sophisticated correlation method based on a modification of the Smith-Watson-Topper approach revealed that all data with different mean stresses in LWR fall along the same curve. The main effect of LWR environments was found to occur in the crack initiation phase that is reduced with respect to that in air. However, the crack growth rate is little affected by the LWR environment, at least for the conditions considered in this work.

While we have obtained a fair number of new results within this PhD work that allowed us to draw some conclusions about the interactions between mean stress and LWR environments,

there are still a lot of open questions that constitute nice opportunities for future research. We were focused on BWR/HWC environment but of course gathering data for PWR environment is necessary. All the other parameters, known to have a strong impact on Fen, such as the strain rate, are also fields of further investigation. As the ultimate goal of this research is to better predict lifetimes of nuclear plant components when subjected to environmental assisted fatigue loading, future research has to be oriented towards experimental programs and development of analytical methods to transfer laboratory scale test data to real components. Isothermal tests on smooth tensile specimens have been used to derive fatigue design curves but they are by far not representative of the complex thermo-mechanical loading and time sequences that prevail in real components. So tests that include different specimen geometries, such as notched specimens, cross specimens with bi-axial loading, membrane specimens, have to be envisaged. Assessment of many combinations of mechanical and thermal loading along with various time sequences and different stress state are of paramount interest. Typically, the issue of the fatigue behavior comparison between hollow specimens, pressurized or not, with solid bars specimens is not fully resolved yet. In fatigue, it is known that the hydrostatic pressure has to be taken into account in fatigue criteria for life predictions. It remains however to be evaluated if this effect really plays a role in hollow specimens and under which conditions. The hollow specimens represent a very relevant type of specimens with the potential to mimic the stress state that exist in real pressurized pipes. Our results also call for additional research in the HCF regime where the effect of LWR environments and mean stress on fatigue limit seem to have an impact on the fatigue limit. Advanced methods of artificial neural network, which present a rapidly growing interest in the community, are promising and interesting approaches to include even more parameters in fatigue life predictions. A significant effort must be devoted to extract, re-analyze, re-assess and train ANN model from the large available databases in the world.

Appendix Part II

A Fatigue test hysteresis loop analysis

Each hysteresis loop was analyzed with the in-house coded programs to investigate the mechanical parameters (elastic strain, plastic strain, effective elastic modulus, back stress, effective stress) and energy parameters (elastic energy and plastic energy).

A.0.1 Mechanical parameter analysis

Fig. A.1 summaries the evolution of elastic/plastic strain and tensile/compressive modulus with loading cycles under the condition of σ_m = +50 MPa and σ_m = -20 MPa for tests in HTW. It is necessary to note that all the parameters are calculated from the hysteresis loop in engineering stress-strain. Thus we called them measured parameters to distinguish from the true values.

For tests with σ_m = +50 MPa, the measured E modulus decreases after 10 to 100 cycles if σ_a ≤ 210 MPa. Similar phenomenon was observed by Pham as well [104]. Elastic modulus is a physical property of material, which is independent of microstructures or heat treatment. Theoretically, it should be constant during cyclic loading. The decrease of measured elastic modulus was interpreted as crack initiation, where the area (wall cross section) starts to decrease. However, the loading force is constant so that the true stress is underestimated in engineering stress calculation. This leads to a decrease of the measured elastic modulus which is lower than the true elastic modulus (which should be between 150 to 160 MPa at 288°C). At high stress amplitudes (≥ 210 MPa), cracks initiate very early, between 10 to 100 cycles. So, at the last stage, substantial tensile mean strain (namely ratcheting) was developed. This may be attributed to localized necking, which further aggravated the decrease of measured elastic modulus. The elastic strain was calculated by stress amplitude divided by measured elastic modulus (for both tensile and compressive). Thus the measured elastic strain increases with further loading. The plastic strain was calculated by the strain difference between the two points, where $\sigma = \sigma_m$ (as Section 2.4.2 describes). For tests with σ_m = +50 MPa, all show larger elastic strain than plastic strain.

For tests with σ_m = -20 MPa, no significant decrease of measured elastic modulus was observed,

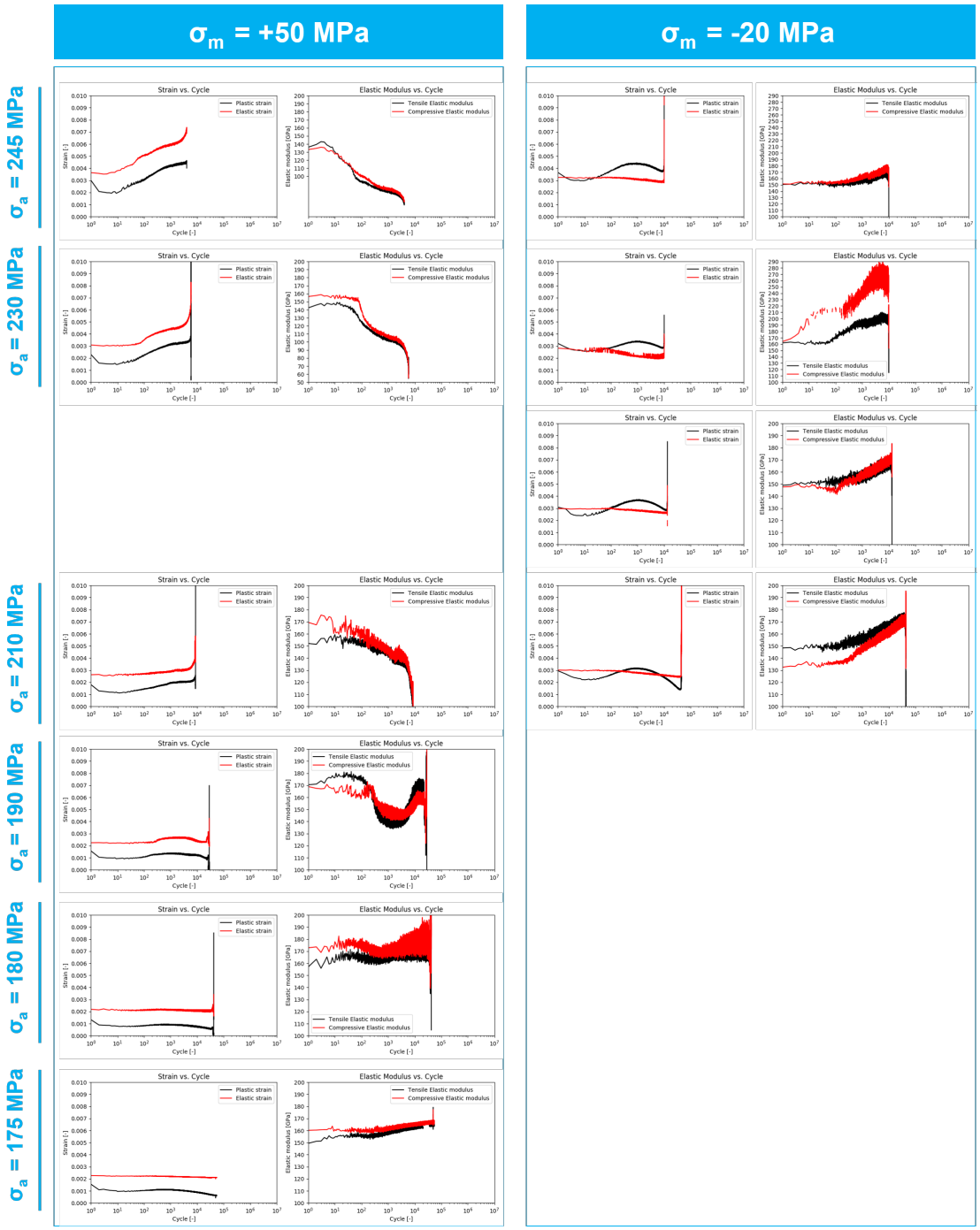

Figure A.1 – Hysteresis loop analysis results (elastic/plastic strain versus cycles and compressive/tensile E modulus versus cycles) of tests with σ_m = +50 MPa and σ_m = -20 MPa.

but increase of elastic modulus occurs at the point secondary hardening starts, which appears in all tests with -20 MPa mean stress. For +50 MPa mean stress tests with secondary hardening occurrence (when $\sigma_a \leq 190$ MPa), increase of measured elastic modulus was observed as well. The detail reason for elastic modulus increase is unclear. For tests with σ_m = -20 MPa, elastic strain slightly decreases, when measured elastic modulus increases.

A.0.2 Strain energy analysis

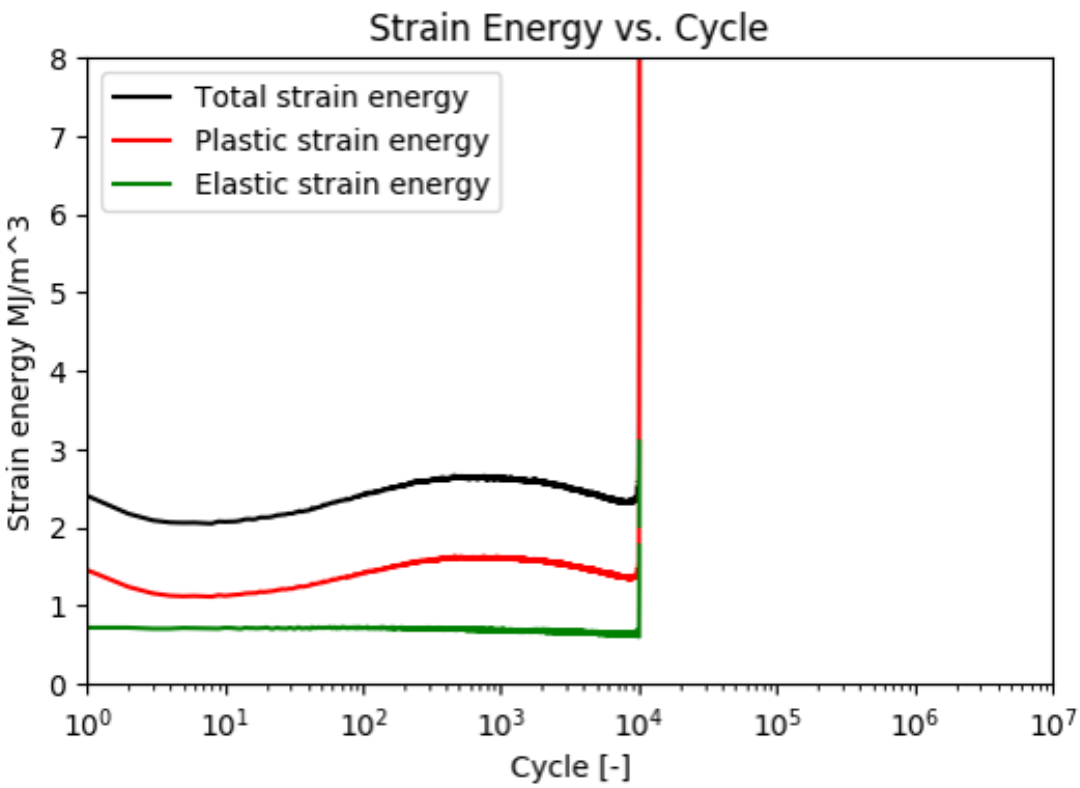

Figure A.2 – Caculated strain energy versus loading cycles of one typical test with σ_a = 245 MPa, σ_m = -20 MPa under load-control in BWR/HWC at 288°C.

B Data analysis programs

A toolkit for raw data processing, data analysis and plotting was developed with *Python*, *Pandas*, *Numpy*, *Scipy* & *Matplotlib*. During a test, cycle number, time, specimen extension and force were recorded. The developed toolkit calculates the strain and stress during the test and enables to extract the maximum and minimum stress as well as the energy density for each cycle. Its work flowchart is depicted in Fig. B.1.

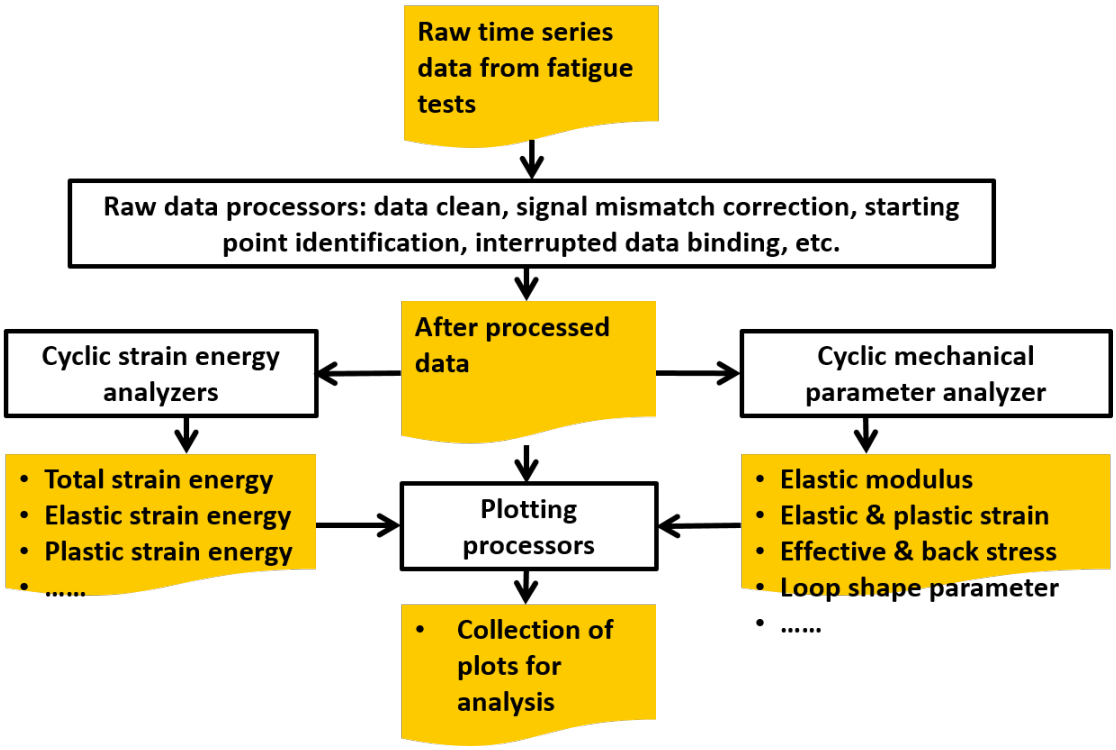

Figure B.1 – Flowchart for raw data processing, data analysis and plotting. All these functions are included my self-developed Toolkit. The script is documented in Appendix B and also accessible in my *GitHub* site: https://github.com/sision0816/fatigueTestDataAnalysis.git.

B.1 Original test data processing

B.1.1 Data processing

These codes are positioned to process the original test data like: identify the starting point, correct the mismatch between time/cycle and loading signals, delete noise data.

```

# -*- coding: utf-8 -*-
"""
Created on Mon Jul 17 14:09:39 2017
@author: chen_w1
"""
import pandas as pd
import numpy as np
from pandas import DataFrame, read_csv
#=====================================================================
# input the read file name and write file name
#=====================================================================
print ('Input the file name you want to analysis:' )
readFile_original = ('SK200_62_experiment_10.6029kN.csv')
print ('Input the file name you want to write the after filtered time
  sequence data:')
writeFile_timeSequence = ('SK200_62_experiment_timeData.csv')
print ('Input the file name you want to write the Max Min data:')
writeFile_maxMin = ('SK200_62_experiment_maxMinData.csv')
 #input data file
df=pd.read_csv(readFile_original,sep=';')
#=====================================================================
# find the starting point of force loading
#=====================================================================
for i in range (len(df.index)):
    print (i)
    if df['Kraft kN'][i:i+2].std() > 0.01:
        break
#delete the before cyclic loading data
filter_df=df.loc[i:,'Weg mm':'MTS mm']
#the Zeit and Zyklus columns
other_df=df[['Zeit s','Zyklus']]
#reset the index of filter_df
filter_df=filter_df.reset_index(drop=True)
#combine the columns together, output the after filtered dataframe
filtered_df=pd.concat([other_df,filter_df],axis=1)
#=====================================================================
# delete the after failure data
#=====================================================================
for j in range(len(filtered_df.index),1,-1):
    if filtered_df['Kraft kN'][j:j+20].std()>0.1:
        break
filtered_df=filtered_df.drop(filtered_df.index[j+1:])
#write the filtered time sequence data into csv
filtered_df.to_csv(writeFile_timeSequence, sep=';', index=False)
```

```
print ('finish')
```

Listing B.1 – Original test data clean

B.1.2 Maximum and minimum filter

```
# -*- coding: utf-8 -*-
"""
Created on Mon Sep 18 10:27:35 2017
@author: chen_w1
"""
import pandas as pd
import numpy as np
from pandas import DataFrame, read_csv
#=====================================================================
# input the read file name and write file name
#=====================================================================
print ('Input the file name you want to write the after filtered time
  sequence data:')
readFile_timeSequence = 'SK200_62_experiment_timeData.csv'
print ('Input the file name you want to write the Max Min data:')
writeFile_maxMin = 'SK200_62_experiment_maxMinData.csv'
# input data file
df=pd.read_csv(readFile_timeSequence,sep=';')
#=====================================================================
# filter the max and min data
#=====================================================================
maxCycle=int(df['Zyklus'].max())
# itterate each cycle
dfmax=pd.DataFrame(columns = ['Zyklus','Zeit s','Weg mm','Kraft kN','MTS
  mm','Temperatur grd'])
dfmin=pd.DataFrame(columns = ['Zyklus','Zeit s','Weg mm','Kraft kN','MTS
  mm','Temperatur grd'])
for cycle in range (1, maxCycle+1):
    if cycle in df['Zyklus'].values:
        print (cycle)
        df2=df[df.Zyklus==cycle]
        df3=df2.max()
        df4=df2.min()
        dfmax=dfmax.append(df3, ignore_index=True)
        dfmin=dfmin.append(df4, ignore_index=True)
dfmax.columns = ['Zyklus','Zeit Max s','Weg Max mm','Kraft Max kN','
  Dehnung_fullrange_SH46 Max mm','Temperatur Max grd']
dfmin.columns = ['Zyklus','Zeit Min s','Weg Min mm','Kraft Min kN','
  Dehnung_fullrange_SH46 Min mm','Temperatur Min grd']
dfMaxMin = pd.merge(dfmax,dfmin,how='outer',on='Zyklus')
# write dataframe to csv
dfMaxMin.to_csv(writeFile_maxMin,sep=';',index=False)
print ('finish')
```

Listing B.2 – Filtrate the maximum and minimum in one cycle

B.1.3 Bind the interrupted parts in one test

```
# -*- coding: utf-8 -*-
"""
Created on Fri Sep 15 11:32:37 2017
@author: chen_w1
"""
import pandas as pd
import numpy as np
from pandas import DataFrame, read_csv,read_excel
import scipy
import scipy.stats

def partsBinding (n):# n is parts number
#=====================================================================
# input the read file name and write file name
#=====================================================================
    for i in range(1,n+1):
        print ('Type in the {}th part file name, including .csv'.format(i))
        globals()['readFile_timeSequence_part{}'.format(i)]  = input() # type in the parts file name with '' and .csv, it is very important
    print ('Type in the output file name, including .csv')
    writeFile_timeSequence_binded = input()
#=====================================================================
# read the csv data file into dataframe
#=====================================================================
    for j in range(1,n+1):
        globals()['df_part{}'.format(j)] = pd.read_csv(globals()['readFile_timeSequence_part{}'.format(j)],sep=';')
    df_binded = df_part1
#=====================================================================
# binding the parts dataframe together
#=====================================================================
    for k in range(2,n+1):
        timeCorrection_temp =  globals()['df_part{}'.format(k)]['Time Sec'][1]
        CycleNrCorrection_temp = globals()['df_part{}'.format(k)]['Cycle'].min()
        traverseCorrection_temp = globals()['df_part{}'.format(k)]['Traverse mm'][1]
        loadCorrection_temp = globals()['df_part{}'.format(k)]['Load kN'][1]
        strainCorrection_temp = globals()['df_part{}'.format(k)]['Strain mm'][1]
        globals()['df_part{}'.format(k)]['Time Sec'] = globals()['df_part{}'.format(k)]['Time Sec'] - timeCorrection_temp + globals()['df_part{}'.format(k-1)]['Time Sec'].max()
        globals()['df_part{}'.format(k)]['Cycle'] = globals()['df_part{}'.format(k)]['Cycle'] - CycleNrCorrection_temp + globals()['df_part{}'.format(k-1)]['Cycle'].max() + 1
        globals()['df_part{}'.format(k)]['Traverse mm'] = globals()['
```

```
df_part{}'.format(k)]['Traverse mm'] - traverseCorrection_temp + globals()['df_part{}'.format(k-1)]['Traverse mm'].iloc[-1]
        globals()['df_part{}'.format(k)]['Load kN'] = globals()['df_part{}'.format(k)]['Load kN'] - loadCorrection_temp + globals()['df_part{}'.format(k-1)]['Load kN'].iloc[-1]
        globals()['df_part{}'.format(k)]['Strain mm'] = globals()['df_part{}'.format(k)]['Strain mm'] - strainCorrection_temp + globals()['df_part{}'.format(k-1)]['Strain mm'].iloc[-1]
        df_binded = pd.concat([df_binded,globals()['df_part{}'.format(k)]],ignore_index=True)
# write the binded .csv file
    df_binded.to_csv(writeFile_timeSequence_binded, sep=';', index = False)
    print ('finish')
    return
```

Listing B.3 – Bind the interrupted parts in one test

B.2 Hysteresis loop analysis

B.2.1 Mechanical analysis

```
# -*- coding: utf-8 -*-
"""
Created on Mon Aug 07 11:09:03 2017
@author: chen_w1
"""
import pandas as pd
import numpy as np
from pandas import DataFrame, read_csv,read_excel
import scipy
import scipy.stats
#=====================================================================
# input the read file name and write file name
#=====================================================================
print ('Input the file name you want to analysis:')
readFile_timeSequence = 'SK200_41_experiment_timeData_binded.csv' # in with csv format and in list
print ('Input the file name of first cycle:')
readFile_firstCycle =  'SK200_41_cycle1_1kN.csv'
#print 'Input the file name you want to write the after mechanical analysis data:'
writeFile_mechanicalAnalysisData = 'experimentHysteresisMechanicalAanalysis_40_0.99_40_0.99.csv'
# read the csv data file into dataframe
df=pd.read_csv(readFile_timeSequence,sep=';')
#=====================================================================
# specimen and test parameters
#=====================================================================
firstCycleFile = pd.read_csv(readFile_firstCycle,sep=';')
extensormeterInitialValue = firstCycleFile['Sandner_1983 mm'][0]
crossSection = 58.905
```

```
gageLength = 15
yieldStrain = 0.0005
#=====================================================================
# Stress strain calculation and transfer to stress strain data
#=====================================================================
df['Stress MPa']=pow(10,3)*df['Kraft kN']/crossSection #Stress unite in MPa
df['Strain']=(df['Sandner_1983 mm']-extensormeterInitialValue)/(gageLength+extensormeterInitialValue)
#=====================================================================
# itterate each cycle
#=====================================================================
# determine the largest cycle number
maxCycle=int(df['Zyklus'].max())
# define the output dataframe of max min data
dfOutput = pd.DataFrame(columns = ['Cycle','Stress Max MPa','Stress Min MPa','Stress Amplitude MPa','Stress Mean MPa','Strain Max','Strain Min','Strain Amplitude','Strain Mean', 'Tensile Elastic Modulus GPa','Compressive Elastic Modulus GPa','Yield Stress MPa','Elastic Strain','Plastic Strain','Anelastic Strain', 'Effective Stress MPa','Back Stress MPa'])
for cycle in range (1, maxCycle-1):
   if cycle in df['Zyklus'].values:
       print (cycle)
       loop=df[df.Zyklus==cycle]
       strainMax = loop['Strain'].max()
       strainMin = loop['Strain'].min()
       strainAmp = (strainMax - strainMin)/2
       strainMean = (strainMax + strainMin)/2
       stressMax = loop['Stress MPa'].max()
       stressMin = loop['Stress MPa'].min()
       stressAmp = (stressMax - stressMin)/2
       stressMean = (stressMax + stressMin)/2
    #=================================================================
    # return the index of data of max strain
    #=================================================================
       maxStrainCount = loop.Strain[loop.Strain==strainMax].index.tolist()[0]
       minStrainCount = loop.Strain[loop.Strain==strainMin].index.tolist()[0]
    #=================================================================
    # regression the linear part, calculate tensile elastic modulus
    #=================================================================
       eModulusSum_tensile = 0
       interceptSum_tensile = 0
       i = 0 #for emodulus Nr. count
       j = 0 # for fitting length shift over the fitting range
       fittingLength_tensile = 40 #set the minimum fitting length
       fittingStartPoint_tensile = maxStrainCount + 20#start fitting from the  maxStrainCount + 10
       fittingEndPoint_tensile = maxStrainCount + 65 #define the ftting end point at maxStrainCount+50, fitting range definition
```

```
69      while fittingStartPoint_tensile + fittingLength_tensile <=
  fittingEndPoint_tensile and loop.index.max() >= fittingEndPoint_tensile
  :
70          j = 0
71          while fittingStartPoint_tensile+j+fittingLength_tensile <=
  fittingEndPoint_tensile:
72              xx_tensile = loop.loc[fittingStartPoint_tensile+j:
  fittingStartPoint_tensile+j+fittingLength_tensile,:]['Strain']
73              yy_tensile = loop.loc[fittingStartPoint_tensile+j:
  fittingStartPoint_tensile+j+fittingLength_tensile,:]['Stress MPa']
74              try:
75                  slope_tensile, intercept_tensile, r_value_tensile,
  p_value_tensile, std_err_tensile = scipy.stats.linregress(xx_tensile,
  yy_tensile)
76              except ValueError:
77                  break
78              eModulus_tensile = 0.001*slope_tensile
79              intercept_tensile = intercept_tensile
80              j+=1
81              if r_value_tensile**2 >= 0.99:
82                  eModulusSum_tensile+=eModulus_tensile
83                  interceptSum_tensile+=intercept_tensile
84                  i+=1
85          fittingLength_tensile+=1
86      try:
87          eModulusAve_tensile = eModulusSum_tensile/i
88          interceptAve_tensile = interceptSum_tensile/i
89      except ZeroDivisionError:
90          eModulusAve_tensile = None
91          interceptAve_tensile = None
92    #==================================================================
93    # regression the compressive part, calculate the compressive elastic
  modulus
94    #==================================================================
95      eModulusSum_compressive = 0
96      interceptSum_compressive = 0
97      h = 0 #for emodulus Nr. count
98      k = 0 # for fitting length shift over the fitting range
99      fittingLength_compressive = 40 #set the minimum fitting length
100     fittingStartPoint_compressive = minStrainCount + 20#start fitting
  from the  maxStrainCount + 10
101     fittingEndPoint_compressive = minStrainCount + 65 #define the
  ftting end point at maxStrainCount+50, fitting range definition
102     while fittingStartPoint_compressive + fittingLength_compressive <=
   fittingEndPoint_compressive:
103         k = 0
104         while fittingStartPoint_compressive+k+
  fittingLength_compressive <= fittingEndPoint_compressive:
105             xx_compressive = loop.loc[fittingStartPoint_compressive+k:
  fittingStartPoint_compressive+k+fittingLength_compressive,:]['Strain']
106             yy_compressive = loop.loc[fittingStartPoint_compressive+k:
  fittingStartPoint_compressive+k+fittingLength_compressive,:]['Stress
```

```
MPa']
                try:
                    slope_compressive, intercept_compressive, r_value_compressive, p_value_compressive, std_err_compressive = scipy.stats.linregress(xx_compressive,yy_compressive)
                except ValueError:
                    break
                eModulus_compressive = 0.001*slope_compressive
                intercept_compressive = intercept_compressive
                k+=1
                if r_value_compressive**2 >= 0.99:
                    eModulusSum_compressive+=eModulus_compressive
                    interceptSum_compressive+=intercept_compressive
                    h+=1
            fittingLength_compressive+=1
        try:
            eModulusAve_compressive = eModulusSum_compressive/h
            interceptAve_compressive = interceptSum_compressive/h
        except ZeroDivisionError:
            eModulusAve_compressive = None
        counts=len(loop.index)
    #=================================================================
    # itterate each data point, yield stress, effective stress and back stress
    #=================================================================
        for count in range(maxStrainCount+50,maxStrainCount+counts):
            try:
                loop['Strain'][count]/((loop['Stress MPa'][count]-interceptAve_tensile)/eModulusAve_tensile)<(1-yieldStrain)
            except TypeError:
                stress_atYieldPoint = None
                yieldStress = None
            except KeyError:
                stress_atYieldPoint = None
                yieldStress = None
            else:
                stress_atYieldPoint = loop['Stress MPa'][count]
                yieldStress = stressMax - stress_atYieldPoint
            try:
                (stressMax - stress_atYieldPoint)/2
            except TypeError:
                effectiveStress = None
                backStress = None
                break
            else:
                effectiveStress = (stressMax - stress_atYieldPoint)/2
                backStress = stressAmp - effectiveStress #instead of stressMax - effectiveStress, because case of with mean stress
                break
    #=================================================================
    # calculate elastic and plastic strain
    #=================================================================
```

```
        loop_right = loop[loop.Strain>strainMean]
        loop_left = loop[loop.Strain<strainMean] #divide one loop into left and right two parts
        index_right = abs(loop_right['Stress MPa']-stressMean).idxmin() # sort the indexs of left and right points most close to the mean stress
        index_left = abs(loop_left['Stress MPa']-stressMean).idxmin()
        plasticStrain = loop['Strain'][index_right] - loop['Strain'][index_left] #plastic strain defined as the strain axis between the right and left intersection points with loop
        try:
            0.001*stressAmp/eModulusAve_tensile
            0.001*stressAmp/eModulusAve_compressive
        except TypeError:
            if eModulusAve_compressive == None:
                if eModulusAve_tensile == None:
                    elasticStrain = None
                else:
                    elasticStrain_tensile = 0.001*stressAmp/eModulusAve_tensile
                    elasticStrain = 2*elasticStrain_tensile
            if eModulusAve_tensile == None:
                if eModulusAve_compressive == None:
                    elasticStrain = None
                else:
                    elasticStrain_compressive = 0.001*stressAmp/eModulusAve_compressive
                    elasticStrain = 2*elasticStrain_compressive
        else:
            elasticStrain_tensile = 0.001*stressAmp/eModulusAve_tensile
            elasticStrain_compressive = 0.001*stressAmp/eModulusAve_compressive
            elasticStrain = elasticStrain_tensile + elasticStrain_compressive
        try:
            anelasticStrain = 2*strainAmp - elasticStrain-plasticStrain
        except TypeError:
            anelasticStrain = None
        dfOutput.loc[len(dfOutput)] = [cycle,stressMax,stressMin,stressAmp,stressMean,strainMax,strainMin,strainAmp,strainMean,eModulusAve_tensile,eModulusAve_compressive,yieldStress,elasticStrain,plasticStrain,anelasticStrain,effectiveStress,backStress] #asign the vale to the dataframe
#  write dataframe to  csv
dfOutput.to_csv(writeFile_mechanicalAnalysisData, sep=';', index = False)
print ('finish')
```

Listing B.4 – Analyze the mechanical parameters (elastic strain, plastic strain, effective stress, back stress, yield stress and elastic modulus) of each hysteresis loop.

B.2.2 Strain energy analysis

```

```

```
# -*- coding: utf-8 -*-
"""
Created on Wed Jul 26 09:26:13 2017
@author: chen_w1
"""
import pandas as pd
import numpy as np
import scipy
from pandas import DataFrame, read_csv,read_excel
#=====================================================================
# input the read file name and write file name
#=====================================================================
print ('Input the file name you want to analysis:')
readFile_timeSequence = 'SK200_41_experiment_timeData_binded.csv' # in
  with csv format and in list
print ('Input the file name you want to read of
  hysteresisMechanicalAnalysis result:')
readFile_hysteresisMechanicalAnalysis = '
  experimentHysteresisMechanicalAanalysis_40_0.99_40_0.99.csv' # in with
  csv format and in list
print ('Input the file name of first cycle:')
readFile_firstCycle = 'SK200_41_cycle1_1kN.csv'
print ('Input the file name you want to write for the strain enenergy
  calculation result:')
writeFile_strainEnergyCalculationResult = '
  experimentStrainEnergyCalculationResult.csv'
#=====================================================================
# read the csv data file into dataframe
#=====================================================================
df=pd.read_csv(readFile_timeSequence,sep=';')
mechanicalAnalysisData = pd.read_csv(
  readFile_hysteresisMechanicalAnalysis,sep=';')
#=====================================================================
# specimen and test parameters
#=====================================================================
firstCycleFile = pd.read_csv(readFile_firstCycle,sep=';')
extensormeterInitialValue = firstCycleFile['Sandner_1983 mm'][0]
crossSection = 58.905
gageLength = 15
#=====================================================================
# #Stress strain calculation and transfer to stress strain data
#=====================================================================
df['Stress MPa']=pow(10,3)*df['Kraft kN']/crossSection #Stress unite in
  MPa
df['Strain']=(df['Sandner_1983 mm']-extensormeterInitialValue)/(
  gageLength-extensormeterInitialValue)
#=====================================================================
# itterate each cycle and calculate the strain energy
#=====================================================================
# determine the largest cycle number
maxCycle=int(df['Zyklus'].max())
# define the output dataframe of max min data
```

```
45 dfOutput = pd.DataFrame(columns = ['Cycle','Stress Max MPa','Stress Min
   MPa','Stress Amplitude MPa','Stress Mean MPa','Strain Max','Strain Min'
   ,'Strain Amplitude','Strain Mean', 'Total Cyclic Strain Energy_simps MJ
   /m3','Plastic Strain Energy_simps MJ/m3', 'Total Cyclic Strain
   Energy_trapz MJ/m3','Plastic Strain Energy_trapz MJ/m3','Elastic Strain
    Energy MJ/m3','Loop Shape Parameter_simps','Loop Shape Parameter_trapz
   '])
46 for cycle in range (1, maxCycle-1):#the maxCycle-1 cycle may cause error
   in the integration
47     if cycle in df['Zyklus'].values:
48         print (cycle)
49         loop=df[df.Zyklus==cycle]
50         indexStrainMin = loop.Strain[loop.Strain==loop.Strain.min()].index
   .tolist()[0] #the index of the min strain
51         indexStrainMax = loop.Strain[loop.Strain==loop.Strain.max()].index
   .tolist()[0] #the index of the max strain
52         strainMax = loop['Strain'].max()
53         strainMin = loop['Strain'].min()
54         strainAmp = (strainMax - strainMin)/2
55         strainMean = (strainMax + strainMin)/2
56         stressMax = loop['Stress MPa'].max()
57         stressMin = loop['Stress MPa'].min()
58         stress_atStrainMin = loop['Stress MPa'][indexStrainMin]
59         stress_atStrainMax = loop['Stress MPa'][indexStrainMax]
60         stressAmp = (stressMax - stressMin)/2
61         stressMean = (stressMax + stressMin)/2
62         loop['Stress MPa'] = loop['Stress MPa'] - stressMin
63         loop['Strain'] = loop['Strain'] - strainMin # shift the origin
   (0,0) of the coodination to (strainMin, stressMin)
64         interval = 4*strainAmp/len(loop)#calculation the point interval
   alone strain axis
65       #==================================================================
66       #  upper half hysteresis
67       #==================================================================
68         yyUpperRight_array = loop.loc[: indexStrainMax,['Stress MPa']].
   values.transpose() #reduce the upper right section
69         xxUpperRight_array = loop.loc[: indexStrainMax,['Strain']].values.
   transpose()
70         yyUpperLeft_array = loop.loc[indexStrainMin:,['Stress MPa']].
   values.transpose() #reduce the Upper left section
71         xxUpperLeft_array = loop.loc[indexStrainMin:,['Strain']].values.
   transpose()
72       #==================================================================
73       #   lower half hysteresis
74       #==================================================================
75         yylower_array = loop.loc[indexStrainMax:indexStrainMin,['Stress
   MPa']].values.transpose()#be care for may be negative values
76         xxlower_array = loop.loc[indexStrainMax:indexStrainMin,['Strain'
   ]].values.transpose()
77       #==================================================================
78       #  intgrate via simps
79       #==================================================================
```

```
80        energy_upperRight_simps = scipy.integrate.simps(yyUpperRight_array
  ,xxUpperRight_array,even='avg')
81        energy_upperLeft_simps = scipy.integrate.simps(yyUpperLeft_array,
  xxUpperLeft_array,even='avg')
82        energy_totalCyclicStrain_simps = energy_upperRight_simps +
  energy_upperLeft_simps # total cyclic strain energy
83        energy_nonplasticStrain_simps = np.absolute(scipy.integrate.simps(
  np.absolute(yylower_array),np.absolute(xxlower_array),even='avg'))#the
  integration would be negative value, should get absolute value for area
84        energy_plasticStrain_simps = energy_totalCyclicStrain_simps -
  energy_nonplasticStrain_simps
85      #==================================================================
86      #    intgrate via trapz
87      #==================================================================
88        energy_upperRight_trapz = scipy.integrate.trapz(yyUpperRight_array
  ,xxUpperRight_array,axis=-1)
89        energy_upperLeft_trapz = scipy.integrate.trapz(yyUpperLeft_array,
  xxUpperLeft_array,axis=-1)
90        energy_totalCyclicStrain_trapz = energy_upperRight_trapz +
  energy_upperLeft_trapz # total cyclic strain energy
91        energy_nonplasticStrain_trapz = np.absolute(scipy.integrate.trapz(
  np.absolute(yylower_array),np.absolute(xxlower_array),axis=-1))#the
  integration would be negative value, should get absolute value for area
92        energy_plasticStrain_trapz = energy_totalCyclicStrain_trapz -
  energy_nonplasticStrain_trapz
93      #==================================================================
94      #    elastic strain energy
95      #==================================================================
96        try:
97            energy_elasticStrain = mechanicalAnalysisData['Elastic Strain'
  ][cycle]*stress_atStrainMax
98        except TypeError:
99            energy_elasticStrain = None
100     #==================================================================
101     #    loop shape parameter
102     #==================================================================
103       squareArea = (strainMax-strainMin)*(stressMax-stressMin)
104       shapeParameter_simps = energy_plasticStrain_simps[0]/squareArea
105       shapeParemeter_trapz = energy_plasticStrain_trapz[0]/squareArea
106       #output the analysis result
107       dfOutput.loc[len(dfOutput)] = [cycle,stressMax,stressMin,stressAmp
  ,stressMean,strainMax,strainMin,strainAmp,strainMean,
  energy_totalCyclicStrain_simps[0],energy_plasticStrain_simps[0],
  energy_totalCyclicStrain_trapz[0],energy_plasticStrain_trapz[0],
  energy_elasticStrain,shapeParameter_simps,shapeParemeter_trapz]
108 #  write dataframe to  csv
109 dfOutput.to_csv(writeFile_strainEnergyCalculationResult, sep=';', index =
    False)
110 print ('finish')
```

Listing B.5 – Analyze the strain energy (elastic strain energy, anelastic strain energy and plastic strain energy) of each hysteresis loop.

B.2.3 Plotting

```python

# -*- coding: utf-8 -*-
"""
Created on Mon Jul 31 12:14:58 2017
@author: chen_w1
"""
import pandas as pd
import numpy as np
from pandas import DataFrame, read_csv,read_excel
import scipy
import matplotlib.pyplot as plt
from matplotlib.ticker import NullFormatter
from matplotlib.ticker import MultipleLocator
# read file
readFile_mechanicalAnalysisData = '
  experimentHysteresisMechanicalAanalysis_40_0.99_40_0.99.csv'
df=pd.read_csv(readFile_mechanicalAnalysisData,sep=';')
#maximum & minimum stress
plt.figure(1)
plt.title('Stress vs. Cycle')
plt.plot(df['Cycle'],df['Stress Max MPa'],'k-',label='Stress max')
plt.plot(df['Cycle'],df['Stress Min MPa'],'r-',label='Stress min')
plt.ylabel('Stress [MPa]')
plt.xlabel('Cycle [-]')
plt.xlim(1,10000000)
plt.ylim(-290,290)
plt.xscale('log')
plt.yticks(np.arange(-290,300,step=50))
plt.axes().yaxis.set_minor_locator(MultipleLocator(10))
plt.legend(loc=0)
#effective stress and back stress
plt.figure(2)
plt.title('Stress vs. Cycle')
plt.plot(df['Cycle'],df['Back Stress MPa'],'b-',label='Back stress')
plt.plot(df['Cycle'],df['Effective Stress MPa'],'r-',label='Effective
  stress')
plt.ylabel('Stress [MPa]')
plt.xlabel('Cycle [-]')
plt.xlim(1,10000000)
plt.ylim(0,290)
plt.yticks(np.arange(0,300,step=50))
plt.axes().yaxis.set_minor_locator(MultipleLocator(10))
plt.xscale('log')
plt.legend(loc='0')
plt.figure(3)
plt.title('Stress vs. Cycle')
plt.plot(df['Cycle'],df['Yield Stress MPa'],'k-',label='Yield stress')
plt.ylabel('Yield stress [MPa]')
plt.xlabel('Cycle [-]')
plt.xlim(1,10000000)
```

```
plt.ylim(0,290)
plt.yticks(np.arange(0,300,step=50))
plt.axes().yaxis.set_minor_locator(MultipleLocator(10))
plt.xscale('log')
plt.legend(loc=0)
plt.tight_layout()
#strain amp, strain mean, srain max and min
plt.figure(4)
strainMax = plt.subplot()
strainMin = plt.subplot()
strainMean = plt.subplot()
plt.title('Strain vs. Cycle')
strainMax.plot(df['Cycle'],df['Strain Max'],'k-',label='Strain max')
strainMin.plot(df['Cycle'],df['Strain Min'],'k--',label='Strain min')
strainMean.plot(df['Cycle'],df['Strain Mean'],'g-',label='Mean strain')
plt.ylabel('Strain [-]')
plt.xlabel('Cycle [-]')
plt.xlim(1,10000000)
plt.ylim(-0.08,0.10)
plt.xscale('log')
plt.legend(loc=0)
strainAmp = strainMax.twinx()
strainAmp.plot(df['Cycle'],df['Strain Amplitude'],'b-',label='Strain
  amplitude')
plt.ylabel('Strain [-]')
plt.xlabel('Cycle [-]')
plt.xlim(1,10000000)
plt.ylim(0,0.01)
plt.xscale('log')
plt.yticks(np.arange(0,0.011,step=0.001))
plt.legend(loc=2)
#plastic and elastic strain
plt.figure(5)
plt.title('Strain vs. Cycle')
plt.plot(df['Cycle'],df['Plastic Strain'],'k-',label='Plastic strain')
plt.plot(df['Cycle'],df['Elastic Strain'],'r-',label='Elastic strain')
plt.ylabel('Strain [-]')
plt.xlabel('Cycle [-]')
plt.xlim(1,10000000)
plt.ylim(0,0.01)
plt.xscale('log')
plt.yticks(np.arange(0,0.011,step=0.001))
plt.legend(loc=0)
#elsatic modulus
plt.figure(6)
plt.title('Elastic Modulus vs. Cycle')
plt.plot(df['Cycle'],df['Tensile Elastic Modulus GPa'],'k-', label='
  Tensile Elastic modulus')
plt.plot(df['Cycle'],df['Compressive Elastic Modulus GPa'],'r-',label='
  Compressive Elastic modulus')
plt.ylabel('Elastic modulus [GPa]')
plt.xlabel('Cycle [-]')
```

```
plt.xlim(1,10000000)
plt.ylim(100,200)
plt.xscale('log')
plt.yticks(np.arange(100,210,step=10))
plt.legend(loc=0)
plt.show()
```

Listing B.6 – Plot the hysteresis loop analysis results.

Elastic modulus calculation is schematically described in Fig. 2.10. As a first step, a section consisting of 20 data points is scanned through the defined min-max range (section between two blue lines) from which the elastic modulus is calculated. Then the number of data point in the section is successively increased by one data point until the length is equal to min-max range length. The elastic modulus values are the fitted slopes (only whose $R^2 > 0.995$ are accepted) at each iteration and overage at the end to yield that final calculated elastic modulus.

Bibliography

[1] M. Dahlberg and D. Bremberg. Fatigue margins for austinitic stainless steels in asme boiler and pressure vessel code- a literature study. Technical Report 2012:50, Swedish Radiation Safety Authority, Sweden, 2012.

[2] M. Higuchi, T. Nakamura, and Y. Sugie. Development of an environmental fatigue evaluation method for nuclear power plants in jsme code. *Journal of Environment and Engineering*, 6(2):452–468, 2011.

[3] O. K. Chopra and G. L. Stevens. Effect of LWR water environments on the fatigue life of reactor materials. Technical Report NUREG/CR-6909, Rev. 1, Argonne National Laboratory, 2018.

[4] H. P. Seifert, S. Ritter, and H. J. Leber. Corrosion fatigue crack growth behaviour of austenitic stainless steels under light water reactor conditions. *Corrosion Science*, 55:61–75, 2012.

[5] H. P. Seifert, S. Ritter, and H. J. Leber. Corrosion fatigue initiation and short crack growth behaviour of austenitic stainless steels under light water reactor conditions. *Corrosion Science*, 59:20–34, 2012.

[6] U.S. NRC. NRC regulatory guide 1.207: Guidlines for evaluating fatigue analysis incorporating the life reduction of metal components due to the effects of the ligh-water reactors environment for new reactors. Technical report, U.S. NRC, March 2006.

[7] EPRI. Environmentally assisted fatigue gap analysis and roadmap for future research: Gap analysis report. Technical Report 1023012, EPRI, Palo Alto, CA, 2011.

[8] EPRI. Environmentally assisted fatigue gap analysis and roadmap for future research: Roadmap. Technical Report 10267241, EPRI, Palo Alto, CA, 2012.

[9] K.J. Mottershead, M. Bruchhausen, T. Métais, S. Cicero, D. Tice, and N. Platts. INCEFA PLUS increasing safety in nuclear power plants by covering gaps in environmental fatigue assessment. volume Volume 1A: Codes and Standards of *Pressure Vessels and Piping Conference*, 07 2016. V01AT01A019.

[10] K.J. Mottershead, M. Bruchhausen, T. Metais, and S. Cicero. INCEFA-PLUS programme overview and update. *Procedia Engineering*, 160:292 – 299, 2016. XVIII International Colloquium on Mechanical Fatigue of Metals (ICMFM XVIII), Gijón (Spain), September 5-7, 2016.

[11] P. Spätig and H.-P. Seifert. Mean stress effect on fatigue life of 316L austenitic steel in air and simulated boiling water reactor hydrogen water chemistry environment. In *17th Int. Conference on Environmental Degradation of Materials in Nuclear Systems - Water Reactors*, volume CD-ROM, Ottawa, Canada, August 2015.

[12] P. Spätig, M. Heczko, T. Kruml, and H.P. Seifert. Influence of mean stress and light water reactor environment on fatigue life and dislocation microstructures of 316L austenitic steel. *Journal of Nuclear Materials*, 509:15 – 28, 2018.

[13] H. D. Solomon, C. Amzallag, A. J. Vallee, and R. E. De Lair. Influence of mean stress on the fatigue behavior of 304L SS in air and PWR water. In *ASME 2005 Pressure Vessels and Piping Conference*, volume Volume 1: Codes and Standards, pages 87–97, Colorado, 2005. ASME. 10.1115/PVP2005-71064.

[14] M. Wöhler. Über die festigkeitsversuche mit eisen und stahl. *Z. Bauwesen*, 20:73–106, 1870.

[15] M. Kamal and M. M. Rahman. Advances in fatigue life modeling: A review. *Renewable and Sustainable Energy Reviews*, 82:940–949, 2018.

[16] H. Mughrabi. Microstructural mechanisms of cyclic deformation, fatigue crack initiation and early crack growth. *Philosophical Transactions of the Royal Society A: Mathematical, Physical and Engineering Sciences*, 373:1–21, 2015.

[17] S. Stanzl-Tschegg, H. Mughrabi, and B. Schoenbauer. Life time and cyclic slip of copper in the vhcfregime. *International Journal of Fatigue*, 29(9):2050 – 2059, 2007. Fatigue Damage of Structural Materials VI.

[18] A. Weidner, D. Amberger, F. Pyczak, B. Schönbauer, S. Stanzl-Tschegg, and H. Mughrabi. Fatigue damage in copper polycrystals subjected to ultrahigh-cycle fatigue below the psb threshold. *International Journal of Fatigue*, 32(6):872 – 878, 2010. Selected Papers of the 17th European Conference of Fracture (ECF 17).

[19] C. Bathias. Relation between endurance limits and thresholds in the field of gigacycle fatigue. *Fatigue Crack Growth Thresholds, Endurance Limits, and Design*, 1372:135–154, 01 2000.

[20] H. Mughrabi. Specific features and mechanisms of fatigue in the ultrahigh-cycle regime. *International Journal of Fatigue*, 28(11):1501 – 1508, 2006. Third International Conference on Very High Cycle Fatigue (VHCF-3).

[21] U. Essmann, U. Gösele, and H. Mughrabi. A model of extrusions and intrusions in fatigued metals i. point-defect production and the growth of extrusions. *Philosophical Magazine A*, 44(2):405–426, 1981.

[22] H. Mughrabi. *Dislocations and properties of real materials*, volume 323, chapter Dislocations in fatigue, page 244–262. The Institute of Metals, London, UK, 1985.

[23] J. Polák and J Man. Experimental evidence and physical models of fatigue crack initiation. *International Journal of Fatigue*, 91:294–303, 2016.

[24] J. Polák. On the role of point defects in fatigue crack initiation. *Materials Science and Engineering*, 92:71 – 80, 1987.

[25] T. Kruml, J. Pola´k, K. Obrtli´k, and S. Degallaix. Dislocation structures in the bands of localised cyclic plastic strain in austenitic 316L and austenitic-ferritic duplex stainless steels. *Acta Materialia*, 45(12):5145 – 5151, 1997.

[26] J. Polák and J. Man. Initiation of vhcf fatigue cracks – experiments and models. *Procedia Engineering*, 101:386–394, 2015.

[27] M. Kamaya. Observation of fatigue crack initiation and growth in stainless steel to quantify low-cycle fatigue damage for plant maintenance. *E-Journal of Advanced Maintenance*, 5:185–200, 2013.

[28] P. Lukáš. Microstructural aspects of low cycle fatigue. In P.D. Portella and K.-T. Rie, editors, *Low cycle fatigue and elastoplastic behaviour ofmaterials*. Elsevier Science Ltd., 1st edition edition, 1998.

[29] Y. Murakami, T. Nomoto, and T. Ueda. Factors influencing the mechanism of super-long fatigue failure in steels. *Fatigue & Fracture of Engineering Materials & Structures*, 22(7):581–590, 1999.

[30] Petr Lukáš. Fatigue Crack Nucleation and Microstructure. In *Fatigue and Fracture*. ASM International, 01 1996.

[31] U. Zerbst, M. Madia, and M. Vormwald. Fatigue strength and fracture mechanics. *Procedia Structural Integrity*, 5:745–752, 2017.

[32] H. Wang, W. Zhang, F. Sun, and W. Zhang. A comparison study of machine learning based algorithms for fatigue crack growth calculation. *Materials*, 10:543, 2017.

[33] W. Li. Short fatigue crack propagation and effect of notch plastic filed. *Nuclear Engineer and Design*, 84:193–200, 2003.

[34] N. E. Dowling. Crack growth during low-cycle fatigue of smooth axial specimens. In *Cyclic Stress-Strain and Plastic Deformation Aspects of Fatigue Crack Growth*. 97-121, 1977. ASTM STP 637.

[35] N. E. Dowling. Geometry effects and the J-integral approach to elastic-plastic fatigue crack growth. In *Cracks and Fracture*, pages 19–32. American Society for Testing and Materials, 1976. ASTM STP 601.

[36] M. H. El Haddad, N. E. Dowling, T. H. Topper, and K. N. Smith. J integral applications for short fatigue cracks at notches. *International Journal of Fracture*, 16(1):15–30, Feb 1980.

[37] K.O. Findley, S.W. Koh, and A. Saxena. J-integral expressions for semi-elliptical cracks in round bars. *International Journal of Fatigue*, 29:822–828, 2007.

[38] O. K. Chopra, W. J. Shack, and J. Muscara. Mechanism of fatigue crack initiation in austenitic stainless steels in light water reactor environments. In *Transations of the 17th International Conference on Structural Mechanics in Reactor Technology (SMiRT 17)*, page 8, 2003.

[39] T. Allen, J. Busby, M. Meyer, and D. Petti. Materials challenges for nuclear systems. *Materials Today*, 13:14–23, 2010.

[40] K. J. Metzner and U. Wilke. European therfat project—thermal fatigue evaluation of piping system "tee"-connections. *Nuclear Engineering and Design*, 235:473–484, 2005.

[41] K. Lida. A review of fatigue failures in LWR plants in japan. *Nuclear Engineering and Design*, 138:297–312, 1992.

[42] H. P. Seifert and S. Ritter. Environmentally-assisted cracking in austenitic light water reactor structural materials– final report of the KORA-I project. Technical report, Paul Scherrer Institute, 2009.

[43] T. Terachi, T. Yamada, T. Miyamoto, K. Arioka, and K. Fukuya. Corrosion behavior of stainless steels in simulated pwr primary water—effect of chromium content in alloys and dissolved hydrogen—. *Journal of Nuclear Science and Technology*, 45:975–984, 2008.

[44] A. Koji. *Effect of temperature, hydrogen and boric acid concentration on IGSCC susceptibility of annealed 316 stainless steel.* Societe Francaise d'Energie Nucleaire - SFEN, France, 2002.

[45] P. Berge, C. Ribon, and P. S. Paul. Effect of hydrogen on the corrosion of steels in high temperature water. *Corrosion-NACE*, 33:173–177, 1977.

[46] L. Dong, Q. Peng, Z. Zhang, T. Shoji, Han E.-H., Wei K., and L. Wang. Effect of dissolved hydrogen on corrosion of 316NG stainless steel in high temperature water. *Nuclear Engineering and Design*, 295:403 – 414, 2015.

[47] Y.-J. Kim. Characterization of the oxide film formed on type 316 stainless steel in 288°C water in cyclic normal and hydrogen water chemistries. *CORROSION*, 51(11):849–860, 1995.

[48] Y.-J. Kim. Analysis of oxide film formed on type 304 stainless steel in 288°C water containing oxygen, hydrogen, and hydrogen peroxide. *CORROSION*, 55(1):81–88, 1999.

[49] A. Turnbull and M. Psaila-Dombrowski. A review of electrochemistry of relevance to environment-assisted cracking in light water reactors. *Corrosion Science*, 33:1925–1966, 1992.

[50] L. G. Bland and J. S. Locke. Chemical and electrochemical conditions within stress corrosion and corrosion fatigue cracks. *npj Materials Degradation*, 12:1–18, 2017.

[51] P.L. Andresen and L.M. Young. Characterization of the roles of electrochemistry, convection and crack chemistry in stress corrosion cracking.

[52] H. J. Leber, M. Niffenegger, and B. Tirbonod. "diagnostik für werkstoffschädigung durch ermüdung", final research report of diagnostik-i for hsk. Technical report, Paul Scherrer Institute, March 26 2006.

[53] W. Karlsen, M. Ivanchenko, U. Ehrnstén, Y. Yagodzinskyy, and H. Hänninen. Microstructural manifestation of dynamic strain aging in aisi 316 stainless steel. *Journal of Nuclear Materials*, 395(1):156 – 161, 2009.

[54] S. G. Hong and S. B. Lee. The tensile and low-cycle fatigue behavior of cold worked 316L stainless steel: influence of dynamic strain aging. *International Journal of Fatigue*, 26(8):899 – 910, 2004.

[55] R. Alain, P. Violan, and J. Mendez. Low cycle fatigue behavior in vacuum of a 316L type austenitic stainless steel between 20 and 600°C part I: Fatigue resistance and cyclic behavior. *Materials Science and Engineering: A*, 229(1):87 – 94, 1997.

[56] American Society of Mechanical Engineers. *Criteria of the ASME boiler and pressure vessel code for design by analysis in sections III and VIII, division 2.* American Society of Mechanical Engineers, New York, 1969.

[57] H. S. Mehta and S. R. Gosselin. Environmental factor approach to account for water effects in pressure vessel and piping fatigue evaluations. *Nuclear Engineering and Design*, 181:175–197, 1998.

[58] H. S. Mehta and H. H. Hwang. Application of draft regulatory guide dg-1144, guidline for environmental fatigue evaluation to a bwr feedwater piping system. In *Proceedings of ASME-PVP 2007*, San Antonio, TX, July 22-26 2007.

[59] M. Higuchi and K. Iida. Fatigue strength correction factors for carbon and low-alloy steels in oxygen-containing high-temperature water. *Nuclear Engineering Design*, 129:293–306, 1991.

[60] T. Nakamura, Saito I., and Y. Asada. Guideline for evaluating fatigue life reduction in the LWR environment. Technical report, Nuclear and Safety Management Division, Agency for Natural Resources and Energy, 2000. in Japanese.

[61] T. Nakamura, Saito I., and Y. Asada. Guidelines on environmental fatigue evaluation for power reactors. Technical report, Thermal and Nuclear Power Engineering Society, 2002.

[62] JSME. Code for nuclear power generation facilities, environmental fatigue evaluation method for nuclear power plants (JSME S NF1-2006). Technical report, Japan Society of Mechanical Engineers, 2006.

[63] O. K. Chopra and G. L. Stevens. Effect of LWR coolant environments on the fatigue life of reactor materials. Technical Report NUREG/CR-6909, ANL-06/08, Argonne National Laboratory, Argonne, February 2007.

[64] M. Higuchi, K. Sakaguchi, Y. Nomura, and A. Hirano. Final Proposal of Environmental Fatigue Life Correction Factor (Fen) for Structural Materials in LWR Water Environment. volume Volume 1: Codes and Standards of *Pressure Vessels and Piping Conference*, pages 111–122, 08 2007.

[65] P. Delobelle. Synthesis of the elastoviscoplastic behavior and modelization of an austenitic stainless steel over a large temperature range, under uniaxial and biaxial loadings, part I: Behavior. *International Journal of Plasticity*, 9(1):65 – 85, 1993.

[66] G. Facheris. *Cyclic plastic material behavior leading to crack initiation in stainless steel under complex fatigue loading conditions*. PhD thesis, ETH ZURICH, ETH ZURICH, 2014. DISS. ETH NO. 21696.

[67] G. Kang, Q. Kan, J. Zhang, and Y. Sun. Time-dependent ratchetting experiments of SS304 stainless steel. *International Journal of Plasticity*, 22(5):858 – 894, 2006.

[68] M. Mizuno, Y. Mima, M. Abdel-Karim, and N. Ohno. Uniaxial Ratchetting of 316FR Steel at Room Temperature— Part I: Experiments . *Journal of Engineering Materials and Technology*, 122(1):29–34, 08 1999.

[69] The initial scope and intent of the section iii fatigue design procedure. Florida, January 1992.

[70] M. Dahlberg and D. Brember. Fatigue margins for austinitic stainless steels in asme boiler and pressure vessel code- a literature study. Technical report, Swedish Radiation Safety Authority, Sweden, 2012. 2012:50.

[71] T. Poulain, J. Mendez, G. Henaff, and L. de Baglion. Influence of surface finish in fatigue design of nuclear power plant components. *Procedia Engineering*, 66:233 – 239, 2013. Fatigue Design 2013, International Conference Proceedings.

[72] T. Poulain, J. Mendez, G. Hénaff, and L. de Baglion. Analysis of the ground surface finish effect on the lcf life of a 304L austenitic stainless steel in air and in pwr environment. *Engineering Fracture Mechanics*, 185:258 – 270, 2017. XVIII International Colloquium Mechanical Fatigue of Metals.

[73] M. Higuchi, K. Sakaguchi, and Y. Nomura. Effects of Strain Holding and Continuously Changing Strain Rate on Fatigue Life Reduction of Structural Materials in Simulated LWR Water. volume Volume 1: Codes and Standards of *Pressure Vessels and Piping Conference*, pages 123–131, 08 2009.

[74] O. K. Chopra. Mechanism and estimation of fatigue crack initiation in austenitic stainless steels in LWR environments. Technical Report NUREG/CR-6787, ANL-01/25, Argonne National Laboratory, Argonne, IL, 2002.

[75] O. K. Chopra. Effects of LWR coolant environments on fatigue design curves of austenitic stainless steels. Technical Report NUREG/CR-5704, ANL-98/31, Argonne National Laboratory, Argonne, IL, 1999.

[76] O. K. Chopra and B. Alexandreanu. Effect of materials heat treatment on fatigue crack initiation in austenitic stainless steels in LWR environments. Technical Report NUREG/CR-6878, ANL-03/35, Argonne National Laboratory, Argonne, IL, July 2005.

[77] K. H. Bae, H. H. Kim, and S. B. Lee. A simple life prediction method for 304L stainless steel structures under fatigue-dominated thermo-mechanical fatigue loadings. *Materials Science and Engineering: A*, 529:370 – 377, 2011.

[78] L. Vincent, J. C. Le Roux, and S. Taheri. On the high cycle fatigue behavior of a type 304L stainless steel at room temperature. *International Journal of Fatigue*, 38:84 – 91, 2012.

[79] M. Miksch, E. Lenz, and R. Löhberg. Loading conditions in horizontal feedwater pipes of LWRs influenced by thermal shock and thermal stratification effects. *Nuclear Engineering and Design*, 84(2):179 – 187, 1985.

[80] M. Kamaya and M. Kawakubo. Mean stress effect on fatigue strength of stainless steel. *International Journal of Fatigue*, 74:20 – 29, 2015.

[81] N. E. Dowling. Mean stress effects in stress-life and strain-life fatigue. In *Second SAE Brasil International Conference on Fatigue*, United States, April 2004. SAE International.

[82] N. E. Dowling. Mean stress effects in strain–life fatigue. *Fatigue & Fracture of Engineering Materials & Structures*, 32(12):1004–1019, 2009.

[83] N. E. Dowling, C. A. Calhoun, and A. Arcari. Mean stress effects in stress-life fatigue and the walker equation. *Fatigue & Fracture of Engineering Materials & Structures*, 32(3):163–179, 2009.

[84] S. P. Zhu, Q. Lei, H. Z. Huang, Y. J. Yang, and W. W. Peng. Mean stress effect correction in strain energy-based fatigue life prediction of metals. *International Journal of Damage Mechanics*, 26(8):1219–1241, 2017.

[85] G. L. Wire, J. T. Kandra, and T. R. Leax. Mean stress and environmental effects on fatigue in type 304 stainless steel. 1999.

[86] X. Yuan, W. Yu, S. Fu, D. Yu, and X. Chen. Effect of mean stress and ratcheting strain on the low cycle fatigue behavior of a wrought 316LN stainless steel. *Materials Science and Engineering: A*, 677:193 – 202, 2016.

[87] N. Miura and Y. Takahashi. High-cycle fatigue behavior of type 316 stainless steel at 288°C including mean stress effect. *International Journal of Fatigue*, 28(11):1618 – 1625, 2006. Third International Conference on Very High Cycle Fatigue (VHCF-3).

[88] J. Colin, A. Fatemi, and S. Taheri. Fatigue Behavior of Stainless Steel 304L Including Strain Hardening, Prestraining, and Mean Stress Effects. *Journal of Engineering Materials and Technology*, 132(2), 02 2010.

[89] P. Li, S.X. Li, Z.G. Wang, and Z.F. Zhang. Fundamental factors on formation mechanism of dislocation arrangements in cyclically deformed fcc single crystals. *Progress in Materials Science*, 56(3):328 – 377, 2011.

[90] P. Li, Z.F. Zhang, X.W. Li, S.X. Li, and Z.G. Wang. Effect of orientation on the cyclic deformation behavior of silver single crystals: Comparison with the behavior of copper and nickel single crystals. *Acta Materialia*, 57(16):4845 – 4854, 2009.

[91] P. Li, S.X. Li, Z.G. Wang, and Z.F. Zhang. Formation mechanisms of cyclic saturation dislocation patterns in [001], [011] and $[1\bar{1}1]$ copper single crystals. *Acta Materialia*, 58(9):3281 – 3294, 2010.

[92] N. Grilli. *Physics-based constitutive modelling for crystal plasticity finite element computation of cyclic plasticity in fatigue*. PhD thesis, EPFL, Lausanne, 2016.

[93] H. Mughrabi. Fatigue, an everlasting materials problem - still en vogue. *Procedia Engineering*, 2(1):3 – 26, 2010. Fatigue 2010.

[94] Y. Li and C. Laird. Cyclic response and dislocation structures of aisi 316L stainless steel. part 1: single crystals fatigued at intermediate strain amplitude. *Materials Science and Engineering: A*, 186(1):65 – 86, 1994.

[95] Y. Li and C. Laird. Cyclic response and dislocation structures of aisi 316L stainless steel. part 2: polycrystals fatigued at intermediate strain amplitude. *Materials Science and Engineering: A*, 186(1):87 – 103, 1994.

[96] M. Gerland, J. Mendez, P. Violan, and B. Ait Saadi. Evolution of dislocation structures and cyclic behaviour of a 316L-type austenitic stainless steel cycled in vacuum at room temperature. *Materials Science and Engineering: A*, 118:83 – 95, 1989.

[97] Karel Obrtlík, Tomásš Kruml, and Jaroslav Polák. Dislocation structures in 316L stainless steel cycled with plastic strain amplitudes over a wide interval. *Materials Science and Engineering: A*, 187(1):1 – 9, 1994.

[98] H. Mughrabi. The cyclic hardening and saturation behaviour of copper single crystals. *Materials Science and Engineering*, 33(2):207 – 223, 1978.

[99] A. T. Winter. A model for the fatigue of copper at low plastic strain amplitudes. *The Philosophical Magazine: A Journal of Theoretical Experimental and Applied Physics*, 30(4):719–738, 1974.

[100] P. Peralta and C. Laird. *Cyclic Plasticity and Dislocation Structures*. 12 2016.

[101] J. Polak, K. Obrtlik, and M. Hajek. Cyclic plasticity in type 316L austenitic stainless steel. *Fatigue & Fracture of Engineering Materials & Structures*, 17(7):773–782, 1994.

[102] S. P. Bhat and C. Laird. The cyclic stress-strain curves in monocrystalline and polycrystalline metals. *Scripta Metallurgica*, 12(8):687 – 692, 1978.

[103] A.H. Cottrell. Lx. the formation of immobile dislocations during slip. *The London, Edinburgh, and Dublin Philosophical Magazine and Journal of Science*, 43(341):645–647, 1952.

[104] M. S. Pham. *FATIGUE BEHAVIOUR OF AISI 316L: Mechanical response, Microstructural evolution, Fatigue crack propagation, Physically-based constitutive modelling*. PhD thesis, ETH ZURICH, 2013. DISS. ETH NO. 20864.

[105] M. S. Pham and S. R. Holdsworth. Role of microstructural condition on fatigue damage development of aisi 316L at 20 and 300°C. *International Journal of Fatigue*, 51:36–48, 2013. 01421123.

[106] M. S. Pham, S. R. Holdsworth, K. G. F. Janssens, and E. Mazza. Cyclic deformation response of aisi 316L at room temperature: Mechanical behaviour, microstructural evolution, physically-based evolutionary constitutive modelling. *International Journal of Plasticity*, 47:143–164, 2013. 07496419.

[107] M. S. Pham and S. R. Holdsworth. Dynamic strain ageing of aisi 316L during cyclic loading at 300°C: Mechanism, evolution, and its effects. *Materials Science and Engineering: A*, 556:122–133, 2012. 09215093.

[108] M. S. Pham and S. R. Holdsworth. Evolution of relationships between dislocation microstructures and internal stresses of aisi 316L during cyclic loading at 293K and 573K (20°C and 300°C). *Metallurgical and Materials Transactions A*, 45:738–751, 2013. 1073-5623 1543-1940.

[109] M. Gerland, J. Mendez, J. Lépinoux, and P. Violan. Dislocation structure and corduroy contrast in a 316L alloy fatigued at (0.3–0.5) Tm. *Materials Science and Engineering: A*, 164(1):226 – 229, 1993. European Research Conference on Plasticity of Materials-Fundamental Aspects of Dislocation Interactions: Low-energy Dislocation Structures III.

[110] G. Baudry and A. Pineau. Influence of strain-induced martensitic transformation on the low-cycle fatigue behavior of a stainless steel. *Materials Science and Engineering*, 28(2):229 – 242, 1977.

[111] U. Krupp, C. West, and H. J. Christ. Deformation-induced martensite formation during cyclic deformation of metastable austenitic steel: Influence of temperature and carbon content. *Materials Science and Engineering: A*, 481-482:713 – 717, 2008. Proceedings of the 7th European Symposium on Martensitic Transformations, ESOMAT 2006.

[112] M. Nakajima, M. Akita, Y. Uematsu, and K. Tokaji. Effect of strain-induced martensitic transformation on fatigue behavior of type 304 stainless steel. *Procedia Engineering*, 2(1):323 – 330, 2010. Fatigue 2010.

[113] M. Gerland, R. Alain, B. Ait Saadi, and J. Mendez. Low cycle fatigue behaviour in vacuum of a 316L-type austenitic stainless steel between 20 and 600°C—part II: Dislocation structure evolution and correlation with cyclic behaviour. *Materials Science and Engineering: A*, 229(1):68 – 86, 1997.

[114] R. S. Barnes. Clusters of point defects in irradiated metals. *Discuss. Faraday Soc.*, 31:38–44, 1961.

[115] L. F. Coffin. A study of the effect of cyclic thermal stresses on a ductile metal. *Trans. Am. Soc. Mech. Eng.*, 76:931–950, 1954.

[116] S. S. Manson. Behaviour of materials under conditions of thermal stress. Technical report, Lewis Flight Propulsion Laboratory, Cleveland, OH, 1954. National advisory board commission on aeronautics: report 110.

[117] J. Morrow. *Fatigue properties of metals*, chapter Fatigue design handbook Sec. 3.2. SAE advance in engineering, pages 21–9. SAE, Warrendale, PA, 1968.

[118] J. Morrow. *Cyclic Plastic Strain Energy and Fatigue of Metals Internal Friction, Damping, and Cyclic Plasticity*. ASTM International, West Conshohocken, PA, 1965.

[119] J. Goodman. *Mechanics applied to engineering*. London : Longmans, Green, 9th ed edition, 1926.

[120] H. Gerber. *Bestimmung der zulässigen Spannungen in Eisen-Constructionen*. Wolf, 1874.

[121] H Dietmann. Festigkeitsberechnung bei mehrachsiger schwingbeanspruchung. *Konstruktion*, 25(5):181–189, 1973.

[122] C. R. Soderberg. title. *ASME Transactions*, 52(APM-52-2):13–28, 1930.

[123] K.N. Smith, T.H. Topper, and P. Watson. *A Stress-strain Function for the Fatigue of Metals*. Defense Technical Information Center, 1969.

[124] K.N. Smith, T. Topper, and P. Watson. A stress–strain function for the fatigue of metals (stress-strain function for metal fatigue including mean stress effect). *J Materials*, 5:767–778, 01 1970.

[125] K. Walker. *The Effect of Stress Ratio During Crack Propagation and Fatigue for 2024-T3 and 7075-T6 Aluminum*, chapter Effects of Environment and Complex Load History on Fatigue Life, pages 1–14. ASTM International, West Conshohocken, PA, 1970. https://doi.org/10.1520/STP32032S.

[126] S. S. Manson and G. R. Halford. Practical implementation of the double linear damage rule and damage curve approach for treating cumulative fatigue damage. *International Journal of Fracture*, 17(2):169–192, Apr 1981.

[127] F. Lorenzo and C. Laird. A new approach to predicting fatigue life behavior under the action of mean stresses. *Materials Science and Engineering*, 62(2):205 – 210, 1984.

[128] A. INCE and G. GLINKA. A modification of morrow and smith–watson–topper mean stress correction models. *Fatigue & Fracture of Engineering Materials & Structures*, 34(11):854–867, 2011.

[129] K. Golos and F. Ellyin. *Total Strain Energy Density as a Fatigue Damage Parameter*, pages 849–858. Springer Netherlands, Dordrecht, 1989.

[130] D. Kujawski. A deviatoric version of the swt parameter. *International Journal of Fatigue*, 67:95 – 102, 2014. Multiaxial Fatigue 2013.

[131] D. Kujawski. Fatigue failure criterion based on strain energy density. *Journal of Theoretical and Applied Mechanics*, 27(1), 1989.

[132] Y. C. Chiou and M. C. Yip. An energy-based damage parameter for the life prediction of AISI 304 stainless steel subjected to mean strain. *Journal of the Chinese Institute of Engineers*, 29(3):507–517, 2006.

[133] S. P. Zhu, H. Z. Huang, Y. Liu, R. Yuan, and L. P. He. An efficient life prediction methodology for low cycle fatigue–creep based on ductility exhaustion theory. *International Journal of Damage Mechanics*, 22(4):556–571, 2013.

[134] S. P. Zhu, H. Z. Huang, L. P. He, Y. Liu, and Z. L. Wang. A generalized energy-based fatigue–creep damage parameter for life prediction of turbine disk alloys. *Engineering Fracture Mechanics*, 90:89 – 100, 2012.

[135] S. P. Zhu, Q. Lei, H. Z. Huang, Y. J. Yang, and W. Peng. Mean stress effect correction in strain energy-based fatigue life prediction of metals. *International Journal of Damage Mechanics*, 26(8):1219–1241, 2017.

[136] Jussi Solin, Sven Reese, Hüseyin Karabaki, and Wolfgang Mayinger. Fatigue performance of stabilized austenitic stainless steels: Experimental investigations respecting operational relevant conditions like temperature and hold time effects. volume 1, 07 2013.

[137] O. K. Chopra and W. J. Shack. A Review of the Effects of Coolant Environments on the Fatigue Life of LWR Structural Materials. *Journal of Pressure Vessel Technology*, 131(2), 01 2009. 021409.

[138] T.T. Pleune and O. K. Chopra. Using artificial neural networks to predict the fatigue life of carbon and low-alloy steels. *Nuclear Engineering and Design*, 197(1):1 – 12, 2000.

[139] M. Al-Assadi, H. A. El Kadi, and I. M. Deiab. Using artificial neural networks to predict the fatigue life of different composite materials including the stress ratio effect. *Applied Composite Materials*, 18(4):297–309, Aug 2011.

[140] A. P. Vassilopoulos, E. F. Georgopoulos, and V. Dionysopoulos. Artificial neural networks in spectrum fatigue life prediction of composite materials. *International Journal of Fatigue*, 29(1):20 – 29, 2007.

[141] V.S. Srinivasan, M. Valsan, K. B. S. Rao, S. L. Mannan, and B. Raj. Low cycle fatigue and creep–fatigue interaction behavior of 316L(N) stainless steel and life prediction by artificial neural network approach. *International Journal of Fatigue*, 25(12):1327 – 1338, 2003.

[142] H. J. Leber, Stefan R., and H. P. Seifert. Thermo-mechanical and isothermal low-cycle fatigue behavior of type 316L stainless steel in high-temperature water and air. *CORROSION*, 69(10):1012–1023, 2013.

[143] M. Ramesh, H. J. Leber, M. Diener, and R. Spolenak. Conducting thermomechanical fatigue test in air at light water reactor relevant temperature intervals. *Journal of Nuclear Materials*, 415(1):23 – 30, 2011.

[144] P. M. Yuzawich and C. W. Hughes. An improved technique for removal of oxide scale from fractured surfaces of ferrous materials. *Practical Metallography*, 1978.

[145] L. De Baglion De La Dufferie. *Comportement et endommagement en fatigue oligocyclique d'un acier inoxydable austénitique 304L en fonction de l'environnement (vide, air, eau primaire REP) à 300°C.* Theses, ISAE-ENSMA Ecole Nationale Supérieure de Mécanique et d'Aérotechique - Poitiers, June 2011.

[146] S. CHAPULIOT. chapuliot formulaire de KI pour les tubes comportant un defaut de surface semi-elliptique longitudinal ou circonferential. Technical Report RAPPORT CEA-R-5900, CEA, 2000.

[147] M. Kamaya. Influence of strain range on fatigue life reduction of stainless steel in pwr primary water. *Fatigue & Fracture of Engineering Materials & Structures*, 40:2194–2203, 2017.

[148] M. Kamaya and M. Kawakubo. Strain-based modeling of fatigue crack growth – an experimental approach for stainless steel. *International Journal of Fatigue*, 44:131–140, 2012.

[149] M. H. El Haddad, K. N. Smith, and T. H. Topper. Fatigue Crack Propagation of Short Cracks. *Journal of Engineering Materials and Technology*, 101(1):42–46, 01 1979.

[150] J. Polak and P. Zezulka. Short crack growth and fatigue life in austenitic-ferritic duplex stainless steel. *Fatigue & Fracture of Engineering Materials & Structures*, 28(10):923–935, 2005.

[151] J. R. Haigh and R. P. Skelton. A strain intensity approach to high temperature fatigue crack growth and failure. *Materials Science and Engineering*, 36:133–137, 1978.

[152] W. Zhang, H. Liu, Q. Wang, and J. He. A fatigue life prediction method based on strain intensity factor. *Materials*, 10:689, 2017.

[153] P. Hutař, J. Poduška, M. Šmíd, Ivo Kuběna, A. Chlupová, L. Náhlík, J. Polák, and T. Kruml. Short fatigue crack behaviour under low cycle fatigue regime. *International Journal of Fatigue*, 103:207 – 215, 2017.

[154] J. R. Rice. A Path Independent Integral and the Approximate Analysis of Strain Concentration by Notches and Cracks. *Journal of Applied Mechanics*, 35(2):379–386, 06 1968.

[155] J. Chen, S. Takezono, K. Tao, and T. Hazawa. Application of fracture mechanics to the surface crack propagation in stainless steel at elevated temperatures. *Acta Materialia*, 45(6):2495 – 2500, 1997.

[156] J. Mann, M. Twite, and M. G. Burke. Analysis of Fatigue Crack Growth in Standard Endurance Test Specimens in Support of Total Life Approaches to Fatigue Assessment. volume Volume 5: High-Pressure Technology; Rudy Scavuzzo Student Paper Symposium and 24th Annual Student Paper Competition; ASME Nondestructive Evaluation, Diagnosis and Prognosis Division (NDPD); Electric Power Research Institute (EPRI) Creep Fatigue Workshop of *Pressure Vessels and Piping Conference*, 07 2016. V005T09A026.

[157] C. F. Shih and J. W. Hutchinson. Fully Plastic Solutions and Large Scale Yielding Estimates for Plane Stress Crack Problems. *Journal of Engineering Materials and Technology*, 98(4):289–295, 10 1976.

[158] M. Kamaya. Environmental effect on fatigue strength of stainless steel in pwr primary water-role of crack growth acceleration in fatigue life reduction. *International Journal of Fatigue*, 55:102–111, 2013.

[159] M. Nezakat, H. Akhiani, S. Penttilä, and J. Szpunar. Oxidation Behavior of Austenitic Stainless Steel 316L and 310S in Air and Supercritical Water. *Journal of Nuclear Engineering and Radiation Science*, 2(2), 02 2016. 021008.

[160] V. Mazánová, V. Škorík, T. Kruml, and J. Polák. Cyclic response and early damage evolution in multiaxial cyclic loading of 316L austenitic steel. *International Journal of Fatigue*, 100:466 – 476, 2017. Multiaxial Fatigue 2016: Experiments and Modeling.

[161] J. M. Lee and S. W. Nam. Effect of crack initiation mode on low cycle fatigue life of type 304 stainless steel with surface roughness. *Materials Letters*, 10(6):223 – 230, 1990.

[162] J. A. Abdalla and R. A. Hawileh. Artificial neural network predictions of fatigue life of steel bars based on hysteretic energy. *Journal of Computing in Civil Engineering*, 27(5):489–496, 2013.

[163] S. K. Paul. A critical review of experimental aspects in ratcheting fatigue: microstructure to specimen to component. *Journal of Materials Research and Technology*, 8(5):4894 – 4914, 2019.

[164] P. Gill, P. James, C. Currie, C. Madew, and A. Morley. An Investigation Into the Lifetimes of Solid and Hollow Fatigue Endurance Specimens Using Cyclic Hardening Material Models in Finite Element Analysis. volume Volume 1A: Codes and Standards of *Pressure Vessels and Piping Conference*, 07 2017. V01AT01A028.

[165] M. Twite, N. Platts, A. McLennan, J. Meldrum, and A. McMinn. Variations in Measured Fatigue Life in LWR Coolant Environments due to Different Small Specimen Geometries. volume Volume 1A: Codes and Standards of *Pressure Vessels and Piping Conference*, 07 2016. V01AT01A025.

[166] K. H. Bae and S. B. Lee. The effect of specimen geometry on the low cycle fatigue life of metallic materials. *Materials at High Temperatures*, 28(1):33–39, 2014.

[167] A. McLennn, P. Spätig, L.R. J.C., J. Waters, P. Gill, J. Beswick, and N. Platts. Incefa-plus project: the impact of using fatigue data generated from multiple specimen geometries on the outcome of a regression analysis. In *ASME 2020 Pressure Vessels and Piping Division Conference*, Minneapolis, USA, 2020.

[168] P. Gill, P. James, C. Currie, C. Madew, and A. Morley. An Investigation Into the Lifetimes of Solid and Hollow Fatigue Endurance Specimens Using Cyclic Hardening Material Models in Finite Element Analysis. volume Volume 1A: Codes and Standards of *Pressure Vessels and Piping Conference*, 07 2017. V01AT01A028.

[169] S. Asada, K. Tsutsumi, Y. Fukuta, and H. Kanasaki. Applicability of Hollow Cylindrical Specimens to Environmental Assisted Fatigue Tests. volume Volume 1A: Codes and Standards of *Pressure Vessels and Piping Conference*, 07 2017. V01AT01A022.

[170] J. P. Hirth. On dislocation interactions in the fcc lattice. *Journal of Applied Physics*, 32(4):700–706, 1961.

[171] Y. Li and C. Laird. Cyclic response and dislocation structures of aisi 316L stainless steel. part 1: single crystals fatigued at intermediate strain amplitude. *Materials Science and Engineering: A*, 186(1):65 – 86, 1994.

[172] H. Mughrabi. The long-range internal stress field in the dislocation wall structure of persistent slip bands. *Physica Status Solidi Applied Research*, 104(1):107–120, November 1987.

[173] S. K. Koh and R. I. Stephens. Mean stress effects on low cycle fatigue for a high strength steel. *Fatigue & Fracture of Engineering Materials & Structures*, 14(4):413–428, 1991.

Wen Chen

Birth 16.08.1988, Chinese with Swiss B permit
Sommerhaldenstrasse 1A, 5200 Brugg, Switzerland
(+41)7621-729-97 chenwen816@gmail.com

PROFESSIONAL SUMMARY

- A highly motivated PhD candidate with extensive industrial experiences (Automotive, telecom TMT) has proven track record in project management, technical writing, innovative thinking, information processing, fast learning and interpersonal skills and also with solid knowledge and experience in materials science & engineering, data science (Python, Mathematica, MATLAB, MySQL), machine learning (ANN), technical regulation & homologation (automotive) and business consulting (Telecom)
- The PhD work was highly evaluated with 2 student grants, one transferred venture project, 7 conference contributions and 6 publications. Supervised 6 apprentices and 2 interns

EDUCATION

- 04.2016 - 03.2020 **PhD student, Group for Structural Integrity**
  Paul Scherrer Institute, Switzerland
  - Second award, Switzerland Chinese venture competition, Switzerland, 2019
  - Candidate of Paul Scherrer Institute Founder Fellowship (PSIFF), Switzerland, 2019
  - ICG-EAC Student Grant, Taiwan, 2019
  - European Commission Grant "Materials resistant to extreme conditions for future energy", Kiev, 2017
- 04.2016 - 03.2020 **PhD student, Materials Science and Engineering**
  EPFL, Lab. Of Reactor Physics, Switzerland
- 08.2011 - 05.2014 **Master degree, Physical Metallurgy and Metal Physics**
  RWTH-Aachen University, Germany
- 09.2007 - 07.2011 **Bachelor degree, Metallurgical Engineering**
  University of Science and Technology Beijing, China
  - Several times was awarded Chinese National Scholarship, 2007-2011
  - Excellent Achievement in Social Practice of Capital University Students, 2009
  - Champion in the USTB Business Simulation Competition, 2009
  - Second place in the Beijing College Student Karate Competition, 2008
  - Excellent volunteer during 2008 Beijing Olympic Games & Paralympic Games, 2008

FURTHER EDUCATION

- 09.2018 - 12.2018 **Startup Campus on "Business Concept", Switzerland**
- 05.2011 - current **Massive Open Online Courses (MOOC):** by Yale, MIT, Wharton School (with certificates)
  Include: machine learning, computer science and programming (python), etc.

SELECTED PUBLICATIONS

- W.Chen, P. Spätig, H.P. Seifert, Mean stress effect on fatigue behavior of austenitic stainless steel in air and LWR conditions, Structural Integrity: Mechanical Fatigue of Metals-Experimental and Simulation Perspectives. Springer (2018).
- W.Chen, P. Spätig, H.P. Seifert, Fatigue behavior of 316L austenitic stainless steel in LRW environment and in air with and without mean stress, MATEC Web of Conferences 165, 03012 (2018).
- B. Kuhn, M. Talik, J. Lopez Barrilao, W. Chen, J. Ning, Microstructure evolution and creep strength of high performance ferritic (Hiperfer) steels, 3rd International ECCC-Creep & Fracture Conference, Rome, Italy, 2014.
- W. Chen, S.B. Wang, J.B. Ge, S.Q. Jiao, H.M. Zhu, Electrochemical synthesis of Nb_5Si_3 intermetallic compound from molten calcium chloride salt, Intermetallics, 25(2012), p66-69.

CONFERENCE CONTRIBUTION

- W. Chen, P. Spätig, H.P. Seifert, Fatigue crack initiation and growth of austenitic stainless steel tube in high-temperature water/air with/without mean stress, July 14-19, San-Antonio, USA, 2019.
- W. Chen, Y.X. Li, P. Spätig, H.P. Seifert, Environmentally-assisted fatigue of austenitic stainless steel in high-temperature water/air with/without mean stress, May 12-17, Tainan, Taiwanm, 2019.
- W. Chen, P. Spätig, H.P. Seifert, Mean stress effect on fatigue behavior of austenitic stainless steel in air and LWR conditions, XIX international Colloquium on Mechanical Fatigue of Metals (ICMFM XIX), September 05-07, Porto, Portugal, 2018.
- W. Chen, P. Spätig, H.P. Seifert , Mean stress effect on fatigue behavior of austenitic stainless steel in air and LWR condition, 22nd European Conference on Fracture (ECF 22), August 28-31, Belgrade, Serbia, 2018.

- W. Chen, P. Spätig, H.P. Seifert, Fatigue behavior of 316L austenitic stainless steel in air and LWR environment with and without mean stress, 12th International Fatigue Congress (FATIGUE 2018), May 27-June 1, Poitier, France, 2018.
- W. Chen, P. Spätig, H.P. Seifert, Fatigue behavior of 316L austenitic steel in air and LWR environment with and without mean stress, 14th Int. Conference on Fracture (IFC 14), June 18-23, Rhodes, Greece, 2017.
- W. Chen, P. Spätig, H.P. Seifert, Mean stress effect on environmental assisted fatigue of 316L austenitic steel in LWR environment, International Workshop on Materials Resistant to Extreme Conditions for Future Energy Systems, June 12-14, Kiev, Ukraine, 2017.

WORK EXPERIENCE

- 04.2016 – 03.2020 **PhD student**
  Paul Scherrer Institute, Villigen, Switzerland
  - Working on SAFE and LEAD projects (sponsored by Swiss nuclear inspector ENSI) and INCEFA+ project (European Horizon 2020 project closely work with 16 European partners)
  - Experimentally & numerically studying the fatigue behavior of stainless steels under different mechanical & environmental loading
- 02.2015 - 03.2016 **Technical regulation & homologation specialist**
  Renault, Beijing, China
- 02.2014 - 02.2015 **Business consultant**
  Ericsson, Ericsson Business Consulting, Beijing, China
- 08.2013- 02.2014 **Scientific researcher for master thesis**
  Jülich Research Centre, IEK-2 Institute, Jülich, Germany
- 05.2013 - 08.2013 **Intern**
  Daimler AG, Intellectual property & technology management, Stuttgart, Germany
- 05.2012 - 04.2013 **Research assistant**
  RWTH-AACHEN University, IEHK Iron & Steel Institute, Aachen, Germany

OTHER ACTIVITIES

- 06.2017 - current Guider for Sunday service, PSI Forum Exhibition Center , Switzerland
- 09.2017 - 09.2018 PhD student representative, EPFL Doctoral School, Switzerland
- 04.2016 - 04.2018 Vice president, Chinese Scholar & Students Association in PSI Aargau, Switzerland
- 07.2014 - current Cofounder, Yurong Karate (a Ed-Tech startup in K-12 market), Beijing
- 12.2013 - 12.2013 Trainee, CDI Business Workshop, Paris
- 09.2011 - 05.2014 Vice president, Chinese Scholar & Students Association, Aachen
- 08.2008 - 09.2008 Volunteer, 2008 Beijing Olympic Games & Paralympic Games, Beijing
- 04.2008 - 08.2008 Trainee, IBM Business Simulation Training, Beijing
- 03.2008 - 06.2012 Co-founder & president, Karate association of USTB Uni., Beijing

LANGUAGE PROFICIENCY

- Chinese: native English: full professional German: professional (C1 level of GER) French: elementary

OTHER SKILLS

- Transferable skills: project management, technical sales, communication, time management, conflict management, marketing strategy, leadership, team work, correct email writing (certificate), innovative thinking (certificate)
- Accounting: accounting, strategy and risk management, economic law (CPA courses)
- Materials characterization & mechanical tests: SEM, TEM, EBSD, ECCI, FIB, EDX, XRD, DIC, fatigue test
- Programming & numerical tools: Python, Mathematica, C, C++, Matlab, MySQL, TensorFlow, Pandas, Numpy, Scipy, Matplotlib, Scikit-learn, Jupyter Notebook/Spyder, Latex, etc.
- Computer application: Microsoft office, AutoCAD, Photoshop, Illustrator, PageMaker, digital image analysis, etc.
- Others: First aid (with Red Cross issued first aid certificate), Karate training, etc.

PERSONAL INTEREST

- Travelling, Karate (once won 2nd in Beijing Karate Competition and being a Karate master), Jiu-jitsu, shooting (member of Shooting Club), football, reading, hiking, biking, cooking, etc.